Blast interactions with inert and reactive materials in heterogeneous explosive systems

Quentin Pontalier

Department of Mechanical Engineering

McGill University, Montreal

December 2022

A thesis submitted to McGill University in partial fulfillment of the requirements of the degree of

Doctor of Philosophy

To my grandfather and mentor, Apy ...

Abstract

Understanding explosion effects are of major interest for the fundamental knowledge but also for several applications. For example, explosions resulting from the detonation of reactive materials in industrial accidents, as well as on the battlefield pose serious hazards. The combination of blast wave effects and the dispersal of solid fragments at supersonic velocities, can cause substantial damage to personnel and structures over a large area. However, the interactions between these two effects remain poorly understood. Therefore, it is important to elucidate the nature of these interactions to improve the prediction and mitigation of the hazards associated with explosions. Conversely, for military or mining applications, it is of interest to understand these interactions to enhance the power of conventional explosives.

Detonating a high explosive is a convenient method to generate a powerful explosion. In the present experimental and numerical work, the interaction between the blast wave pressure field and the multiphase gas-particle flow generated by the detonation of heterogeneous explosive charges is evaluated. The two configurations investigated are comprised of either i) a solid high explosive charge surrounded by inert solid and/or liquid materials, forming a stratified system or ii) a liquid high explosive uniformly embedded with either inert or reactive metallic particles. While the first configuration is typically studied for blast wave mitigation, the second configuration is more relevant for blast wave enhancement studies. In the first configuration, the stratified system is comprised of a spherical explosive charge surrounded by either a bulk liquid layer, or a packed layer of granular material, either dry or saturated with water. Various materials are tested at different ratios of the mass of material to the explosive mass (M/C). Experimental results show that the peak blast pressure in the near field is always reduced in comparison to the peak blast pressure generated by a homogeneous explosive charge of the same volume. The blast attenuation is mainly attributed to the transfer of heat and momentum from the explosive gases to the solid/liquid material. A comprehensive comparison of the blast attenuation between liquid and granular layers demonstrates that the latter are much more efficient at mitigating the blast wave. The greater blast attenuation effectiveness of a powder layer is primarily attributed to the work done in compacting the porous particle layer. In comparison, for a powder layer saturated with liquid, the blast attenuation is similar to a bulk liquid since the load-bearing capability of the interstitial water limits compaction. The M/C ratio is found to be the dominant parameter for mitigation effectiveness, whereas the material properties play a secondary role. The attenuation efficiency is also not uniform at all distances from the charge. This phenomenon is attributed to

the influence of the expanding cloud of solid/liquid material, which acts effectively as a porous piston, on the blast wave. The piston effect, which has not been characterized in the literature for explosively dispersed liquids and powders, reduces the blast pressure decay with distance and must be taken into account in the design of blast wave mitigation systems. Numerical simulations based on a two-fluid model are consistent with the experimental results and reproduce the trends of the peak blast pressure decay with distance. They demonstrate that the direction of the heat transfer gradients and the drag force between the materials and the surrounding gas, which depends on M/C and the particle size, directly impact the blast mitigation efficiency at different distances from the charge. This result suggests that blast mitigation systems must be adapted as a function of the distance from the explosion center.

In the second experimental configuration, the charge is composed of a gelled liquid explosive uniformly embedded with a dilute suspension of inert (glass) or reactive (aluminum or magnesium) particles. Investigating the blast enhancement of metalized explosives is of interest to understand the fundamentals underlying metal chemical reactions at high pressure. Studying these explosive systems is also important for designing enhanced blast explosives (EBX), for military or mining applications. As for the first configuration, experiments show a peak blast pressure reduction in the mid field with added glass particles, compared with a charge of the same volume containing the baseline gelled liquid explosive alone. Similar to the stratified systems with inert material, with embedded glass particles, the peak blast pressure recovers to that of the baseline in the far field, due to the aforementioned piston effect. For trials with constant volume explosive charges with embedded reactive particles, the blast pressure is systematically higher than that of the baseline charge with no particles. This pressure augmentation is directly attributed to the exothermic particle reaction counteracting the reduction in explosive mass with the addition of the particles. The first signs of blast enhancement are observed a few hundred microseconds after detonation, suggesting that anaerobic particle reactions within the detonation products, on microsecond timescales, contribute to the augmentation of the blast pressure. This experimental observation contradicts previous models that assume that the particles react only aerobically with the surrounding air outside of the fireball on millisecond timescales. Furthermore, the blast augmentation is not a systematic function of particle size. This result implies that conventional models for particle reaction that depend on particle surface area are not valid for describing the particle combustion that occurs in the high temperature and pressure environment within the detonation products. Numerical calculations are carried out using the same model as for the first configuration but including a simplified particle reaction model in which the timescale and amount of particle energy release are systematically varied. The results indicate that at least half of the maximum particle chemical energy must be released within the first tens of microseconds to explain the blast enhancement in the far field for higher particle mass loading, and nearly all of the particle energy for small particle mass loading.

Abrégé

La compréhension des effets des explosions présente un intérêt majeur pour la recherche fondamentale mais aussi pour plusieurs applications. Par exemple, les explosions résultant de la détonation de matériaux réactifs dans les accidents industriels ou sur le champ de bataille sont extrêmement dangereuses. La combinaison des effets de souffle et de la dispersion de fragments solides à des vitesses supersoniques, peut causer des dommages substantiels au personnel et aux bâtiments sur une large surface. Cependant, les interactions entre ces deux effets restent peu comprises. Il est donc important d'élucider la nature de ces interactions afin d'améliorer la prédiction et l'atténuation des risques associés aux explosions. Inversement, pour des applications militaires ou minières, il est intéressant de comprendre ces interactions afin d'améliorer la puissance des explosifs conventionnels.

Une méthode pratique pour générer une explosion puissante est de faire détoner un explosif. Dans le présent travail expérimental et numérique, l'interaction entre le champ de pression de l'onde de souffle et l'écoulement multiphasique gaz-particules généré par la détonation de charges explosives hétérogènes est évaluée. Les deux configurations étudiées sont composées soit i) d'une charge explosive solide entourée de matériaux solides et/ou liquides inertes, formant un système stratifié, soit ii) d'une charge explosive liquide mélangée avec des particules métalliques inertes ou réactives. Alors que la première configuration est généralement étudiée pour l'atténuation des ondes de souffle, la deuxième configuration est plus pertinente pour les études d'amélioration des ondes de souffle. Dans la première configuration, le système stratifié est constitué d'une charge explosive sphérique entourée soit d'une couche de liquide pur, soit d'une couche tassée de matériau granulaire, sèche ou saturée d'eau. Divers matériaux sont testés à différents rapports de masse matériau-explosif (M/C). Les résultats expérimentaux montrent que la pression de souffle maximale dans le champ proche est toujours réduite par rapport à la pression de souffle maximale générée par une charge explosive homogène de même volume. L'atténuation du souffle est principalement attribuée au transfert de chaleur et de quantité de mouvement des gaz explosifs vers le matériau solide/liquide. Une comparaison exhaustive de l'atténuation du souffle entre les couches liquides et granulaires démontre que ces dernières sont beaucoup plus efficaces pour atténuer l'onde de souffle. La plus grande efficacité d'atténuation des couches de poudre granulaire est principalement attribuée au travail effectué pour compacter la couche poreuse de particules. En comparaison, pour une couche de poudre saturée de liquide, l'atténuation du souffle est similaire à celle d'un liquide pur puisque la capacité de

résistance aux contraintes de l'eau interstitielle permet de limiter la compaction. Le rapport M/C s'avère être le paramètre dominant dans l'efficacité d'atténuation, alors que les propriétés des matériaux jouent un rôle secondaire. L'efficacité d'atténuation n'est pas non plus constante à toutes les distances de la charge initiale. Ce phénomène est attribué à l'influence du nuage de matériaux solides/liquides en expansion qui agit comme un piston poreux sur l'onde de souffle. Cet effet piston, qui n'a jamais été caractérisé dans la littérature pour des liquides et poudres explosivement dispersés, réduit le déclin du pic de pression du souffle avec la distance et doit être pris en compte dans la conception des systèmes d'atténuation du souffle. Les simulations numériques basées sur un modèle à deux fluides sont cohérentes avec les résultats expérimentaux et reproduisent les tendances générales du déclin du pic de pression avec la distance. Elles démontrent que la direction des gradients de transfert de chaleur et de la force de traînée entre l'écoulement et les matériaux, qui dépend elle-même du ratio M/C et de la taille des particules, a un impact direct sur l'efficacité d'atténuation du souffle à différentes distances de la charge initiale. Ce résultat suggère que les systèmes d'atténuation du souffle doivent être adaptés en fonction de la distance par rapport au centre de l'explosion.

Dans la deuxième configuration expérimentale, la charge est composée d'une suspension de particules inertes (verre) ou réactives (aluminium ou magnésium) uniformément diluée dans un explosif liquide gélifié. L'étude de l'amélioration de l'effet de souffle des explosifs métallisés est particulièrement pertinente pour comprendre les principes fondamentaux de la réaction des métaux à haute pression ou pour la conception d'explosifs à effet de souffle amélioré (EBX), pour des applications militaires ou minières. Comme pour la première configuration, les expériences montrent une réduction du pic de pression du souffle dans le champ moyen avec l'ajout de particules de verre, par rapport à une charge de même masse contenant seulement l'explosif liquide gélifié. Comme pour les systèmes stratifiés avec des matériaux inertes, si des particules de verre sont incorporées, le pic de pression revient à celui de la ligne de base dans le champ lointain, en raison de l'effet piston susmentionné. Pour les essais avec des charges explosives mélangées avec des particules réactives à volume constant, la pression de souffle est systématiquement plus élevée que celle de la charge de référence sans particules. Cette augmentation de pression est directement attribuée aux réactions exothermiques particulaires qui contrebalancent la réduction de la masse explosive due à l'ajout de particules. Les premiers signes d'augmentation du souffle sont observés quelques centaines de microsecondes après la détonation, ce qui suggère que les réactions anaérobies des particules dans les produits de détonation, à l'échelle de la microseconde, contribuent à l'augmentation de la pression du souffle. Cette observation expérimentale contredit les modèles précédents qui supposent que les particules réagissent uniquement de manière aérobie avec l'air environnant, à l'extérieur de la boule de feu sur des échelles de temps de quelques millisecondes. De plus, l'augmentation de la pression de souffle n'est pas une fonction monotone de la taille des particules. Ce résultat implique que les modèles conventionnels de réaction qui dépendent de la surface particulaire ne sont pas valables pour décrire la combustion des particules qui se produit dans l'environnement

de haute température et de pression situé à l'intérieur des produits de détonation. Des calculs numériques sont effectués en utilisant le même modèle que pour la première configuration, mais en incluant un modèle simplifié de réaction particulaire dans lequel l'échelle de temps et la quantité d'énergie libérée par les particules sont variées systématiquement. Les résultats indiquent qu'au moins la moitié de l'énergie chimique maximale des particules doit être libérée dans les premières dizaines de microsecondes pour expliquer l'augmentation de pression de souffle dans le champ lointain pour un chargement massique de particules élevé, et presque toute l'énergie pour un faible chargement massique de particules.

Acknowledgements

First and foremost, I thank my supervisor, Prof. David Frost. David tirelessly wrote me letters of support, read and edited my manuscript drafts, supported me financially, and offered me the possibility to present my work at international conferences. Thank you, David, for all of this and for your faith in my ability to finalize this thesis manuscript. I also thank Dr. Jason Loiseau for his guidance and unofficial supervision during my doctoral journey's second half. Dr. Jason Loiseau was always present for venting, advice, and detailed comments on my work.

I am also grateful to my thesis committee members, Prof. Evgeny Timofeev and Prof. Jeffrey Bergthorson for their comments on my literature review and thesis proposal. I want to thank Evgeny for his precious assistance with publishing my papers in the *Shock Waves* journal and Jeff for letting me practise talks in his research group. I would also like to thank Jan Palecka and Dr. Phillipe Julien for their precious support during the difficult time of my comprehensive preliminary oral exam. I also thank Dr. Samuel Goroshin for sharing his knowledge of metal combustion and his interpretations.

Thank you, Prof. Hoi Dick Ng at Concordia University, for introducing me to McGill professors and Prof. John H.S Lee/Prof. Andrew Higgins for helping me choose a Ph.D. supervisor. I also must thank my former colleagues (Dr. Stefan Brieschenk, Dr. Tamara Sopek, Dr. Wilson Chan, and Prof. Tim McIntyre) from the Center for Hypersonics at the University of Queensland (Brisbane, QL, Australia) for their strong recommendation letters towards McGill admission. They inspired me and continue to inspire me as researchers and individuals.

I also thank Rick Guilbeault for his expert technical assistance with the experiments and all the staff at the Canadian Explosive Research Laboratory (CERL, Nepean, ON, Canada). The financial support from Dr. Fan Zhang for the experiments carried out at Suffield, AB, Canada, was also greatly appreciated. Similarly, I would like to thank all Fluid Gravity Engineering Inc (St. Andrews, Scotland) staff for their technical assistance with the numerical simulations and interesting discussions. Special thanks to Dr. Aaron Longbottom and Dr. Alec Milne for providing the EDEN hydrocode and their scientific comments on my computational papers. I would also like to thank Maxime Lhoumeau for helping me perform the numerical simulations.

I would also like to thank all the past and current students from the Alternative Fuel Lab (AFL), the Shock Waves Physics Group (SWPG), and other students from the Mechanical Engineering Department for the scientific or casual discussions, the many shared pitchers of ale and for making my graduate life entertaining. I also thank the Mechanical Engineering

department administrative staff, Connie Greco, Anne-Marie Pierre, Mary Fiorilli, Gregory Doyle, and Shumirai Wamambo, for their support and keeping me on track.

I would like to express my gratitude to the final jury of my Ph.D. oral examination Aliki Thomas (McGill), Evgeny Timofeev (McGill), Bantwal Rabindranath Baliga (McGill), Pascal Hubert (McGill), Stephen Yue (McGill), Marcia Cooper (Texas A&M), for treating me respectfully, for their thorough thesis review and their very relevant comments on my work.

Finally, and above all, I would like to extend my full gratitude to my loving family for their invaluable support, understanding, and for believing in me throughout my entire life. I dedicate the present thesis manuscript to my grandfather and mentor, Apy, a former geologist, who has always supported my desire to pursue physics studies since my youngest age. Apy, unfortunately, passed away a few months before my thesis submission. I would also thank all my friends on all the continents I visited for their strong support, including my "Zbeul" brethren and sistren in Quebec, without whom my thesis would probably not have been completed.

Original contributions to knowledge

The original work detailed in this thesis is comprised of 3 published journal manuscripts (Chapters 3, 4, 5) and 1 published conference manuscript (Chapter 6).

Part II

Chapter 3 - (Journal) Publication: “Experimental investigation of blast mitigation and particle–blast interaction during the explosive dispersal of particles and liquids" in *Shock Waves* [1]
Q. Pontalier, J. Loiseau, S. Goroshin, D. L. Frost

This chapter presents the most extensive blast wave pressure mitigation analysis to date, for a spherical high explosive charge (C-4) surrounded by a liquid or solid granular layer. The experimental dataset gathers selected results from a decade of field trials. The extensive comparison of the blast wave pressure attenuation by the liquids and the solid particle beds shows that the latter are clearly more efficient at mitigating the blast wave. The results also demonstrate that the dispersed material acts as a porous piston on the blast wave. This piston effect, which has never been characterized in the literature for explosively dispersed powders or liquids, contributes to reducing the blast wave mitigation effectiveness in the far field. Consideration of this piston effect in the design of mitigation systems is crucial to reduce the risk of explosions encountered during industrial accidents, terrorist attacks or transportation of energetic materials.

Chapter 4 - (Journal) Publication: “Numerical investigation of particle–blast interaction during explosive dispersal of liquids and granular materials" in *Shock Waves* [2]
Q. Pontalier, M. Lhoumeau, A. M. Milne, A. W. Longbottom, D. L. Frost

This numerical study shows that a two-phase model based on a formulation similar to that of Baer and Nunziato [3] is able to reproduce the trends of the experimental results found in the previous chapter. A parametric study is carried out to investigate the dominant factors of blast wave mitigation. The results confirm that the mass of mitigant to explosive mass ratio (M/C) is the primary parameter of blast wave attenuation, whereas the particle size plays a secondary role. The porous piston effect is effectively predicted by the numerical simulations. This effect is attributed to the direction reversal of the heat transfer gradients and the drag force

between the materials and the surrounding gas. This phenomenon was never reported in related studies despite using similar numerical strategies. The spatial region affected by the porous piston effect depended on the properties of the dispersed material layer, suggesting that blast wave attenuation systems must be tailored according to the distance from the explosion center.

Part III

Chapter 5 - (Journal) Publication: “Blast enhancement from metalized explosives" in *Shock Waves* [4]
Q. Pontalier, J. Loiseau, S. Goroshin, F. Zhang, D. L. Frost

The blast wave pressure resulting from the detonation of spherical metalized explosive charges at constant volume is studied experimentally. The charges are comprised of dilute suspensions of aluminum and magnesium particles, embedded in gelled and sensitized nitromethane. The exothermic and anaerobic reactions of the particles are found to contribute to the blast wave pressure enhancement a few hundred microseconds after detonation. The blast wave pressure augmentation is also not a systematic function of particle size. These experimental observations contradict previous models, which assume that the particles react only aerobically with the ambient air outside of the fireball, on millisecond timescales. Those models are therefore inadequate to describe the particle reaction inside the detonation products of metalized explosives. The systematic peak blast overpressure augmentation observed for these metallized explosive charges suggests a high capacity to break rocks. Therefore, metalized explosives with a small loading of particles are interesting for mining applications.

Chapter 6 - (Conference) Publication: “Numerical investigation of blast enhancement with metalized explosives" in *32nd International Symposium on Shock Waves (ISSW 32)* [5]
Q. Pontalier, A. Longbottom, S. Cargill, C. Grapes, A. Milne, J. Loiseau, S. Goroshin, F. Zhang, D. L. Frost

In this chapter, the timescale and the amount of particle energy release for aluminized charges are investigated. These two parameters are systematically varied in order to reproduce the experimental blast wave pressures of the previous chapter. A simplified reaction model in which the energy is deposited in the particle phase and then released to the surrounding gas by convective heat transfer is used. The results indicate that a substantial amount of energy must be released at very fast timescale to reproduce the experimental blast wave pressure. It is found that at least half of the maximum particle chemical energy must be released within the first tens of microseconds to explain the blast enhancement in the far field, for particle mass fraction between 10% and 50%. For a particle mass fraction of 10%, nearly all of the particle energy must be released. The results of this chapter indicate that a model based solely on the energy

release of metal particles and neglecting chemical aspects may be sufficient to estimate the blast wave pressure of metalized explosives.

References

[1] Q. Pontalier, J. Loiseau, S. Goroshin, and D. L. Frost. Experimental investigation of blast mitigation and particle-blast interaction during the explosive dispersal of particles and liquids. *Shock Waves*, 28(3):489–511, 2018, doi:10.1007/s00193-018-0821-5.

[2] Q. Pontalier, M. Lhoumeau, A. Milne, A. Longbottom, and D. L. Frost. Numerical investigation of particle-blast interaction during explosive dispersal of liquids and particles. *Shock Waves*, 28(3):513–531, 2018, doi:10.1007/s00193-018-0820-6.

[3] M. R. Baer and J. W. Nunziato. A two-phase mixture theory for the deflagration-to-detonation transition (ddt) in reactive granular materials. *International Journal of Multiphase Flow*, 12(6):861–889, 1986, doi:10.1016/0301-9322(86)90033-9.

[4] Q. Pontalier, J. Loiseau, S. Goroshin, F. Zhang, and D. L. Frost. Blast enhancement from metalized explosives. *Shock Waves*, 31:203–230, 2021, doi:10.1007/s00193-021-00994-z.

[5] Q. Pontalier, A. Longbottom, S. Cargill, C. Grapes, J. Loiseau, S. Goroshin, D. L. Frost, and F. Zhang. Numerical investigation of blast enhancement with metalized explosives. In *32nd International Symposium on Shock Waves*, pages 1–13, Singapore, 2019. doi:10.3850/978-981-11-2730-4_0323-cd.

Quentin Pontalier
December 2022

Contribution of authors

I hereby declare that except where specific reference is made to the work of others, the contents of this dissertation are original and have not been submitted in whole or in part for consideration for any other degree or qualification in this, or any other University. This dissertation is the result of my own work and includes nothing which is the outcome of work done in collaboration, except where specifically indicated in this declaration.

Part II

Chapter 3 - (Journal) Publication: "Experimental investigation of blast mitigation and particle–blast interaction during the explosive dispersal of particles and liquids" in *Shock Waves* [1]
Q. Pontalier, J. Loiseau, S. Goroshin, D. L. Frost

In this manuscript, experimental data from a large number of trials carried out over a decade were reported. The experimental protocol was originally developed by David Frost, Samuel Goroshin and Jason Loiseau. They carried out the experiments at the field facilities at the Canadian Explosive Research Laboratory (CERL) in Nepean, ON. I participated in the design and in the operation of the more recent trial series [2]. I developed the original image processing method to track the blast wave propagation. I proceeded to the selection of the trials and carried out all the data analysis, including the blast trajectory sensitivity analysis. I wrote the manuscript. David Frost provided scientific input and editorial comments. Using the same experimental dataset, I also analyzed the terminal particle jet velocities and compared the results (reported in another publication [3]) with the velocities predicted by the Gurney model.

Chapter 4 - (Journal) Publication: "Numerical investigation of particle–blast interaction during explosive dispersal of liquids and granular materials" in *Shock Waves* [4]
Q. Pontalier, M. Lhoumeau, A. M. Milne, A. W. Longbottom, D. L. Frost

In this manuscript, I presented the results of computations that I carried out to model the experimental results presented in Chapter 3, with the EDEN hydrocode. Maxime Lhoumeau carried out some simulations under my direction. Aaron Longbottom and Alec Milne, researchers at Fluid Gravity Engineering (FGE Inc.) and authors of the hydrocode used, provided technical

assistance with using the code and scientific input. I proceeded to the choice of the explosive and the particle EOS based on previous work carried at FGE and elsewhere. I developed the original numerical parametric study. I determined the time-distance trajectories of the particles and blast wave, and carried out an analysis of the momentum flux, based on the respective work of Milne et al. [5] and Frost et al. [6]. I wrote the manuscript with editorial comments provided by David Frost. Using the same numerical model, I also developed an original investigation of the energy partition in heterogeneous explosive systems with stratified liquid/particles [7].

Part III

Chapter 5 - (Journal) Publication: "Blast enhancement from metalized explosives" in *Shock Waves* [8]
Q. Pontalier, J. Loiseau, S. Goroshin, F. Zhang, D. L. Frost

The experimental results presented in this manuscript were obtained by David Frost, Samuel Goroshin, and Jason Loiseau using the experimental test site of Defense Research and Development Canada (DRDC) in Suffield, Alberta. I did not participate directly in the experiments, since my access to the DRDC test site was restricted due to security considerations. However, I participated in flyer experiments at CERL which used the same explosive charge design [9]. Fan Zhang provided the funding for the experiments. I provided input on the test matrix and on the experimental setup. I developed the original image processing algorithm (which differs from that of Chapter 3). I applied the data analysis methodology to evaluate the blast enhancement and determine the contribution of early particle reaction. I also developed the original fireball luminosity analysis. I selected the trials to analyze and conducted all of the data reduction. I wrote the manuscript with scientific and editorial input from my co-authors.

Chapter 6 - (Conference) Publication: "Numerical investigation of blast enhancement with metalized explosives" in *32nd International Symposium on Shock Waves (ISSW 32)* [10]
Q. Pontalier, A. Longbottom, S. Cargill, C. Grapes, A. Milne, J. Loiseau, S. Goroshin, F. Zhang, D. L. Frost

In this manuscript, I presented the results of computations that I completed using the EDEN hydrocode. I spent several months at FGE (St. Andrews, Scotland) and important guidance on the numerical aspects and how to run EDEN were provided by my colleagues at FGE who are acknowledged as co-authors. My co-authors Jason Loiseau, Samuel Goroshin, and Fan Zhang are included for their experimental contributions summarized in the paper. I developed the original energy release analysis which was subsequently used to model flyer plate experiments [11]. I carried out a sensitivity analysis of the explosive and particle EOS. I wrote the manuscript and David Frost provided editorial comments.

References

[1] Q. Pontalier, J. Loiseau, S. Goroshin, and D. L. Frost. Experimental investigation of blast mitigation and particle-blast interaction during the explosive dispersal of particles and liquids. *Shock Waves*, 28(3):489–511, 2018, doi:10.1007/s00193-018-0821-5.

[2] B. J. Marr, Q. Pontalier, J. Loiseau, S. Goroshin, and D. L. Frost. Suppression of jet formation during explosive dispersal of concentric particle layers. *AIP Conference Proceedings*, 1979(July), 2018, doi:10.1063/1.5044930.

[3] J. Loiseau, Q. Pontalier, A. M. Milne, S. Goroshin, and D. L. Frost. Terminal velocity of liquids and granular materials dispersed by a high explosive. *Shock Waves*, 28(3):473–487, 2018, doi:10.1007/s00193-018-0822-4.

[4] Q. Pontalier, M. Lhoumeau, A. Milne, A. Longbottom, and D. L. Frost. Numerical investigation of particle-blast interaction during explosive dispersal of liquids and particles. *Shock Waves*, 28(3):513–531, 2018, doi:10.1007/s00193-018-0820-6.

[5] A. M. Milne, E. Floyd, A. W. Longbottom, and P. Taylor. Dynamic fragmentation of powders in spherical geometry. *Shock Waves*, 24(5):501–513, 2014, doi:10.1007/s00193-014-0511-x.

[6] D. L. Frost, C. Ornthanalai, Z. Zarei, V. Tanguay, and F. Zhang. Particle momentum effects from the detonation of heterogeneous explosives. *Journal of Applied Physics*, 101(11):1–14, 2007, doi:10.1063/1.2743912.

[7] Q. Pontalier, M. Lhoumeau, and D. L. Frost. Blast wave mitigation in granular materials. *AIP Conference Proceedings*, 1979(1):110014, 2018, doi:10.1063/1.5044933.

[8] Q. Pontalier, J. Loiseau, S. Goroshin, F. Zhang, and D. L. Frost. Blast enhancement from metalized explosives. *Shock Waves*, 31:203–230, 2021, doi:10.1007/s00193-021-00994-z.

[9] J. Loiseau, S. Goroshin, D. L. Frost, A. J. Higgins, and F. Zhang. Ability of metalized gelled nitromethane to accelerate a flyer plate. In *16th International Detonation Symposium*, Cambridge, U.S.A., 2018.

[10] Q. Pontalier, A. Longbottom, S. Cargill, C. Grapes, J. Loiseau, S. Goroshin, D. L. Frost, and F. Zhang. Numerical investigation of blast enhancement with metalized explosives. In *32nd International Symposium on Shock Waves*, pages 1–13, Singapore, 2019. doi:10.3850/978-981-11-2730-4_0323-cd.

[11] Q. Pontalier, J. Loiseau, A. Longbottom, and D. L. Frost. Simulating the propulsive capability of explosives loaded with inert and reactive materials. *AIP Conference Proceedings*, 2272, 2020, doi:10.1063/12.0000829.

Quentin Pontalier
December 2022

Table of contents

List of figures

List of tables

List of abbreviations

1D One Dimension

2D Two Dimensions

3D Three Dimensions

AFL Alternative Fuel Laboratory

AN Ammonium Nitrate

ANFO Ammonium Nitrate Fuel Oil

AOAV Action On Armed Violence

AP Ammonium Perchlorate

BCE Before Common Era

BKW Becker - Kistiakowsky - Wilson (scientists names)

BOS Background Oriented Schlieren

BTF BenzoTriFuroxan

BTNEN Bis (2,2,2-TriNitroEthyl) Nitramine

C-4 Composition C-4

CCTV Closed-Circuit TeleVision

CDPI Critical Diameter for Particle Ignition

CE Common Era

CERL Canadian Explosive Research Laboratory

CFD Computational Fluid Dynamic

CJ Chapman - Jouguet (scientists names)

DRDC Defence Research and Development Canada

DSC Differential Scanning Calorimetry

DTRA Defense Threat Reduction Agency

EBX Enhanced Blast Explosive

EDR Extreme Dynamic Range

EOS Equation Of State

FEM Finite Element Method

FGE Fluid Gravity Engineering

FVM Finite Volume Method

GMB Glass Micro-Balloons

HE High Explosive

HMX High Melting point eXplosive

IED Improvised Explosive Device

IPN IsoPropyl Nitrate

JCZ Johnes - Cowpertwaite - Zwisler (scientists names)

JWL Jones - Wilkins - Lee (scientists names)

LiF Lithium Fluoride

LLNL Lawrence Livermore National Laboratory

MKS Meter, Kilogram, Second

NG NitroGuanidine

NM NitroMethane

OB Oxygen Balance

PE PolyEthylene

PMMA Poly(Methyl MethAcrylate)

R.E. Relative Error

RDX Royal Demolition eXplosive

RGB Red Green Blue

RMI Richtmyer - Meshkov Instability

RTI Rayleigh - Taylor Instability

SEM Scanning Electron Microscope

SiC Silicon Carbide

START Study of Terrorism And Responses to Terrorism

SWPG Shock Waves Physics Group

TGA ThermoGravimetric Analysis

TMD Theoretical Maximum Density

TNT TriNitroToluene

VOD Velocity Of Detonation

WK Wood - Kirkwood (scientists names)

WWI World War I

WWII World War II

ZND Zel'dovich - Neumann - Döring (scientists names)

Chapter 1

General introduction

1.1 Explosions in nature

Explosions are caused by a sudden energy release from a localized source and occur in a wide variety of natural systems, at various length scales. For instance, at astrophysical scales, cataclysmic events occur during the explosion of supergiant stars, commonly called supernovae. Supernovae (Fig. 1.1a) release a colossal amount of energy (10^{51} ergs = 10^{44} J = 10^{28} megatons of TNT [1]) which is dissipated by various physical mechanisms. The different mechanisms include the generation of intense radiation (gamma-rays bursts) that can be detected many light years away from the source, the dispersal of ejecta, or the propagation of a shock wave traveling at a fraction of the speed of light. The hot star material dispersed by supernovae across the universe will recombine and form the base of new star systems, after several millions of years.

On earth, explosions occur during certain types of volcanic eruptions. The violent eruptions are caused by the dissolution of gas within the viscous magma. The depressurization of the volcanic fluid leads to the exsolution and release of the high-pressure gases into the atmosphere that drives a blast wave followed by a multiphase flow composed of ash, dust, and pyroclastic material. These materials are rapidly projected high into the atmosphere (up to 10's of kilometers) and may pose serious threats to the nearby environment. One of the most spectacular volcanic explosions was the eruption of Mount Vesuvius in 79 BCE (Fig. 1.1b), one of the deadliest eruptions in European history. The cataclysm ejected a cloud of hot ash with a very high volumetric flow rate (10^4 [2] - 10^5 m^3/s [3]) and with a thermal energy equivalent to several times the energy of the Hiroshima bomb. Several Roman cities were completely obliterated. The ash traveled to a height of 33 kilometers above the crater, and fell on the cities of Pompei and Herculaneum. The preserved remains of the people that tried to flee the city are still visible in the excavated archaeological site. Other occurrences of natural explosions include permafrost explosions [4] and the explosive seed dispersal of flower plants [5].

(a) (b)

Fig. 1.1 (a) A supernova remnant forming the Crab Nebula, first detected by Japanese, Chinese and probably Native Americans astronomers in 1054 CE. The picture is a reconstruction obtained from 24 camera exposures taken in 1999-2000 by NASA/ESA's Hubble telescope [6]. **(b)** Painting of the Mount Vesuvius eruption of 79 BCE by John Martin [7].

1.2 Explosion hazards resulting from human activities

Explosions can also result from human activities. Numerous uncontrolled explosions during domestic or industrial accidents have occurred throughout history. These accidents present serious hazards for human lives and for building structures. In Canada, the Halifax (Nova Scotia) explosion [8] during WWI provides a good example of the damage that may be caused by an explosion resulting from human activity. The explosion occurred on December 6th, 1917 when a French cargo ship partially loaded with trinitrotoluene (TNT) collided with a Norwegian vessel in the strait connecting Halifax Harbour to Bedford Bassin. The explosion released the energy of approximately 2.9 kilotons of TNT (12 000 GJ) and the blast killed directly, or indirectly (tsunami, collapse of buildings, traumatic blast injuries) roughly 2000 people with more than 9000 injured. The blast wave initially propagated at a hypersonic velocity (Mach 23) and was felt more than 200 km from the explosion source. An area of 160 hectares was completely destroyed. Fig. 1.2 shows the aftermath of the Halifax explosion. This accidental event is commonly referred as the largest non-nuclear explosive event in history.

More recently, on August 4th 2020, approximately 2750 tonnes of ammonium nitrate (a chemical fertilizer used in agriculture) exploded in the Port of Beirut (Lebanon). The substantial quantity of ammonium nitrate (AN) was originally confiscated from a Moldovan cargo ship, the *Rhosus*, by the harbor authorities due to unpaid bills. The shipment was stored in Warehouse 12 and remained there for six years, despite the numerous alerts of the customs officials warning the government of the potential hazards. It is hypothesized that during all these years, the AN, which is normally stable at atmospheric conditions, increased its ability to detonate by

Fig. 1.2 Aftermath of the Halifax explosion [17]

absorbing contaminants (dust, etc.) and moisture from the surrounding air [9]. The AN was initiated by a primary explosion of nearby pyrotechnics which triggered the huge explosion less than a minute later. The energy released was estimated to lie between 0.3 and 1.1 kilotons of TNT [10–15]. The explosion produced seismic waves equivalent to those released by an earthquake of magnitude 3 - 4 [15] and were felt on the island of Cyprus, more than 250 km away. The blast wave devastated the harbour and nearby buildings, whereas an orange cloud of nitrogen dioxide gas was formed above the site. The explosion claimed the lives of 218 people and more than 7000 were injured, mainly due to the shattering of windows and the collapse of buildings impacted by the blast wave. The Beirut accident occurred five years after the Tianjin (China) explosion [16], also involving AN ($\sim$ 800 tons), and which claimed the lives of 173 people with about 800 injured.

Since the year 2000, the world has seen a sharp increase in the number of terrorist attacks leading to a high number of casualties. According to the National Consortium for the Study of Terrorism and Responses to Terrorism (START), the number of attacks increased by almost 850% between 2000 and 2014 [18]. In 2019 (the most recent date in the database), the number of attacks had reduced by 59% compared to year 2014, but remained still high with more than 8000 attacks reported. Among the attacks, almost 50% included explosions with more than 100 000 incidents being reported from 1970 to 2019, as shown in Fig. 1.3. Bomb attacks can utilize various devices, including remotely-activated devices, suicide vests, car or truck bombs and air-launched bombs. In 2020, the Action on Armed Violence (AOAV) group [19] reported that the majority of the people that suffered death or injury due to explosive weapons in the world were civilians (59%). About 56% of the civilian casualties resulted from manufactured explosive weapons whereas 43% resulted from improvised explosive devices (IEDs).

1.3 High explosives as a tool to investigate explosive effects

Considering the serious threats that explosions may pose to human health and infrastructure, it is of interest to predict, evaluate and quantify explosion hazards in order to mitigate the risks. In

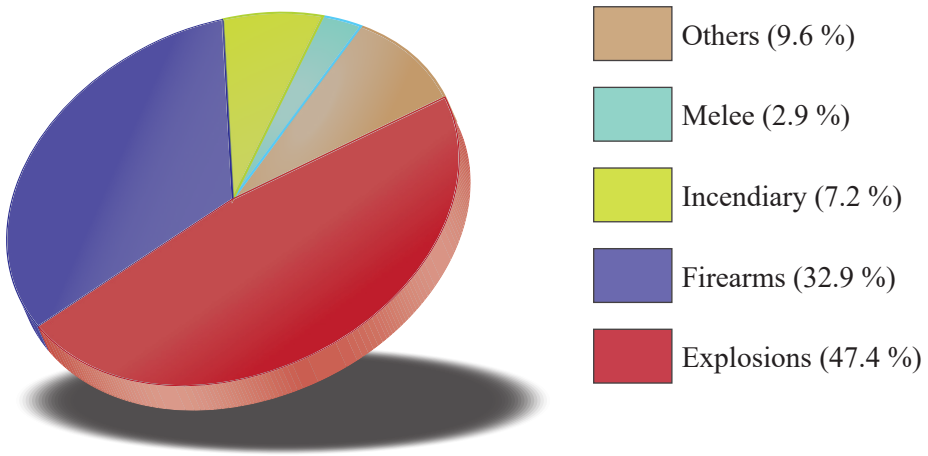

Fig. 1.3 Classification of the different types of terrorist attacks reported from 1970 and 2019 from a sample of 201,183 incidents (adapted from [18]).

that respect, high explosives remain one of the best tools to simulate the effects of explosions due to their ability to generate strong blast waves. Historically, high explosives (HE) were developed for military purposes but now, on a mass basis, the largest use of explosives is for civilian applications. For example, HE are used extensively in the mining industry to break rocks or for earthmoving. They are also widely used for demolition and may be used for the shock synthesis of materials. This widespread use of explosives in the civilian world has motivated scientists to continue studying high explosives and their effects.

HE have moderate energy densities. By comparison, gasoline has an energy density of 46 MJ/kg (34 MJ/L), wheras TNT has an energy density of 4.6 MJ/kg (6.9 MJ/L). Nevertheless, the specific power of HE greatly exceeds fuels and approaches the power output of a national electric grid. HE are, in general, metastable and self-oxidizing energetic materials, but typically require an initiation source to release their energy. The nature of the initiation process depends on the type of explosive and its sensitivity. Detonation of an HE charge typically generates the following sequence of events:

- Creation of a high-pressure, high-temperature volume of products, commonly denoted a fireball
- Generation and radial propagation of a decaying blast wave
- Radial dispersal of solid fragments away from the explosion center, from casing or embedded material.

The fireball is initially comprised of high-pressure hot gaseous and condensed products. Expansion of the fireball generates a turbulent flow and is directly of use for doing work on the surroundings. The pressure in the expanding fireball eventually falls below atmospheric pressure, limiting the extent of the fireball to an area close to the explosion center. In contrast, the blast

wave can propagate and induce high-pressure loads far from the explosion center. The impact of the blast wave can lead to injuries to nearby personnel and structural damage that depends on the proximity to the explosive and hence the blast overpressure, as shown in Table 1.1. These properties make the blast wave the most hazardous effect of a lightly-cased explosive. For heavily-cased explosives, the dispersal of fragments by the explosion is also a substantial hazard, especially in the near field. The fragments initially travel at supersonic velocities, and may penetrate and lacerate the human body as well as structures. Note that the three events, i.e., fireball formation, blast wave propagation, and material dispersal are not independent, and interact closely. For example, the blast wave generation reduces the energy available to sustain exothermic reactions in the fireball and to accelerate solid material. On the contrary, the energy released by chemical reactions and the dispersal of material may support the blast wave propagation providing that the timescale of the energy release is sufficiently fast and that the motion of the material does not lag too much behind the blast front.

Explosive effects generated by high explosives can be probed either by experimental means or by using numerical tools. The effects of high explosives can be scaled (to a certain limit) such that large-scale accidents can be simulated at smaller scales in laboratories or in field test sites. Nevertheless, above certain limits, the ability to accurately scale explosive effects declines. Consequently, expensive large-scale facilities remain essential to probe explosive effects, by reproducing as closely as possible natural or man-made explosions. Nevertheless, the number of these facilities remains limited in the world and are not easily accessible. Conversely, performing numerical simulations avoids the costs of expensive trials and bypasses the need to access restricted test sites. Moreover, they may be useful to probe regions close to the explosion center where *in-situ* diagnostics fail to give accurate results. Given the complexities of the transient, turbulent, multiphase flow generated by an explosive charge, numerical simulations are expected to be most useful for probing the sensitivity of the properties of the flow and pressure fields to various parameters. Also of interest is investigating the temporal and spatial variations in the partition of energy between the various components in the flow.

1.4 General thesis overview

This thesis manuscript systematically studies the effect of the interactions between the three primary features of an explosion generated by an explosive charge (fireball, blast wave and dispersed materials) on the blast strength. Particular emphasis is put on studying the interactions between the dispersed particles and the surrounding gases (detonation products or air) and how these interactions influence the pressure field and the properties of the blast wave. The main objective of this thesis is to understand the fundamental aspects of blast wave propagation in high-velocity multiphase flows. Although the multiphase flow studied in this thesis results from the detonation of chemical explosives, some elements of the results can be generalized to natural explosions, as will be discussed in conclusion. Nevertheless, the results of this thesis

Table 1.1 Damage on building structures and on the human body for various ranges of peak blast overpressure (ΔP_s - defined in Appendix A). Table adapted from [20].

ΔP_s **(bars)**	**Damage on structures**	**Type of injuries**
0.035 - 0.075 ($\sim$ 1 psi)	Window glass shatters.	Light injuries.
0.1 - 0.15 ($\sim$ 2 psi)	Moderate damage to buildings (windows and doors blown out).	Moderate injuries due to flying debris. Threshold for eardrum rupture.
0.15 - 0.2 ($\sim$ 3 psi)	Collapse of wood frame buildings (residential homes).	20% fatality indoors. 0% fatality outdoors.
0.4 - 0.6 ($\sim$ 7 - 9 psi)	Severe damage to concrete buildings.	Eardrum rupture (50% of cases).
0.7 - 0.8 ($\sim$ 10 - 12 psi)	Total destruction of most buildings.	Eardrum rupture (100% of cases). Threshold for lung injuries.
$>$ 3.8 ($>$ 55 psi)	Total destruction of all buildings.	Lethality (100%).

also have practical applications in predicting potential hazards associated with uncontrolled explosions (terrorist attacks, industrial accidents, or transportation of energetic materials). These predictions could be used to improve the design of mitigation systems. Conversely, studying the aforementioned interactions may help understand the fundamentals of chemical reactions of metals at high pressure or in designing enhanced blasting explosives (EBX) for military or mining applications. In the present work, the nature of these interactions is qualitatively and quantitatively described for two heterogeneous explosive configurations consisting of either i) an explosive charge surrounded with a layer of inert material or ii) an explosive charge embedded with reactive particles. While the first configuration is commonly studied to investigate the blast wave mitigation, the second configuration is more relevant to blast wave enhancement studies. The work presented here is comprised of a combined experimental and numerical effort. This thesis lies on the border of fundamental and engineering physics and involves a large range of fundamental subjects (thermodynamics, combustion, compressible flows, material science, chemistry, etc.

In Part I, the general features of heterogeneous explosive systems are described in Chapter 2, together with a review of the relevant literature. This chapter is primarily addressed to a reader familiar with the concepts pertaining to blast wave research and who wishes to understand quickly the scope of the work carried out in this thesis. However, the reading of this chapter necessitates understanding several prerequisite concepts. These concepts are reviewed in Appendix A, which is dedicated to new students preparing to pursue research work in the field of explosive-generated blast waves. The properties of homogeneous explosives and their effects are described there as well as the theory of blast waves with very few mathematical developments. This chapter was

primarily written to be accessible to engineering students with a background in thermophysics and fluid dynamics. Part II gathers the experimental (Chapter 3) and the numerical (Chapter 4) work pertaining to the explosive configuration with a layer of inert material. Each chapter is comprised of a published paper which is included in the original published form. Similarly, Part III is comprised of two published papers (Chapters 5 and 6), gathering respectively, the experimental and the numerical work pertaining to the explosive configuration with embedded reactive materials. Finally, in part IV, general conclusions are drawn in Chapter 7. After the main body of thesis, there are several appendices, including the Appendix A noted above, a brief summary of the main assumptions of the model used to carry out the numerical simulations (Appendix B), and supplementary materials of Chapter 3 in Appendix C.

Statement of condolences

The author would like to express his sincere sympathies to all those affected by the accidental events or the deliberate attacks mentioned in this chapter.

Note on the thesis format

The format of the present thesis complies with most of the guidelines for manuscript-based theses given by the McGill Graduate and Postdoctoral Studies (GPS) office which can be found here[1]. The guidelines specify that each published paper must be included in its original format and form a thesis chapter without any material addition or correction. Hence, specific reference sections and paper appendices are reported at the end of these chapters. Transitions must be included between the published papers. The guidelines also stipulate that the thesis manuscript must include a general introduction and a literature review at the beginning of the thesis, covering the scope of all published papers. A general discussion, conclusion, and appendices must also be presented at the end of the manuscript. Such a format inevitably increases the length of the thesis since some references and content are repeated across the different chapters. Note, however, that the discussion section at the end of the manuscript has been removed since the results are extensively discussed in the papers and the transitions, and repeating the same material will be tedious for the reader.

[1] https://www.mcgill.ca/gps/thesis/thesis-guidelines/preparation/manuscript-based-article-based-theses

Summary

- Explosions can result from natural or human activities.
- Uncontrolled explosive effects are serious hazards for human health and building structures.
- High explosives (HE) are often used to simulate explosive events.
- Explosions from high explosive charges have three primary features: a fireball, a blast wave, and a cloud of dispersed materials.
- In configuration 1 (Part II), the interaction between the three different features and the effect on the blast strength is investigated to evaluate the blast wave mitigation capability of explosives charges surrounded by material layers.
- In configuration 2 (Part III), the interaction between the three different features and the effect on the blast strength is investigated to evaluate the blast enhancement capability of metalized explosives.

References

[1] D. Branch and J. C. Wheeler. *Supernova explosions*. Springer, 2017, doi:10.1007/978-3-662-55054-0.

[2] L. Gurioli, B. F. Houghton, K. V. Cashman, and R. Cioni. Complex changes in eruption dynamics during the 79 AD eruption of Vesuvius. *Bulletin of Volcanology*, 67(2):144–159, 2005, doi:10.1007/s00445-004-0368-4.

[3] A. W. Woods. Sustained explosive activity: Volcanic eruption columns and Hawaiian fountains. *Modeling Volcanic Processes: The Physics and Mathematics of Volcanism*, 9780521895:153–172, 2009, doi:10.1017/CBO9781139021562.008.

[4] E. Chuvilin, N. Sokolova, D. Davletshina, B. Bukhanov, J. Stanilovskaya, C. Badetz, and M. Spasennykh. Conceptual models of gas accumulation in the shallow permafrost of northern west siberia and conditions for explosive gas emissions. *Geosciences*, 10(5), 2020, doi:10.3390/geosciences10050195.

[5] H. Hofhuis and A. Hay. Explosive seed dispersal. *New Phytologist*, 216(2):339–342, 2017, doi:10.1111/nph.14541.

[6] Image credit: NASA/ESA, J. Hester, and A. Loll. Crab Nebula, https://www.nasa.gov/feature/goddard/2017/messier-1-the-crab-nebula.

[7] Image credit: J. Martin. The destruction of Pompeii and Herculaneum (oil paint on canvas), https://www.tate.org.uk/art/artworks/martin-the-destruction-of-pompeii-and-herculaneum-n00793.

[8] A. Ruffman and C. D. Howell. *Ground zero: a reassessment of the 1917 explosion in Halifax harbour*. Nimbus Publishing, Print., 1994.

[9] J. M. Dewey. The TNT and ANFO equivalences of the Beirut explosion. *Shock Waves*, 31(1):95–99, 2021, doi:10.1007/s00193-021-00992-1.

[10] S. E. Rigby, T. J. Lodge, S. Alotaibi, A. D. Barr, S. D. Clarke, G. S. Langdon, and A. Tyas. Preliminary yield estimation of the 2020 Beirut explosion using video footage from social media. *Shock Waves*, 30(6):671–675, 2020, doi:10.1007/s00193-020-00970-z.

[11] C. Stennett, S. Gaulter, and J. Akhavan. An estimate of the TNT-equivalent net explosive quantity (NEQ) of the Beirut port explosion using publicly-available tools and data. *Propellants, Explosives, Pyrotechnics*, 45(11):1675–1679, 2020, doi:10.1002/prep.202000227.

[12] H. J. Pasman, C. Fouchier, S. Park, N. Quddus, and D. Laboureur. Beirut ammonium nitrate explosion: are not we really learning anything? *Process Safety Progress*, 39(4), 2020, doi:10.1002/prs.12203.

[13] C. J. Aouad, W. Chemissany, P. Mazzali, Y. Temsah, and A. Jahami. Beirut explosion: TNT equivalence from the fireball evolution in the first 170 milliseconds. *Shock Waves*, 2021, doi:10.1007/s00193-021-01031-9.

[14] J. S. Díaz. Explosion analysis from images: Trinity and Beirut. *European Journal of Physics*, 42(3), 2021, doi:10.1088/1361-6404/abe131.

[15] C. Pilger, P. Gaebler, P. Hupe, A. C. Kalia, F. M. Schneider, A. Steinberg, H. Sudhaus, and L. Ceranna. Yield estimation of the 2020 Beirut explosion using open access waveform and remote sensing data. *Scientific Reports*, 11(1):1–14, 2021, doi:10.1038/s41598-021-93690-y.

[16] P. Huang and J. Zhang. Facts related to August 12, 2015 explosion accident in Tianjin, China. *Process Safety Progress*, 34(4):313–314, 2015, doi:10.1002/prs.11789.

[17] W. James. A view across the devastation of Halifax after the Halifax explosion, looking toward the Dartmouth side of the harbour. IMO (involved ship) can be seen aground on the far side of the harbour - Halifax after 6th December 1917, 1917, https://canadiangeographic.ca/articles/the-disaster-that-reshaped-a-city/.

[18] Global Terrorism Database (GTD), https://www.start.umd.edu/gtd/.

[19] J. Dathan. Explosive violence monitor 2020. Technical report, Action on Armed Violence (AOAV), 2020, https://reliefweb.int/sites/reliefweb.int/files/resources/Explosive-Violence-Monitor-2020-V3-single-pages.pdf.

[20] G. F. Kinney and K. J. Graham. *Explosive shocks in air (Second edition)*. Springer, 1985, doi:10.1007/978-3-642-86682-1.

Part I

Chapter 2

Heterogeneous explosive systems with stratified layers of material or embedded solid particles

2.1 Heterogeneous explosive systems - Definition

Characterizing heterogeneous explosives among various explosive systems is not trivial. For example, bulk liquid explosives are considered to be homogeneous assuming that they do not contain suspended particles or gas bubbles. However, most conventional solid explosives, such as plastic-bonded explosives, are formed by heterogeneous agglomerations of crystals and binders when observed at microscopic scales. For a specific explosive formulation, the molecular structure and arrangement play a role in the sensitivity to detonation but have limited influence on the propagation of the blast wave or the fireball dynamics. The explosive reactants decompose over a very short timescale such that a negligible fraction of the reactants is left unburnt by the end of the detonation reaction zone. Furthermore, the blast wave properties of conventional explosives can be scaled such that blast effects can be predicted for virtually any explosive formulation of various masses, at any distance from the charge. Consequently, most conventional explosives are categorized as homogeneous (see Appendix A for a review of homogeneous explosives) even if they exhibit a certain degree of heterogeneity at the microscale.

In contrast, in heterogeneous explosives systems, the size of the heterogeneities is often several orders of magnitude larger than that of the explosive molecule. These heterogeneities perturb the detonation wave propagation. One such heterogeneous explosive system consists of mixing solid, chemically inert particles of high density within conventional explosives. In this case, during detonation propagation, the particles and the surrounding product gases may not reach equilibrium inside the detonation zone, and the diffraction of the detonation wave around the particles may cause a fraction of the explosive reactants to exit the sonic surface and burn within the Taylor wave [1]. These effects modify the detonation properties

(detonation velocity, detonation pressure and expansion rate of the products) and, thus, alter the fireball thermodynamics and the air-blast pressure. This situation is further complicated if the solid particles react chemically. If the particle burn exothermically and anaerobically with the detonation products, or aerobically with the surrounding air, the explosive propulsive power, the thermal load of the fireball, and the strength of the blast wave may be enhanced. In this case, blast effects cannot be predicted accurately using traditional scaling laws.

Another explosive system commonly referred to as heterogeneous consists of surrounding a homogeneous explosive charge by a material layer. This configuration generates a complex multiphase flow. When the detonation wave reaches the outer explosive surface, a decaying shock wave is transmitted into the material layer. The intricate interplay between this propagating shock wave and the material layer results in explosive features differing from those observed during the detonation of a homogeneous explosive charge alone. For example, the fireball size and temperature may be substantially reduced, and the air blast pressure may be considerably attenuated. These phenomena are often attributed to the transfer of thermal energy from the detonation products to the kinetic and internal energy of the material layer. Hence, conventional scaling laws will also fail at predicting blast effects for this heterogeneous explosive system.

This chapter reviews past work and the general features observed for explosive charges with these two configurations. Section 2.2 describes heterogeneous explosive systems comprised of a conventional explosive charge surrounded by stratified layers of material, whereas the configuration involving solid particles embedded within a homogenous explosive charge is reviewed in section 2.3.

2.2 Heterogeneous explosive systems with stratified layers of material

Investigating the detonation of a solid high-explosive charge surrounded by stratified material layers is of interest for i) studying the dynamics of the dispersal of the material layer and, ii) analyzing the influence of the dispersed layer on the blast wave propagation. In this section, the state of the experimental and modeling research of this explosive configuration is reviewed.

2.2.1 Mechanisms of jet formation

The explosive dispersal in air of a layer of solid particles or a layer of liquid surrounding a spherical high-explosive charge generates a turbulent, multiphase flow, typically with the formation of jet-like structures [2]. These features do not appear in the case of an underwater explosion, suggesting that the formation of jets is strongly dependent on the presence of an outer boundary (material layer-air interface). It implies that the impedance mismatch between the layers of materials with the surrounding air plays a significant role. As a result, one hypothesis

is that classical hydrodynamic instabilities such as the Rayleigh-Taylor (RT) or Ritchmyer-Meshkov (RMI) instability may be responsible for producing the jets. However, Milne et al. have shown that the timescales involved in the process of the formation of these structures are too short [3] to be explained by the previously cited instabilities. Several researchers have investigated the mechanism of the formation of these jets, including Frost et al. [2, 4], Zhang et al. [5, 6], Ripley et al. [7], Milne et al. [3, 8, 9] and Xue et al. [10, 11]. These investigations have included both medium- to large-scale experiments and numerical simulations. At this time, the wave dynamics inherent in the formation of jets are not yet fully understood for all materials, but we will present in this section an outline of the primary mechanisms involved in the breakup of a granular or liquid layer. Although the study of the physical processes underlying jet formation is not the primary objective of this thesis, knowledge of these processes may be of interest to better understand the interaction between the blast wave and the material layer.

Solid powders

A general mechanism for the explosive dispersal of a granular layer can be described in terms of a two-step process including first i) shock compaction, and then ii) dynamic fragmentation upon release and expansion of the compacted layer. When a high-explosive charge surrounded by a layer of inert material is detonated, a shock wave propagates into the material, compacting the material to a degree which depends on the initial bed porosity, particle compressive strength, and local strength of the shock wave. For example, thin layers of soft material may be entirely compacted whereas thick layers of hard and tough materials may only consolidate close to the charge. When the shock wave reaches the surface of the material layer, a blast wave is transmitted into the surroundings and an expansion wave propagates back into the compacted material, causing it to expand radially outwards. The tension induced within the compacted bed of material causes it to break up into fragments that have a size (δ) that is experimentally observed to be on the order of the thickness of the compacted layer when the expansion wave reaches the inner surface of the layer [2, 8]. The fragments move radially outwards, shedding fine fragments in their wake and leading to the formation of jet-like structures. These jets follow ballistic trajectories and the maximum travel distance depends on the jet velocity, rate of shedding, and areal density of the jet tip. The number of jets is inversely dependent on the mass of mitigant to explosive (M/C) ratio but the ability to form jets is more dependent on the material toughness. Materials with high compressive strength and high toughness such as steel shot are less likely to form jets [2] whereas other materials such as aluminum, brass, sand or silicon carbide form jets. A schematic of the proposed mechanism is presented in Figure 2.1 as well as sequences of photography of the explosive dispersal of silicon carbide (Fig. 2.2) and steel (Fig. 2.3) particles. Further support for the proposed mechanism for the formation of particles jets shown in Figure 2.1 has been provided by the extensive experimental and computational study reported in the thesis by Marr [12]. Marr demonstrated the key role of

shock consolidation, and the role of material strength, in the governing mechanism responsible for the jetting phenomenon. He carried out explosive dispersal experiments with binary particle mixtures, containing both “non-jetting" particles (steel shot) and “jetting" particles (silicon carbide) [13]. By constructing a charge with an inner concentric layer of steel particles, the strength of the shock wave was reduced sufficiently to eliminate the formation of jets from the silicon carbide layer.

Despite very different properties, many granular powders form jets when explosively dispersed. For example, granular powders of sand, glass, aluminum, silicon carbide, granulated sugar or brass all form jets. This empirical observation suggests that most material properties do not play a significant role in the jet formation mechanism. Compared to other powders, the main property of non-jet-forming steel powders is their high compressive strength, suggesting that toughness is the dominant parameter controlling the formation of jets.

Recent studies have shown that, depending on the compaction regimes, the stress imposed on dry or wet porous granular powders is either hydrodynamic or strongly dependent on deviatoric stress [14–16]. Good agreement is found between numerical simulations and experiments for the compaction of granular powders if the yield strength of the powder is assumed to depend on the shock pressure. These results suggest that particle fracture during compaction of the layer is very likely in the context of the explosive dispersal of powders. For example, Marr [12] showed that both glass and steel particles fracture for typical shock loads encountered in explosive dispersion events ($\sim$ 1 GPa), although steel particles experienced a lower level of fragmentation. Nevertheless, glass powders form jets unlike steel powders. This observation suggests that jet formation is independent of the fracture of individual particles but rather depends on the degree of consolidation of the material layer. Post-mortem recovery of consolidated steel powder fragments indicated that the steel particles underwent compaction. However, numerical simulations showed that the effects of compaction were limited to a thin layer around the explosive charge [12], with a significant fraction of the layer remaining largely unconsolidated during the initial shock propagation. This effect results in the dispersion of a diffuse layer of particles upon further expansion of the detonation products. Conversely, for other powders of lesser toughness, the layer is consolidated throughout its thickness, making it possible for the entire layer to fracture during the propagation of the release wave, as shown in Figure mechanism. Furthermore, as mentioned earlier, the number of jets appears to depend primarily on the M/C ratio rather than on the material properties. Configurations with large M/C ratios produce larger initial fragments upon layer fracture. Conversely, configurations with small M/C values produce smaller initial fragments. Therefore, since the number of jets correlates with the size of these initial fragments, the number of jets is higher for configurations with smaller initial fragments and small M/C values. In secondary order, at a fixed M/C ratio, the number of jets could fluctuate depending on the material properties, but this effect remains to be quantified.

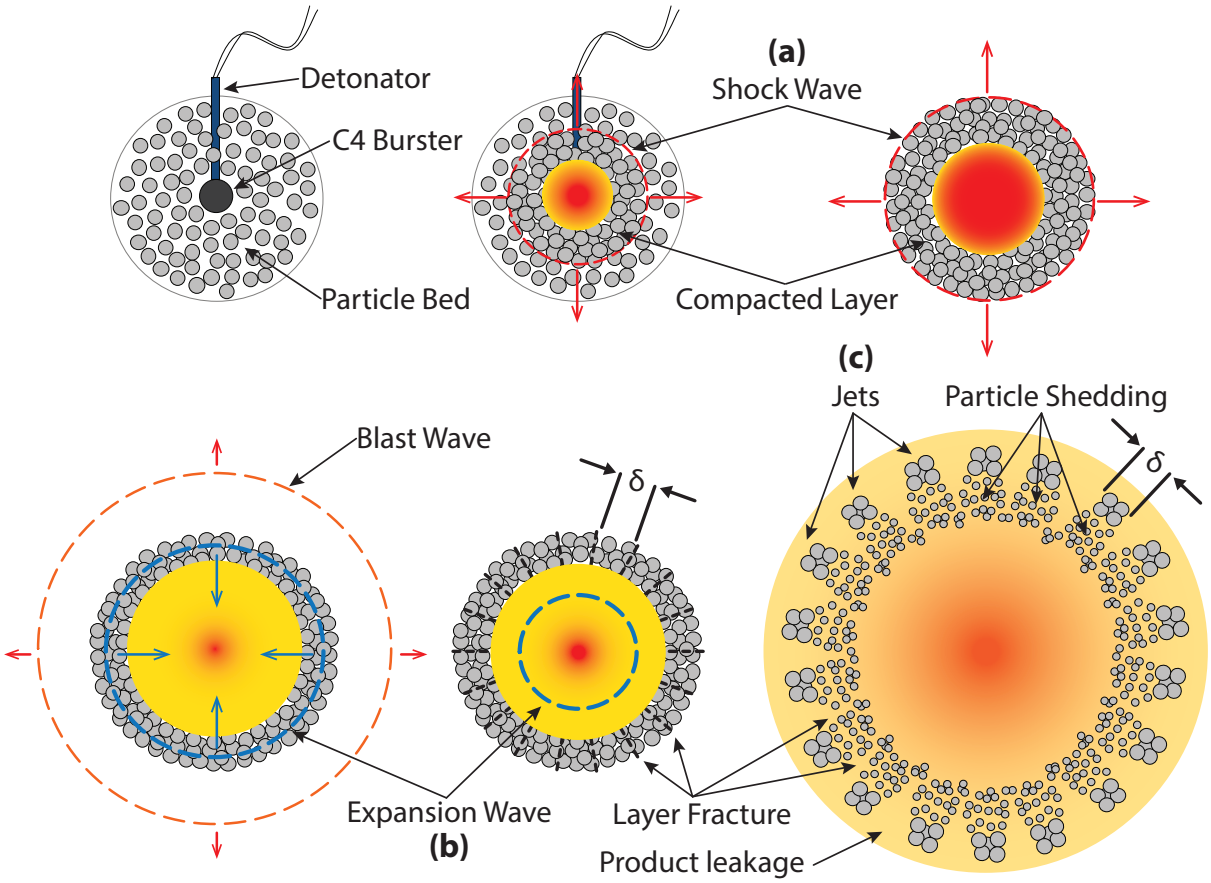

Fig. 2.1 Schematic of the proposed explosive dispersal mechanism leading to the formation of coherent jet structures (Figure courtesy of Frost et al. [2]).

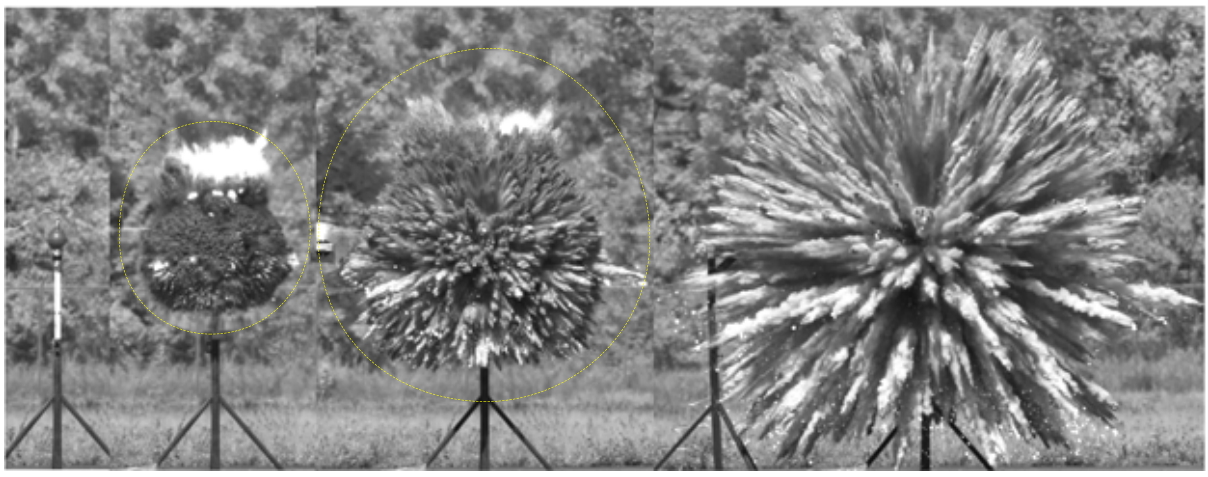

Fig. 2.2 Single video frames taken during the explosive dispersal of SiC particles. Charge diameter is 12.7 cm, mass of silicon carbide (SiC) is 1512 g, mass of C-4 is 75 g, giving M/C = 20.2. Pictures were taken 0, 1, 2, and 4 ms after detonation of the charge. The dashed yellow circles in the middle two images show the approximate locations of the blast wave. Figure and caption courtesy of Loiseau et al. [17].

Fig. 2.3 Single video frames taken during the explosive dispersal of S110 steel shot. Charge diameter is 12.7 cm, mass of steel is 4130 g, mass of C-4 is 75 g, giving $M/C = 55.1$. Pictures were taken 0, 2, 4, and 6 ms after detonation of the charge. Figure and caption courtesy of Loiseau et al. [17].

Liquids

In the late 1980's, Grady theorized the dynamic breakup of a liquid layer and predicted fragment sizes for a surface-tension-dominated regime (low strain rates) and a viscous-dominated regime (high strain rates) [18], although he noted a lack of experimental data to confirm his model. In a recent study on the explosive dispersal of liquids, Milne et al. showed that the fragment sizes of liquids do not match Grady's predictions [9]. They showed that explosive dispersal of liquids also, in general, leads to the formation of jets but suggested that other phenomena, such as cavitation within the liquid layer behind the expansion wave, govern jet formation. The number of jets formed during the explosive dispersal of liquids is closely related to the volumetric distribution of nucleated cavitation sites when the liquid shell is put in tension, assuming a constant and uniform number of nucleation sites per unit of volume [9]. As a result, contrary to solid particles, the number of jet features increases with M/C. They speculated that at a critical ratio, additional nucleation sites may merge such that the number of jets is determined by the number of cavitation sites at the explosive-liquid interface. This leads to a constant number of jets for a value of M/C beyond this saturation point. Figure 2.4 exhibits an example of the jets formed during the explosive dispersal of a bulk water layer. In the case of liquids, the maximum travel distance of the jets depends on the initial jet velocity, the liquid volatility (i.e., the evaporation rate), and the aerodynamic shedding rate of the liquid, which depends on the liquid surface tension.

Solid powders saturated with water

Contrary to dry powders or bulk liquids, the mechanisms of jet formation for granular powders saturated with water remain poorly studied. However, phenomenological observations indicate

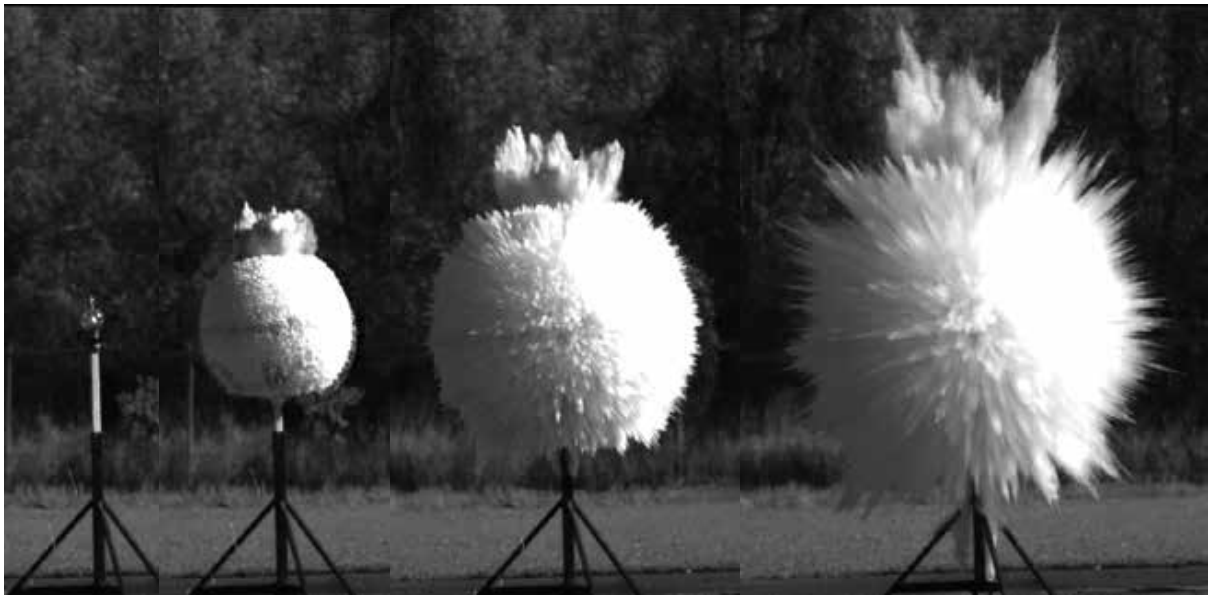

Fig. 2.4 Single video frames taken during the explosive dispersal of a bulk water layer. Charge diameter is 12.7 cm, mass of water is 940 g, mass of C-4 is 28 g, giving $M/C = 33.6$. Pictures shown were taken at 0, 1, 2, and 4 ms after detonation of the charge. Image sequence obtained from experiments carried out at CERL, in October 2012 (D. Frost, personal communication, 2016).

that liquid addition has an important influence on particle dispersal morphology. For example, saturating a porous bed of silicon carbide (SiC) particles with water (Fig. 2.5) suppresses the formation of the large coherent jets observed for dry powders (Fig. 2.2). Instead, a large number of fine jets are dispersed. These fine jets are most likely composed of a SiC/water droplet slurry. In the case of wetted steel particles, the dispersed layer of steel particles (Fig. 2.6) is more coherent than for the dispersal of the dry powder (Fig. 2.3). The physical processes leading to the difference in morphology between dry and wetted powders remain elusive. Nevertheless, the similarities between the jet morphology for wetted powders and bulk liquids suggest that cavitation of the liquid at the particle surface could also explain the jet formation for powders saturated with water.

2.2.2 Jet velocity

Explosively dispersed material can cause substantial damage to personnel and structures, especially in the near field. In this region, Frost et al. [19] showed that the particle momentum flux exceeds the gas momentum flux and, thus, is the primary contributor to the impulse applied to a structure. Hence, estimating the jet velocities is of interest to evaluate the potential hazards from the impact of various explosively-dispersed material layers. Comparing jet velocities with the Gurney velocity is of interest for this purpose. The Gurney method was originally formulated in 1943 by R.W. Gurney to predict the fragment velocities of spherical or cylindrical metal casings

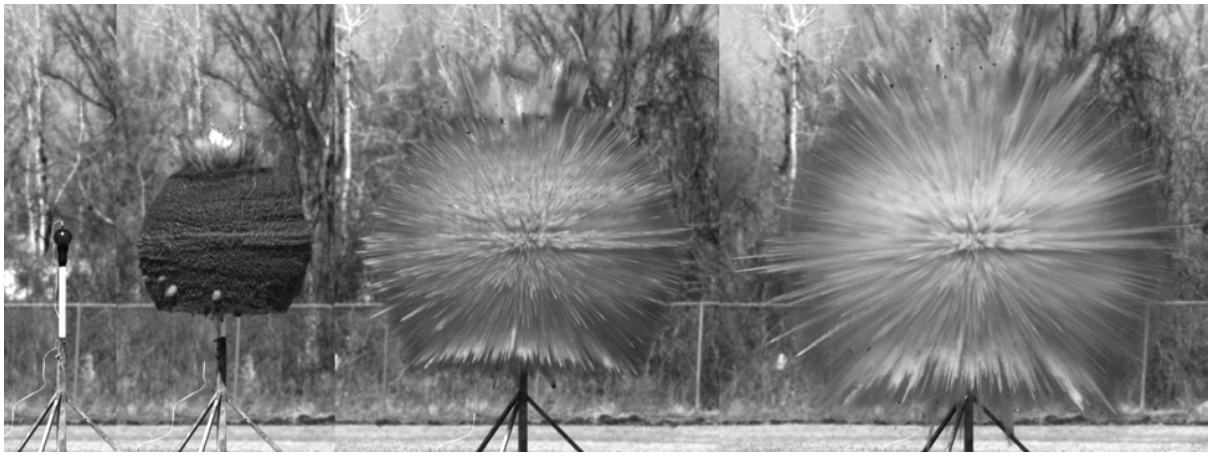

Fig. 2.5 Single video frames taken during the explosive dispersal of a bed of SiC particles saturated with water. Charge diameter is 12.7 cm, mass of SiC is 1511 g, mass of water is 338 g, mass of C-4 is 28.3 g, giving $M/C = 65.3$. Pictures shown were taken at 0, 2, 4, and 6 ms after detonation of the charge. Figure and caption courtesy of Loiseau et al. [17].

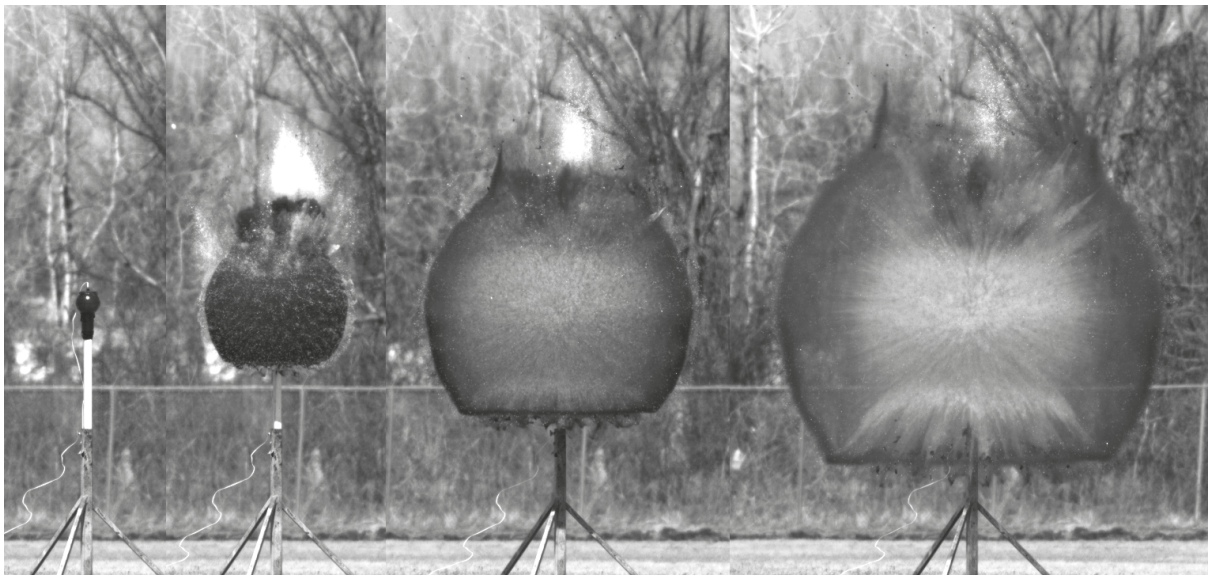

Fig. 2.6 Single video frames taken during the explosive dispersal of a bed of S110 steel shot saturated with water. Charge diameter is 12.7 cm, mass of steel shot is 4410 g, mass of water is 338 g, mass of C-4 is 28.3 g, giving $M/C = 168$. Pictures were taken at 0, 2, 4, and 6 ms after detonation of the charge. In the second frame, the fine fragments of the glass casing are visible just outside the layer of steel particles. The shell of steel particles becomes thin enough at later times so that the formation of jets of water droplets is visible within the shell of steel particles in the last frame. Figure and caption courtesy of Loiseau et al. [17].

driven by a high-explosive core and has been extended to numerous geometries and systems involving the explosive acceleration of material to terminal velocity [20, 21]. Assuming that the explosive acceleration of a casing could be described by the instantaneous conversion of a portion of the explosive chemical energy into gasdynamic potential energy of the detonation products, Gurney was able to derive the terminal velocity of explosively accelerated materials. This velocity is a function of the Gurney energy, the mass ratio of casing to explosive (M/C), and a coefficient which depends on the geometry of the charge. The Gurney energy was empirically determined to be the fraction of the explosive chemical energy converted to global kinetic energy in the system. Detailed derivations of the Gurney velocity and model assumptions are variously described in the literature by Jones [22], Kennedy [23], and Dehn [21]. Gurney's methodology continues to be the primary analytical technique to predict the terminal velocity of explosively accelerated materials. However, little is known about the velocity of dispersed porous layers or bulk liquids. In a recent study, Loiseau et al. [17] have demonstrated that the terminal jet velocities of explosively dispersed liquid layers correlated well with Gurney's predictions. The correspondence is explained by the relative incompressibility of the liquids. Conversely, in the case of the explosive dispersal of granular particles, Gurney's velocity overpredicts the terminal velocity by 25% to 60%, depending on M/C. This velocity discrepancy between granular powders and bulk liquids is attributed to the loss of energy due to the work done in collapsing the interstitial pores and compaction of the granular material [17, 24]. For granular powders saturated with water, the terminal jet velocities are similar to those of the liquids. It is assumed that the interstitial liquid is capable of bearing stress and prevents the consolidation of the powder. These experimental observations suggest that compaction of the granular powders plays not only a key role in the jet formation but also in the dynamics of the jets.

2.2.3 Blast wave interactions with the dispersed material layers

The mitigation of blast waves has been an important concern over the latter half of the 20$^{\text{th}}$ century with the widespread utilization of commercial explosives. Also, with the increase in the number of accidental and deliberate explosive events, it is important to be able to determine the potential hazards to humans and structures due to blast loads. One particularity of blast waves is that, unlike material dispersal whose effects are limited to the near field due to aerodynamic drag, blast waves can propagate far from the explosion epicenter and cause damage over a large area. It is then of interest to find techniques to attenuate the strength of a blast wave to reduce its destructive power. A common technique to mitigate the blast wave strength from an explosive charge is to surround the charge with either an inert liquid or solid medium. To minimize the production of large high-velocity fragments, solid particles are often used. A particular geometry that has been studied in the past consists of a spherical high-explosive charge surrounded by a spherical shell of mitigating material.

Solid powders

The effects of blast attenuation by surrounding an explosive charge with a granular layer have been previously investigated. Sand has been used as a mitigating material and a peak overpressure attenuation of 5 – 40% has been demonstrated [25, 26]. A mixture of sand and cement has also shown the capacity to significantly mitigate the effects of blast waves [27]. Glass, steel, and ceramics [28], porcelain, plastic, claydite, and polyethylene spheres [29], and also perlite and pumice [30] have been studied. However, it is not clear, a priori, which properties of the granular media are most important for mitigation performance. Material density has been cited as a relevant parameter, suggesting that the transfer of momentum is an important source of energy dissipation [31]. Porosity of the granular medium is also significant, and the energy loss during the mitigation process has been attributed to the complex interaction of the blast wave with the compacting, impedance-mismatched medium [31, 32]. Particle size and the length of the granular layer [28] have been cited as potential mitigation parameters and the collapse of voids. However, the experiments in this study were carried out in a shock tube and it is difficult to extrapolate these results to the mitigation of a spherical freely expanding blast wave. In particular, shock tube experiments lead to a step rise in pressure, which is distinctly different from the pressure profile in a blast wave. The particle crushing and rearrangement during wave propagation have also been proposed as another mechanism of blast attenuation [30]. The configuration of the granular medium around the high explosive charge, including the addition of air gaps, also influences mitigation efficiency [28]. Finally, the energy dissipation via acceleration of the mitigant bed reduces the energy available to support the blast wave and can be related to the M/C ratio [17].

Liquids

The mitigation performance of liquid layers or multiphase liquid systems has likewise been investigated. Numerical predictions by Cheng et al. [33] of blast mitigation with water surrounding a spherical charge indicate that a reduction in peak overpressure by up to 80% is potentially possible at a scaled distance of $Z = 1$ m/kg$^{1/3}$. However, such a reduction is found at a water-to explosive mass ratio (M/C) of 10. At a more practical mass ratio of 3, the attenuation is closer to 60%. The study also shows that the mitigation performance increases with M/C suggesting that the loss of energy by transfer of momentum is an important dissipation mechanism. In addition, at a constant M/C, the attenuation worsens with the addition of an air gap between the charge and the liquid, which is explained by the reduction of the water layer thickness. Experimental studies using water and glycerine in a bulk form have confirmed the possibility of such reductions [31, 34], with relatively similar mitigation values observed for the two liquids.

The blast wave attenuation implies an energy loss to the mitigant layer, which has been attributed to the acceleration of the liquid and subsequent fragmentation of the liquid into fine droplets as well as thermal effects related to liquid vaporization [33, 34]. Several studies

have investigated mitigation with two-phase media such as bubbly liquids [35, 36] or a liquid droplet mist [34, 37]. Within such compressible two-phase media, the propagation of waves is considerably modified due to the impedance mismatch between the phases and the collapse of pores.

A great deal of work on blast mitigation with multiphase media has been carried by Gelfand and Silnikov [38], and they have developed a commercial blast mitigation system comprised of a gelled liquid with embedded compressible foam balls. Recent studies have investigated the mitigation properties of aqueous foams within a confined area [25, 39–41]. Aqueous foams are two-phase systems composed of gas cells trapped in a continuous liquid phase. In such a medium, a reduction of the peak overpressure by up to an order of magnitude, relative to that of a bare high-explosive charge, was observed [39]. Impulses, on the contrary, are less reduced with a maximum reduction of 50% and more subject to fluctuations attributed to measurement errors such as drift in the baseline pressure with time that occurs with certain types of pressure transducers. The attenuation is attributed to the momentum loss in the complex 3D multiphase structure of these media and is related to the number of gas cells found within the foams [25]. The high heat capacity of the liquid phase and the compressibility of the gas bubbles also play a significant role in the mitigation process [42].

2.2.4 Numerical modeling

The computational modeling of heterogeneous explosive systems with stratified layers of material is of interest for two main reasons. First, the predictive capability of such computations may be useful to avoid performing expensive experimental trials in restricted facilities. Secondly, they are of interest for probing flow field regions inaccessible to experimental diagnostics. For example, in the near field region, the local flow-field high temperatures and pressures are often beyond the operational nominal range of most pressure transducers. Furthermore, the opacity of the detonation products prevents the collection of light emission data and obscures the blast wave visualization with optical diagnostics (spectrometer, high-speed video camera, etc.).

Complete modeling of the explosive dispersal of a particle layer must first consider the initial shock propagation through the particle layer, consolidation of the layer, fracturing of the layer upon release, and the formation of incipient jets. Then, the computations must be capable of simulating the transmission of the shock as a blast wave into the surrounding air, the expansion of the dense gas-particle medium, and finally, the dilute gas-particle regime after the particle cloud has expanded over a sufficient volume. Such extensive characterization of the multiphase flow field is generally too computationally demanding. To cope with this constraint, researchers have to either restrict the resolution of the numerical domain or adapt the numerical strategy to the specific explosive dispersal feature of interest. For instance, Eulerian-Lagrangian simulations are appropriate to model the dynamics and the formation of jets [43]. Such mesoscale models must consider the multiple particle-particle [44] and local particle-flow

interactions [45]. They may also be adapted to model the blast propagation in the near field [46]. However, this numerical strategy is unadapted to model the blast wave propagation over several meters unless using exascale computing. Since blast wave properties are usually recorded in the far field, validation with experimental data requires a large numerical domain. Hence, the Eulerian-Eulerian strategy where both the particle and gas phases are continua advected through a fixed mesh is the most popular strategy to model far-field blast waves [47–49]. In this strategy, the governing equations describing the motion and the properties of both phases at large scales are supplemented by exchange terms to represent the interactions between the phases at smaller scales. Defining accurate exchange and closure terms remains a significant challenge for modelers. Characterizing and calibrating compaction EOS for the particle phase is also a complex task since experimental data for dynamically shock-loaded powders/liquids at very high pressures are scarce.

2.2.5 Outstanding issues addressed in Part II

After several decades of investigation, blast wave attenuation is still an active field of research, and several questions remain unanswered. For example, there is no consensus on the most efficient material characteristics for attenuating a blast wave. Blast mitigation performance has been investigated in many configurations but correlating the results between the various studies is arduous. This problem is mainly due to the absence of systematic material comparison for a given experimental setup and the difficulty of isolating the effect of a single parameter. The relation between jet dispersal and blast wave attenuation has not yet been established for heterogeneous explosive systems with stratified liquid or granular layers. As reviewed in section 2.2.2, terminal jet velocities of non-jetting powders are slightly faster than that of jetting powders. However, the main driver for jet acceleration is the expansion of the detonation products. In contrast, powder consolidation results primarily from the dissipation of the shock wave energy in the material layer. Hence, jetting powders could be more efficient at mitigating the blast wave than reducing the jet velocities compared to non-jetting powders. Furthermore, blast mitigation and jet formation have been mainly studied for dry granular powders and bulk liquids. However, little experimental blast wave attenuation data are available in the literature for wetted granular powders. Wetted granular layers seem to behave like liquids with respect to jet acceleration. Still, their behavior with respect to the blast wave attenuation remains to be determined.

Several experimental data demonstrated a reduction of the blast wave mitigation effectiveness with distance. For example, Kitagawa et al. [25] have investigated the blast wave mitigation from a pentaerythritol tetranitrate (PETN) charge surrounded by a sand layer. Data clearly showed a reduction of the peak blast pressure attenuation from 40% in the near field to 5% in the far field, compared to the unmitigated explosive. However, this result was not interpreted. **The central hypothesis in the work presented in part II is that the reduction in the mitigation**

effectiveness results from the far-field interaction between the dispersed materials and the blast wave front.

As described in section 2.2.4, two-fluid models are the most appropriate models to simulate blast wave propagation in the far field. Previous computations using such a numerical strategy demonstrated that accurately modeling the exchange terms between the phases is essential to capture the blast wave mitigation. Nevertheless, Milne et al. [8] showed that modeling the formation of jets was not necessary to predict accurately the trajectories of the inner and outer layers of the explosively dispersed material. This suggests that a simple 1D multiphase model may be used to gain some insight into the interaction of the dispersed particles with the surrounding gases and blast wave.

In Chapter 3, the blast wave mitigation from spherical charges surrounded by various bulk liquids, dry powders, and wetted powders is systematically investigated. Of interest is to search for the possible existence of a dominant material characteristic controlling the degree of mitigation. Of additional interest is to evaluate the sensitivity of the blast wave attenuation to the presence or the absence of explosive dispersed jets and classify wetted powders with respect to the blast attenuation. Further experimental evidence of the reduction of the mitigation effectiveness with distance is also investigated. In Chapter 4, numerical simulations are carried out to model the general trends of the experimental results of Chapter 3. The same 1D, two-phase numerical strategy previously used by Milne et al. [8] is employed. The computations aim to evaluate the blast mitigation sensitivity to various parameters. The dynamic interaction between the particles and the surrounding gas, which cannot be readily determined experimentally, is also explored.

2.3 Heterogeneous explosive systems with embedded solid particles

Adding materials within a conventional solid or liquid explosive is of interest for various applications. For example, adding large fractions of inert materials within such explosives may help decrease the detonation velocity (VOD) or the detonation pressure. Explosive mixtures mixed with inert materials are also used to modify the shape of the detonation wave, in the design of explosive lenses, or to reduce the shock pressure transmitted into a driven material [50, 51]. For air-blast applications, these explosive mixtures can enhance the blast pressure at late times via drag and contribute to structural loading due to direct material impact [19]. Conversely, adding reactive materials to high-explosive (HE) formulations is a well-established practice to increase the energetic output of explosions. Metallic particles are particularly of interest due to their high energy density when reacting with various oxidizers and the potential coupling between dispersed burning particles and the expanding blast. Aluminized explosives were first proposed and patented at the turn of the 20^{th} century [52, 53]. These explosives were widely

used during WWII in high-performance applications such as naval torpedoes (Torpex - 42% RDX, 40% TNT, 18% powdered aluminum) and aerial bombs (Tritonal – 80% TNT, 20% aluminum powder). In the modern context, metalized explosives are used in military ordnance to maximize air-blast impulse or to increase damage through a combination of material acceleration and enhanced blast effects. Metals may also augment the earth-moving capability of blasting explosives in the mining industry by enhancing the expansion work done by the products [54]. Finally, studying metalized explosives provides an interesting framework for understanding metal reaction fundamentals at very high pressures. Probing metal reaction in extreme conditions may also contribute to understanding accidents involving the detonation of explosives stored in an environment rich in metal dusts [55]. This section first reviews the state of research on metal reactions in various physical conditions and how these reactions can influence the blast wave. Then the main findings of the experimental and numerical blast wave studies with heterogeneous explosive systems with embedded solid particles are covered. Finally, the outstanding issues addressed in part III and related to this explosive configuration are delineated.

2.3.1 Combustion of metallic particles at ambient pressure

The combustion of metallic particles releases a significant amount of energy. Indeed, metal fuels possess a high volumetric energy density compared to fossil fuels, making them attractive for several applications. More specifically, metal fuels could replace other fuels to power heavy industries, transportation systems, or the electrical network. The combustion of metallic particles provides a source of clean energy with zero-carbon emissions and produces oxides that can be recycled [56]. Considerable progress has been made in understanding how dispersed metal particles burn, although there is some confusion in the literature regarding the definitions of fundamental concepts such as “reaction” or “ignition”. Combustion modes of metallic particles have been extensively studied at McGill in propagating [57] or stabilized flames [58] at atmospheric pressure and relatively low slip velocities ($\approx$ 10 m/s). In these conditions, particles below a critical diameter react predominantly in a mode limited by the kinetics of the metal reaction, which depends upon the temperature at the particle surface and the oxidizer concentration (reaction rates following an Arrhenius law [59, 60]). In this regime and under these flow conditions, the oxidizer temperature is close to the temperature at the particle surface. Conversely, if sufficiently heated, large particles can burn in a diffusion-limited regime limited by the diffusion of oxidizer towards the particles. In this mode, the temperature at the particle surface is generally significantly higher than the oxidizer temperature. Consequently, “ignition" is defined as the discontinuous transition between these two modes, and only particles above a critical diameter experience ignition [61, 62]. This analysis for dense particle suspensions contradicts models defining an external ignition temperature based on single-particle combustion experiments. Results from a wide variety of single-particle experiments have been collected by Beckstead [63] who proposed a correlation for the burn time of single aluminum particles.

The correlation suggested that the particle burn times depended primarily on the particle surface area and followed a d^n law where d was the particle diameter with $n \approx 2$. Nevertheless, the data exhibited significant scatter, and extrapolation of the burn time correlation to other systems such as those including suspensions with a high concentration of particles [62] has been shown to be not valid.

When reactive particles are added to an explosive, if the initial particle mass fraction is high, heat loss to the particles and expansion of the products may inhibit particle reaction during detonation propagation. However, the particle reaction modes described above may come into play on millisecond timescales as the particles are heated from contact with the hot shocked air around the charge. Note that the explosively-dispersed particles propagate at significant velocities ($\approx$ 1 km/s) when encountering the surrounding air. Consequently, the results for particles burning in flames with low slip velocities cannot be extrapolated to heterogeneous explosive systems with solid particles. Tanguay [64] investigated the reaction of metal rods and spherical aluminum and magnesium particles (5-100 μm) in high-speed flows of oxygen and hydrogen. He concluded that the particles burned on their surface, in the kinetic regime, with the burning times correlated with $d^{0.5}$. He also hypothesized that in the high-temperature detonation products, the metal would melt. He further postulated that, in the non-quiescent high-Weber number flows generated by explosions, molten metal droplets of size greater than about 14 μm could break up and that most of the chemical reactions could occur in the wake of the particle. He concluded that the chemical reaction rate at the particle surface could be completely decoupled from the energy release.

2.3.2 Reaction of metallic particles at the detonic stage

If the initial particle mass fraction is lower, then experimental evidence shows that considerable particle reaction may occur on the microsecond timescales for the detonation to propagate. Probing the particle reaction at the timescale of the detonation is problematic with *in-situ* diagnostics due to the extreme flow conditions and due to the optically-thick nature of the detonation products. Hence, most interpretations pertaining to particle reaction for the so-called detonics regime have been derived from indirect measurements of the detonation parameters (VOD, detonation pressure, heat of detonation) for various explosive mixtures with different types of particles. From detonation studies, there is a growing body of evidence that metal particles can react at this timescale and contribute to the acceleration ability of a metal casing [65–74]. Case-pushing capability and early signs of metal reaction seem to appear regardless of the explosive formulations used. In particular, metallic particles were observed to react at microsecond timescales in several conventional explosives including RDX [65–67], RDX-ammonium perchlorate (AP) [68], HMX [69, 70], nitroguanidine (NG) and bis (2,2,2-trinitroethyl) nitramine (BTNEN) [70]. Early-time contribution of Al reaction was also observed in hydrogen-free compounds such as

benzotrifuroxan (BTF) [71], carbon-free substances such as ammonium nitrate (AN) [72] or liquids such as nitromethane (NM) [73–75].

At the detonics stage, metal particles may react and release energy on two different timescales, namely i) within the detonation chemical reaction zone ($\leq$ 1 µs) therefore contributing to increasing the detonation energy, or ii) in the Taylor wave, on timescales of 10 - 100 microseconds, to augment the propulsive power of the explosive. At this date, the degree of metal reaction during either regime is still being debated. It is frequently assumed that the timescale of the reaction zone is too short for overcoming the passivating metal oxide layer which limits significant exothermic metal reactions. Consequently, metallic particles are often considered to be chemically inert within the detonation reaction zone [76–80]. This interpretation was popular to explain the VOD deficit in TNT-aluminum mixtures [76, 77]. The phenomenon was attributed to thermalization effects, compression, and heat transfer to the particles resulting in the reduction of the detonation energy [76, 77]. In contrast, the possibility of metal reaction has also been considered within the reaction zone. Cook et al. attributed the velocity deficit to endothermic reactions [81]. However, in TNT and RDX-Al mixtures, Cook et al. [82] also showed that the weakly exothermic reactions leading to the formation of gaseous aluminum suboxides like $Al_2O(g)$ could be followed by a rapid and substantial exothermic chemical condensation of $Al_2O_3(s)$ in an appreciable fraction in the reaction zone. However, they hypothesized that the exothermicity associated with chemical condensation of $Al_2O_3(s)$ served mainly to heat the detonation products but was not sufficient to increase significantly the work produced by the gases. They concluded that aluminized explosives could have relatively low casing-pushing ability (or brisance) but a high blast enhancement potential, when the $Al_2O_3(s)$ content increases upon further expansion of the products. Additional evidence that aluminum can react promptly in the reaction zone is given by recent experimental results that a mixture consisting of fine aluminum particles mixed with water (with 10% added hydrogen peroxide) can support the propagation of a detonation wave [83, 84].

The effects of particle size, initial mass fraction, type of metal, and morphology on the detonation wave have likewise been investigated. When sub-millimetric chemically inert particles (e.g., glass, steel) or additives (lithium fluoride, LiF) are added to conventional explosives, the detonation performance and casing/flyer-pushing ability unambiguously decreases [69, 85, 86] compared to the base explosive. The performance decline is associated with the transfer of heat and momentum, and compressive and explosive dilution effects. Conversely, for most explosive formulations with chemically reactive metals, reducing the particle size in the micron-scale range may increase slightly the casing pushing ability [65], although this phenomenon is not systematically observed in all studies [67, 74]. However, the performance is reduced with the addition of nano-scale particles [68, 73, 87]. It was postulated that the augmentation of the particle surface area could increase the reaction rate and thus increase the energy release to accelerate the casing, for micrometric particles. Conversely, for nanoparticles, the increase in surface area was compensated by the higher fraction of the passivating oxide layer and agglom-

eration effects, explaining the poor performance. Increasing the particle mass fraction does not necessarily result in better detonation performance since net exothermicity may not be sufficient to compensate for the reduction of explosive mass, and the energy spent to accelerate and heat the particles. Moreover, despite being exothermic, metal reactions may also reduce the total number of moles of gas in the detonation products, hence diminishing casing-pushing capability. Experimental results suggest that an initial particle loading of about 15% is optimum [66, 69, 74]. Finally, the type of metal and particle morphology could also have an influence on the detonation parameters and the casing-pushing ability. Loiseau et al. [74] showed that gelled NM mixtures with aluminum particles have a larger flyer plate-pushing ability compared to mixtures with magnesium, silicon, or titanium particles, at a mass fraction of 15%. It was also demonstrated that flake aluminum mixed with phlegmatized RDX resulted in lower VOD compared to mixtures with spherical particles due to the higher porosity introduced by the flakes [85].

2.3.3 Blast wave interactions with the dispersed solid particles

Blast wave interactions with inert particles

The blast wave overpressure generated by explosive charges comprised of packed beds (92 wt%) of inert steel beads saturated with sensitized NM was previously investigated by Frost et al. [19]. They found that both the recorded peak pressure and the positive-phase impulse values were reduced by a factor of about 2 in the near field, compared to a bare NM charge with the same explosive mass. Using cantilever gauges and free-piston impulse gauges, they demonstrated that the momentum flux of the particles exceeded that of the gas, suggesting that the loading from particle impacts is the primary hazard in this region. Zhang et al. [5] presented experimental data showing the free-field air blast mitigation for the same charges. The blast mitigation effectiveness was not readily apparent from the published data since the explosive mass between the bare and mitigated charge was different. However, if the data are scaled with the traditional cube root scaling law [88], the results reveal a diminution of the mitigation efficiency with an attenuation of 75% in the mid field down to 10% in the far field. This observation suggests that similarly to heterogeneous explosive systems with stratified layers of inert particles, the far-field interaction between the particles and the blast wave could be responsible for the reduction of the mitigation effectiveness with distance. However, the mitigation effectiveness with dilute suspensions (mass fraction < 60 wt%) of inert particles mixed with conventional explosives has not yet been characterized at all distances from the charge.

Blast wave interaction with reactive metallic particles

For the particle reaction to increase the casing/flyer pushing ability, the metal reaction must have a net volumetric exothermicity superior to that of the base explosive itself to augment the blast wave pressure of metalized explosives. The energy released from the metal reaction

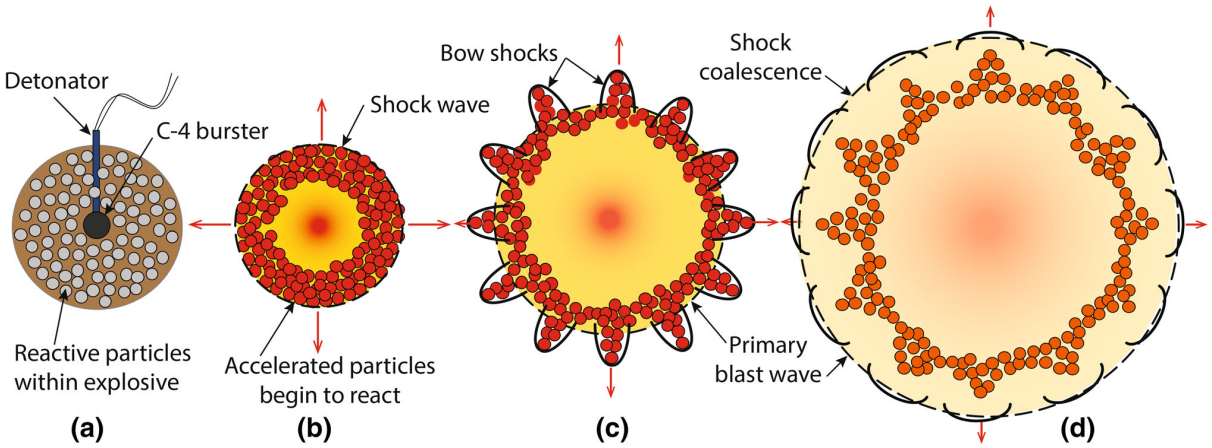

Fig. 2.7 Schematic of the events that are hypothesized to occur following the detonation of a high-explosive charge with embedded reactive particles (Figure courtesy of Frost [89]).

must compensate for the reduction of the explosive mass with particle dilution, and for the energy spent accelerating and heating the particles. Moreover, the chemical reactions and the subsequent energy release must occur sufficiently rapidly to couple with the blast wave. The time and length scales inherent to detonation waves or blast waves of heterogeneous explosive systems differ considerably. For example, since most heterogeneous explosives are fuel rich, metallic particles are most likely to react anaerobically with the detonation product species such as carbon dioxide (CO_2(g)) or water vapour (H_2O(g)). Anaerobic reactions at the 1-100 µs timescale are the predominant chemical reactions in detonation studies since the particles have no time to escape the products due to their inertia. Conversely, the particles or the detonation product species may also react with the surrounding air, at millisecond timescales and outside of the fireball, to contribute to enhancing the blast wave. However, the relative importance of each type of reaction remains elusive and depends on several factors including the oxygen balance of the base explosive, the nature of the metal, particle properties and dynamics, and initial particle mass loading. Afterburning effects following the recompression of the dispersed particle-gas mixture by the secondary shock and ground-reflected shock may also release additional energy that may couple with the blast wave. Similar to the explosive systems with stratified layers of materials, the dispersed particles locally perturb the flow field and may catch up and penetrate the blast wave front. The dispersed particles may be structured in the form of jets traveling at a supersonic speed and driving bow shocks ahead of the jet tips. The propensity to jet formation seems related to the initial particle mass fraction and reactivity. As the particle jets slow due to aerodynamic drag, the primary blast wave coming from behind may coalesce with the bow shocks, hence increasing the blast pressure. This hypothesized scenario is schematically depicted in Fig. 2.7. The scenario depicted in the figure corresponds to a fuel-rich charge with a high particle mass loading in which the particles are not completely consumed during the timescale of detonation wave propagation.

Frost et al. [90] studied the critical (charge) diameter for particle ignition (CDPI) of fuel rich heterogeneous explosive systems with packed beds of metallic particles saturated with sensitized NM. In these highly fuel-rich charges, they observed different reactivity patterns according to particle size and spherical charge diameters. For example, magnesium particles under 100 µm showed signs of "prompt" reactions for all charge diameters from 3.5 to around 20 cm. The "prompt" reactions were defined as reactions that were sufficiently short (typically < 1ms) to influence strongly the blast propagation. However, if the particle size was increased to 200 µm, only particles inserted in charges with large diameters (> 20 cm) exhibited signs of prompt reaction. For smaller diameter charges, delayed particle reaction (0.5 - 4 ms after detonation) or no reaction at all was observed. If the particle size was further increased above 200 µm, the particles never experienced a prompt reaction. For charges experiencing reaction delays, the delay increased (3 - 16 ms).

In the case of spherical charges with aluminum particles, the reaction pattern was more complex [91]. Evidence of prompt reaction throughout the dispersed cloud of particles was observed for intermediate-sized particles (60 µm particles) and for a charge diameter of around 20 cm. However, for some trials, particle reaction was observed only at discrete locations within the cloud. For the same charge diameter but varying particle size, reactions occurred either at discrete spots or were delayed, especially for the smallest particles. When reducing charge diameters below 20 cm, the probability of experiencing prompt reaction throughout the cloud decreased. The different reaction regimes for charges with packed beds of aluminum particles are illustrated in Fig. 2.8. The complex ignition behavior is influenced by the high particle mass loading in the charges (the Al solid mass fraction varied from 77 to 80 wt%). At these mass loadings, there is insufficient oxidizer in the explosive products to react all of the aluminum. For cases in which the particles ignite at discrete locations, as the particle cloud expands and mixes with the ambient air, flame propagation through the remaining aluminum powder was often observed at later times. Note that the results for NM/Al charges presented in this thesis in Chapter 5 utilized charges with lower particle loadings, and prompt particle reaction was always observed uniformly throughout the particle cloud. Charges with packed beds of zirconium particles were also tested and showed evidence of prompt reaction. However, the existence of a CDPI for these charges was not investigated.

The different reaction regimes had a strong influence on the blast wave pressure. For example, the peak blast pressure was augmented by an order of magnitude whereas the positive-phase impulse was increased by a factor of about 5 for charges with magnesium particles reacting promptly, compared to charges with particles experiencing a delayed reaction. The particle size generating the highest peak overpressure and impulses was 85 µm. Charges with aluminum particles experiencing prompt reaction also showed a higher blast enhancement capability compared to particles with delayed reaction. However, the scatter in the results was larger than for the trials with magnesium particles. For these charges, intermediate-sized particles (36 µm) generated the highest blast overpressures. The difference in reactivity pattern and blast

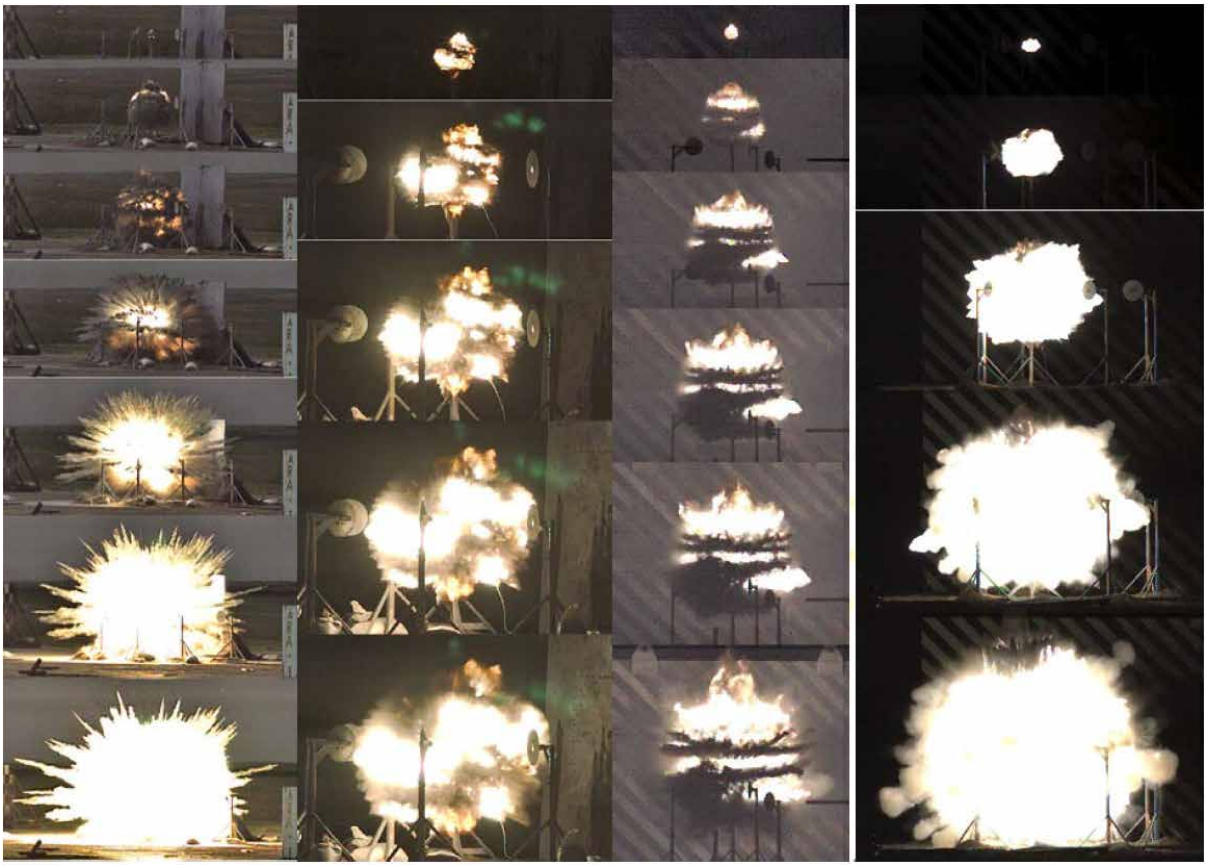

(a) **(b)** **(c)** **(d)**

Fig. 2.8 Variation of aluminum particle combustion regimes with particle and charge size. **(a)** delayed initiation of particle reaction for 12.3 cm dia charge with H-10 particles; times are 0, 0.7, 2, 4, 6, 8, and 10 ms; **(b)** prompt combustion at discrete locations within particle cloud for 9.3 cm dia charge with H-50 particles; time between frames 200 μs, **(c)** prompt, but nonuniform combustion of particles for 12.3 cm dia charge with H-95 particles; times between photographs 250 μs, except for last photograph which is 1 ms after the previous; **(d)** prompt combustion uniformly throughout particle cloud, for 12.3 cm dia charge with H-50 particles; times are 0.040, 0.2, 0.6, 1.6 and 3 ms, respectively (Figure and caption courtesy of Frost and Zhang [91]).

performance for various charge diameters suggests that the scale of the charge is an important factor in the design of metalized explosives. Stronger blast waves are generated with bigger charges indicating that the particle residence time in the hot detonation products may govern the blast enhancement for high particle loadings. Moreover, the fact that the smallest particles did not provide the highest blast performance suggests that the particle reaction rate is not driven by the metal surface area but rather by the thermodynamic state within the fireball.

In [91], Frost et al. argued that the traditional Hopkinson's scaling law [88] for homogeneous explosives was not appropriate to evaluate the metal reaction efficiency. Instead, they proposed to normalize the blast overpressure results by the energy release of the most exothermic particle reaction pathway (i.e., particle reaction with the O_2 of the surrounding air). For both charges with aluminum and magnesium particles, they found that the results did not collapse by a large margin with the Baker [92] database for homogeneous explosives. This result suggests that all of the particle reaction energy did not couple to the blast wave even if the particles reacted promptly. Even if Hopkinson's law is not informative in assessing the reaction efficiency for metalized explosives, it is nevertheless of interest to evaluate the blast enhancement capability between the base explosive and the metalized mixture at a constant volume. This comparison was not carried out in [91] but the results indicated that the peak blast overpressure for the charges with metallic particles was attenuated in the near field compared to that of the bare explosive charge of the same volume. However, the overpressure was augmented in the far field, presumably due to the combined particle reaction and particle piston effect (hypothesized in section 2.2). Conversely, the positive-phase impulse was systematically augmented at all distances from the charges. These results suggest that the particle reaction may be substantial enough to compensate for the reduced mass associated with particle dilution but not fast enough to contribute to supporting the blast wave front at early times.

One other salient phenomenon of the dispersal dynamics of packed beds of particles saturated with a liquid explosive is the formation of jets. The difference in jetting pattern is shown in Fig. 2.8. In the first sequence shown, the formation of coherent jets is visible. For this particular charge, the detonation failed to propagate fully through the NM/Al mixture, and the blast overpressure was two orders of magnitude less than the other cases which exhibit prompt particle reaction. When the detonation failed, the formed products dispersed the remaining NM/Al slurry in a manner similar to the dispersal of an inert liquid/particle mixture shown in Figure. 2.5. For the case of prompt particle reaction shown in the last sequence in Figure. 2.8, the formation of prominent coherent jets does not occur. Rather, in this case the reaction of the aluminum particles produces fine (submicron) aluminum oxide particles, which are entrained into the billowing jets at the fireball interface which develop due to the Rayleigh-Taylor instability (RTI). As such, the billowing structure of the jets in heterogeneous explosive systems with embedded particles is another indicator of early-time particle reaction.

The air-blast enhancement capability of metalized explosives has also been investigated for charges with diluted particle suspension (< 60 wt%) within conventional explosives. For

example, Trzciński et al. [93] evaluated the blast characteristics for NM charge with particles ($\sim$ 63 μm) made of an aluminum-magnesium alloy. They varied the initial particle mass fraction from 15% to 60% and found that the peak blast overpressure and the blast impulse were systematically increased for all mass fractions. The highest peak overpressure and impulse values were obtained for a particle mass loading of 30% at 2.0 from the charge up to 45% at 2.5 m. Relatively to the baseline NM alone, these values represented an augmentation of 37.5% for the peak pressure and 41% for the positive-phase impulse. They hypothesized that the blast augmentation resulted from partial particle anaerobic reactions at 20 - 40 μs followed by particle aerobic reactions with air. They also noted that the presence of magnesium could enhance the reaction rate of aluminum. When mixed with HMX at a mass fraction of 15 wt%, aluminum particles showed evidence of fast reaction [69]. The exothermic reactions augmented the blast pressure by 38% at 1.52 m from the charge, compared to HMX-LiF with the same mass of additive. However, in Al-phlegmatized RDX mixtures, the blast enhancement was not significant [94]. Also in sub-gram RDX-based aluminized explosives, Peuker et al. [95] showed that the blast enhancement was not a function of particle size for particles between 3 and 40 μm. The blast enhancement was found to be associated with roughly half anaerobic particle reaction and half aerobic reaction.

2.3.4 Numerical modelling

In a simplified 1D, single-phase, Eulerian model, Zarei and Frost [96] evaluated the influence of the timescale and location of the energy release on the blast overpressure. The total energy released was based on 1 kg of TNT, but a fraction of this energy was released in different locations, at different timescales to investigate the effect on the blast pressure field. This second energy release qualitatively represented the energy release associated with particle reaction in heterogeneous explosives systems. They found that the blast wave impulse was greater when the energy was released immediately behind the blast front than when released uniformly within the detonation products. Hence, to significantly support the blast front, they hypothesized that the metal particles must be sufficiently large (small particles tend to accommodate more quickly with the surrounding flow and lag behind the blast front). If the energy was released over a longer timescale or within the expanding products the peak blast overpressure was reduced but the positive-phase impulse was augmented. Using a 1D two-phase Eulerian model based on the theory of Baer and Nunziato [97], Leadbetter et al. [98] explored the energy partition between anaerobic and aerobic particle reaction in aluminized explosives. The particles were assumed to react when the surrounding gas temperature exceeded the metal melting point ($>$ 933 K) with a conventional burning time law ("d^2 law"). They found that the fraction of particles reacting anaerobically was greater than those burning aerobically, for large charge diameters ($\leq$ 21.3) and small particles (13 μm). Conversely, for intermediate-sized particles (54 μm), the proportion of aerobic reactions was not significant unless the charge diameter was excessively

large (250 cm). Using also a model based on the Baer and Nunziato approach, implemented in the CTH code [99], Cooper et al. [100] investigated the effects of enhanced blast explosives (EBX). The explosive modeled consisted of a mixture comprised of isopropyl nitrate (IPN), RDX, aluminum flakes and a gelling agent. They compared the results of shock tube problems with simulations carried out with the EDEN hydrocode (the code used in the present thesis) and found good agreement. They also reproduced well the near-field expansion experimental data of the spherical charges.

Analytical and numerical modeling of metalized explosives remains very challenging. For single-phase numerical models, a major issue is to define accurately an EOS for the metalized explosive. Since the metallic particles and the detonation products are generally not in thermal and mechanical equilibrium, chemical equilibrium codes fail to provide accurate detonation parameters [101]. The computed pressure-volume relation of the expanding products is also not correct. Hence, calibration of EOS such as the JWL EOS for the products is often performed using empirical experimental data and cylinder/flyer plate expansion tests. Advanced calibration techniques were proposed by several researchers [102–104]. For example, using previous experimental data, Jackson [103] developed a calibration method based solely on the VOD and initial explosive reactant density. This methodology could bypass the need for performing cylinder tests for each metalized explosive mixture and the determination of up to seven formulation-specific parameters. As for the modeling of heterogeneous explosive systems with stratified particles, two-phase models require a precise description of the multiphase gas-particle dynamics. Moreover, since particle reaction rates and mechanisms remain largely unknown, researchers resort to making several physical assumptions (e.g., Al gasification rate in the detonation products [66], local isentropic Al reaction process [65], etc.). However, such sub-grid models lack *in-situ* experimental data for validation.

2.3.5 Outstanding issues addressed in Part III

Despite more than a century of research, the effects of metalized explosives on blast wave propagation remain poorly understood. From previous work carried out at the detonics stage, it appears clear that metallic particles can react with the detonation products to boost the propulsive power of conventional explosives. However, in the blast wave community, the contribution of early-time metal reaction has been largely ignored or assumed not to contribute significantly to the blast wave enhancement. Instead, the blast pressure augmentation is assumed to result primarily from the aerobic particle reactions with oxygen in the air. Most particle reaction models used to characterize metalized explosives are based on the results from single particle experiments burning in flames at ambient pressure where the particle burning times are correlated to the surface area. Nevertheless, a growing body of evidence shows that such models are inadequate to model metal reactions in metalized explosives.

First, these models do not take into account the collective heating effects inside the dispersed particle suspension which may increase the particle reaction rate [61]. Secondly, explosively dispersed particles often travel at high velocities which can affect their reaction rate [64]. For example, the higher oxidizer diffusion may increase the reaction or lead to quenching effects, depending on the nature of the metal. Thirdly, few experimental studies have suggested that anaerobic particle reactions in the detonation products could influence the blast enhancement. The flow conditions in a condensed phase explosive, right after the detonation wave, are substantially different from that of a flame with pressures approaching tens of GPa, temperatures of about 3500 - 4000 K, and slip velocities above 1 km/s. Under these extreme conditions, the particle reaction mechanism and transport properties are completely unknown. At high pressures, the chemical reaction of reactive metal particles may not be activated in the same way as for metal vapors with oxygen. Indeed, at such extreme pressures characteristic of supercritical fluids, phases are not well separated, and the density of the particles is of the same order as the density of the supercritical fluid in the detonation products. Consequently, the reaction may be driven by the hydrodynamics of dissolution. Metal oxides could dissolve and be no more a barrier to the dissolution of the pure metal. Hence, the metals may react anaerobically instead with the detonation products, but the hydrogen or carbon oxide products produced by the metal reaction may still react sufficiently quickly with air to enhance the blast wave. **The central hypothesis in the work presented in part III is that significant early anaerobic particle reactions occur with water vapor in the products to produce hydrogen. This hydrogen burns quickly with the air at the fireball interface, resulting in the contribution of aerobic reactions to the blast enhancement. Hence, the contributions of aerobic reactions observed in previous experiments could be related to the hydrogen burning and not from the particle reacting in direct contact with air**.

Based on previous experiments, it appears that the initial particle mass loading is an important factor controlling the degree of metal reaction and the blast enhancement. Conventional explosives mixed with dilute particle suspensions of particles showed stronger signs of particle reactivity with the detonation products and better blast augmentation, as opposed to mixtures with high particle mass loadings. Consequently, investigating these mixtures seems more appropriate to test the aforementioned hypothesis. In Chapter 5, the hypothesis of early particle reaction is probed experimentally for diluted suspensions of aluminum and magnesium suspended in gelled NM. Different initial particle mass fractions are tested to evaluate the presence of an optimum fraction to enhance the blast wave pressure. For aluminum, three particle sizes are also investigated to assess if traditional burning models depending on particle surface area are consistent with the results. To gain insight into the contribution of the particle reaction, the blast wave pressure results are compared with explosives mixed with a suspension of inert glass particles. Of interest is to evaluate if the addition of a dilute suspension of inert particles within the explosive effectively mitigates the blast pressure. Also of interest is to determine if the dispersal of embedded particles leads to jet formation and how the mitigation effectiveness

varies with distance, in comparison to explosive systems with stratified systems. As mentioned earlier, the particle reaction mechanisms during the explosive dispersal of metalized explosives are largely unknown, especially at early time. To bypass this major issue, a simple energetic model is employed in Chapter 6 to evaluate the shortest timescale of particle energy release. The same 1D two-phase model as in part II is used. The methodology consists of varying the amount and the timescale of energy release, defined as two independent parameters, to match experimental data.

Summary

- Heterogeneous explosive systems with stratified material layers are investigated in Part II. Heterogeneous explosive systems with embedded solid particles are investigated in Part III.
- These two configurations are investigated experimentally and numerically.
- **Central hypothesis of part II:** the reduction of the blast mitigation effectiveness with distance results from the particle-blast interactions in the far field.
- **Central hypothesis of part III:** metallic particles react primarily anaerobically within microsecond timescales to enhance the blast wave pressure. The hydrogen produced by the particle reactions with water vapor within the detonation products reacts quickly within the turbulent mixing zone at the fireball interface to further increase the blast pressure.

References

[1] C. L. Mader, J. D. Kershner, and G. H. Pimbley. Three-dimensional modeling of inert metal-loaded explosives. *Journal of Energetic Materials*, 1(4):293–324, 1983, doi:10.1080/07370658308012323.

[2] D. L. Frost, J. Loiseau, B. J. Marr, and S. Goroshin. Particle segregation during explosive dispersal of binary particle mixtures. In *AIP Conference Proceedings*, volume 1793, pages 1–7. AIP Publishing, 2017, doi:10.1063/1.4971702.

[3] A. M. Milne, C. Parrish, and I. Worland. Dynamic fragmentation of blast mitigants. *Shock Waves*, 20:41–51, 2010, doi:10.1007/s00193-009-0235-5.

[4] D. L. Frost, Y. Grégoire, O. Petel, S. Goroshin, and F. Zhang. Particle jet formation during explosive dispersal of solid particles. *Physics of Fluids*, 24:091109, 2012, doi:10.1063/1.4751876.

[5] F. Zhang, D. L. Frost, P. A. Thibault, and S. B. Murray. Explosive dispersal of solid particles. *Shock Waves*, 10(6):431–443, 2001, doi:10.1007/PL00004050.

[6] F. Zhang, R. C. Ripley, A. Yoshinaka, C. R. Findlay, J. Anderson, and B. von Rosen. Large-scale spray detonation and related particle jetting instability phenomenon. *Shock Waves*, 25(3):239–254, 2015, doi:10.1007/s00193-014-0525-4.

[7] R. C. Ripley, L. Donahue, and F. Zhang. Jetting instability mechanisms of particles from explosive dispersal. *Journal of Physics: Conference Series*, 500(15):152012, 2014, doi:10.1063/1.3686594.

[8] A. M. Milne, E. Floyd, A. W. Longbottom, and P. Taylor. Dynamic fragmentation of powders in spherical geometry. *Shock Waves*, 24(5):501–513, 2014, doi:10.1007/s00193-014-0511-x.

[9] A. M. Milne, A. Longbottom, D. L. Frost, J. Loiseau, S. Goroshin, and O. Petel. Explosive fragmentation of liquids in spherical geometry. *Shock Waves*, 27:383–393, 2017, doi:10.1007/s00193-016-0671-y.

[10] K. Xue, F. Li, and C. Bai. Explosively driven fragmentation of granular materials. *European Physical Journal E*, 36(8):1–16, 2013, doi:10.1140/epje/i2013-13095-x.

[11] K. Xue, L. Sun, and C. Bai. Formation mechanism of shock-induced particle jetting. *Physical Review E*, 94(2):022903, 2016, doi:10.1103/PhysRevE.94.022903.

[12] B. J. Marr. *The explosive dispersal of heterogeneous systems surrounding high-explosive charges*. PhD thesis, McGill University, 2020, https://escholarship.mcgill.ca/concern/theses/00000446f.

[13] B. J. Marr, Q. Pontalier, J. Loiseau, S. Goroshin, and D. L. Frost. Suppression of jet formation during explosive dispersal of concentric particle layers. *AIP Conference Proceedings*, 1979(July), 2018, doi:10.1063/1.5044930.

[14] M. A. Cooper, A. W. Sapp, S. Guo, and T. J. Vogler. Imaging perturbed shock propagation in powders. *Review of Scientific Instruments*, 91(025109), 2020, doi:10.1063/1.5131348.

[15] M. Hudspeth, J. Olles, A. Mandal, J. Williams, S. Root, and T. Vogler. Strength of porous α- SiO_2 in a shock loaded environment: Calibration via Richtmyer-Meshkov instability and validation via Mach lens. *Journal of Applied Physics*, 128(205901), 2020, doi:10.1063/5.0028026.

[16] T. J. Vogler and M. C. Hudspeth. Tamped Richtmyer–Meshkov instability experiments to probe high-pressure material strength. *Journal of Dynamic Behavior of Materials*, 7(2):262–278, 2021, doi:10.1007/s40870-020-00288-y.

[17] J. Loiseau, Q. Pontalier, A. M. Milne, S. Goroshin, and D. L. Frost. Terminal velocity of liquids and granular materials dispersed by a high explosive. *Shock Waves*, 28(3):473–487, 2018, doi:10.1007/s00193-018-0822-4.

[18] D. E. Grady. The spall strength of condensed matter. *Journal of the Mechanics and Physics of Solids*, 36(3):353–384, 1988, doi:10.1016/0022-5096(88)90015-4.

[19] D. L. Frost, C. Ornthanalai, Z. Zarei, V. Tanguay, and F. Zhang. Particle momentum effects from the detonation of heterogeneous explosives. *Journal of Applied Physics*, 101(11):1–14, 2007, doi:10.1063/1.2743912.

[20] R. W. Gurney. The initial velocities of fragments from bombs, shell and grenades. Tech. Rep. (45), US Army Ballistic Research Laboratory, Aberdeen Proving Ground, Maryland, USA, 1943, https://apps.dtic.mil/sti/pdfs/ADA800105.pdf.

[21] J. T. Dehn. Models of explosively driven metal. Technical report, US Army Ballistic Research Laboratory, Aberdeen Proving Ground, Maryland, USA, 1984, https://apps.dtic.mil/sti/pdfs/ADA151942.pdf.

[22] G. E. Jones, J. E. Kennedy, and L. D. Bertholf. Ballistics calculations of Gurney, R. W. *American Journal of Physics*, 48(4):264–269, 1980, doi:10.1119/1.12135.

[23] J. E. Kennedy. The Gurney model of explosive output for driving metal. In J. A. Zukas and W. P. Walters, editors, *Explosive Effects and Applications*, chapter 7, pages 221–257. Springer New York, New York, NY, 1998, doi:10.1007/978-1-4612-0589-0_7.

[24] A. M. Milne. Gurney analysis of porous shell. *Propellants, Explosives, Pyrotechnics*, 41(4):665–671, 2016, doi:10.1002/prep.201600016.

[25] K. Kitagawa, S. Yamashita, K. Takayama, and M. Yasuhara. Attenuation properties of blast wave through porous layer. *Proc. 26th International Symposium on Shock Waves*, 1(1990):73–78, 2007, doi:10.1007/978-3-540-85168-4_10.

[26] V. F. Nestrenko. Shock (blast) mitigation by "soft" condensed matter. In *MRS Symp. Proc.*, volume 759, pages MM4.3.1–4.3.12, 2003, doi:10.1557/PROC-759-MM4.3.

[27] V. V. Golub, F. K. Lu, S. A. Medin, O. A. Mirova, A. N. Parshikov, V. A. Petukhov, and V. V. Volodin. Blast wave attenuation by lightly destructable granular materials. *Shock Waves: Proceedings of the 24th International Symposium on Shock Waves (Beijing, China, July 2004)*, pages 989–994, 2005, doi:10.1007/978-3-540-27009-6_151.

[28] A. Britan, G. Ben-Dor, O. Igra, and H. Shapiro. Shock waves attenuation by granular filters. *International Journal of Multiphase Flow*, 27(4):617–634, 2001, doi:10.1016/S0301-9322(00)00048-3.

[29] S. P. Medvedev, S. M. Frolov, and B. E. Gel'fand. Attenuation of shock waves by screens of granular material. *Journal of engineering physics*, 58(6):714–718, 1990, doi:10.1007/BF00872723.

[30] B. Langhorst, C. Cook, J. Schondel, and H. S. Chu. Material systems for blast-energy dissipation. In *IMPLAST 2010 Conference*, pages 1–8, Providence, Rhode Island, USA, 2010. Society for Experimental Mechanics.

[31] R. M. Allen, D. J. Kirkpatrick, A.W. Longbottom, A. M. Milne, and N. K. Bourne. Experimental and numerical study of free-field blast mitigation. In *AIP Conference Proceedings*, volume 706, pages 823–826, 2004, doi:10.1063/1.1780363.

[32] K. Endo, K. Kitagawa, and M. Yasuhara. Diffusion effect of blast pressure in porous complex media. In *39th AIAA Fluid Dynamics Conference*, number June in Fluid Dynamics and Co-located Conferences, pages 1–9, San Antonio, Texas, 2009. American Institute of Aeronautics and Astronautics, doi:10.2514/6.2009-3569.

[33] M. Cheng, K. C. Hung, and O. Y. Chong. Numerical study of water mitigation effects on blast wave. *Shock Waves*, 14(3):217–223, 2005, doi:10.1007/s00193-005-0267-4.

[34] A. D. Resnyansky and T. G. Delaney. Experimental study of blast mitigation in a water mist. Technical report, DSTO Defence Science and Technology Organisation, Edinburgh, South Australia, Australia, 2006, https://apps.dtic.mil/sti/pdfs/ADA465909.pdf.

[35] I. J. Campbell and A. S. Pitcher. Shock waves in a liquid containing gas bubbles. *Proceedings of the Royal Society of London. Series A. Mathematical and Physical Sciences*, 243(1235):534–545, 1958, doi:10.1098/rspa.1958.0018.

[36] B. E. Gelfand. Blast waves attenuation in two-phase media. In *Symposium on Interdisciplinary Shock Wave Research*, pages 150–166, Sendai, Japan, 2004.

[37] D. Schwer and K. Kailasanath. Blast mitigation by water mist (3) - mitigation of confined and unconfined blasts. Technical Report (3), Naval Research Laboratory, Washington D.C., USA, 2006, https://apps.dtic.mil/sti/pdfs/ADA452669.pdf.

[38] B. E. Gelfand and M. V. Silnikov. Explosions and blast control. Technical report, NPF Asterion, St. Petersburg, 2004.

[39] E. Del Prete, A. Chinnayya, L. Domergue, A. Hadjadj, and J.-F. F. Haas. Blast wave mitigation by dry aqueous foams. *Shock Waves*, 23(1):39–53, 2013, doi:10.1007/s00193-012-0400-0.

[40] W. F. Hartman, B. A. Boughton, and M. E. Larsen. Blast mitigation capabilities of aqueous foam. Technical report, Sandia National Laboratories, Albuquerque, New Mexico, USA, 2006, https://www.osti.gov/servlets/purl/877732.

[41] R. Raspet, S. K. Griffiths, J. M. Powers, H. Krier, T. D. Panczak, P. B. Butler, and F. Jahani. Attenuation of blast waves using foam and other materials. Technical report, US Army Construction Engineering Construction Laboratory, Champaign, Illinois, USA, 1989, https://apps.dtic.mil/sti/pdfs/ADA203148.pdf.

[42] A. Britan, H. Shapiro, and G. Ben-Dor. Foams for blast mitigation. In Paul Stevenson, editor, *Foam engineering: fundamentals and applications*, chapter 19, pages 477–512. John Wiley & Sons, 2012, doi:10.1002/9781119954620.

[43] K. Xue, J. Liu, C. Feng, Y. Gan, and C. Bai. Explosively driven hierarchical particle jetting. *Chemical Engineering Science*, 202:250–269, 2019, doi:10.1016/j.ces.2019.03.043.

[44] H. Mo, F. S. Lien, F. Zhang, and D. S. Cronin. A numerical framework for the direct simulation of dense particulate flow under explosive dispersal. *Shock Waves*, 28(3):559–577, 2018, doi:10.1007/s00193-017-0741-9.

[45] Y. Ling, A. Haselbacher, and S. Balachandar. Importance of unsteady contributions to force and heating for particles in compressible flows. Part 2: Application to particle dispersal by blast waves. *International Journal of Multiphase Flow*, 37(9):1013–1025, 2011, doi:10.1016/j.ijmultiphaseflow.2011.07.002.

[46] A. V. Marayikkottu and D. A. Levin. Influence of particle non-dilute effects on its dispersion in particle-laden blast wave systems. *Journal of Applied Physics*, 130(3):1–19, 2021, doi:10.1063/5.0047516.

[47] T. McGrath, J. St. Clair, and S. Balachandar. Modeling compressible multiphase flows with dispersed particles in both dense and dilute regimes. *Shock Waves*, 28(3):533–544, 2018, doi:10.1007/s00193-017-0726-8.

[48] Y. Sugiyama, T. Homae, T. Matsumura, and K. Wakabayashi. Numerical study on the attenuation effect on the blast wave of encircling a high explosive with granular media. *Journal of Applied Physics*, 127(16):164701, 2020, doi:10.1063/1.5143351.

[49] Y. Sugiyama, T. Homae, T. Matsumura, and K. Wakabayashi. Numerical study on the mitigation effect of glass particles filling a partially confined space on a blast wave. *International Journal of Multiphase Flow*, 136:103546, 2021, doi:10.1016/j.ijmultiphaseflow.2020.103546.

[50] V. F. Nesterenko. *Dynamics of heterogeneous materials*. Springer New York, NY, 2001, doi:10.1007/978-1-4757-3524-6.

[51] J. Loiseau, J. Huneault, O. E. Petel, S. Goroshin, D. L. Frost, A. J. Higgins, and F. Zhang. Development of multi-component explosive lenses for arbitrary phase velocity generation. *Journal of Physics: Conference Series*, 500(PART 19), 2014, doi:10.1088/1742-6596/500/19/192010.

[52] R. Escales. UK24377 (Patent), 1899.

[53] G. Roth. Performance of explosives (Patent), 1900.

[54] P-A. Persson, R. Holmberg, and J. Lee. *Rock blasting and explosives engineering*. CRC Press, 1993, doi:10.1201/9780203740514.

[55] R. Eckhoff. *Dust explosions in the process industries: identification, assessment and control of dust hazards*. Gulf Professional Publishing, 2003, doi:10.1016/B978-0-7506-7602-1.X5000-8.

[56] J. M. Bergthorson, S. Goroshin, M. J. Soo, P. Julien, J. Palecka, D. L. Frost, and D. J. Jarvis. Direct combustion of recyclable metal fuels for zero-carbon heat and power. *Applied Energy*, 160:368–382, 2015, doi:10.1016/j.apenergy.2015.09.037.

[57] J. Palecka, P. Julien, S. Goroshin, J. M. Bergthorson, D. L. Frost, and A. J. Higgins. Quenching distance of flames in hybrid methane-aluminum mixtures. *Proceedings of the Combustion Institute*, 35(2):2463–2470, 2015, doi:10.1016/j.proci.2014.06.116.

[58] M. Soo, P. Julien, S. Goroshin, J. M. Bergthorson, and D. L. Frost. Stabilized flames in hybrid aluminum-methane-air mixtures. *Proceedings of the Combustion Institute*, 34(2):2213–2220, 2013, doi:10.1016/j.proci.2012.05.044.

[59] S. Arrhenius. Über die dissociationswärme und den einfluss der temperatur auf den dissociationsgrad der elektrolyte. *Zeitschrift für Physikalische Chemie*, 4:96 – 116, 1889, doi:doi.org/10.1515/zpch-1889-0408.

[60] S. Arrhenius. Über die reaktionsgeschwindigkeit bei der inversion von rohrzucker durch säuren. *Zeitschrift für Physikalische Chemie*, 4, 1889, doi:10.1515/zpch-1889-0416.

[61] M. Soo, S. Goroshin, J. Bergthorson, and D. L. Frost. Reaction of a particle suspension in a rapidly-heated oxidizing gas. *Propellants, Explosives, Pyrotechnics*, 40(4):604–612, 2015, doi:10.1002/prep.201400269.

[62] M. Soo, X. Mi, S. Goroshin, A. J. Higgins, and J. M. Bergthorson. Combustion of particles, agglomerates, and suspensions – A basic thermophysical analysis. *Combustion and Flame*, 192:384–400, 2018, doi:10.1016/j.combustflame.2018.01.032.

[63] M. W. Beckstead. Correlating aluminum burning times. *Combustion, Explosion and Shock Waves*, 41(5):533–546, 2005, doi:10.1007/s10573-005-0067-2.

[64] V. Tanguay. *Combustion of reactive metal particles in high-speed flow of detonation products*. PhD thesis, McGill University, 2009, https://escholarship.mcgill.ca/concern/theses/02870x706.

[65] J. Duan, C. Wu, F. J. An, and S. S. Liao. A quasi-analytical model of aluminized explosive products under strong constraint. *Advances in Mechanical Engineering*, 9(11):1–10, 2017, doi:10.1177/1687814017739511.

[66] X. Yuan, C. Wu, F. An, S. Liao, M. Zhou, Z. Shi, and D. Xue. A non-isentropic model of aluminized explosives involved with the reaction degree of aluminum powder for post-detonation burning behavior. *Physics of Fluids*, 32(2), 2020, doi:10.1063/1.5139692.

[67] X. Li, H. Pei, X. Zhang, and X. Zheng. Effect of aluminum particle size on the performance of aluminized explosives. *Propellants, Explosives, Pyrotechnics*, 45(5):807–813, 2020, doi:10.1002/prep.201900308.

[68] A. Lefrancois, G. Baudin, C. Le Gallic, P. Boyce, and J-P. Coudoing. Nanometric aluminum powder influence on the detonation efficiency of explosives. In *12th International Detonation Symposium*, San Diego, U.S.A., 2002.

[69] V. W. Manner, S. J. Pemberton, J. A. Gunderson, T. J. Herrera, J. M. Lloyd, P. J. Salazar, P. Rae, and B. C. Tappan. The role of aluminum in the detonation and post-detonation expansion of selected cast HMX-based explosives. *Propellants, Explosives, Pyrotechnics*, 37(2):198–206, 2012, doi:10.1002/prep.201100138.

[70] M. N. Makhov, M. F. Gogulya, A. Yu. Dolgoborodov, M. A. Brazhnikov, V. I. Arkhipov, and V. I. Pepekin. Acceleration ability and heat of explosive decomposition of aluminized explosives. *Combustion, Explosion and Shock Waves*, 40(4):458–466, 2004, doi:10.1023/B:CESW.0000033569.77449.d9.

[71] B. C. Tappan, L. G. Hill, V. W. Manner, S. J. Pemberton, M. A. Lieber, C. E. Johnson, and V. E. Sanders. Reactions of powdered aluminum with explosives that selectively form carbon dioxide or water as oxidizers. *International*

Journal of Energetic Materials and Chemical Propulsion, 15(4):339–350, 2016, doi:10.1615/IntJEnergeticMaterialsChemProp.2017011503.

[72] D. L. Robbins, E. K. Anderson, M. U. Anderson, S. I. Jackson, and M. Short. Cylinder test characterization of an ammonium nitrate and aluminum powder explosive. *15thInternational Detonation Symposium*, 803:826–835, 2014.

[73] G. Baudin, A. Lefrancois, D. Bergues, J. Bigot, and Y. Champion. Combustion of nanophase aluminum in the detonation products of nitromethane and TNT. In *11th International Detonation Symposium*, Colorado, U.S.A., 1998.

[74] J. Loiseau, S. Goroshin, D. L. Frost, A. J. Higgins, and F. Zhang. Ability of metalized gelled nitromethane to accelerate a flyer plate. In *16th International Detonation Symposium*, Cambridge, U.S.A., 2018.

[75] Y. Kato, K. Murata, and S. Itoh. Detonation characteristics of packed beds of aluminum saturated with nitromethane. *Proceedings of the 13th International Detonation Symposium, IDS 2006*, pages 187–195, 2006.

[76] L. S. Wise. Effect of aluminum on the rate of detonation of TNT. Tech. Rep. No. 1550, Picatinny Arsenal, Dover, NJ, 1945, https://apps.dtic.mil/sti/pdfs/AD0654028.pdf.

[77] J. L. Copp and A. R. Ubbelohde. Physico-chemical processes occurring at high pressures and temperatures - Part II: The effect of "inert" components on detonation. *Transactions of the Faraday Society*, 44(0):658–669, 1948, doi:10.1039/TF9484400658.

[78] P. J. Haskins, M. D. Cook, and R. I. Briggs. The effect of additives on the detonation characteristics of a liquid explosive. In *AIP Conference Proceedings*, volume 620, 2002, doi:10.1063/1.1483680.

[79] S. K. Chan. Reaction delay of aluminum in condensed explosives. *Propellants, Explosives, Pyrotechnics*, 39(6):897–903, 2014, doi:10.1002/prep.201400093.

[80] W. A. Trzciński and L. Maiz. Thermobaric and enhanced blast explosives - properties and testing methods. *Propellants, Explosives, Pyrotechnics*, 40(5):632–644, 2015, doi:10.1002/prep.201400281.

[81] M. A. Cook, A. S. Filler, R. T. Keyes, W. S. Partridge, and W. Ursenbach. Aluminized explosives. *The Journal of Physical Chemistry*, 61(2):189–196, 1957, doi:10.1021/j150548a013.

[82] M. A Cook, A. S. Filler, T. K. Robert, W. S. Partridge, and W. O. Ursenbach. Thermohydrodynamics and reaction kinetics in some metalized explosives. In *Proceedings of the 2nd International Detonation Symposium*, pages 1–16, Washington, District of Columbia, 1955.

[83] M. M. Schmitt, P. R. Bowden, B. C. Tappan, and D. Henneke. Steady-state shock-driven reactions in mixtures of nano-sized aluminum and dilute hydrogen peroxide. *Journal of Energetic Materials*, 36(3):266–277, 2018, doi:10.1080/07370652.2017.1376233.

[84] J. Loiseau, G. Chase, S. Goroshin, and D. L. Frost. Detonation and metal acceleration of aluminum-water mixtures. In *16th International Detonation Symposium*, Cambridge, U.S.A., 2018.

[85] W. A. Trzciński, S. Cudzilo, and L. Szymańczyk. Studies of detonation characteristics of aluminum enriched RDX compositions. *Propellants, Explosives, Pyrotechnics*, 32(5):392–400, 2007, doi:10.1002/prep.200700201.

[86] J. Loiseau, W. Georges, D. L. Frost, and A. J. Higgins. The propulsive capability of explosives heavily loaded with inert materials. *Shock Waves*, 28(July):709–741, 2018, doi:10.1007/s00193-017-0781-1.

[87] P. Brousseau, H. E. Dorsett, M. D. Cliff, and C. J. Anderson. Detonation properties of explosives containing nanometric aluminum powder. In *12th Internation Detonation Symposium*, pages 1–10, San Diego, U.S.A., 2002.

[88] G. F. Kinney and K. J. Graham. *Explosive shocks in air (Second edition)*. Springer, 1985, doi:10.1007/978-3-642-86682-1.

[89] D. L. Frost. Heterogeneous/particle-laden blast waves. *Shock Waves*, 28(3):439–449, 2018, doi:10.1007/s00193-018-0825-1.

[90] D. L. Frost, F. Zhang, S. Murray, and S. McCahan. Critical conditions for ignition of metal particles in a condensed explosive. In *12th International Detonation Symposium*, pages 1–10, San Diego, CA, U.S.A.

[91] D. L. Frost and F. Zhang. The nature of heterogeneous blast explosives. In *19th International Symposium on Military Aspects of Blast and Shock (MABS 19)*, Calgary, Canada, 2006.

[92] W. E. Baker. *Explosions in air*. University of Texas Press, Austin, 1973.

[93] W. A. Trzciński, J. Paszula, and S. Grys. Detonation and blast wave characteristics of nitromethane mixed with particles of an aluminium - magnesium alloy. *Propellants, Explosives, Pyrotechnics*, 35(2):85–92, 2010, doi:10.1002/prep.200900041.

[94] W. A. Trzciński, S. Cudziło, and J. Paszula. Studies of free field and confined explosions of aluminium enriched RDX compositions. *Propellants, Explosives, Pyrotechnics*, 32(6):502–508, 2007, doi:10.1002/prep.200700202.

[95] J. M. Peuker, H. Krier, and N. Glumac. Particle size and gas environment effects on blast and overpressure enhancement in aluminized explosives. *Proceedings of the Combustion Institute*, 34(2):2205–2212, 2013, doi:10.1016/j.proci.2012.05.069.

[96] Z. Zarei and D. L. Frost. Simplified modeling of blast waves from metalized heterogeneous explosives. *Shock Waves*, 21(5):425–438, 2011, doi:10.1007/s00193-011-0316-0.

[97] M. R. Baer and J. W. Nunziato. A two-phase mixture theory for the deflagration-to-detonation transition (ddt) in reactive granular materials. *International Journal of Multiphase Flow*, 12(6):861–889, 1986, doi:10.1016/0301-9322(86)90033-9.

[98] J. Leadbetter, R. C. Ripley, F. Zhang, and D. L. Frost. Multiple energy scaling of blast waves from heterogeneous explosives. In *21st International Colloquium on the Dynamics of Explosions and Reactive Systems (ICDERS)*, Poitiers, France, 2007.

[99] J. M. McGlaun, S. L. Thompson, and M. G. Elrick. CTH: A three-dimensional shock wave physics code. *International Journal of Impact Engineering*, 10(1-4):351–360, 1990, doi:10.1016/0734-743X(90)90071-3.

[100] M. A. Cooper, M. R. Baer, R. G. Schmitt, M. J. Kaneshige, R. J. Pahl, and P. E. DesJardin. Understanding enhanced blast explosives : a multi-scale challenge. In *19th International Symposium on Military Aspects of Blast and Shock (MABS 19)*, pages 1–23, Calgary, Canada, 2006.

[101] C. Capellos, E. L. Baker, S. Nicolich, W. Balas, J. Pincay, and L. I. Stiel. Eigenvalue detonation of combined effects aluminized explosives. *AIP Conference Proceedings*, 955(2007):357–360, 2007, doi:10.1063/1.2833055.

[102] C. Mortensen and P. C. Souers. Optimizing code calibration of the JWL explosive equation-of-state to the cylinder test. *Propellants, Explosives, Pyrotechnics*, 42(6):616–622, 2017, doi:10.1002/prep.201700031.

[103] S. I. Jackson. Scaling of the detonation product state with reactant kinetic energy. *Combustion and Flame*, 190:240–251, 2018, doi:10.1016/j.combustflame.2017.12.008.

[104] J. Garno, F. Ouellet, S. Bae, T. L. Jackson, N. H. Kim, R. Haftka, K. T. Hughes, and S. Balachandar. Calibration of reactive burn and Jones-Wilkins-Lee parameters for simulations of a detonation-driven flow experiment with uncertainty quantification. *Physical Review Fluids*, 5(12):1–24, 2020, doi:10.1103/PhysRevFluids.5.123201.

Part II

Preamble to Chapter 3

In the next chapter, the blast wave pressure produced by a spherical C-4 explosive charge surrounded by stratified layers of various material is investigated to determine the effect of the material dispersal on the blast wave properties. This experimental paper compiles and analyses data collected from a large number of field trials carried out over a decade. The configurations tested are schematically depicted in Fig. 2.9 and include either (a) a dry packed layer of granular material, (b) a packed layer of granular material saturated with water or (c) bulk liquid layers.

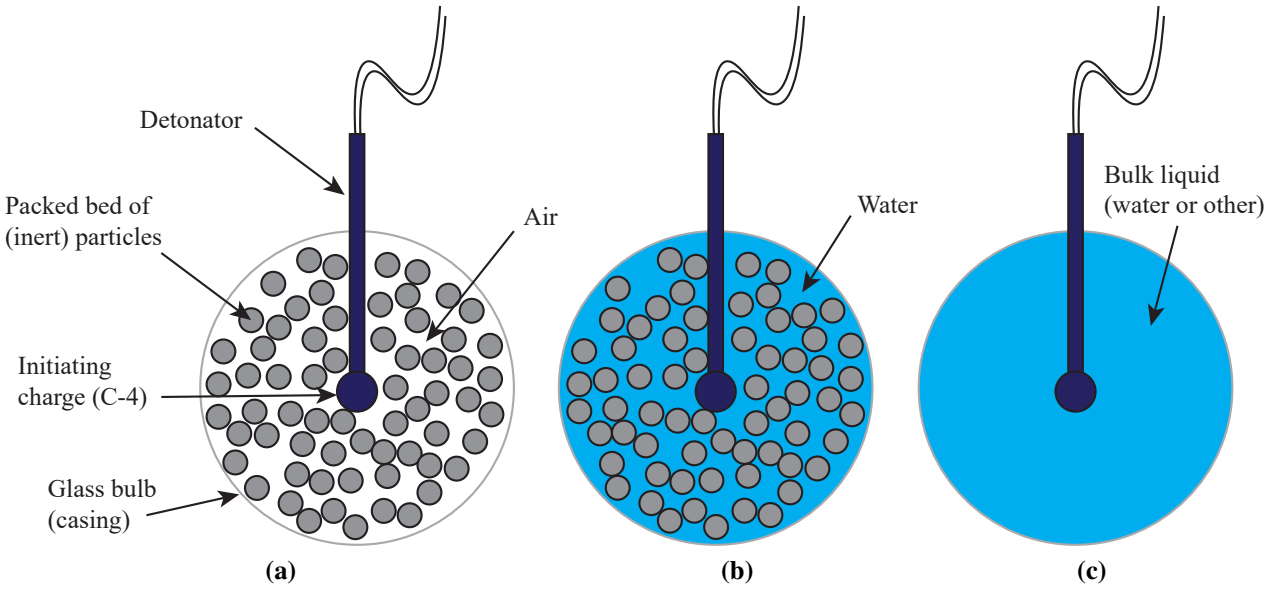

Fig. 2.9 Experimental configurations tested in Chapter 3.

The blast mitigation effectiveness of these configurations is compared. It is of particular interest to determine if configuration (b) behaves closer to configuration (a) or to configuration (c), with respect to the blast wave attenuation. The influence of the presence or the absence of jets on the blast wave pressure is also evaluated. The possible existence of a dominant parameter controlling the degree of mitigation is also of interest. Finally, the potential reduction of the mitigation effectiveness with distance, hypothesized in the previous chapter, is evaluated. It should be noted that the simplified configurations studied in Chapter 3 are not intended to study any particular attenuation system. Rather, the main objective is to understand the fundamental

interactions between the dispersed materials and the blast wave and to evaluate the blast wave pressure reduction. Nevertheless, the reported results have practical applications for hazard prediction and design of blast wave attenuation systems. This chapter is comprised of on a paper published in the *Shock Waves* journal.

Chapter 3

Experimental investigation of blast mitigation and particle–blast interaction during the explosive dispersal of particles and liquids

Q. Pontalier, J. Loiseau, S. Goroshin, D. L. Frost, *Shock Waves*, 2018.
doi:10.1007/s00193-018-0821-5

Abstract

The attenuation of a blast wave from a high explosive charge surrounded by a layer of inert material is investigated experimentally in spherical geometry for a wide range of materials. The blast wave pressure is inferred from extracting the blast wave velocity with high-speed video as well as direct measurements with pressure transducers. The mitigant consists of either a packed bed of particles, a particle bed saturated with water, or a homogeneous liquid. The reduction in peak blast wave overpressure is primarily dependent on the mitigant to explosive mass ratio, M/C, with the mitigant material properties playing a secondary role. Relative peak pressure mitigation reduces with distance and for low values of M/C (< 10) can return to unmitigated pressure levels in the mid-to-far field. Solid particles are more effective at mitigating the blast overpressure than liquids, particularly in the near field and at low values of M/C, suggesting that the energy dissipation during compaction, deformation, and fracture of the powders plays an important role. The difference in scaled arrival time of the blast and material fronts increases with M/C and scaled distance, with solid particles giving the largest separation between the blast wave and cloud of particles. Surrounding a high-explosive charge with a layer of particles reduces the positive-phase blast impulse, whereas a liquid layer has no influence on the impulse in the far field. Taking the total impulse due to the blast wave and material impact into account

implies that the damage to a nearby structure may actually be augmented for a range of distances. These results should be taken into consideration in the design of explosive mitigant systems.

Electronic supplementary material The online version of this article (https://doi.org/10.1007/s00193-018-0821-5) contains supplementary material which are reproduced in Appendix C with permission from Springer Nature.

Keywords Blast wave mitigation · Powder compaction · Particle–blast interaction · Explosive particle dispersal

3.1 Introduction

Blast waves generated by the detonation of high explosives are a serious hazard for nearby personnel and structures, and hence the mitigation of blast waves is an important practical concern. One common technique for reducing the strength of a free-field air blast is to surround a high-explosive charge with a layer of liquid, granular material, and/or porous cellular material. A variety of blast energy dissipation mechanisms have been proposed, and the relative importance of the different mechanisms for blast wave mitigation depends on the particular media used.

The use of a liquid layer for blast attenuation has been investigated experimentally and numerically. Numerical predictions of blast mitigation with water surrounding a spherical charge indicate that a reduction in peak overpressure by up to 80% is possible with a mass of mitigant to explosive ratio M/C of 10, although the droplet-blast interaction was not considered in this study [1]. Experimental studies using water and glycerine in a bulk form have confirmed the possibility of such a reduction [2, 3], with similar mitigation observed for the two liquids, ranging from almost 90% in the mid field to 80% in the far field for $M/C = 34$ (water)–44 (glycerine) [3]. The blast wave attenuation implies an energy loss to the mitigant layer, which has been attributed to the acceleration of the liquid and subsequent fragmentation of the liquid into fine droplets as well as thermal effects related to liquid vaporization [1, 3]. Several studies have investigated the mitigation performance using a two-phase medium such as a liquid droplet mist [3, 4] or aqueous foam [5–9] within a confined area. For mists, the maximum peak blast overpressure attenuation was numerically predicted to be 70% in the mid field, with droplet sizes of 27.5 μm and a mass loading of 2, defined as the ratio of water to gas mass within a computational cell [4]. For aqueous foams, reductions of the peak overpressure, relative to that of a bare high-explosive charge, were observed experimentally between 90% and 95%, at scaled distances between 1 m/kg$^{1/3}$ and 3 m/kg$^{1/3}$, respectively [5]. The attenuation is attributed to the momentum loss in the complex 3D multiphase structure of these media and is related to the number of gas cells found within the foams [8]. The high heat capacity of the liquid phase and the compressibility of the gas bubbles also play a significant role in the mitigation process [10].

The mitigation performance of granular materials has likewise been investigated extensively. Sand has been proposed as a potential candidate [8, 11] to mitigate a blast wave. In small-scale experiments, the attenuation of the peak overpressure has been observed to decrease with distance from a value of 40% in the near field to 5% in the far field with M/C between 0.1–0.2 [8]. Glass, steel, and ceramic [12], porcelain, plastic, claydite, and polyethylene spheres [13] have also been studied. In large-scale experiments, perlite and pumice have been used to reduce the strength of the blast wave. For example, small pockets of pumice (5.7-cm-thick, $m = 1.62$ kg) placed in the far field reduced the peak blast overpressure by 66% and the blast impulse by 84% [14]. However, it is not clear, *a priori*, which properties of the granular media are most important for mitigation performance. Material density has been cited as a relevant parameter, suggesting that the transfer of momentum from the explosion to the particles is an important determinant of blast attenuation [2]. Porosity of the granular medium is also a significant factor, resulting in energy dissipation during the shock-medium interaction leading to compaction of the medium [2, 15]. The particle size and thickness of granular layers have also been cited as potential mitigation parameters [12]. Particle crushing and rearrangement during void collapse have been proposed as other contributions to energy dissipation [14]. Compaction mechanisms have been extensively studied by research groups investigating the response of dry or water-saturated soils subjected to blast loadings [16–18]. These studies focus mainly on the shock transmission to buried structures or underground facilities and the formation of craters [18]. Finally, the energy dissipation via acceleration of the mitigant bed has been analyzed in a companion paper as a function of the mitigant mass to charge mass M/C [19], which is correlated with the velocity of the explosively dispersed material according to classical Gurney analysis [20, 21].

When a high-explosive charge surrounded by a layer of inert material is detonated, a shock wave propagates into the material, radially compacting the material to a degree which depends on the initial bed porosity, particle compressive strength and local strength of the shock wave. When the shock wave reaches the surface of the material layer, a blast wave is transmitted into the surroundings and an expansion wave propagates back into the compacted material, causing it to expand radially outwards [22, 23]. The tension induced within the compacted bed of material causes it to break up into fragments that have a size on the order of the thickness of the compacted layer when the expansion wave reaches the inner surface of the layer [24]. The fragments move radially outwards, shedding particles in their wake and leading to the formation of jet-like structures, an example of which is shown in Fig. 3.1. Particle jetting is a common feature of high-explosive particle dispersal, however jet formation is not observed for particles with high compressive strength [22]. The explosive dispersal of liquids, in general, also leads to the formation of droplet jets (see Fig. 3.1b for an example for a layer of glycerol), although other phenomena, such as cavitation within the liquid layer behind the expansion wave, govern jet formation [25]. The explosive dispersal of liquid-saturated particle beds leads to the formation of droplet jets similar to the case of liquid dispersal, and is discussed in a companion paper [19]. Although the mechanism of jet formation is not addressed in the present paper, it is of interest

to determine whether or not the presence of particle/droplet jets influences the degree of blast wave attenuation.

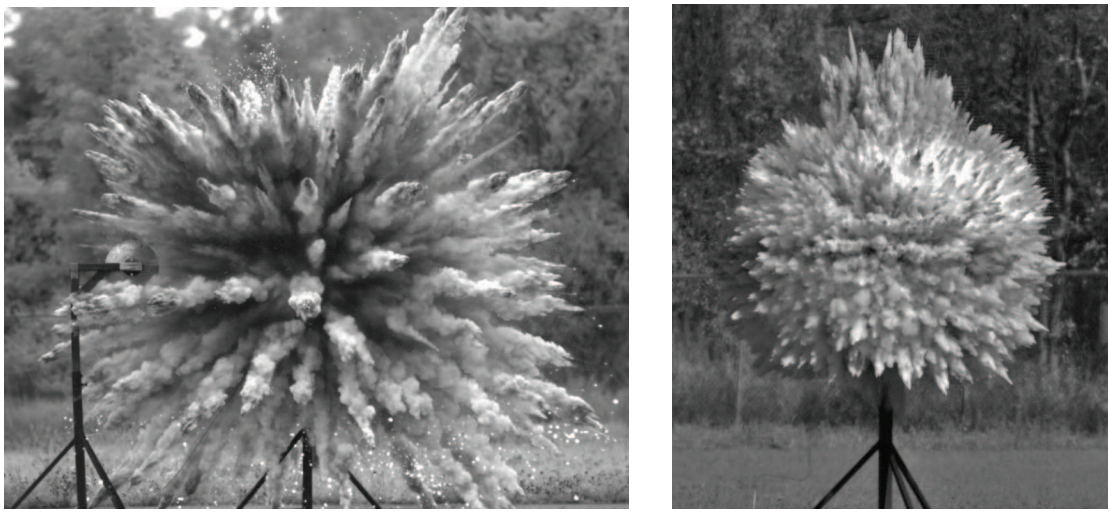

(a) **(b)**

Fig. 3.1 Jet formation for **(a)** silicon carbide powder with mass ratio M/C of 54 and for **(b)** glycerol with a mass ratio of 5.8.

The present study examines the relative blast wave mitigation performance of a layer of either a granular material, liquid, or a liquid-saturated particle bed surrounding an high-explosive charge in spherical geometry. A variety of different mitigant materials are tested, including powders with a range of particle size, density, and packed bed porosity, covering a wide range of mitigant to charge mass ratios. In some experiments, the blast wave peak overpressure and impulse were obtained using fast-response pressure transducers located at various locations from the charge. The peak blast wave overpressure history very near the charges was determined with high-speed videography, by measuring the blast wave velocity with image analysis and then inferring the peak blast wave overpressure using the Rankine-Hugoniot relation. The particle-blast interaction is also investigated to quantify the potential blast pressure recovery as a function of distance. This paper is structured in the following way: Section 3.2 describes the experimental conditions and section 3.3 details the video processing steps used to extract the blast wave pressure. Section 3.4 presents the experimental results for the effect of mitigant properties on the attenuation of the blast wave pressure and impulse and a discussion of the implications of the results regarding suitable material properties for blast mitigation is presented in section 3.5. A complimentary dataset is also attached with the paper as supplementary material.

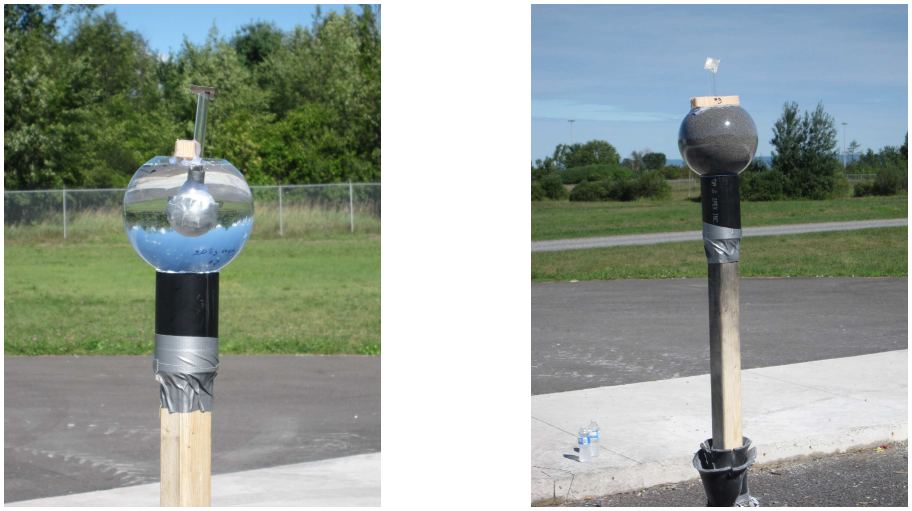

(a) **(b)**

Fig. 3.2 Glass bulb with a central C-4 burster filled with either **(a)** water or **(b)** iron powder. The detonator is inserted into the C-4 through the plastic tube visible protruding above the charge. The tube and C-4 are held in place by the visible wooden cross piece which is attached to the bulb.

3.2 Experimental overview

The charge casings used in the present study consisted of thin-walled (1-mm-thick) commercial glass light bulbs with the filaments removed. Either G40 (nominal dia 12.7 cm) or G25 (nominal dia 9.5 cm) bulbs were used. A spherical ball of C-4 (15–82 g) formed by hand was placed in the middle of the glass sphere with a plastic tube attached to allow the insertion of an electric detonator into the C-4 prior to the test. For the dispersal of liquids with a high-explosive charge, the C-4 was placed within a hollow polyethylene sphere ($m = 12.0$ g, nominal dia 3.5 cm) to isolate it from the liquid and provide a means by which the C-4 could be held rigidly in place at the centre of the charge. The PE sphere was cut in half, filled with C-4, then reassembled. The detonator tube was epoxied to the sphere and held in place with a wooden cross-piece visible at the top of the bulb in Fig. 3.2. Flow of detonation products up the tube perturbs the symmetry of the motion at the top of the charge (see Fig. 3.1b) but has no effect on the lateral motion of the material or blast. In the case of solid particles, bare C-4 charges were used. The charge was prepared by filling the sphere half full of powder, then placing the C-4 ball with attached tube in the center of the sphere, then filling the remainder of the powder such that the C-4 was held in place by the powder. The charges were supported by a section of plastic tube attached to the end of a wooden rod, with a height of burst of 1.5 m.

For some trials, the blast overpressure was recorded with piezoelectric pressure transducers (PCB 113A24, risetime $\lesssim 1$ μs) mounted in lollipop-style gauges (lollipop dia 30 cm) at various distances from the charge (1.1 m, 2.0 m, 4.0 m), as shown in the photograph in Fig. 3.3. The distance for the farthest transducer was chosen such that the ground-reflected wave arrived at

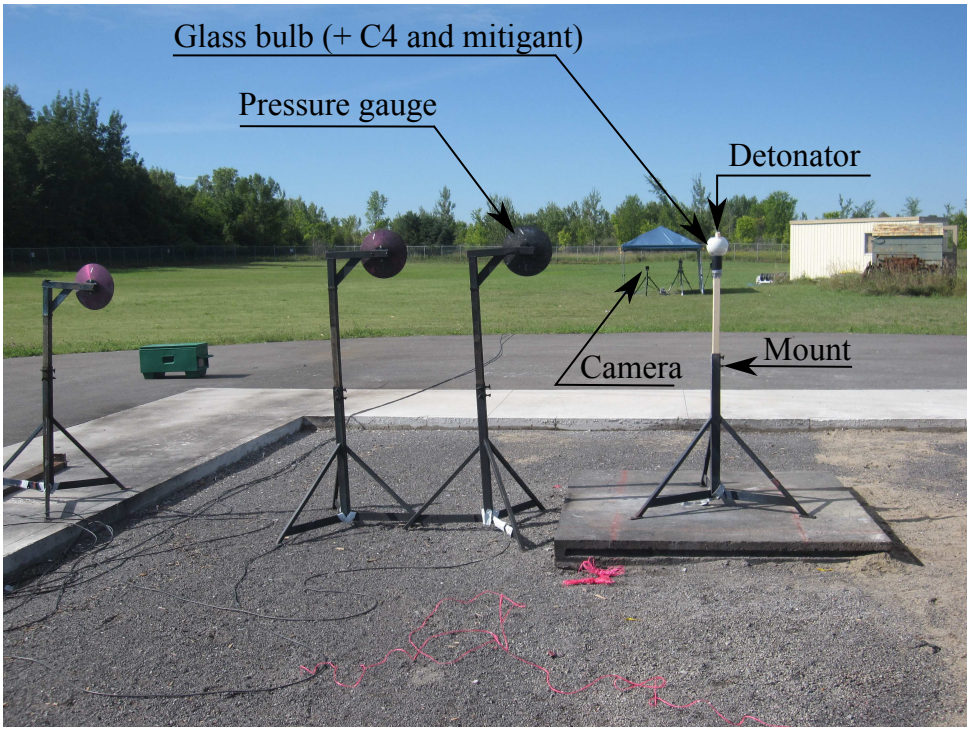

Fig. 3.3 Photograph of test site with charge, pressure gauge stands, and high-speed videocameras in the background.

the transducer location after the end of the positive phase of the blast wave signature so that the positive-phase impulse measurement is not influenced by the reflected wave. It was not possible to position a gauge stand nearer than about 1 m from the charge as the direct impact of particles with the gauge obscured the blast pressure signal.

The explosive particle dispersal was recorded with a high-speed Photron SA5 videocamera recording at 10,000 fr/s. Prior to a test, a photograph of a checkerboard scale was taken to establish an absolute length scale. For a resolution of 1024 $\times$ 744 pixels, with a camera-charge distance of 30 m, the physical size of a pixel ranged from 3.1–4.5 mm, depending on the magnification (either a 135 mm or 180 mm lens was used).

A wide variety of mitigant materials were tested. Solid particles included: Chronital S-30 stainless steel shot (Vulkan Blast Shot), SAE J827 standard S-110 steel shot, pure iron (FE-114, Atlantic Equipment Engineers), glass (Potters Ballotini impact glass beads, #10 and #13 sizes), brass (BR-102, Atlantic Equipment Engineers), titanium (TI-109, Atlantic Equipment Engineers), aluminum (H-95, Valimet Inc.), silicon carbide (240 grit), sand (commercial toy box sand), and granulated and icing sugar (commercial products). The liquids used included water, glycerol, ethanol, vegetable oil, and sodium polytungstate, a high-density liquid used for gravity separation. To increase the density of the liquids, several glycerol trials were carried out with an equal mass of tungsten carbide powder (1 μm, Geoliquids Inc.) added. In some trials, uniform mixtures of two powders were tested, including silicon carbide powder mixed with various volume fractions of steel or glass powder. In a subset of tests, a bed of solid particles

Table 3.1 Properties of solid particles and liquids tested.

Materials	Bulk density (g/cm^3)	Mean size (μm)
Chronital steel (S-30)	4.6 ± 0.17	280
Iron (FE-114)	3.35 ± 0.34	220
Steel shot (S-110)	4.46 ± 0.33	280
Glass (Potters #13)	1.5 ± 0.08	68
Glass (Potters #10)	1.37 ± 0.16	120
Silicon carbide (30 grit)	1.67 ± 0.16	600
Aluminum (H-95)	1.50 ± 0.09	116
Titanium (TI-109)	1.78 ± 0.22	< 150
Brass (BR-102)	3.31 ± 0.45	< 150
Sand	1.67 ± 0.09	500 nom.
Granulated Sugar	0.92 ± 0.07	525
Icing Sugar	0.71 ± 0.16	20
Water	1	N/A
Ethanol	0.789	N/A
Glycerol	1.126	N/A
Vegetable oil	0.915	N/A
Sodium polytungstate	2.82	N/A

was fully saturated with water. Bulk densities of the powders were measured experimentally by determining the mass of a known volume of powder. Depending on how the powders are tapped, the bulk density can vary. In Table 3.1, the average between the untapped and tapped values is reported. The particle size distributions are monomodal, with the mean size provided by the manufacturers. In total, blast wave properties were extracted from 78 trials of 27 different mixtures spanning a range of mitigant to high-explosive mass ratio (M/C) from 3.8 to 297.1. A total of 44 trials were conducted with dry powders, 21 trials with neat liquids, and 13 trials with water-saturated particles. A summary of all the trials tested is attached in the supplementary material.

3.3 Video analysis procedure

Optical diagnostics are commonly used to visualize shock waves and blast waves. In lab-scale experiments, shadowgraphy, interferometry, black and white or colour Schlieren videography are widely employed, especially in supersonic-hypersonic facilities but also for small-scale explosion tests. These techniques have been reviewed by Kleine and al. [26] and Panigrahi and al. [27]. The Background Oriented Schlieren (BOS) [28, 29] technique is largely applied to visualizing blast waves in free-field tests [30, 31]. This technique consists of subtracting all the video images containing the blast front from the same, fixed image of an undistorted background. This method has also proven to be effective in visualizing underwater shock waves [32]. To improve the visualization of the blast wave in the field and diminish the errors associated with

the extraction of the blast wave trajectory, it is also common to place a striped (or zebra) board behind the charge [33].

In the present paper, two different methods are used to extract the position of the spherical blast wave as a function of time and involve the use of several image processing techniques. If the blast wave peak overpressure is sufficiently high, it is possible to observe the wave front directly from the raw video images as a result of the diffraction of the background light by the density gradient across the blast wave. Once the location of the wave front has been determined, a circle may be fitted manually to the most spherical portion of the blast front. Due to a lack of symmetry of the blast wave for certain trials, the center of the circle does not necessarily correspond to the exact location of the charge but is typically very close. This procedure is repeated for each video image, maintaining the same center for all the images. If the circle does not perfectly match the wave front in all directions, the edge of the circle is placed to precisely coincide with the left side of the blast wave. The choice of the left side is motivated by the presence of pressure gauges on the right side that may slightly perturb the blast wave motion. This method has the advantage of being relatively fast (i.e., no computational time is involved), taking into account the sphericity of the blast front, and also avoiding the addition, or removal, of information associated with any image processing technique.

Above a mass ratio of around 50, the blast wave is weak enough that it is difficult to discern the blast wave front against the uneven pixel grayscale level of the background in individual video frames. To enhance the visibility of the blast front in these cases, it is necessary to perform inter-frame image processing. The choice of image processing scheme depends on the brightness, contrast and pixel intensity of the particular trial. However, the basic procedure is to compare consecutive images so that only portions of the image that are moving (such as a blast wave) are retained. This method differs slightly from the BOS technique since the video images are not subtracted from a unique image but rather subtracted from the previous image. At this point, various routines are used to enhance the image contrast, apply a thresholding function, filter the image, and despeckle the image until the blast wave front is distinctly visible. An overview of the typical sequence of image processing routines used is shown in Fig. 3.4.

First, a Matlab Bit-xor transformation is applied to two consecutive frames. The Bit-xor function compares bits of the same pixel in the two different images and returns 0 if bits are equal and 1 otherwise. Pixels which have the same value (from 0 to 256) are converted to black and others become more and less grey. Then, the contrast of the resulting image is enhanced (*imadjust* function) and a threshold is set to 4, 5, or 6 depending on the magnification ratio and the image properties. As a consequence, only pixels with a value above this threshold become visible. The next steps consist of removing the noise from the images. In the first instance, images are converted to binary, i.e., black and white. Then, several loops (about 10) of the speckle removal algorithm are used to remove the smallest noise structures. This algorithm consists of a small 2D-median filter (3×3) which replaces an input pixel at a specific location by the median value of the input pixel and its 8 neighbours. If most of the pixels surrounding

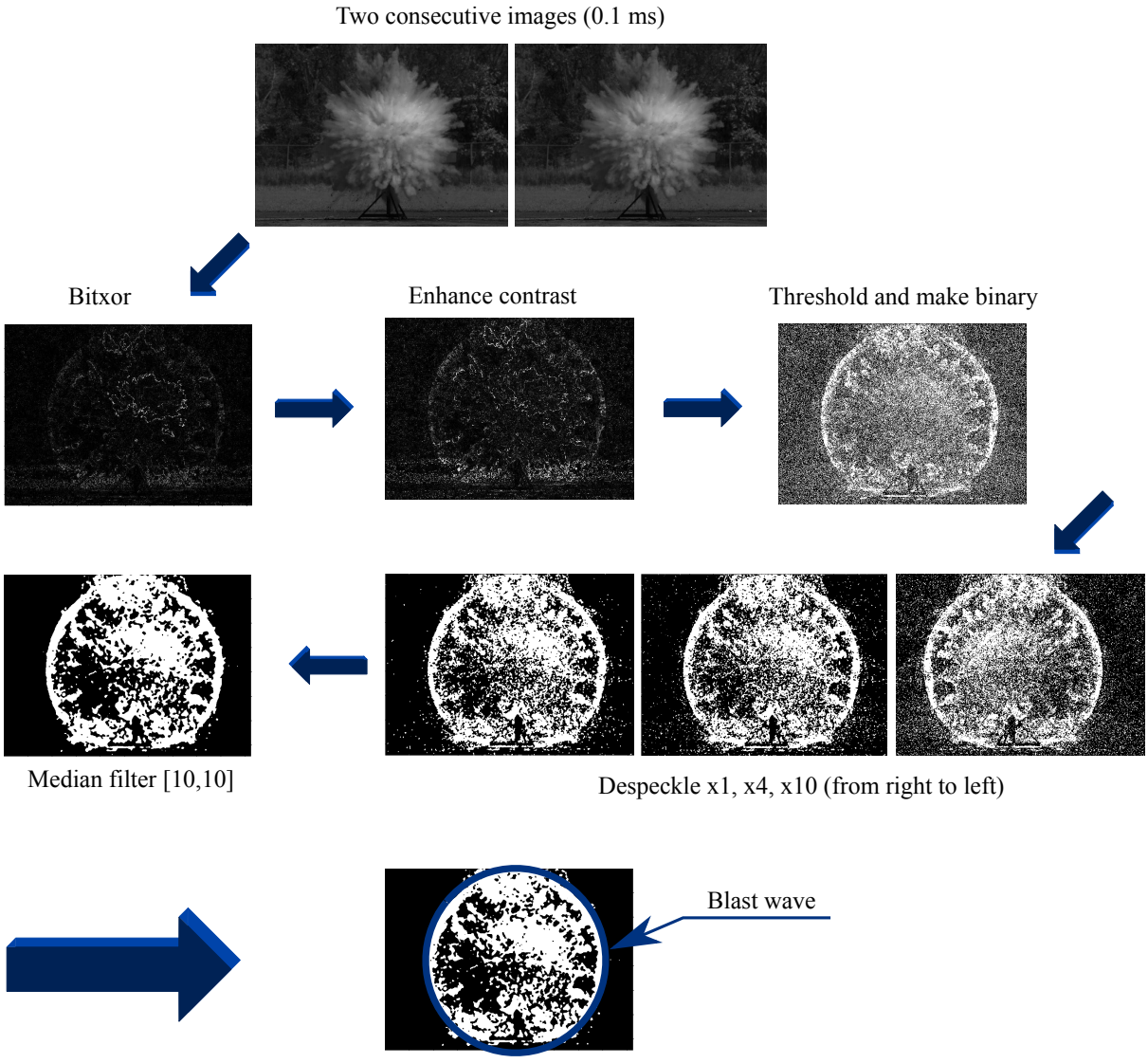

Fig. 3.4 Different steps of video processing.

the input pixel are black, the output pixel will be black, and if not, the output pixel will be white. In the end, to eliminate the largest noise structures, a larger median filter (10×10) is applied. The size of this filter depends also on the image properties. The ultimate goal of removing the undesirable pixels is to automatically fit circles to the blast wave front. Since all of the noisy pixels surrounding the blast front have been removed, it is then possible to detect the first and last white pixels on different specific lines that should belong to the blast front. Then, with at least three points, a circle may be fitted. One drawback of image processing techniques is that inevitably some information is either added to or removed from the image. In particular, the blast front may not be perfectly smooth and several “holes" on the blast front may appear (Fig. 3.5). The appearance of these holes is primarily attributed to the non-uniformity of the background (presence of trees in Fig. 3.1) and makes it difficult to accurately detect the blast front. However, in the present study, the circles are fitted manually since the holes are too numerous on the processed images. Several image processing techniques may be applied to reconstruct the blast wave front by pixel interpolation. The use of a uniform background would also serve to decrease the numbers of these undesirable image artifacts. After applying the various image processing techniques, care must be taken to distinguish the front of the particle cloud, which may appear as a front similar to a shock wave, from the blast wave front itself. Once the trajectory of the blast wave has been unambiguously identified, the procedure for fitting a circle to the blast wave described previously is applied.

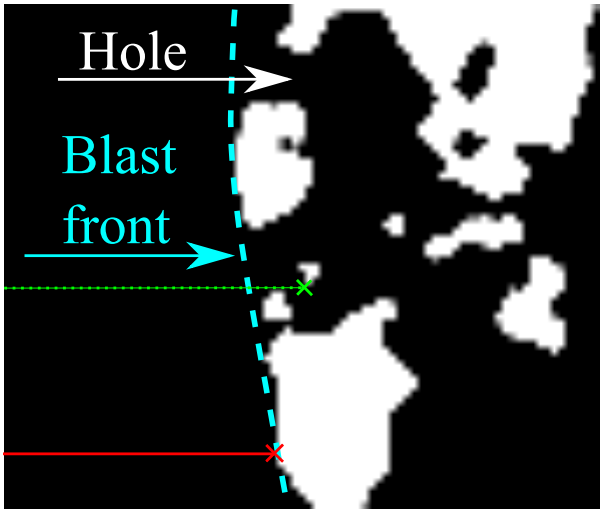

Fig. 3.5 Close-up of blast wave front from a processed image. Due to non-uniformities in the initial background image, “holes" may appear in the blast wave front. Under these circumstances, a circle is manually fitted to the blast wave front.

With the image analysis procedure described above, the spherical blast radius can be determined. Pixel counts are converted to distance via the pre-trial scale image. Intra-frame positions and times are used to determine the shock trajectory, and the shock velocity is extracted by differentiating a polynomial line of best fit to the position-time data points. Fig. 3.6 shows an

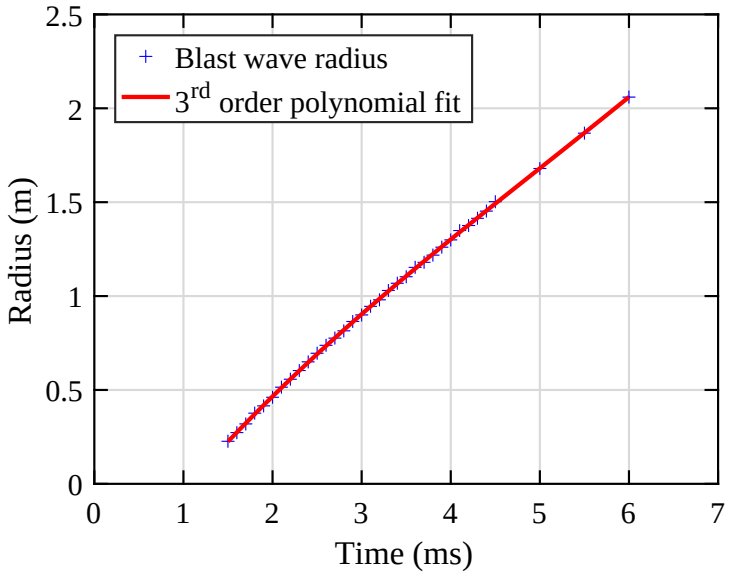

Fig. 3.6 Blast wave radius as a function of time for the high-explosive dispersal of titanium particles saturated with water with $M/C = 42.69$. Blue crosses refer to the blast radius extracted at a specific instant. The red line corresponds to a 3rd order polynomial fit. To obtain the velocity profile this fit is differentiated.

example of a radius-time history plotted for a trial in which titanium particles saturated with water were explosively dispersed.

Several methods can be used to obtain the history of the blast wave velocity. First, the instantaneous velocity can be determined at a specific instant based on the change in position between two frames:

$$v(i) = \frac{R(i+1) - R(i-1)}{t(i+1) - t(i-1)} \tag{3.1}$$

Where:

$$\begin{aligned} i &= \text{image number} \\ R(i) &= \text{position of the blast in the image number } i \\ t(i) &= \text{time of the image number } i \\ v(i) &= \text{blast velocity in the image number } i \end{aligned}$$

An example of the velocities calculated in this way is shown by the blue crosses in Fig. 3.7. The small changes in distance of the blast from one video frame to the next leads to large fluctuations in the velocity due to the lack of precision in determining the shock front location (discussed at the end of the section). To obtain a smoother variation in the blast front velocity, the shock wave trajectory is fit with a 3rd order polynomial, as shown in Fig. 3.6. The polynomial is then differentiated to get the velocity history, which is shown as the solid red curve in Fig. 3.7.

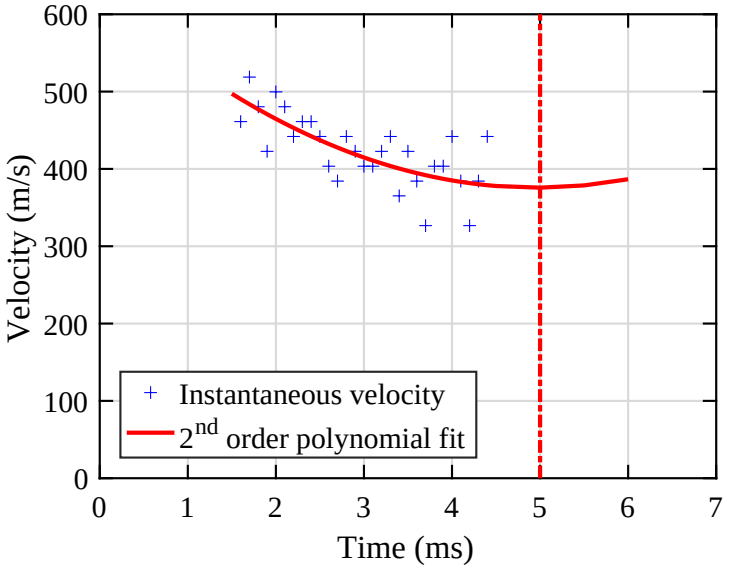

Fig. 3.7 Velocity profile for titanium particles saturated with water with $M/C = 42.69$. Solid red line corresponds to a 2nd order polynomial fit (derivative of the 3rd order polynomial fit of the position vs. time curve). Note that for the last 3 points of Fig. 3.6, instantaneous velocities are not calculable with Eq. (3.1), so not reported. At the right of the dotted-dashed line, data are not taken into account in the overpressure calculations.

This fitting function works well for trials with a mass ratio above 11. However, for mass ratios below this value, the fit is not accurate enough, especially at early times. As a result, in the range of mass ratio between 3.7 and 11, a rational mode fit, i.e., a ratio of a linear function and a second order polynomial, as shown below in Eq. (3.2),

$$R(t) = \frac{at + b}{a't^2 + b't + c'} \tag{3.2}$$

is chosen instead. A comparison between the two fitting functions for a low value of M/C is shown in Fig. 3.8. Note that at later times, the velocity fitting function starts to increase and diverge from the instantaneous velocity values. This occurs due to the nature of the fitting function, which reaches a minimum and then increases. Hence, at later times, the curve fits do not follow the velocity data points, which tend to reach a plateau value. This is a non-physical behaviour, and hence the velocity values to the right of the vertical dashed lines are discarded.

The Mach number and the pressure ratio across the shock are then determined from the velocity profile. The Mach number M_a is calculated assuming the air acts as an ideal gas, with the speed of sound, c, given by Eq. (3.3), with γ taken to be constant and equal to 1.405, i.e.:

$$c = \sqrt{\gamma RT} \tag{3.3}$$

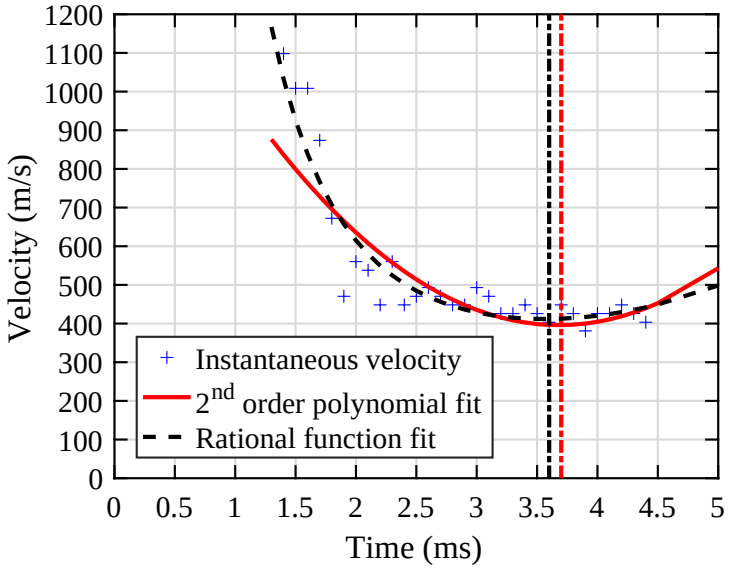

Fig. 3.8 Velocity profile for ethanol at $M/C = 3.76$. Solid red line corresponds to a 2^{nd} order polynomial fit. Dashed black line corresponds to the derivative of the rational fit of the position vs. time curve. To the right of the dotted-dashed lines, the velocity begins to increase and is not considered reliable.

where:

$c =$ speed of sound (m/s)

$\gamma = 1.405$ (ratio of specific heats)

$R = 286.9$ J/kg-K (specific gas constant)

$T =$ temperature in Kelvins

The blast wave is assumed to propagate into undisturbed air, at temperatures ranging from 5–25°C, depending on the trial conditions. Once the speed of sound is determined, the pressure ratio across the blast can be determined using the Hugoniot jump relation (Eq. (3.4), [34]), assuming that the shock front is relatively thin, and γ is constant:

$$\frac{P}{P_0} = \frac{2\gamma}{\gamma+1} M_a^2 - \frac{\gamma-1}{\gamma+1} \tag{3.4}$$

When the pressure ratio across the blast is extracted from the blast trajectory, it is of interest to compare the different methods of extraction, from raw videos or using the video analysis procedure to analyze any discrepancies. At an intermediate value of M/C, where both methods can be performed, the match is relatively accurate as shown in Fig. 3.9. However, if the center of the blast wave is not taken to be fixed during the processing, a more noticeable discrepancy appears. For the purpose of this study, the center of the circles remains fixed for all the videos analyzed.

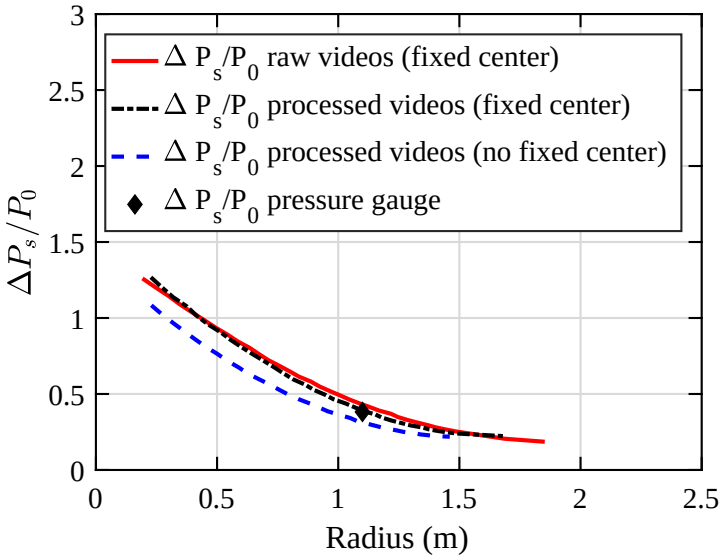

Fig. 3.9 Blast peak overpressure as a function of the blast radius for titanium saturated with water at $M/C = 42.69$. The red line corresponds to the overpressure extracted from raw videos. Black dotted-dashed line corresponds to the overpressure extracted from the processed video considering the center of the circle fixed and the blue dashed line considering the center not fixed. The diamond symbol indicates the value measured with the pressure transducer.

To study the TNT equivalence of bare explosive charges, Dewey [35] and Kleine and al. [36] have suggested fitting the blast radius-time curve to the following form:

$$R(t_a) = A + Bct_a + C\ln(1+ct_a) + D\sqrt{\ln(1+ct_a)} \tag{3.5}$$

where R is the blast radius, c the speed of sound, t_a the time of shock arrival at a given location, and A, B, C, D, are least-squares fit coefficients. B is often set equal to one to ensure that the blast velocity at later times approaches that of the speed of sound. The advantage of such a fit is its monotonicity. As a consequence, this fit is not associated with any changes in its trend after a certain time, as mentioned earlier for the third-order polynomial. However, this fit overpredicts the peak overpressure value compared to the first pressure gauge value and underpredicts the value for the second gauge. For the first gauge, the third-order polynomial is closer to the value obtained with the pressure transducer (Fig. 3.10). The last pressure gauge is not accessible for comparison as it is outside of the camera view. For the purpose of this study, since the interest is mainly in the near field, blast trajectories are fitted with the third-order polynomial for all the trials tested.

The number of parameters that influence the precision of the pressure measurements from pressure transducers or from high-speed videography are numerous. Some variation in the experimental parameters is inevitable, including the centering of the burster charge, the packing fraction of the powder, presence of voids within the C-4 burster charge, and so on. Pressure transducers are also subject to spurious signals from fragment impact as well as baseline drift

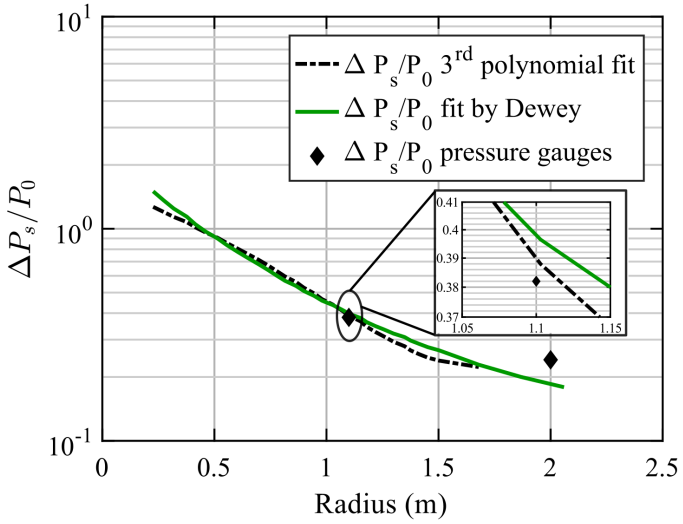

Fig. 3.10 Comparison of peak overpressures between the 3rd order polynomial and the fit by Dewey and Kleine for titanium particles saturated with water at $M/C = 42.69$ from processed videos (the centers of the circles are fixed). At 1.1 m, the peak overpressure value for the third-order polynomial is closer to the value obtained with the pressure gauge as compared to the other fit. The fit by Dewey and Kleine enables to access a more extensive range but underpredicts the pressure gauge measurement at 2.0 m. The camera view does not include the last gauge and hence the comparison at 4.0 m is impossible.

from thermal effects. Estimation of the peak overpressure from the video extraction procedure is also subject to multiple sources of error, including errors in scaling the distances and errors in determining the shock front location from a lack of contrast or a non-uniform background. Furthermore, in the very near field, the presence of hot reacted gas (fireball) and particles projected ahead of the blast wave front may modify its propagation rate. Due to the higher temperature compared to the ambient air, the speed of sound c, the Mach number M_a and value of γ will be modified and hence the assumption of a constant value of γ in Eq. (3.4) is no longer valid.

A rough estimation may be obtained for the error associated with the extraction of the blast front position. This error is one or two pixels, but is averaged by the fitting process of the radius-time curve and a value of one pixel is retained. Depending on the distance from the charge and M/C, the corresponding error in velocity is estimated to range from a maximum of 40 m/s for blast fronts far from the explosion center and for high M/C, to a maximum of 100 m/s in the near field and for low M/C. In percentage, the error linked to the estimation of the velocity and the Mach number corresponds to about 10%, and will be multiplied by 2 (20%) when converted to peak pressure due to the square exponent of the Mach number in Eq. (3.4).

Due to the difficulty in precisely calculating the error margins for the reasons noted above, and for clarity, the error bars have been removed on all the following plots to facilitate a more direct comparison between the results. The reproducibility of the method is analyzed in the following

Table 3.2 Comparison between peak pressures obtained with the video analysis and pressure gauges measurements at 1.1 m from the explosion center. The relative errors (R.E.) expressed in % are listed in the last column.

Materials	C (g)	M (g)	M/C	Z (m/kg$^{1/3}$)	$\frac{P}{P_0}$ (videos)	$\frac{P}{P_0}$ (gauges)	R.E. (%)
Steel 110	75	1600	21.3	2.34	1.52	1.36	11.8
Steel 110	75	4130	55.1	2.34	1.30	1.28	1.6
Steel 110	28	4192	149.7	3.25	1.11	1.10	0.01
Glass dry #13	75	488	6.5	2.34	1.71	1.62	5.6
Glass dry #13	28	1312	46.9	3.25	1.20	1.19	0.8
Glass dry #13	28	1294	46.2	3.25	1.12	1.10	1.8
Glass dry #10	75	1328	17.7	2.34	1.40	1.43	2.1
Glass dry #10	28	1328	47.4	3.25	1.06	1.11	4.5
Glass dry #10	28	1332	47.6	3.25	1.14	1.12	1.8
Water	28	902	32.2	3.25	1.40	1.43	2.1
Water	28	374	13.35	3.25	1.48	1.48	0.0
Glass wet #13	75	676	9.0	2.34	1.94	1.83	6.0
Glass wet #13	75	1744	23.25	2.34	1.76	1.69	4.1
Glass wet #13	28	1744	62.3	3.25	1.21	1.25	3.2
Glass wet #13	28	1788	63.9	3.25	1.27	1.23	3.3
Glass wet #10	28	1830	65.4	3.25	1.26	1.25	0.08
Glass wet #10	75	1748	23.3	2.34	1.80	1.79	0.01
Titanium wet	75	3202	42.7	2.34	1.39	1.38	0.07
Titanium wet	75	3182	42.4	2.34	1.33	1.52	12.5

sections and also illustrated in the supplementary material by comparing trials at similar M/C. The degree of scatter in the results for trials with the same materials with similar M/C values is illustrated by comparing curves (e) and (f) for glass from Fig. 3.12 (although the particle size differs in these two trials) and curves (h) and (j) for water in Fig. 3.17. Discrepancies between the peak pressures inferred from the high-speed videography and values measured directly by the pressure transducer located at a distance of 1.1 m from the charge center are analyzed in Table 3.2. Depending on the charge mass used (28 g or 75 g), the corresponding scaled distance is either $Z = 2.34$ m/kg$^{1/3}$ or $Z = 3.25$ m/kg$^{1/3}$. The comparison for dry powders is limited to two types of material, including S-110 steel shot, Ballotini impact glass beads (both #10 and #13 sizes). The errors calculated range from zero to a maximum discrepancy of 12.5%. Note that the conversion of the peak pressure into peak overpressure and the use of the logarithmic scale in Figs. 3.12, 3.17 and the figures presented in the supplementary material exaggerate these errors.

3.4 Results

In this section, the experimental results are presented in the following way. Section 3.4.1 presents the typical blast pressure histories recorded with pressure transducers. Section 3.4.2 details the results relative to peak overpressures for both granular mitigants and liquids or liquid/powder

mixtures. In section 3.4.3, a comparison is made between the arrival times of blast waves with that of particles. Finally, in section 3.4.4, a comparison of positive-phase impulses is given for both types of material.

3.4.1 Blast overpressure profile

In addition to the estimation of peak blast overpressure using image analysis of the blast wave trajectories, overpressure measurements were obtained with piezoelectric pressure transducers in selected trials (all the values are reported in the supplementary material). The pressure gauge data were limited to measurements at either three or five specific locations and were placed relatively far from the charge so that the pressure field very near the charge was not obtained. In the near field, the glancing impact of high-velocity particles with the transducer can introduce spurious spikes on the pressure signals. Pressure gauges were triggered as soon as the blast passed the first gauge. Fig. 3.11 illustrates the typical overpressure measurements obtained with the gauges at three different locations for the dispersal of glass particles saturated with water, with $M/C = 62.3$, recorded with a time resolution of 0.2 μs or 5 μs (oscilloscope time resolution for each trial is reported in the supplementary material). For aesthetics, the high-frequency noise in the signals due to impact of the particles with the gauge or gauge stand has been smoothed with a Savitzki-Golay filter with a first order polynomial and a frame size of 21, on the curves of Fig. 3.11. Nevertheless, the peak blast overpressures have been determined using the raw pressure data. As any spurious high-frequency noise fluctuations make a negligible contribution to the blast impulse, the blast impulses have been calculated using the trapezoid method of integration using the raw data. Note that for each curve, the second pressure spike due to the arrival of the ground-reflected wave occurs after the completion of the primary positive phase of the signal. These signals were used to determine the positive-phase impulse of the blast wave at various locations.

3.4.2 Peak overpressure

The peak overpressures derived from videography results are plotted as a function of scaled distance, Z, defined as,

$$Z = \frac{R}{W^{1/3}} \tag{3.6}$$

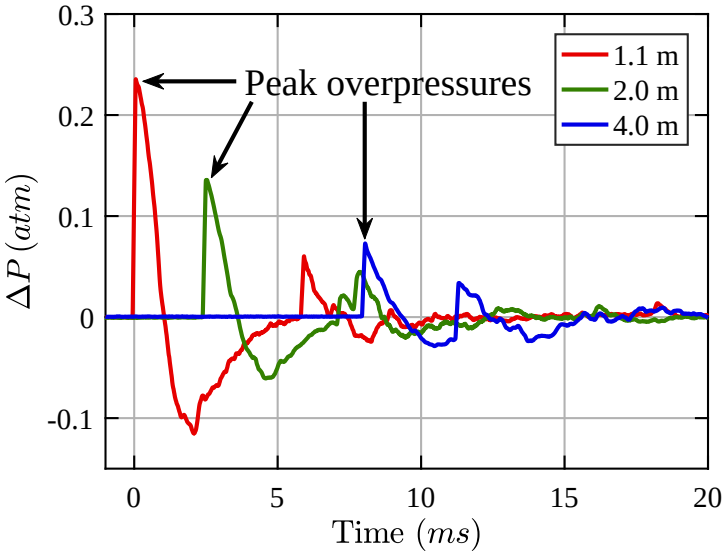

Fig. 3.11 Blast overpressure as a function of time captured with pressure gauges for glass (Ballotini #13 impact) beads saturated with water at $M/C = 62.3$.

where:

$$Z = \text{scaled distance } (\text{m/kg}^{1/3})$$
$$R = \text{dimensional distance } (\text{m})$$
$$W = (\text{charge mass in equivalent TNT}) = \text{mass of explosive } (\text{kg}) \times \varepsilon \text{ (effectiveness factor)}$$

for all trials in subsequent sections. Following Kinney and Graham [37], the equivalent TNT charge mass, W, is equal to the mass of C-4 multiplied by an relative effectiveness factor, ε. In the present study, for peak overpressures, a value of $\varepsilon = 1.39$ is taken for C-4 which is a bit above the common value of 1.37 (Swisdak, [38]) but still in the range of accepted values (1.16–1.47 depending on the distance from the charge [39]). A value of 1.39 was chosen to fit with previous experimental data in the region of interest 0.5 m/kg$^{1/3}$ < Z < 12 m/kg$^{1/3}$. The normalized peak overpressure is defined by $\frac{\Delta P_s}{P_0}$, with $\Delta P_s = P_s - P_0$, with P_s representing the value of the blast peak pressure and P_0 = 1 atm. The scaled distance is a useful engineering parameter to compare strengths of blast waves generated by high explosives of different masses and composition. The classical blast scaling law [37] asserts that, for given atmospheric conditions, two explosions should give identical blast waves at a given scaled distance Z.

Granular mitigants

Fig. 3.12 shows the peak overpressure as a function of scaled distance in a log-log plot for different dry granular mitigants and mass ratios ranging from 3.9 to 57.1. The solid red line corresponds to the peak overpressure of a bare C-4 charge based on the Kinney and Graham

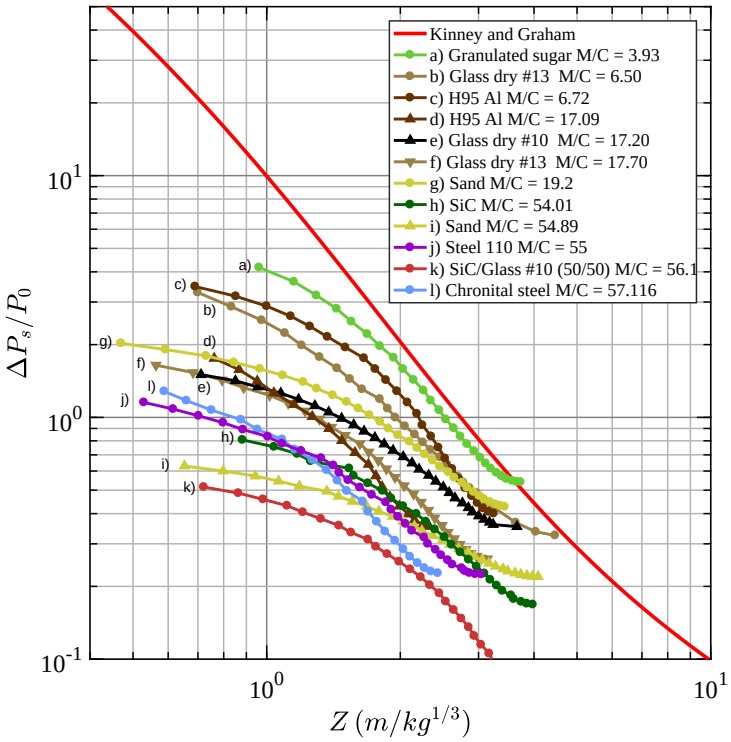

Fig. 3.12 Blast wave peak overpressure as a function of scaled distance, Z, for dry powders obtained by videography.

database [37]. This curve is based upon the assumption that the blast propagates in undisturbed atmospheric air (modelled as an ideal gas), outside of the detonation products. The peak overpressures for the eight different materials, and a mixture of silicon carbide and glass particles are shown. The curves extracted from the videos are spread over a range of scaled distances from $Z = 0.5$ m/kg$^{1/3}$ to $Z = 4.0$ m/kg$^{1/3}$. In some cases the saturation of the camera sensor by the fireball radiation obscures the visibility of the blast wave front at early times. As a result, the curves do not start at the same Z values. Also, depending on M/C, the blast wave emerges from the cloud of fragments at different times and hence may be first visible at different Z values. In particular, with increasing M/C, the blast wave front is visible much closer to the charge compared to low M/C values. This phenomenon is explored more fully in section 3.4.3.

At scaled distances less than one, the peak overpressure is reduced by about one order of magnitude with the pressure reduction increasing with increasing M/C, regardless of the mitigant material, as expected. Also, for all the materials studied, it is interesting to note that the decay rates of the mitigated overpressure curves do not follow the decay of a bare charge in air. In particular, in the near field, the blast overpressure from a mitigated charge decays significantly more slowly than for a representative bare high-explosive charge described by the Kinney and Graham curve. However, after $Z = 2$ m/kg$^{1/3}$, the mitigated overpressure decay rate of certain materials approaches the decay rate of the baseline bare charge in air. Furthermore, for the

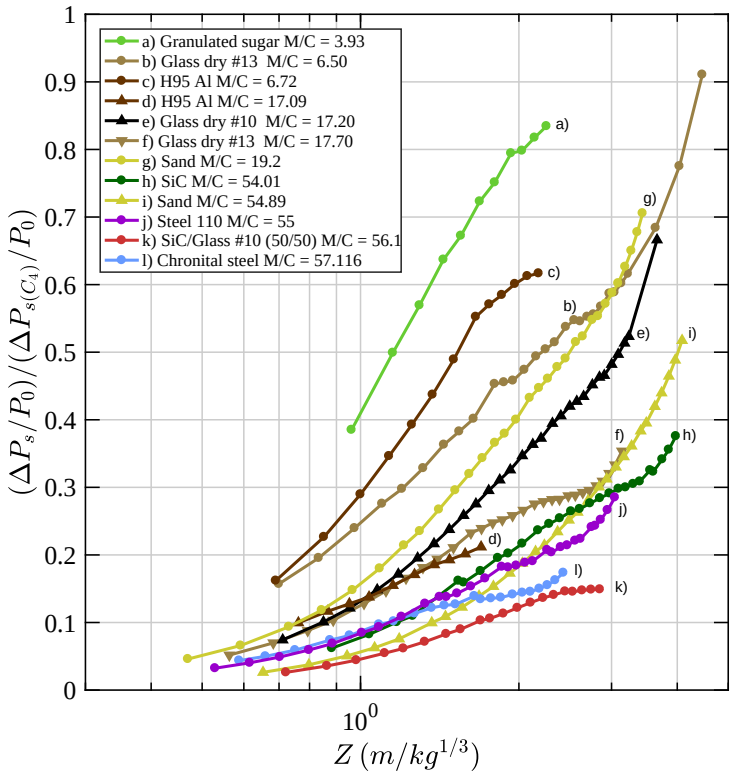

Fig. 3.13 Ratio of the mitigated blast wave peak overpressure over the peak overpressure of a blast wave for a bare HE charge in air (Kinney and Graham database) as a function of the scaled distance, Z, for dry powders.

smallest M/C value tested, the normalized overpressure recovers to almost the same value as that of an unmitigated charge in the far field.

To facilitate the comparison between the peak overpressure of the mitigated charges with a bare charge, the ratio of the mitigated overpressure to that of the baseline case for a bare charge from Kinney and Graham is shown in Fig. 3.13 for all reported trials with dry powders. The greatest degree of mitigation occurs at small scaled distances, and the pressure mitigation decreases monotonically with distance from the charge. For clarity, the ends of several curves have been omitted (not represented on the graphs), when the artefact of the velocity fitting procedure described earlier produced errors in the velocity (and hence blast pressure). However, the pressure attenuation continues to decrease in the far field as shown in Fig. 3.16.

Adding more material mass for a given high-explosive mass increases the mitigation effect in the near field (Fig. 3.13), with mitigated pressures normalized with the baseline case ranging from a low value (i.e., greatest pressure mitigation) of 2.6% at $Z = 0.7$ m/kg$^{1/3}$ for a mixture of SiC and glass with $M/C = 56$, to a high value of 91% at $Z = 4.5$ m/kg$^{1/3}$ for glass dry #13 with $M/C = 6.5$.

To illustrate the dependence of pressure mitigation on M/C in the near-to-mid field, 2 values of scaled distance were arbitrarily chosen ($Z = 0.8$ and 1.5 m/kg$^{1/3}$) and then at these values of Z, the corresponding mitigated overpressure values were extracted from Fig. 3.12. Fig. 3.14 shows

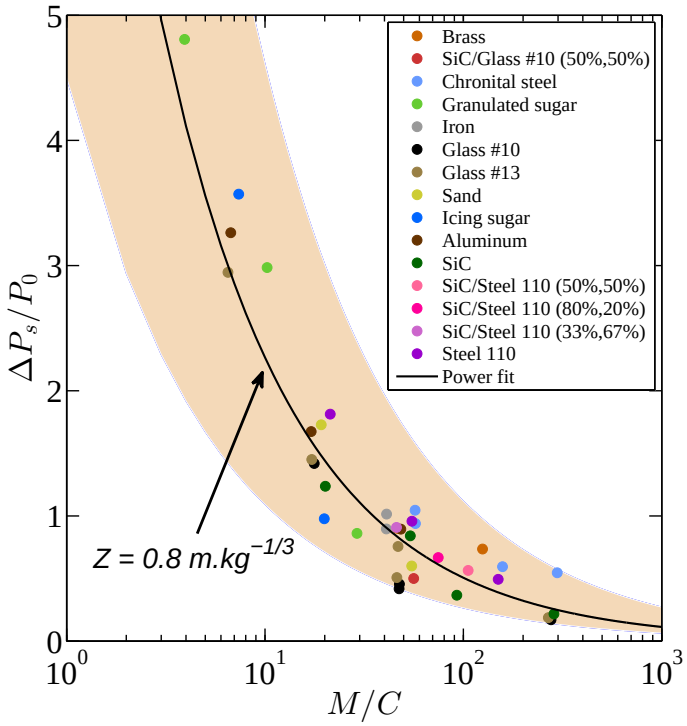

Fig. 3.14 Blast wave peak overpressure as a function of M/C at $Z = 0.8$ m/kg$^{1/3}$ in the case of solid powders. Data points for granulated sugar ($M/C = 3.93$) and SiC ($M/C = 54.01$) have been extrapolated from Fig. 3.12. The data point for brass at $M/C = 46.85$ is obscured by other data points and thus is not visible.

the results for the mitigated overpressure as a function of M/C for $Z = 0.8$ m/kg$^{1/3}$ clustered within a broad band (data for $Z = 1.5$ m/kg$^{1/3}$ are omitted for clarity but are reported in the supplementary material). At each scaled distance, the overpressures are reduced with increasing M/C. The decay rates are a weak function of M/C and can be represented by the following power law fits:

$$\frac{\Delta P_s}{P_0} = \alpha \times \left(\frac{M}{C}\right)^{-\beta} \tag{3.7}$$

Where:

$$(\alpha, \beta) = (10.14, 0.651) \text{ for } Z = 0.8 \text{ m/kg}^{1/3}$$
$$(\alpha, \beta) = (5.64, 0.611) \text{ for } Z = 1.5 \text{ m/kg}^{1/3}$$

The reproducibility of the results using the videography method can be analyzed by comparing the results for trials for a specific material at similar M/C values, e.g., Chronital steel ($M/C \approx 57$), glass #10 and #13 ($M/C \approx 47$) or iron ($M/C \approx 41$). A maximum discrepancy of 14% in terms of peak pressure is observed for glass #13. The M/C ratio appears to be the primary factor in

reducing the overpressure for a given Z value, and the solid particle material properties play a secondary role. To quantify the influence of different types of materials at a specific M/C value on the overpressure reduction, each set of materials possessing at least three data points has been fitted with similar power laws in Fig. 3.15. The results for the different materials fall within a broad band, but there seem to be some systematic differences in the mitigation performance. Care must be taken in comparing the differences, since the data from the various materials span different ranges of mass ratio M/C. With the above caution in mind, the peak overpressure mitigation efficiency of the powders can be sorted from the least efficient to the most efficient, respectively: Chronital steel $(\alpha,\beta) = (4.67, 0.388)$, S-110 steel $(\alpha,\beta) = (13.96, 0.668)$, H-95 aluminum $(\alpha,\beta) = (11.14, 0.655)$, SiC (240 grit) $(\alpha,\beta) = (10.48, 0.692)$, granulated sugar $(\alpha,\beta) = (17.71, 0.864)$, glass #13 $(\alpha,\beta) = (11.68, 0.749)$ and glass #10 $(\alpha,\beta) = (8.91, 0.729)$. The coefficients of the power laws indicate that the inclusion of data at very low M/C values makes the fits steeper. However, the power laws can be still considered as weak ($\beta < 1$). A maximum discrepancy of approximately 50% is obtained between Chronital steel and glass #10 at $M/C = 60$. The discrepancy between glass #10 and glass #13 is around 15% at $M/C = 20$. Trials from Fig. 3.14, not shown in Fig. 3.15, such as icing sugar and sand, have peak overpressure values comprised between the aluminum and the glass curves. Conversely, iron and brass have peak overpressure values closer to the two curves for steel. The addition of silicon carbide to S-110 steel powders appears to slightly reduce the peak overpressure compared to pure steel powders. The comparison at $Z = 1.5$ m/kg$^{1/3}$, given in the supplementary materials, indicates that the discrepancy between glass #10 and Chronital steel reduces slightly to 40% but that the discrepancy between the two glass powders increases to 25%.

Peak overpressures obtained with pressure gauges in the mid-to-far field are shown in Fig. 3.16. As expected, the peak overpressure decreases with M/C as a weak power law and the mitigation of the peak overpressure continues to decrease with distance. The comparison between glass powders and steel indicates that glass particles continue to outperform steel at reducing the peak blast overpressure. Indeed, S-110 steel has peak overpressure values comparable to that of glass even with mass ratios about three times higher ($M/C = 149.7$ compared with $M/C \approx 47$). At $M/C \approx 20$, S-110 steel appears to have lower peak overpressure values than glass #10 but is subject to high uncertainties when comparing with the videography results (11.8%). In the same fashion, sand outperforms aluminum with comparable peak overpressure values for M/C respectively at 52 and 120. On the other hand, the effect of particle size for glass powders is not clear given the discrepancy (almost 50% between glass #13 at $M/C \approx 47$ and $Z = 3.24$ m/kg$^{1/3}$) but glass #13 performs better than glass #10 in the far field, contrary to the behaviour in the near field at $M/C = 17 - -19$.

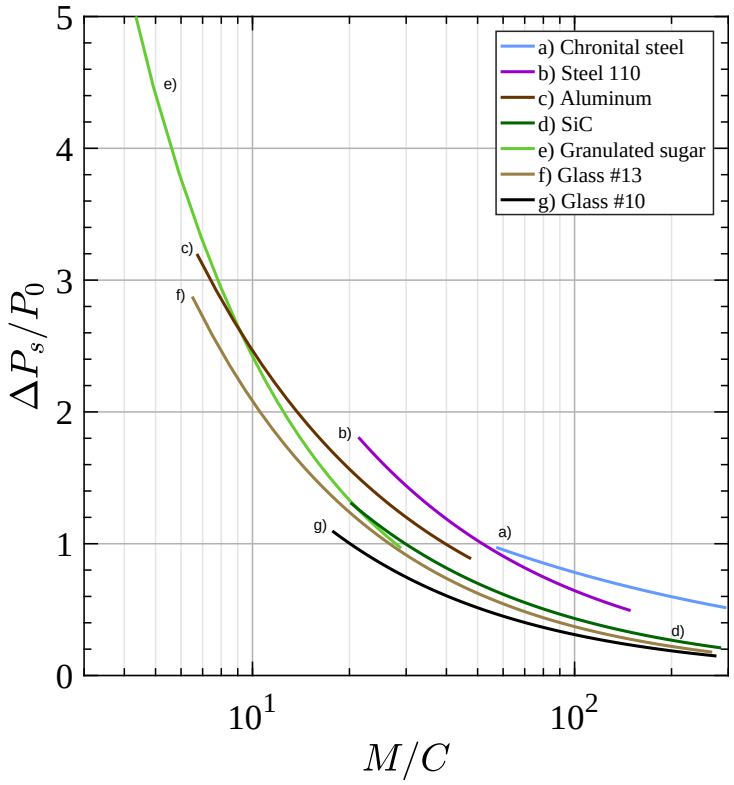

Fig. 3.15 Comparison between blast wave peak overpressure of different solid powders as a function of M/C at $Z = 0.8$ m/kg$^{1/3}$.

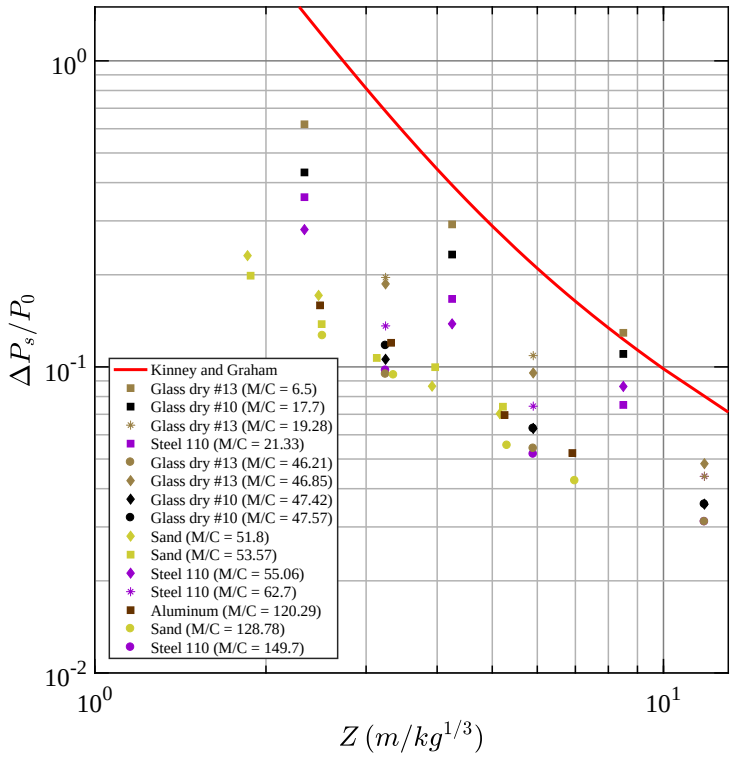

Fig. 3.16 Blast wave peak overpressure as a function of scaled distance, Z, for dry powders obtained from pressure gauges.

Liquids and powders saturated with water

In the same manner as in Fig. 3.12, Fig. 3.17 presents the decay of peak blast overpressure as a function of scaled distance for mitigants consisting of pure liquids or powders fully saturated with water. Fig. 3.18 presents the normalized results for the liquid and saturated particle trials. The reduction in peak overpressures with liquids and powders saturated with water surrounding the charge follows the same trend as for solid powders with large pressure reductions at small scaled distances and with the pressures approaching more closely to that of a bare charge for $Z > 2$ m/kg$^{1/3}$, except for the case of the largest values of M/C. As for solid powder the attenuation can be quantified in the far field from the pressure gauge data (Fig. 3.21). From Fig. 3.18, the case of S-110 steel shot saturated with water, with $M/C = 168$, generates the highest attenuation with a value of 2% at a scaled distance of $Z = 0.7$ m/kg$^{1/3}$. On the other hand, for all the materials with $M/C < 35$ (except for curve h)) the peak blast overpressure recovers to a value similar to that of an unmitigated charge for scaled distances of $Z > 2$ m/kg$^{1/3}$.

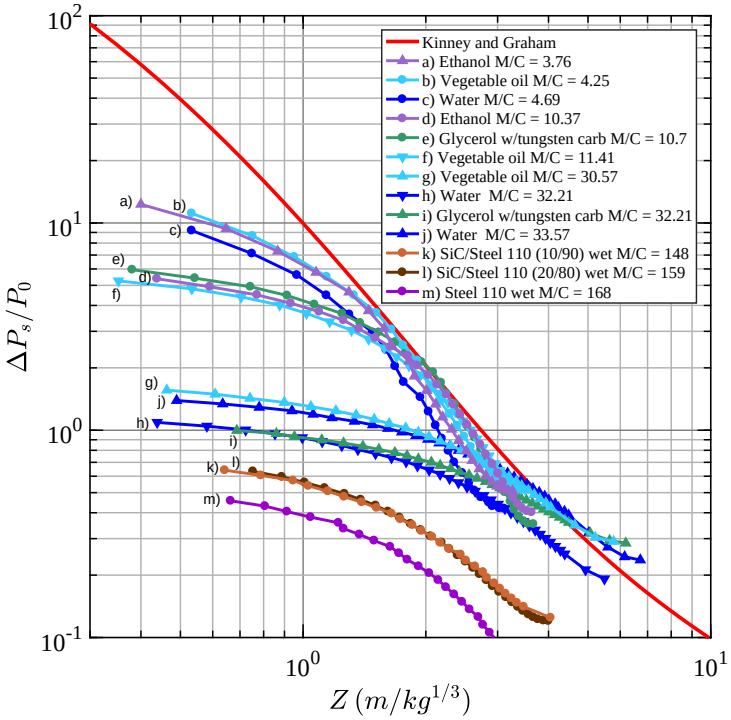

Fig. 3.17 Blast wave peak overpressure as a function of the scaled distance, Z, in the case of liquids/powders saturated with water.

A similar analysis is presented for the liquid experiments, where the peak overpressure is plotted as a function of M/C for two values of scaled distance. These results follow a similar power law decay as with the solid powders, but with different coefficients for Eq. (3.7): $(\alpha, \beta) = (26.37, 0.85)$ for $Z = 0.8$ m/kg$^{1/3}$ and $(\alpha, \beta) = (10.88, 0.699)$ for $Z = 1.5$ m/kg$^{1/3}$. As for solid powders, the reduction in peak overpressure for $Z = 0.8$ m/kg$^{1/3}$ as a function of M/C is shown in Fig. 3.19 (the graph for $Z = 1.5$ m/kg$^{1/3}$ is given in the supplementary material). Here the

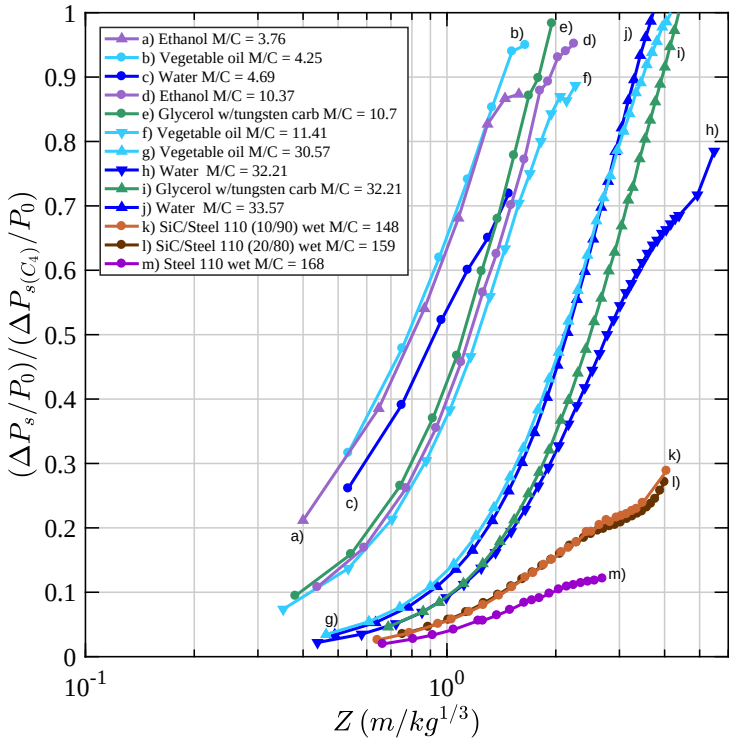

Fig. 3.18 Normalized blast wave peak overpressure versus scaled distance for liquids and powders saturated with water.

reproducibility of the videography method is given for glycerol ($M/C \approx 6$), water ($M/C \approx 30$), titanium wet ($M/C \approx 40$) and glass wet ($M/C \approx 60$). A maximum discrepancy of 13% in terms of peak pressure is observed for water.

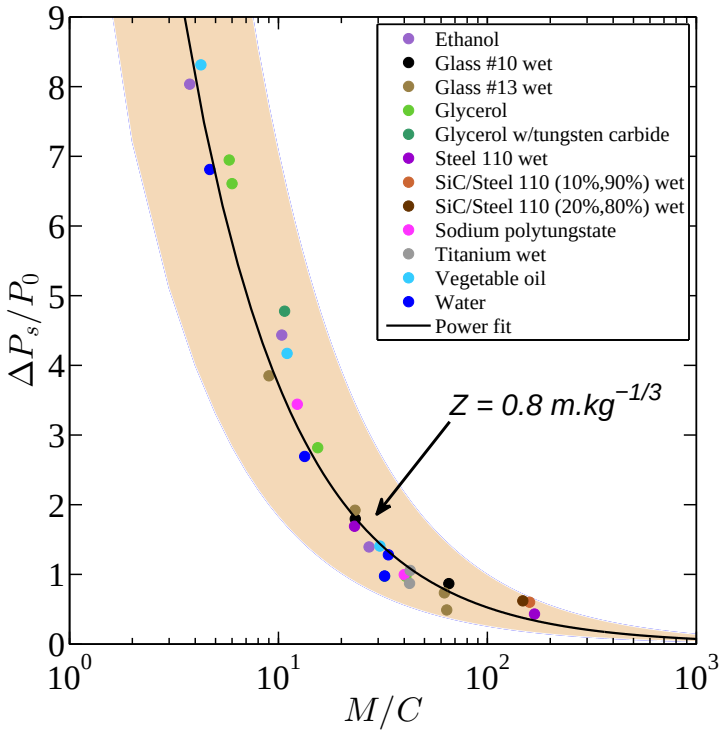

Fig. 3.19 Blast wave peak overpressure as a function of M/C at $Z = 0.8$ m/kg$^{1/3}$ in the case of liquids/powders saturated with water. Data points for several trials are not visible because they are obscured by other data points (e.g., glycerol w/tungsten $M/C = 32.21$ is behind the water data point and similarly glycerol $M/C = 40.75$ is obscured by the sodium polytungstate data).

Blast mitigation performances can be compared on a per material basis in Fig. 3.20. In comparison with dry powders, the results for liquids and saturated particles as a function of M/C fall within a much tighter band, indicating that the material properties play a relatively minor role in this case. Nevertheless, water $(\alpha,\beta) = (28.94, 0.93)$ appears to produce the largest peak overpressure attenuation, whereas glycerol $(\alpha,\beta) = (40.42, 1.00)$ and vegetable oil $(\alpha,\beta) = (32.51, 0.90)$ produce the least. Ethanol $(\alpha,\beta) = (28.57, 0.88)$ and glass #13 wet $(\alpha,\beta) = (35.75, 0.98)$ fall in between with similar performances. The discrepancy between the best mitigant (water) and the worst mitigants (vegetable oil, glycerol) falls between 15% and 20%, depending on the mass ratio. At $Z = 0.8$ m/kg$^{1/3}$, this discrepancy appears to increase slightly to 23–27%. The addition of tungsten carbide powder to glycerol slightly reduces the blast attenuation shown in Fig. 3.19 for low M/C, but the mixture has a similar mitigation performance with the other liquids at $M/C \approx 32$. Moreover, all the powders saturated with water have relatively similar mitigation performances. Nevertheless, contrary to solid powders, the effect of particle size is not clear. Indeed, at $M/C = 23$, glass #10 has a lower peak overpressure but a higher peak overpressure at $M/C \approx 63$ compared to glass #13. Peak overpressures values for sodium polytungstate fall between the peak overpressure values for glycerol and water.

As for Fig. 3.16, Fig. 3.21 presents the peak overpressure for liquids or powders saturated with water in the mid-to-far field obtained with pressure gauges. The peak overpressure mitigation,

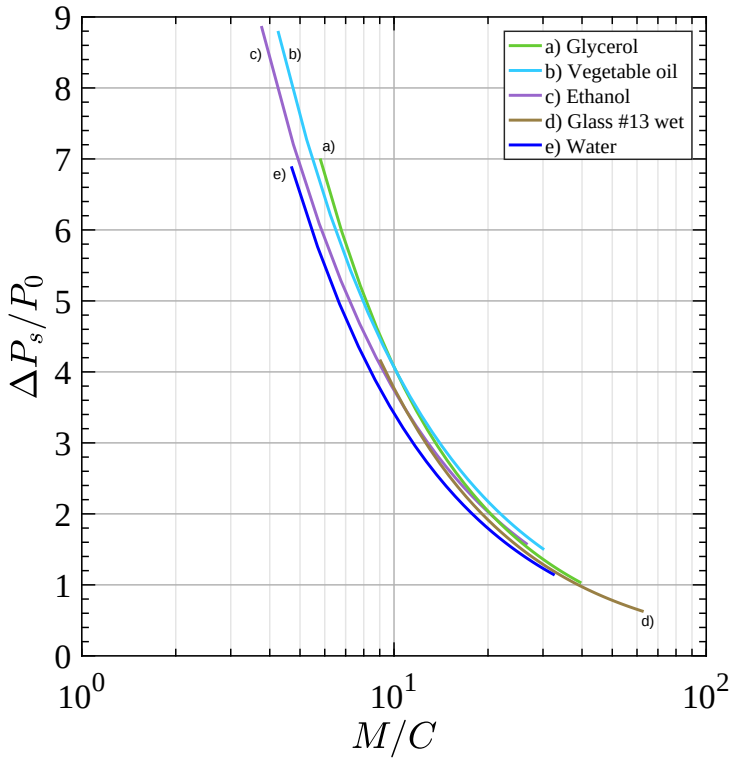

Fig. 3.20 Comparison between blast wave peak overpressure as a function of M/C at $Z = 0.8$ m/kg$^{1/3}$ in the case of liquids or powders saturated with water.

as for solid powders, decreases in the far field and scales as a weak power law of M/C. At similar M/C values, glass wet #13 attenuates the peak overpressure slightly better in the far field compared to glass wet #10. At low M/C values, water and glass wet have similar peak overpressure values but the wetted powders have higher mitigation performances at high M/C values.

To facilitate the comparison of the peak blast overpressure attenuation performance of solid particles versus liquids (or particles saturated with water) for a given M/C ratio, the power law fits to the data shown in Figs. 3.14 and 3.19 are normalized by the value of the baseline bare charge in air and plotted in Fig. 3.22. In the near field, for $Z = 0.8$ m/kg$^{1/3}$, for M/C values greater than about 30, the blast overpressure is highly attenuated, with values less than 10% of the value for a bare charge for both granular mitigants and liquids or water-saturated powder beds. Moreover, in the same region, for small M/C values, powders are about twice as effective at mitigating blast overpressure. As M/C increases, the differences are reduced and all materials exhibit a similar mitigation performance.

3.4.3 Arrival time

To visualize the relative position between the leading edge of the particles or particle jets (the method of extraction of jet trajectories is discussed in another publication [19]) and the blast

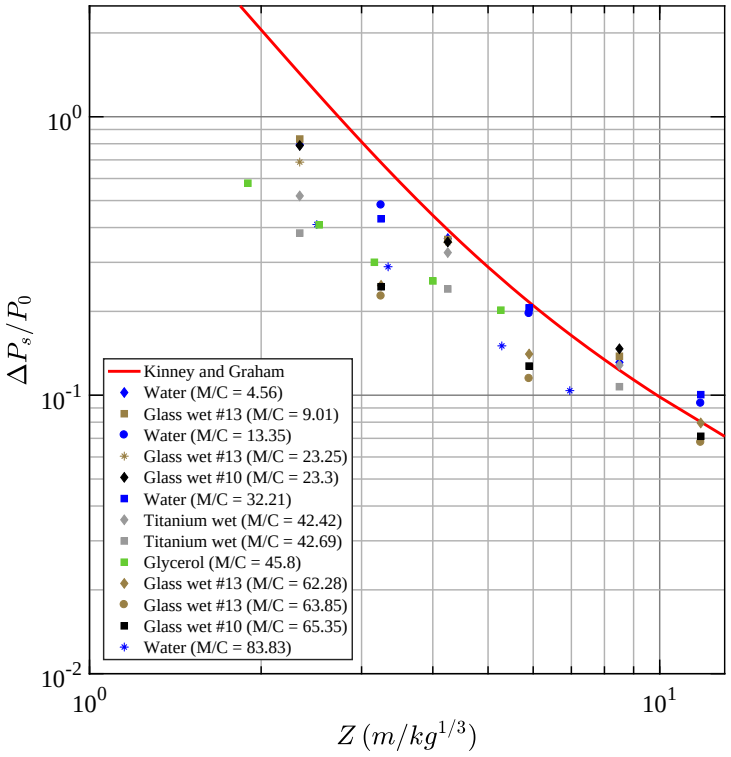

Fig. 3.21 Blast wave peak overpressure as a function of scaled distance, Z, for liquids or powders saturated with water obtained with pressure gauges.

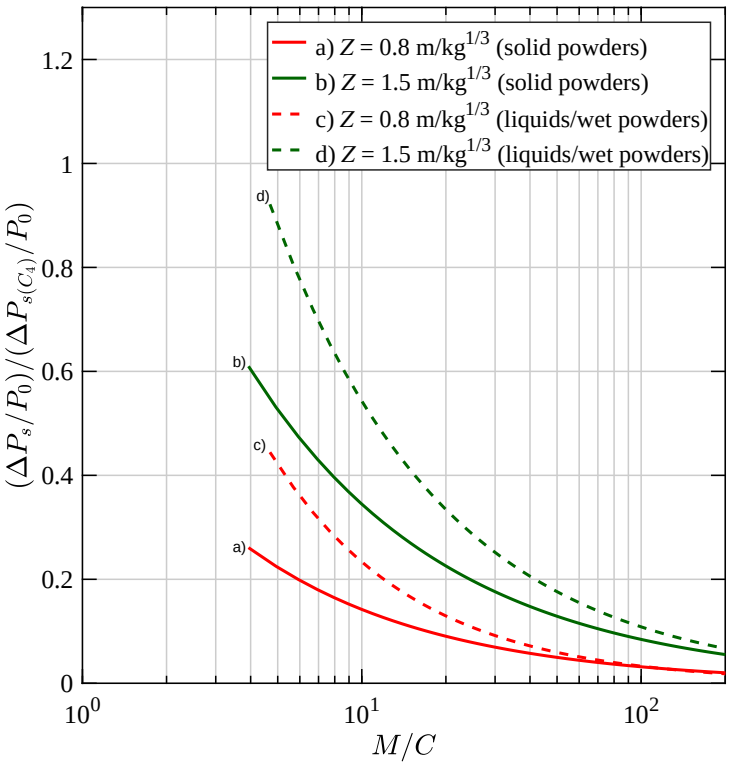

Fig. 3.22 Effective peak blast overpressure mitigation as a function of M/C for solid powders and liquids/powders saturated with water in the near-to-mid field, at two different scaled distances.

wave for each trial, it is convenient to plot the arrival time of each front as a function of distance, determined from video footage, on the same graph, in the manner of Brode [40]. Similar to the scaling of distance, the arrival time may be scaled as follows:

$$t_s = \frac{t_a}{W^{1/3}} \tag{3.8}$$

where:

t_s = scaled blast arrival time (ms/kg$^{1/3}$)

t_a = actual blast arrival time (ms)

W = charge mass in equivalent TNT (defined previously)

Fig. 3.23 shows the blast wave and material arrival times, as a function of Z, for three arbitrary materials at different M/C values for granular mitigants. Similarly, Fig. 3.24 shows the arrival times for liquids/powders saturated with water, determined using the same spherical fitting technique. Time zero corresponds to the time of detonation of the burster charge and the material location is determined by finding the maximal spatial extent of the particles or particle jets at a given time. These graphs indicate that the trajectories of blast waves for a mitigated charge are retarded compared to an ideal blast wave for a bare high-explosive charge. For the relatively light aluminum particles, with a low value of M/C, the particles follow closely behind the blast wave. However, for steel particles with a large value of M/C, the jets lags behind the blast front at a considerable distance.

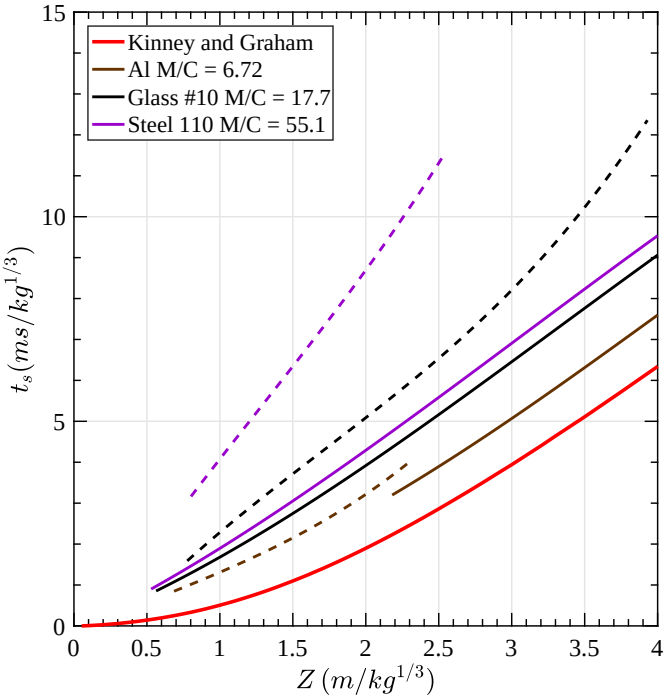

Fig. 3.23 Scaled time of arrival as a function of the scaled distance for granular powders. (-) Blast wave, (- -) Jets.

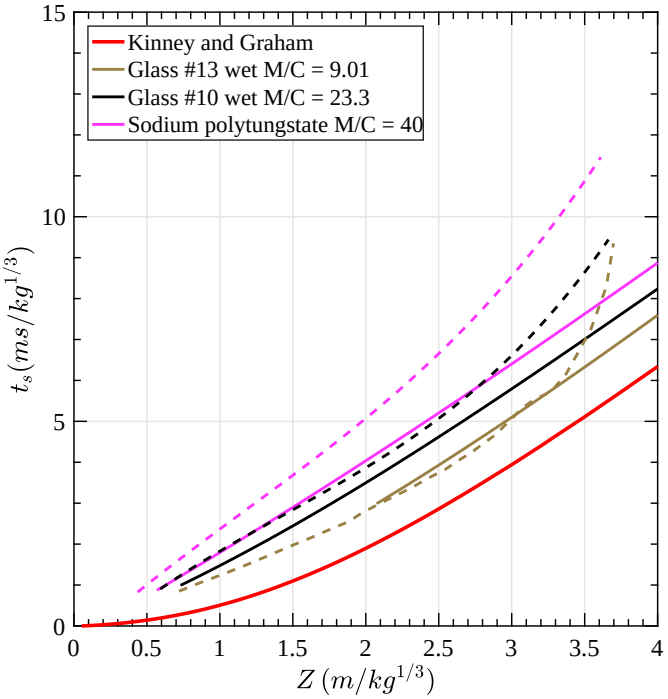

Fig. 3.24 Scaled time of arrival as a function of the scaled distance for liquids. (-) Blast wave, (- -) Jets.

For the case of liquids or powders saturated with water, the liquid droplets follow more closely behind the blast wave than for solid particles. For the case of glass powder saturated with

water, it is difficult to distinguish between the glass particles and water droplets, although in this case the jets rapidly decelerate some distance from the charge, possibly due to breakup and vaporization of the droplets. Furthermore, the jets may overtake the blast front for the lowest M/C values, as seen in Fig. 3.24 for $Z < 3$ m/kg$^{1/3}$.

The effect of M/C on the separation between the blast wave and the leading edge of the particle cloud is illustrated in Fig. 3.25, which shows a single photographic frame from three different experiments, taken at the same scaled time of 2.2 ms/kg$^{1/3}$. For each experiment, the original photograph is shown on the left and a processed image is shown on the right. The original image is subtracted from a consecutive image to highlight the parts of the image that are moving, including the blast wave and particle fronts, such that the distance between the blast wave and particle front is readily visible. Contrary to the previous video processing technique, no pixel noise filter was applied, and hence scattered black pixels are still evident in the background. The upper two photographs show the dispersal of dry powders (S-110 steel at the top, with $M/C = 55.1$ and #10 glass powders in the middle, with $M/C = 17.7$). As the mass ratio decreases, the distance between the particle front and the blast wave decreases, as expected. The picture on the bottom shows the dispersal of a wetted bed of #10 glass powder. Even though the M/C value (23.3) is higher than for the dry powder, the material jets (a mixture of liquid and powder) for the slurry case follow more closely behind the blast wave than for the dry powder. This indicates that with dry powder beds, there is greater energy dissipation during particle dispersal and the material velocity is less.

To make a more quantitative comparison of the distance between the material front and the blast wave for liquid and granular mitigants, it is convenient to plot the difference of the scaled arrival time between the materials and the blast wave as a function of M/C in Fig. 3.26 according to:

$$\Delta t_s = t_{s_{jets}} - t_{s_{blast}} \tag{3.9}$$

To obtain such a plot, the scaled arrival times of both the blast wave and material front have been extracted from the fitted time versus distance trajectory plots. At each Z value, the difference between the scaled times were extracted for 31 trials for granular mitigants and 24 trials for liquids/powders saturated with water. For clarity, all the data points are not represented on the graph. For each scaled distance, a linear function was fitted to the data points, with the error bars representing the maximum data point divergence for the whole curves. Solid powders show the largest scatter in the results due to the difficulty in extracting an unambiguous value for the particle front, particularly far from the charge center when the particle density is low and for non-jetting powders (e.g., steel). In the case of liquids or powders saturated with water, the scatter is mainly attributed to the differences between liquids and powders saturated with water, the latter sustaining the coherence of the jets close to the blast front over longer distances and less subject to drag.

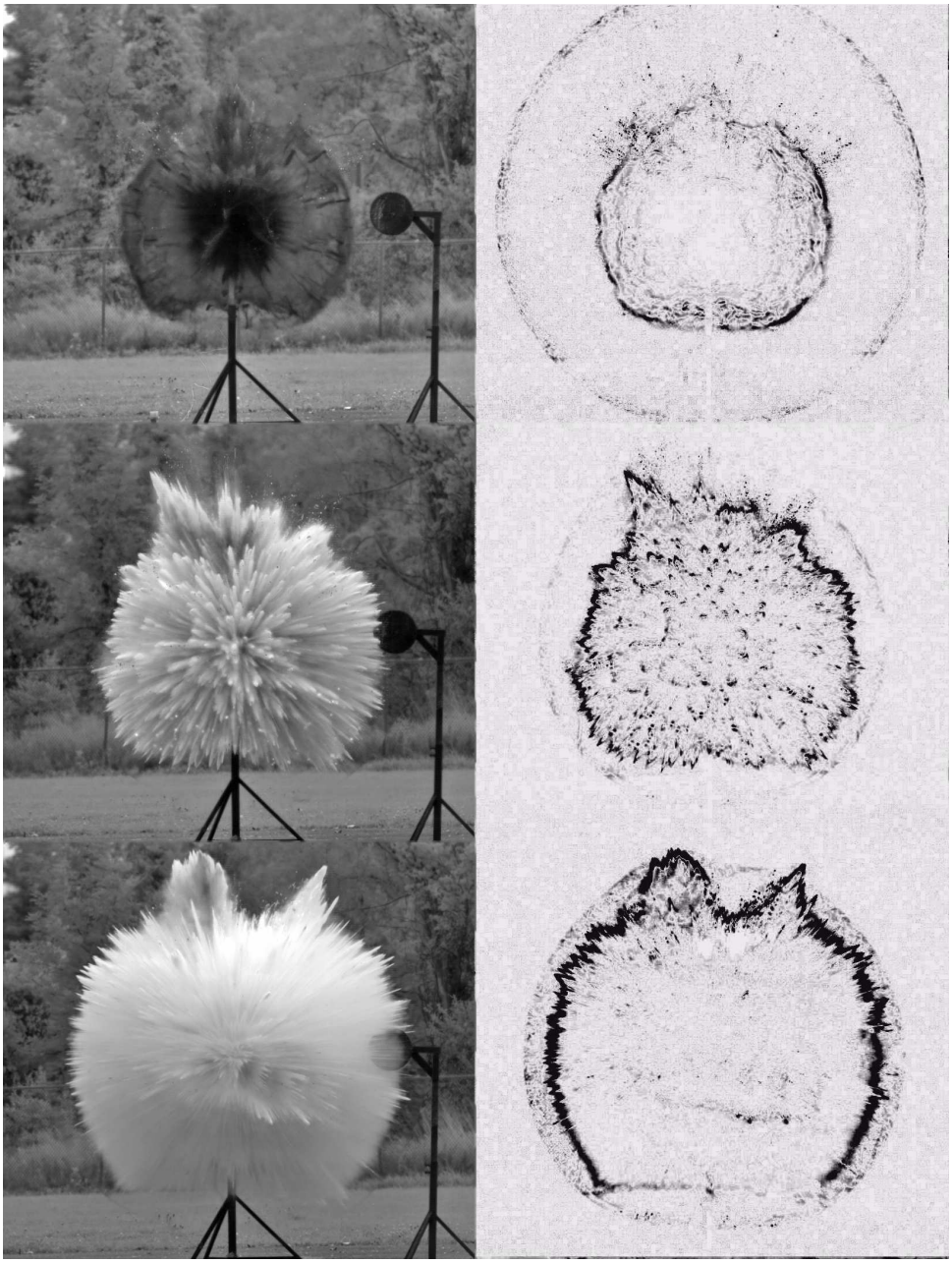

Fig. 3.25 Single photographic frames (on the left) from 3 different experiments at the same scaled time (see Eq. (3.8)) of 2.2 ms/kg$^{1/3}$ as a function of M/C. The pictures on the right show the same image, subtracted from a consecutive image, to enhance the visibility of the blast wave. No pixel noise filters are applied to the images so scattered black pixels are still visible in the background. The top image is for the dispersal of S-110 steel shot ($M/C = 55.1$), the middle image the dispersal of dry #10 glass beads ($M/C = 17.7$), and the bottom image the dispersal of a bed of #10 glass beads saturated with water ($M/C = 23.3$). In each case the high-explosive mass is 75 g. All of the photographs are at the same scale (the circular lollipop gauge mount, visible on the right, has a diameter of 30 cm). Note that the jets can overtake the blast at the top of the charge due to the jetting of detonation products up the tube housing the detonator. Moreover, the jets can also penetrate the blast front on the sides in the near field and for low M/C values (see Fig. 3.26).

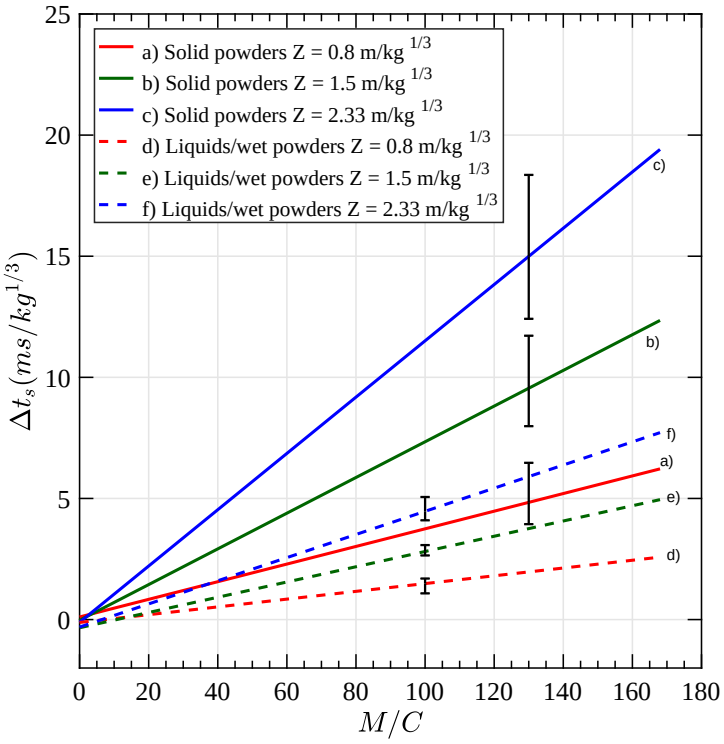

Fig. 3.26 Separation between blast waves and jets (difference in scaled arrival time) as a function of M/C for solid powders and liquids/powders saturated with water at $Z = 0.8$ m/kg$^{1/3}$, $Z = 1.5$ m/kg$^{1/3}$ and $Z = 2.33$ m/kg$^{1/3}$. The negative separation for the lowest M/C values shows the possibility that the jets to overtake the blast front.

It is clear that the difference in scaled time between the material and blast fronts increases with M/C and Z. Moreover, at given M/C and Z values, solid powders lead to the highest separation between the blast wave and the cloud of fragments. This discrepancy between liquids and solid powders continues to increase with increasing Z and M/C. Even if jets particles/droplets can overtake the blast on top of the charge due to burster/jetting effects (see Fig. 3.25), generally jets lag behind the blast front on the sides. However, for very low M/C values, jets may cross the blast front on the sides. This effect is indicated in Fig. 3.26 by the negative Δt_s values.

3.4.4 Positive-phase impulse

The positive-phase blast impulse is an important parameter when assessing the potential for structural damage due to blast waves. The positive-phase impulse I^+ is defined as the area under the curve of the first positive section of the overpressure curve, i.e.:

$$I^+ = \int_{t_a}^{t_f} \frac{\Delta P}{P_0} dt \tag{3.10}$$

with $t_f = t_a + t_d$, t_a being the time of arrival of the blast wave, and t_d being the duration time of positive overpressure. For the convenience of comparing results from experiments with different high-explosive masses, it is of interest to define a scaled impulse as follows:

$$I_s^+ = \frac{I^+}{W^{1/3}} \tag{3.11}$$

where:

I^+ = positive-phase blast wave impulse (bar·ms)
I_s^+ = scaled positive-phase blast wave impulse (bar·ms/kg$^{1/3}$)
W = charge mass in equivalent TNT (defined previously)

with a relative effectiveness factor $\varepsilon = 1.15$ in the definition of W, which was determined empirically by Bogosian et al. [39], and differs from the relative effectiveness factor for pressure. The impulse data are obtained for all trials by integrating the blast overpressure-time history obtained with the side-on piezoelectric pressure transducers. The trapezian method of integration has been used with a minimum of 140 points associated with the positive overpressure phase. The time resolution of the pressure measurements was between 0.2 μs and 5 μs (depending on the trial - see supplementary material). Another method for determining blast impulse using optical data to characterize the density gradients within the flow field has been reviewed by Biss and McNesby [41]. This method is not practical in the present situation due to the presence of a non-uniform background and the presence of compacted fragments that perturb the local pixel intensity. In this data set, due to the high density of particles in the near field, pressure gauges

are located relatively far from the charge center corresponding to a scaled distance between $Z = 1.98$ m/kg$^{1/3}$ to $Z = 12.57$ m/kg$^{1/3}$.

Impulses for dry powder mitigants

Fig. 3.27 presents the scaled impulse results for 5 different types of powders. In all cases, the blast impulse falls below the values for a bare charge from Kinney and Graham, by up to a factor of 5. The spread in the results is the result of variations in the M/C value. Reproducibility of the results can be obtained by comparing glass #10 and #13 at $M/C \approx 47$. The maximum discrepancy is found to be 21% for glass #13 at $Z = 6.29$ m/kg$^{1/3}$.

At high M/C values, aluminum and sand have lower impulse values compared to steel even if their mass ratios are lower (120.29 and 128.78, respectively, compared to 149.7) suggesting that steel particles attenuate less. However, at an M/C value around 50, the impulses between sand and steel are relatively similar for Z just above 2 m/kg$^{1/3}$ but a discrepancy appears for higher Z and steel impulses are more reduced. This discrepancy is attributed to the noisy overpressure-time signal for the sand trial. Also, at $M/C = 21.3$, steel generates similar impulses as glass at $M/C \approx 47$. Particle size seems also to affect the impulses. Contrary to peak overpressures in the near field, glass #13 particles appear to attenuate the impulses more at $M/C \approx 47$. Also, glass #13 $M/C = 6.5$ appears to have similar impulses (or even lower for $Z > 8$ m/kg$^{1/3}$) compared to glass #10 $M/C = 17.7$. Fig. 3.28 shows the average dependence of scaled impulses with M/C for 3 different Z values for M/C between 17.7 and 149.7. The data can be fit once again with power law fits (straight lines in logarithmic scale) according to Eq. (3.7) with the following coefficients:

$$(\alpha, \beta) = (1.356, 0.517) \text{ for } Z = 3.46 \text{ m/kg}^{1/3}$$
$$(\alpha, \beta) = (0.807, 0.506) \text{ for } Z = 6.29 \text{ m/kg}^{1/3}$$
$$(\alpha, \beta) = (0.463, 0.535) \text{ for } Z = 12.57 \text{ m/kg}^{1/3}$$

For comparison, several data points for steel and glass #10 have been extrapolated from Fig. 3.27 and added to Fig. 3.28. Steel particles appear to have lower positive-phase impulses compared to glass, especially for $M/C < 63$. Conversely, on average, glass #13 has lower impulses compared to glass #10.

Impulse for liquid and water-saturated powder mitigants

In a similar manner, the scaled impulses for liquids and liquid-saturated powders, are plotted as a function of Z and M/C (for given Z values) in Figs. 3.29 and 3.30, respectively. In the far field, most of the positive-phase impulses are found to be above the Kinney and Graham curve except for $Z < 3$ m/kg$^{1/3}$. The reproducibility is given by titanium wet with a maximum discrepancy of

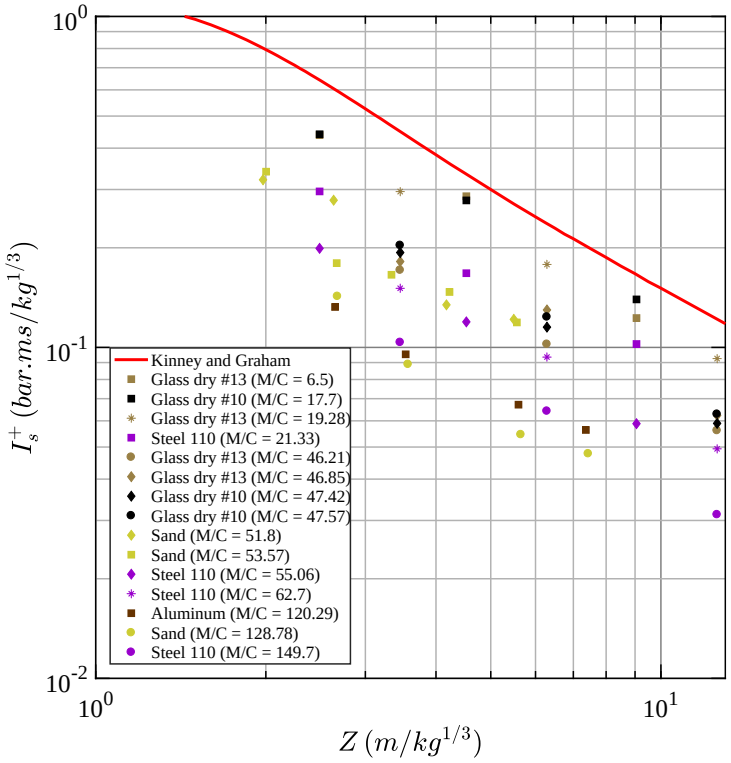

Fig. 3.27 Scaled positive-phase blast wave impulse as a function of scaled distance Z for the case of solid powders.

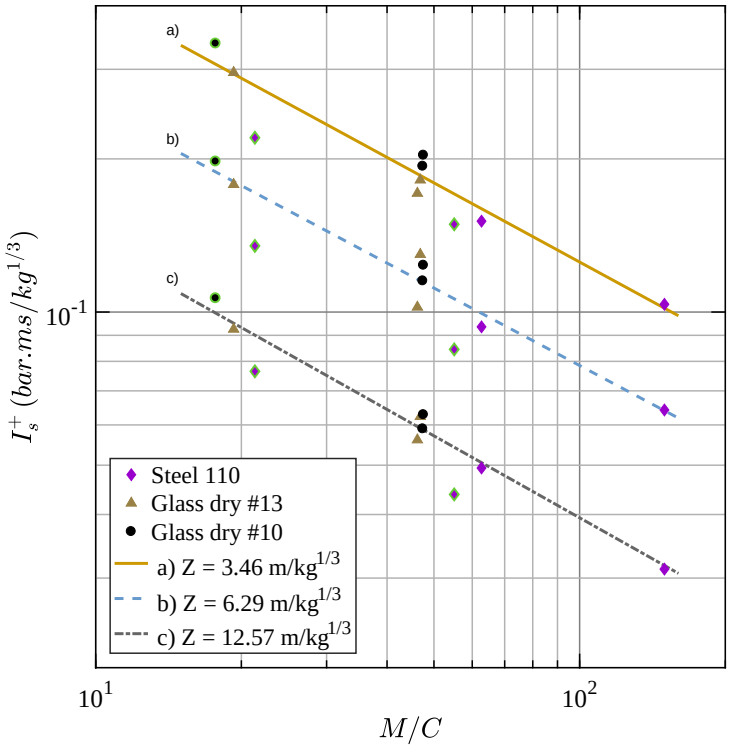

Fig. 3.28 Scaled impulse as a function of M/C at three different scaled distances Z for solid powders. Green-edged dots are extrapolated from Fig. 3.27.

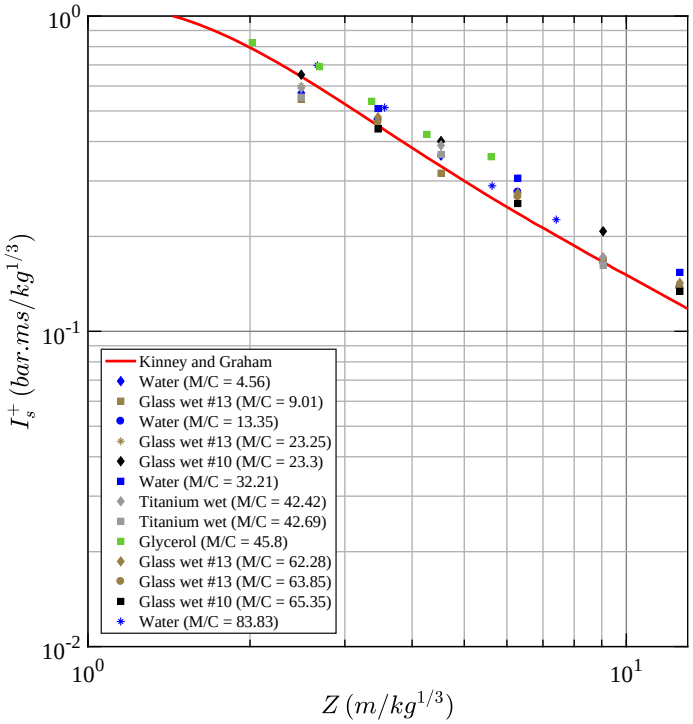

Fig. 3.29 Scaled positive-phase impulse as a function of scaled distance Z for an high explosive surrounded by a liquid or powder saturated with water.

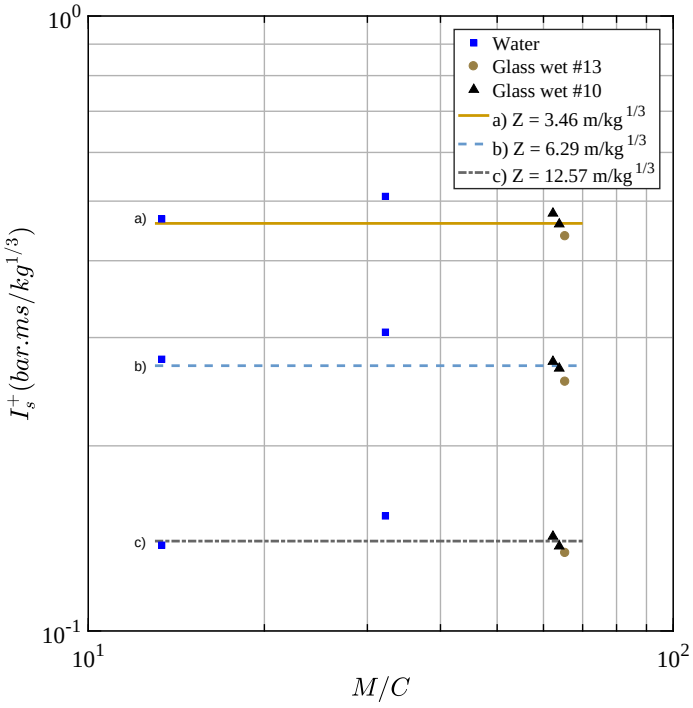

Fig. 3.30 Scaled impulse as a function of M/C at three different fixed scaled distances Z for liquids or powders saturated with water.

6.5% at $Z = 2.49$ m/kg$^{1/3}$. In contrast with powders, liquid mitigants have virtually no influence on the decay of the scaled positive-phase impulse with distance, in comparison with a bare HE charge. Furthermore, from Fig. 3.30, the scaled impulse does not depend on M/C. No clear trend can be extracted on a material basis except that on average, powders saturated with water appear to have lower impulses than liquids. Also, contrary to solid powders, glass #10 wet has slightly lower impulses compared to glass #13 wet.

Similarly to Fig. 3.22, Fig. 3.31 shows the comparison of the average attenuation of the blast positive-phase impulse for solid particles versus liquids (or particles saturated with water) for M/C between 15 and 160, in the far field. Note that the normalized impulse values for liquids/particles saturated with water are higher than unity since impulse values are above the Kinney and Graham curve in Fig. 3.29. On average, for each type of material, the normalized impulse increases more slowly with scaled distance, though not linearly. For solid powders, a discrepancy between $Z = 6.29$ m/kg$^{1/3}$ and $Z = 12.57$ m/kg$^{1/3}$ is visible for low M/C but disappears at high M/C. At $M/C = 15$, solid powders have impulse values of 72.7%, 75.9%, 77.6% at respectively $Z = 3.46$ m/kg$^{1/3}$, 6.29 m/kg$^{1/3}$ and 12.57 m/kg$^{1/3}$, normalized to that for liquids/powders saturated with powders. At $M/C = 160$, the percentages drop to 21.4%, 22.9% and 21.8%.

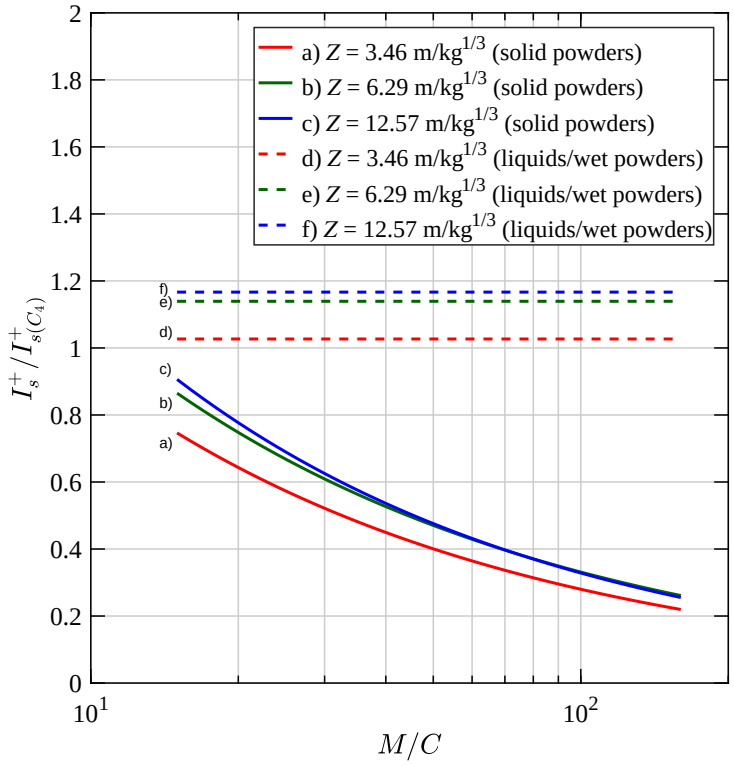

Fig. 3.31 Effective blast wave impulse mitigation as a function of M/C for solid powders and liquids/powders saturated with water in the far field, at three different scaled distances.

3.5 Discussion

Figs. 3.12, 3.13, 3.17, and 3.18 demonstrate that the peak blast overpressure from a high-explosive charge may be reduced by more than one order of magnitude by surrounding the charge with a layer of mitigating material, provided that the mass of mitigant is sufficiently large, relative to the high-explosive mass. The mitigation is most effective in the near field for solid powders, particularly for scaled distances of $Z < 2$ m/kg$^{1/3}$. The attenuation of the peak overpressure is primarily dependent on the M/C ratio, for a given scaled distance as shown in Figs. 3.14 and 3.19. Since the mitigant mass, or mass ratio, is the key parameter controlling the effectiveness of blast mitigation, it is likely that the transfer of momentum and heat (investigated numerically in another publication [42]) from the detonation products to the particles is the primary mechanism for reducing the blast overpressure in the near field. Increasing the inert mass surrounding a high-explosive charge will increase the amount of thermal energy extracted from the expanding detonation products. For the case of liquids, which are relatively incompressible, there will be little compaction work done on the liquid as the shock propagates through it, and little evaporation over this short timescale. Hence, the transfer of momentum and heat to the liquid will again be primarily responsible for the mitigation of the peak blast overpressure in the near field.

For the case of solid powders, the compaction of the porous bed and deformation of the particles also contribute to mitigating the blast overpressure. The relative importance of compaction compared with the transfer of heat and momentum can be determined by comparing the average decay of peak blast overpressure as a function of M/C for liquids and solids powders in the near field ($Z = 0.8$ m/kg$^{1/3}$) (see Fig. 3.22). The absolute value compared to unity for liquids/wet powders (dashed line c) reflects the degree of mitigation due to the heat and momentum transfer and the difference between this curve and the curve for solid powders (solid line a) is a measure of the additional pressure reduction due to compaction effects. The reduction of pressure due to compaction at low M/C values is less significant than the reduction due to the transfer of heat and momentum, but it is still important. For M/C values above 100, the pressure reduction is dominated by the transfer of heat and momentum and the contribution of compaction is negligible. This result is expected as compaction losses will be most important near the high-explosive charge due to decay of the shock pressure with distance inside the particle bed. With the increase of inert mass around the charge, the compaction losses do not significantly increase, and hence become relatively less important to the overall energy transfer.

In a recent publication, Milne [43] used hydrocode calculations to develop an empirical correlation for the particle velocity obtained during the explosive dispersal and showed that the velocity deficit, in comparison with the conventional Gurney velocity, is largely due to losses during the powder compaction stage. A similar argument likely explains the pressure mitigation effect of powders. Liquids, in contrast with powders, have negligible initial porosity, and hence energy dissipation due to pore collapse does not play a role during shock propagation through

the liquid. For powders saturated with water, the interstitial liquid between the particles is capable of supporting stress, and hence preventing the formation of force chains and limiting particle-interaction driven by deformation and compaction. Other phenomena play a role during the explosive dispersal of liquids, including cavitation behind the inward-propagating expansion wave generated when the shock wave reaches the liquid surface. Re-compaction of the bubbly liquid generated by cavitation by the expanding explosive products, and breakup of the liquid into droplets and subsequent droplet evaporation will also occur, as discussed in a recent publication on the dynamics of liquid dispersal [25]. It is likely that the energy consumed by these processes is eventually returned to the flow field through particle drag and expansion of the vapour produced, leading to the lack of impulse deficit observed experimentally in the far field.

As a secondary effect, at a specific M/C value, the material properties appear to influence the peak overpressure reduction. In particular, particles that form jets when explosively dispersed show a higher peak overpressure attenuation in the near field compared to particles that are less prone to form jets (i.e., Chronital steel, S-100 steel). A difference of up to 50% in peak overpressure values can be observed (Fig. 3.15), at given M/C values, between the heavier steel (Chronital steel, the worst mitigant) and the glass powder with the largest particle size (glass #10, the best mitigant). The higher heat capacity of the glass particles [42] and the ability of these particles to deform, crush or fracture more easily is a possible explanation for this difference of mitigation. All materials that are easily deformed, crushed or fractured (e.g., glass #13, granulated sugar, icing sugar) show mitigation performances closer to the glass #10 powder. Conversely, heavy metal particles, such as S-110 steel, iron and brass, have peak overpressure values closer to that of Chronital steel. Ductile metals, such as aluminum, as well as hard, but brittle powders like silicon carbide and sand exhibit intermediate values. When homogeneously mixed with silicon carbide, S-110 steel exhibits a higher mitigation performance, suggesting that compaction and fracturing of the brittle component still occurs in a powder mixture. In the case of liquids or powders saturated with water, differences are less with a maximum discrepancy of 20% between water, the best mitigant and glycerol the worst mitigant (Fig. 3.20). Ethanol and vegetable oil have intermediate peak overpressure values. Factors that may contribute to the difference in the mitigation performances include the heat absorption and the heat required to vaporize the liquids. Indeed, ethanol has a lower latent enthalpy of vaporization on a mass basis [44] and specific heat [45] ($\Delta H_{\text{vap}} = 846$ kJ/kg, $c_{\text{p}} = 2.3 - -2.72$ kJ/(kg-K), at temperatures between 0°C and 40°C) compared to water ($\Delta H_{\text{vap}} = 2257$ kJ/kg, $c_{\text{p}} = 4.19$ kJ/(kg-K)). On the other hand, glycerol is denser than the two previous liquids and possesses a higher heat of vaporization ($\Delta H_{\text{vap}} = 974$ kJ/kg) compared to ethanol but has a slightly higher c_{p} ($c_{\text{p}} = 2.43$ kJ/(kg-K)). Similar arguments could explain differences in the peak overpressure mitigation in the near field for vegetable oil and sodium polytungstate. Conversely, the addition of particles in liquids (e.g., glycerol with tungsten carbide) or the addition of water to a powder bed, may affect the vaporization of the liquids, hence reducing the mitigation

performance in the near field. To explore the importance of different liquid properties on blast attenuation more fully, detailed hydrocode calculations are needed, in which the heat transfer to the liquid, liquid fragmentation into droplets and vaporization effects are all considered. Blast attenuation during particle dispersal is explored computationally in a companion paper [46], and while heat transfer effects are considered, liquid fragmentation is not modelled in this work.

The rate of decay of the peak overpressure in the near field ($Z < 2$ m/kg$^{1/3}$) for powder and liquid mitigants is less than for an unmitigated high-explosive charge (see Figs. 3.12 and 3.17). It is likely that the motion of particles influences the blast wave propagation, even if the particle front does not follow closely behind the blast front. It is hypothesized that the particle front is effectively acting as a porous piston, which generates pressure disturbances. Each particle, or group of particles in close proximity, will drive a bow shock ahead of it (if particle velocities are higher than the local speed of sound), which collectively perturb the local flow field. These perturbations are all the more important in the near field where the local particle density is high. These pressure disturbances propagate upstream in the hot, post-shocked air, augmenting the pressure and impulse behind the blast wave. As the blast wave expands radially, it slows down, and ultimately the disturbances are able to catch the blast wave and influence the peak overpressure. In the far field ($Z > 2$ m/kg$^{1/3}$), the blast front and front of the cloud of particles are well separated. In this zone, the particle density becomes quite low due to the radial expansion of the particle front, and the particle influence on the blast wave propagation becomes insignificant. Hence, in the far field, the rate of decay of the peak overpressure becomes closer to that of an unmitigated blast wave (Figs. 3.12 and 3.17) but mitigation performances continue to decrease in the far field (Figs. 3.16 and 3.21). In the present experiments, combustion in the dispersed material cloud was only observed in a few cases (e.g., for icing sugar and ethanol). However, the combustion was only initiated after the blast propagation and hence had no influence on the blast wave motion.

Jets of solid particles and liquid droplets exhibit somewhat different dynamics. For a given M/C, solid particle jets initially have a lower velocity than liquid jets due to losses during compaction of the particle bed. However, jets of liquid droplets are subject to fragmentation, which increases the droplet surface area and causes the liquid jets to decelerate more rapidly than solid particle jets [25]. Particles accelerate at early times when they are still within the detonation products and hence are not visible by videography. As soon as the particles leave the detonation products, they begin to decelerate due to drag with the surrounding gas and the momentum of the particles will be converted back to momentum of the gas. Hence, even in the far field, pressure disturbances still influence the pressure field behind the blast front and contribute to the blast impulse. Furthermore, all momentum losses by evaporation of the liquid behind the blast front will be converted back into momentum of the gas. As a result, for liquids, the blast momentum is totally recovered behind the leading shock front independently of M/C and the pressure impulse is essentially the same as an unmitigated charge (Fig. 3.30). For solid powders, a part of the total blast momentum is permanently lost during the compaction

and implies a reduction in blast impulse (Fig. 3.27). By increasing the mass ratio, impulses are reduced similarly to peak overpressures and follow the same decay as a function of M/C (Figs. 3.28, 3.31). As noted earlier, the rate of decay is higher at low M/C due to the loss of momentum by compaction but diminishes at high M/C when compaction losses becomes less significant compared to the transfer of heat and momentum to the particles.

The investigation of the effect of material properties on the peak blast overpressure and positive-phase impulse attenuation is more complex in the far field. Indeed, the blast attenuation in the far field is a consequence of two factors: i) the energy/momentum loss during the shock propagation in the initial material layer, and ii) the blast energy/momentum recovery through the motion of the particles mentioned in the previous paragraph. The latter effect depends mainly on the ability of the particles to give their energy back to the flow by drag, which depends on the shape, velocity, size and density of the dispersed particles. In particular, the largest glass particles (glass #10) attenuate the peak blast overpressure more in the near field than the far field (Fig. 3.15) but appear to mitigate both the peak overpressure and the impulse less in the far field (Figs. 3.16, 3.27). This phenomenon indicates that the blast overpressure recovers faster for the glass #10 particles. This phenomenon is counter-intuitive since smaller particles are more subject to drag and should be able to give their energy back to the flow more quickly. Hence, the blast pressure should be higher in the far field for the smallest particles. It is hypothesized that during the compaction of the initial particle bed, the glass #10 particles fracture into smaller fragments than that for the glass #13 powder. In addition, steel particles are found to be better at reducing the blast pressure in the far field, contrary to the near field. This effect can be attributed to the higher particle size of the steel shot, compared to the glass particles (see Table 3.1), which decreases the overpressure recovery as mentioned earlier. The non-jetting behaviour of the steel particles may also diminish the energy/momentum recovery process compared to jetting powders, although this appears to be a secondary effect since the blast mitigation for steel particles (non-jetting) is on the same order as for iron particles (jetting), which have a similar density. In the case of liquids or solid powders, the comparison between materials in the far field is difficult due to the lack of statistics. Nevertheless, powders saturated with water show, on average, slightly better impulse attenuations than liquids, suggesting that residual compaction can occur during the propagation of the initial shock through wetted powders.

It is found that solid powders are more effective than liquids at mitigating peak blast overpressures and impulses. However, in practical situations, the loading on a structure consists of not only the impulse due to the interaction of the blast wave and subsequent air flow, but also the impulse from the impact of the particles [47]. Hence, in many cases the reduction in blast impulse may be overwhelmed by the particle impulse [48]. Furthermore, to obtain a significant reduction in the peak overpressure in the far field, a large amount of inert material is required relative to the high-explosive mass. For example, to obtain an order of magnitude reduction in blast overpressure at a scaled distance of $Z = 2$ m/kg$^{1/3}$ requires a mass ratio of 50.

3.6 Conclusions

The mitigation of a blast wave created by the detonation of a high explosive was investigated experimentally. Various types of mitigants including a wide range of solid particles, liquids, and particles saturated with water have been tested. The peak blast wave overpressure was inferred from the analysis of the blast wave motion from the high-speed video records and the positive-phase blast impulse was determined from side-on pressure transducers at several distances from the charge. The primary results of this study are as follows:

1. Solid powders, liquids, or powders saturated with a liquid can be used as blast wave mitigants. However, solid powders outperform liquids with respect to mitigating the blast wave peak overpressure, especially in the near field and at low ratios of the mass of mitigant to the high-explosive charge. The difference in mitigation performance is likely due to the energy loss during the compaction and deformation of solid powders at early times.

2. The comparison between mitigation efficiencies of solid powders and liquids suggests that mitigation is mainly due to the transfer of heat and momentum. However, at low M/C, shock-induced compaction of the particle bed and particle deformation of the particles is a significant contributing factor for the blast mitigation for solid powders. At high M/C, the relative contribution of deformation/compaction compared to the transfer of heat and momentum becomes negligible.

3. The decay of the blast peak overpressure for both granular solid and liquid mitigants as a function of M/C follows a weak power law function. The decay of blast impulse as a function of M/C for the solid powders also exhibits a power law decay. However, in the case of the liquids or liquid-saturated powders, blast impulses in the far field are essentially the same or slightly higher as that of an unmitigated charge with the same high-explosive mass and does not depend on the mass ratio.

4. The degree of blast mitigation in the near field with either powders or liquids/wet powders surrounding a charge is primarily dependent on M/C. The material properties play a secondary role in the mitigation process. In the case of solid particles, jetting powders (all the powders tested except steel) show higher mitigation performances than non-jetting powders (steel), by up to 50%. Glass particles show the best peak blast overpressure and impulse attenuation. Factors that likely contribute to the good performance of glass particles include its high heat capacity, and the tendency of the powder to deform and fracture. Other easily crushable, brittle or ductile powders (e.g., sugar, silicon carbide, sand, aluminum) are found to attenuate the blast more than dense metallic powders (iron, brass, S-110 steel and Chronital steel). In the case of liquids, the difference in mitigation performance is small (up to 20%). Water appears to attenuate the blast the most in the near

field possibly due to its higher heat capacity and heat of vaporization. Water-saturated powders attenuate the blast slightly more in the far field compared to liquids, indicating that residual compaction may occur during the propagation of the shock through the initial bed.

5. It is hypothesized that the slower rate of decay of the peak blast overpressure in the near field for a mitigated charge versus an equivalent bare charge is due to pressure support induced by the motion of the mitigant which effectively acts as a porous piston. The local pressure disturbances from the particle-flow interaction eventually catch up to the leading shock front and perturb the peak overpressure. This particle-blast interaction, which depends principally on the properties of the dispersed materials (e.g., shape, particle/droplet size, density, etc.), generates a complex blast mitigation dependence on material properties in the far field. In a companion paper, the details of the particle-blast wave interaction are explored more fully with hydrocode calculations [46].

Acknowledgements The authors thank Rick Guilbeault at the Canadian Explosive Research Laboratory for assistance with the experiments, A. Longbottom of Fluid Gravity Engineering for discussions and the Defense Threat Reduction Agency for financial support. The authors also acknowledge the assistance of Yann Grégoire for the processing of the images in Fig. 3.25. The authors would also like to thank the three anonymous reviewers for their many constructive comments.

References

[1] M. Cheng, K. C. Hung, and O. Y. Chong. Numerical study of water mitigation effects on blast wave. *Shock Waves*, 14(3):217–223, 2005, doi:10.1007/s00193-005-0267-4.

[2] R. M. Allen, D. J. Kirkpatrick, A.W. Longbottom, A. M. Milne, and N. K. Bourne. Experimental and numerical study of free-field blast mitigation. In *AIP Conference Proceedings*, volume 706, pages 823–826, 2004, doi:10.1063/1.1780363.

[3] A. D. Resnyansky and T. G. Delaney. Experimental study of blast mitigation in a water mist. Technical report, DSTO Defence Science and Technology Organisation, Edinburgh, South Australia, Australia, 2006, https://apps.dtic.mil/sti/pdfs/ADA465909.pdf.

[4] D. Schwer and K. Kailasanath. Blast mitigation by water mist (3) - mitigation of confined and unconfined blasts. Technical Report (3), Naval Research Laboratory, Washington D.C., USA, 2006, https://apps.dtic.mil/sti/pdfs/ADA452669.pdf.

[5] E. Del Prete, A. Chinnayya, L. Domergue, A. Hadjadj, and J.-F. F. Haas. Blast wave mitigation by dry aqueous foams. *Shock Waves*, 23(1):39–53, 2013, doi:10.1007/s00193-012-0400-0.

[6] B. E. Gelfand. Blast waves attenuation in two-phase media. In *Symposium on Interdisciplinary Shock Wave Research*, pages 150–166, Sendai, Japan, 2004.

[7] R. Raspet, S. K. Griffiths, J. M. Powers, H. Krier, T. D. Panczak, P. B. Butler, and F. Jahani. Attenuation of blast waves using foam and other materials. Technical report, US Army Construction Engineering Construction Laboratory, Champaign, Illinois, USA, 1989, https://apps.dtic.mil/sti/pdfs/ADA203148.pdf.

[8] K. Kitagawa, S. Yamashita, K. Takayama, and M. Yasuhara. Attenuation properties of blast wave through porous layer. *Proc. 26th International Symposium on Shock Waves*, 1(1990):73–78, 2007, doi:10.1007/978-3-540-85168-4_10.

[9] W. F. Hartman, B. A. Boughton, and M. E. Larsen. Blast mitigation capabilities of aqueous foam. Technical report, Sandia National Laboratories, Albuquerque, New Mexico, USA, 2006, https://www.osti.gov/servlets/purl/877732.

[10] A. Britan, H. Shapiro, and G. Ben-Dor. Foams for blast mitigation. In Paul Stevenson, editor, *Foam engineering: fundamentals and applications*, chapter 19, pages 477–512. John Wiley & Sons, 2012, doi:10.1002/9781119954620.

[11] V. F. Nestrenko. Shock (blast) mitigation by "soft" condensed matter. In *MRS Symp. Proc.*, volume 759, pages MM4.3.1–4.3.12, 2003, doi:10.1557/PROC-759-MM4.3.

[12] A. Britan, G. Ben-Dor, O. Igra, and H. Shapiro. Shock waves attenuation by granular filters. *International Journal of Multiphase Flow*, 27(4):617–634, 2001, doi:10.1016/S0301-9322(00)00048-3.

[13] S. P. Medvedev, S. M. Frolov, and B. E. Gel'fand. Attenuation of shock waves by screens of granular material. *Journal of engineering physics*, 58(6):714–718, 1990, doi:10.1007/BF00872723.

[14] B. Langhorst, C. Cook, J. Schondel, and H. S. Chu. Material systems for blast-energy dissipation. In *IMPLAST 2010 Conference*, pages 1–8, Providence, Rhode Island, USA, 2010. Society for Experimental Mechanics.

[15] K. Endo, K. Kitagawa, and M. Yasuhara. Diffusion effect of blast pressure in porous complex media. In *39th AIAA Fluid Dynamics Conference*, number June in Fluid Dynamics and Co-located Conferences, pages 1–9, San Antonio, Texas, 2009. American Institute of Aeronautics and Astronautics, doi:10.2514/6.2009-3569.

[16] Z. Wang and Y. Lu. Numerical analysis on dynamic deformation mechanism of soils under blast loading. *Soil Dynamics and Earthquake Engineering*, 23(8):705–714, 2003, doi:10.1016/S0267-7261(03)00076-9.

[17] Y. Lu, Z. Wang, and K. Chong. A comparative study of buried structure in soil subjected to blast load using 2D and 3D numerical simulations. *Soil Dynamics and Earthquake Engineering*, 25(4):275–288, 2005, doi:10.1016/j.soildyn.2005.02.007.

[18] R. D. Ambrosini, B. M. Luccioni, R. F. Danesi, J. D. Riera, and M. M. Rocha. Size of craters produced by explosive charges on or above the ground surface. *Shock Waves*, 12(1):69–78, 2002, doi:10.1007/s00193-002-0136-3.

[19] J. Loiseau, Q. Pontalier, A. M. Milne, S. Goroshin, and D. L. Frost. Terminal velocity of liquids and granular materials dispersed by a high explosive. *Shock Waves*, 28(3):473–487, 2018, doi:10.1007/s00193-018-0822-4.

[20] R. W. Gurney. The initial velocities of fragments from bombs, shell and grenades. Tech. Rep. (45), US Army Ballistic Research Laboratory, Aberdeen Proving Ground, Maryland, USA, 1943, https://apps.dtic.mil/sti/pdfs/ADA800105.pdf.

[21] P. W. Cooper. *Explosives engineering*. Wiley-VCH, wiley-vch edition, 1996.

[22] D. L. Frost, J. Loiseau, B. J. Marr, and S. Goroshin. Particle segregation during explosive dispersal of binary particle mixtures. In *AIP Conference Proceedings*, volume 1793, pages 1–7. AIP Publishing, 2017, doi:10.1063/1.4971702.

[23] D. L. Frost, Y. Grégoire, O. Petel, S. Goroshin, and F. Zhang. Particle jet formation during explosive dispersal of solid particles. *Physics of Fluids*, 24:091109, 2012, doi:10.1063/1.4751876.

[24] A. M. Milne, E. Floyd, A. W. Longbottom, and P. Taylor. Dynamic fragmentation of powders in spherical geometry. *Shock Waves*, 24(5):501–513, 2014, doi:10.1007/s00193-014-0511-x.

[25] A. M. Milne, A. Longbottom, D. L. Frost, J. Loiseau, S. Goroshin, and O. Petel. Explosive fragmentation of liquids in spherical geometry. *Shock Waves*, 27:383–393, 2017, doi:10.1007/s00193-016-0671-y.

[26] H. Kleine, E. Timofeev, and K. Takayama. Laboratory-scale blast wave phenomena - Optical diagnostics and applications. *Shock Waves*, 14(5-6):343–357, 2005, doi:10.1007/s00193-005-0279-0.

[27] P. K. Panigrahi and K. Muralidhar. Laser Schlieren and Shadowgraph. In *Methods in Heat and Mass Transfer: Visualization and Analysis*, chapter 2, pages 23–46. Springer-Verlag New York, 2012, doi:10.1007/978-1-4614-4535-7.

[28] L. Venkatakrishnan and G. E. A. Meier. Density measurements using the Background Oriented Schlieren technique. *Experiments in Fluids*, 37(2):237–247, 2004, doi:10.1007/s00348-004-0807-1.

[29] D. Ramanah, S. Raghunath, D. J. Mee, T. Rösgen, and P. A. Jacobs. Background oriented schlieren for flow visualisation in hypersonic impulse facilities. *Shock Waves*, 17(1-2):65–70, 2007, doi:10.1007/s00193-007-0097-7.

[30] M. J. Hargather. Background-oriented schlieren diagnostics for large-scale explosive testing. *Shock Waves*, 23(5):529–536, 2013, doi:10.1007/s00193-013-0446-7.

[31] O. K. Sommersel, D. Bjerketvedt, S. O. Christensen, O. Krest, and K. Vaagsaether. Application of background oriented schlieren for quantitative measurements of shock waves from explosions. *Shock Waves*, 18(4):291–297, 2008, doi:10.1007/s00193-008-0142-1.

[32] S. Yamamoto, Y. Tagawa, and M. Kameda. Application of background-oriented schlieren (BOS) technique to a laser-induced underwater shock wave. *Experiments in Fluids*, 56(5):1–7, 2015, doi:10.1007/s00348-015-1960-4.

[33] J. G. Anderson, S. L. Parry B, and D. V. Ritzel. Time Dependent Blast Wave Properties From Shock Wave Tracking With High Speed Video. In *24th International Symposium on Military Aspects of Blast and Shock (MABS 24)*, pages 1–20, Halifax, Canada, 2016.

[34] I. J. Campbell and A. S. Pitcher. Shock waves in a liquid containing gas bubbles. *Proceedings of the Royal Society of London. Series A. Mathematical and Physical Sciences*, 243(1235):534–545, 1958, doi:10.1098/rspa.1958.0018.

[35] J. M. Dewey. The properties of a blast wave obtained from an analysis of the particle trajectories. *Proceedings of the Royal Society of London. Series A, Mathematical and Physical Sciences*, 324:275–299, 1971, doi:10.1098/rspa.1971.0140.

[36] H. Kleine, J. M. Dewey, K. Ohashi, T. Mizukaki, and K. Takayama. Studies of the TNT equivalence of silver azide charges. *Shock Waves*, 13(2):123–138, 2003, doi:10.1007/s00193-003-0204-3.

[37] G. F. Kinney and K. J. Graham. *Explosive shocks in air (Second edition)*. Springer, 1985, doi:10.1007/978-3-642-86682-1.

[38] M. M. Jr. Swisdak. Explosion Effects and Properties - Part 1 - Explosion effects in air. Technical report, White Oak, Silver spring, Maryland, 1975, https://apps.dtic.mil/sti/pdfs/ADA018544.pdf.

[39] D. Bogosian, M. Yokota, and S. Rigby. TNT equivalence of C-4 and PE4: A review of traditional sources and recent data. In *24th International Symposium on Military Aspects of Blast and Shock (MABS 24)*, pages 1–15, 2016.

[40] H. L. Brode. Blast wave from a spherical charge. *Physics of Fluids*, 2(1959):217–229, 1959, doi:10.1063/1.1705911.

[41] M. M. Biss and K. L. McNesby. Optically measured explosive impulse. *Experiments in Fluids*, 55(6), 2014, doi:10.1007/s00348-014-1749-x.

[42] Q. Pontalier, M. Lhoumeau, and D. L. Frost. Blast wave mitigation in granular materials. *AIP Conference Proceedings*, 1979(1):110014, 2018, doi:10.1063/1.5044933.

[43] A. M. Milne. Gurney analysis of porous shell. *Propellants, Explosives, Pyrotechnics*, 41(4):665–671, 2016, doi:10.1002/prep.201600016.

[44] https://www.engineeringtoolbox.com/fluids-evaporation-latent-heat-d_147.html.

[45] https://www.engineeringtoolbox.com/specific-heat-fluids-d_151.html.

[46] Q. Pontalier, M. Lhoumeau, A. Milne, A. Longbottom, and D. L. Frost. Numerical investigation of particle-blast interaction during explosive dispersal of liquids and granular materials. *Shock Waves*, 28(3):513–531, 2018, doi:10.1007/s00193-018-0820-6.

[47] R. Cheesman and C. Tilbury. Blast and debris in the near field - diagnostic techniques and calculational tools to predict combined impulse loading. In *24th International Symposium on Military Aspects of Blast and Shock (MABS 24)*, pages 1–20, Halifax, Canada, 2016.

[48] D. L. Frost, C. Ornthanalai, Z. Zarei, V. Tanguay, and F. Zhang. Particle momentum effects from the detonation of heterogeneous explosives. *Journal of Applied Physics*, 101(11):1–14, 2007, doi:10.1063/1.2743912.

Transition to Chapter 4

In the previous chapter, the blast wave mitigation of spherical solid explosive (C-4) charges surrounded by either a bulk liquid, a packed bed of particles or a packed bed of particles saturated with water was investigated experimentally. The materials tested included a wide variety of particles and liquids. The blast attenuation effectiveness for these three configurations was compared. In the near field, all the configurations tested attenuated the blast wave pressure compared to the blast wave pressure of the bare explosive charge alone. The blast wave attenuation was mainly attributed to the transfer of heat and momentum from the explosive gases to the solid/liquid material. However, granular materials performed better at attenuating the blast wave, which was hypothesized to be due to the work done in compacting the porous layer. This observation correlated well with the results of a companion paper [1] devoted to the analysis of the terminal velocity of the jets of material. In this complementary study, the velocity of the liquid jets was predicted by the conventional Gurney theory [2] for hard casings. The terminal velocity of the jets of granular materials was less than that for the liquids. The deficit of the jet velocities for the packed bed of particles was also directly attributed to the energy losses in compacting the powders. Powders saturated with water behaved like a liquid with respect to both the blast wave attenuation and the terminal jet velocity. It was hypothesized that the load-bearing capability of the interstitial water limited compaction.

For a given explosive mass, increasing the mass of the material layer enhanced the blast wave mitigation effectiveness with the type of material playing a secondary role. Jetting powders (all the powders tested except steel) showed higher mitigation performance than non-jetting powders (steel), suggesting that the formation of jets could be responsible for additional energy losses. Moreover, easily crushable, brittle, and ductile powders (e.g., sugar, silicon carbide, sand, aluminum) performed better than dense metallic powder (iron, brass, S-110 steel and Chronital steel) at reducing the blast wave pressure. This body of evidence suggested that compaction was an important mechanism of blast wave attenuation.

Finally, the blast mitigation effectiveness was found to decrease with distance. This phenomenon was attributed to the influence of the expanding cloud of solid/liquid material, which acted effectively as a porous piston, on the blast wave. The piston effect, contributed to the reduction of the peak blast overpressure decay, even if the material lagged at a noticeable distance behind the blast wave front. It was hypothesized that the phenomenon occurred during

the deceleration phase of the jets, which was associated with aerodynamic shedding. During this phase, the bow shocks previously attached to the jets, traveled into the hot, post-shocked medium behind the blast wave front. In this medium, the sound velocity of the gas was higher than that of the ambient air, such that any pressure disturbances in this region traveled at a higher speed than the blast wave front. Hence, in the far field, the pressure disturbances merged with the blast front, contributing to supporting the peak blast overpressure. This porous piston effect had not previously been characterized in the literature but should be taken into account in the design of blast wave mitigation systems.

In the next chapter, numerical simulations in 1D are carried out with a multiphase hydrocode with the aim to determine if the general trends of the blast wave pressure decay observed experimentally may be reproduced computationally. The computational model can also be used to determine the dependence of the blast mitigation on various parameters and to explore the dynamic interaction between the particles and the surrounding gases (air or detonation products), which cannot be readily determined experimentally. The hydrocode EDEN [3] developed by researchers at Fluid Gravity Engineering Ltd. is used to carry out the computations. A two-phase model, based on a similar formulation to that of Baer and Nunziato [4] and integrated in EDEN is used. A brief summary of the operation of EDEN and the assumptions in the model are given in Appendix B. The blast wave pressure is computed over a large range of distances, including in the near field (close to the outer extent of the initial material layer), which was not probed experimentally. A parametric study is also performed to evaluate the influence of the particle size and the degree of the initial packed bed porosity on the blast wave pressure. The relative importance of the potential hazards caused by the blast effects compared to the effects resulting from the material dispersal is discussed. The discussion is based on a comparison of the momentum fluxes which is related to the impulsive loading on a nearby structures, at different distances from the charge. The numerical simulations also aim to validate the hypothesis by which the pressure disturbances generated by the motion of the dispersed materials contribute to supporting the peak blast overpressure. This chapter is comprised of a paper published in the *Shock Waves* journal.

References

[1] J. Loiseau, Q. Pontalier, A. M. Milne, S. Goroshin, and D. L. Frost. Terminal velocity of liquids and granular materials dispersed by a high explosive. *Shock Waves*, 28(3):473–487, 2018, doi:10.1007/s00193-018-0822-4.

[2] R. W. Gurney. The initial velocities of fragments from bombs, shell and grenades. Tech. Rep. (45), US Army Ballistic Research Laboratory, Aberdeen Proving Ground, Maryland, USA, 1943.

[3] Development team EDEN. EDEN user manual. Technical Report 12, Fluid Gravity Engineering (FGE), St, Andrews, Scotland, 2011.

[4] M. R. Baer and J. W. Nunziato. A two-phase mixture theory for the deflagration-to-detonation transition (ddt) in reactive granular materials. *International Journal of Multiphase Flow*, 12(6):861–889, 1986, doi:10.1016/0301-9322(86)90033-9.

Chapter 4

Numerical investigation of particle–blast interaction during explosive dispersal of liquids and granular materials

Q. Pontalier, M. Lhoumeau, A. Milne, A. Longbottom, and D. L. Frost, *Shock Waves*, 2018.
doi:10.1007/s00193-018-0820-6

Abstract

Experiments show that when a high explosive charge with embedded particles or a charge surrounded by a layer of liquid or granular material is detonated, the flow generated is perturbed by the motion of the particles and the blast wave profile differs from that of an ideal Friedlander form. Initially, the blast wave overpressure is reduced due to the energy dissipation resulting from compaction, fragmentation, heating of the particle bed and acceleration of the material. However, as the blast wave propagates, particle-flow interactions collectively serve to reduce the rate of decay of the peak blast wave overpressure. Computations carried out with a multiphase hydrocode reproduce the general trends observed experimentally, and highlight the transition between the particle acceleration/deceleration phases, which is not accessible experimentally, since the particles are obscured by the detonation products. The dependence of the particle-blast interaction and the blast mitigation effectiveness on three parameters is investigated systematically. The reduction in peak blast overpressure is, as in experiments, primarily dependent on the mass ratio of material to explosive, with the particle size, density and initial porosity of the particle bed playing secondary roles. In the near field, the blast overpressure decreases sharply with distance as the particles are accelerated by the flow. When the particles decelerate due to drag, energy is returned to the flow and the peak blast overpressure recovers and reaches values similar to that of a bare explosive charge for low mass ratios. Time-distance trajectory plots of the particle and blast wave motion with the pressure field superimposed illustrate the

weak pressure waves generated by the motion of the particle layer which travel upstream and perturb the blast wave motion. Computation of the particle and gas momentum flux in the multiphase flow generated during explosive particle dispersal indicates that, for glass particles, the particle momentum flux is the dominant term in the near field. These results are cautionary in circumstances where liquid or solid materials are used to surround an explosive charge with the goal of reducing the loading on nearby structures.

Keywords Explosive particle dispersal · Blast–particle interaction · Momentum exchange · Hydrocode simulation

4.1 Introduction

Surrounding a high-explosive charge with a layer of liquid or porous granular material is a common method to reduce the blast wave signature in the immediate vicinity of the charge. The mitigation of the blast wave is attributed to the dissipation of energy during compaction of a porous material and the transfer of thermal and kinetic energy to the mitigant material [1]. While a number of investigators have experimentally studied the mitigation effectiveness of a variety of materials in the near field (see [2] for a review of past work in this area), relatively little attention has been devoted to examining the interaction of the dispersed material with the blast wave and nearby structures. In some cases, despite a reduction in the blast strength, due to the momentum imparted to the material, the total loading on structures may actually be increased in comparison with a bare explosive charge [3].

In a recent experimental study of the explosive dispersal of liquids and granular materials, the terminal velocity attained by the material [4] and the decay of the blast wave overpressure [2] were determined for a wide range of materials. Loiseau et al. [4] showed that for liquids, the terminal velocity agrees well with the predictions of the classical Gurney model, and depends primarily on the liquid to explosive mass ratio, M/C. For granular materials, the Gurney model over-predicts the terminal velocity by 25 % to 60 %, with the velocity deficit attributed to energy dissipation during collapse of the porous particle bed and possible particle deformation. The velocity deficit is insensitive to the presence of particle jetting as well as the properties of the granular material. Pontalier et al. [2] found that while the addition of a layer of particles around the explosive charge reduced the peak blast overpressure in the near field, further from the charge the overpressure recovered nearly to the value corresponding to a bare charge, for $M/C < 10$. They hypothesized that the particles collectively act effectively as a porous piston with the pressure disturbances from individual particles, or clusters of particles, eventually reaching the blast wave and reducing the rate of decay of the peak blast overpressure. Depending on the size and density of the particles, the explosively dispersed particles may also reach and penetrate the blast wave and perturb the quiescent gas upstream of the blast wave front [5, 6].

A model for the complete process of explosive dispersal of a particle layer must consider first the shock propagation through the particle layer, compaction of the layer, transmission of the shock as a blast wave into the surrounding air, expansion of the dense gas-particle medium and finally the dilute gas particle regime after the particle cloud has expanded over a sufficient volume. Some authors have used the model problem of the sudden release of a pressurized gas-particle mixture to investigate the subsequent multiphase flow, while not considering the initial compaction phase (e.g., [7]). Other researchers have carried out computations to explore some aspects of the overall problem, such as shock interactions with particles and droplets [8], detailed particle-particle interactions [9], or later-time impulse effects from particles [10]. A further complication is that the transient multiphase flow that is generated during explosive dispersal of particles (or liquids) is typically characterized by a non-uniform particle distribution taking the form of clusters of particles or particle jets [11–14]. A mesoscale model for the multiple particle-particle and particle-flow interactions and formation of particle jets is computationally demanding and beyond the scope of the present investigation.

Experimentally, it is observed that the the maximum material velocity is relatively insensitive to the degree of particle jetting and material properties [4], while the blast wave overpressure may depend weakly on the formation of jets [2]. This suggests that a simple 1D multiphase model, which does not account for multidimensional jet formation, may be used to gain some insight into the interaction of the dispersed particles with the flow and blast wave, and to see if the general experimental trends are qualitatively reproduced. The model may then be used to determine the influence of experimental parameters, such as the mass ratio of inert material to explosive M/C, particle size and density, initial bed porosity, as well as the difference between dispersal of a layer of particles and liquid. In the present paper, the basis of the computational model will first be described, followed by results of simulations to explore the interaction between the dispersed particles and flow behind the blast wave. To facilitate a comparison with experimental results, calculations are carried out with two types of granular powders (glass and steel) and one liquid (water). Emphasis is placed on exhibiting the dependence of various parameters on the decay of the blast wave peak overpressure and impulse, compared to an explosive-generated flow without particles. The results are interpreted with the use of time-distance trajectory plots that illustrate the relative motion of the particles and blast wave.

4.2 Computational model

The calculations in the present paper are carried out with the EDEN multiphase hydrocode developed by scientists at Fluid Gravity Engineering Ltd (UK). This code has been extensively validated with experimental results for the explosive dispersal of powders and liquids. For example, Milne et al. [13] obtained good agreement with particle radius-time data obtained from radiographic images of the explosive compaction and dispersal of a spherical bed of glass beads. To match the experimental data it was found that a key assumption was necessary, in particular,

that the compaction energy was not recovered upon expansion of the particle bed. This has the consequence that a spall layer is not formed during the compaction and expansion of the porous particle bed, which is consistent with the radiographic results. The basic equations that form the basis of the model are given in an Appendix in a previous publication [11].

The charge configuration used consists of a central spherical ball of C-4 explosive surrounded with a spherical layer of particles or liquid. Contrary to experiments [2], the liquid is in direct contact with the explosive charge. Detonation of the C-4 charge proceeds with a program burn function and the detonation products are modelled with the classical Jones-Wilkins-Lee (JWL) equation of state [15]. To model the compaction of the porous particle bed, the Herrmann P-α porous solid equation of state is used, with the Murnaghan equation of state used for the solid, given by (Eq. (4.1)):

$$\begin{cases} K = \rho_{s0} C_s^2 \\ n = 4S - 1 \\ P_s = \frac{K}{n}\left[\left(\frac{\rho_s}{\rho_{s0}}\right)^n - 1.0\right] + P_{s0} \end{cases} \tag{4.1}$$

where ρ_{s0} is the initial solid material density, C_s corresponds to the solid sound speed, S is the slope of the shock/particle velocity curve, and P_{s0} is the initial solid pressure.

The particle configuration pressure, β, is assumed to be a function of the solid volume fraction ϕ_s and takes the following form (Eq. (4.2)):

$$\beta = a\left[\frac{(\phi_{s1} - \phi_{s0})^2}{(\phi_{s1} - \phi_s)} - (\phi_{s1} - \phi_{s0})\right] \tag{4.2}$$

where P_s and ρ_s are, respectively, the pressure in the solid medium and the density of the solid particles. ϕ_{s0} is the initial value of the particle volume fraction for a packed particle bed ($\phi_{s0} = \rho_{bulk}/\rho_{s0}$), and ϕ_{s1} is the maximum particle volume fraction attained during compaction. The dependence of particle configuration pressure on solid volume fraction ϕ_s describes how the inter-particle force within the particle bed evolves as a function of ϕ_s. The steepness of this dependence is given by the coefficient a. Values for the parameters used in the above equations (Eqs. 4.1 and 4.2) for glass and steel particles are given in Table 4.1. The values fall in the range of experimental values, i.e., #13 Ballotini glass impact beads (particle size of 68 µm ± 22, and $\rho_{bulk} = 1500 \pm 80$ kg.m^{-3}) and S110 hardened steel shot (particle size of 340 µm ± 160, and $\rho_{bulk} = 4460 \pm 330$ kg.m^{-3}), for the glass and steel beads, respectively. The particles are also considered to be spherical and maintain the same initial size throughout the explosive dispersal event.

Water is modelled using a Tait equation of state, i.e. (Eq. (4.3)):

$$P_l = K'\left[\left(\frac{\rho_l}{\rho_{l0}}\right)^{n'} - 1\right] \tag{4.3}$$

Table 4.1 Parameters used in the numerical simulations for glass, steel particles, and water. The bulk density (ρ_{bulk}) corresponds to the density of the powders including interstitial voids.

Material	Glass	Steel	Water
Particle size (μm)	50	300	100
ρ_{bulk} (kg.m^{-3})	1440	4873.2	N.A.
ρ_{s0} (kg.m^{-3})	2500	7860	N.A.
C_s^2 (m/s)	2300	4610	N.A.
S	1.59	1.275	N.A.
ϕ_{s0}	0.576	0.620	N.A.
ϕ_{s1}	0.99	1	N.A.
a (Pa)	6.5×10^8	1.67×10^{11}	N.A.
ρ_{l0} (kg.m^{-3})	N.A.	N.A.	1000
n'	N.A.	N.A.	7.15
K' (Pa)	N.A.	N.A.	3.047×10^8

where, P_l, ρ_l being, respectively, the pressure in the liquid medium and the density of the liquid droplets. ρ_{l0} corresponds to the initial density of water. The water is assumed to fracture upon pressure release into droplets with an imposed size of 100 μm, which is the order of magnitude of droplet sizes observed in past work [11]. The values of the coefficients in Eq. (4.3) are reported in Table 4.1, in MKS units.

4.3 Results and discussion

In this section, numerical results are presented for the three different materials considered. Glass particles, which tend to form prominent particle jets when explosively dispersed, were chosen to compare with the extensive experimental data available. Steel particles, which have a higher density and toughness than glass particles, tend *not* to form jets when dispersed, but to expand in a diffuse layer. Since the formation of jets is not considered in the present calculations, the effect of jetting on the comparison between the computations and experimental results can be examined. Water was chosen for a liquid dispersal case due to the availability of experimental data. First, peak blast wave overpressures and impulses for a unmitigated C-4 charge determined numerically are compared with tabulated experimental values (section 4.3.1). Then, mitigation efficiencies, i.e., the reduction in blast overpressure compared to a bare charge, are compared with experimental data for the three different materials (section 4.3.2). A systematic study of the influence of initial bed properties on blast peak overpressure and impulse is presented in section 4.3.3. Finally, the particle-blast interaction is explored through examination of blast overpressure profiles (section 4.3.4), time of arrival (section 4.3.5), momentum fluxes, and spatially integrated momenta of both particles and the gas (sections 4.3.6 and 4.3.7).

4.3.1 Bare C-4 charge

Prior to investigating the influence of different types of materials on the blast wave, it is of interest to compare the EDEN numerical predictions for a bare C-4 charge with the tabulated database from Figure 6-4 of Kinney and Graham [16]. This figure shows peak overpressures at 1 atm and 15°C computed for a spherical charge of conventional chemical explosive with energy release equivalent to one kilogram of TNT, as a baseline test. Fig. 4.1 shows the comparison between the calculated and referenced normalized peak overpressure $\Delta P_{max}/P_0$, with $\Delta P_{max} = P_{max} - P_0$, P_{max} being the maximum local pressure (Fig. 4.1a), and scaled impulses I_s^+ (Fig. 4.1b). These parameters are plotted as a function of scaled distance Z defined as follows (Eq. (4.4)):

$$Z = \frac{R}{W^{1/3}} \tag{4.4}$$

where:

Z = scaled distance (m/kg$^{1/3}$)
R = dimensional distance (m)
W = (charge mass in equivalent TNT) = mass of C-4 (kg) $\times$ ε (effectiveness factor)

with the same effectiveness factor $\varepsilon = 1.39$ as for experimental data [2] for a C-4 charge mass of 100 g.

The scaled blast impulse and arrival time (analyzed in section 4.3.5) are defined, respectively, by (Eqs. 4.5 and 4.6):

$$I_s^+ = \frac{I^+}{W^{1/3}} \tag{4.5}$$

and,

$$t_s = \frac{t_a}{W^{1/3}} \tag{4.6}$$

where:

I_s^+ = blast wave scaled impulse (bar.ms/kg$^{1/3}$)
I^+ = blast wave positive phase impulse (bar.ms)
t_s = scaled blast arrival time (ms/kg$^{1/3}$)
t_a = actual blast arrival time (ms)
W is the charge mass in equivalent TNT defined previously

with $\varepsilon = 1.15$ for impulses and $\varepsilon = 1.39$ for arrival times, in conformity with [2]. Overall, good agreement for the peak overpressures is found, with a maximal overpressure discrepancy of 30 % in the region 1 m/kg$^{1/3} < Z < 3$ m/kg$^{1/3}$ where the computed values fall below the tabulated values. Scaling laws have been also verified with different charge masses (75 g, 28 g and 1 kg). Changing the mass of C4 will just shift the curve to the left (higher explosive mass) or to

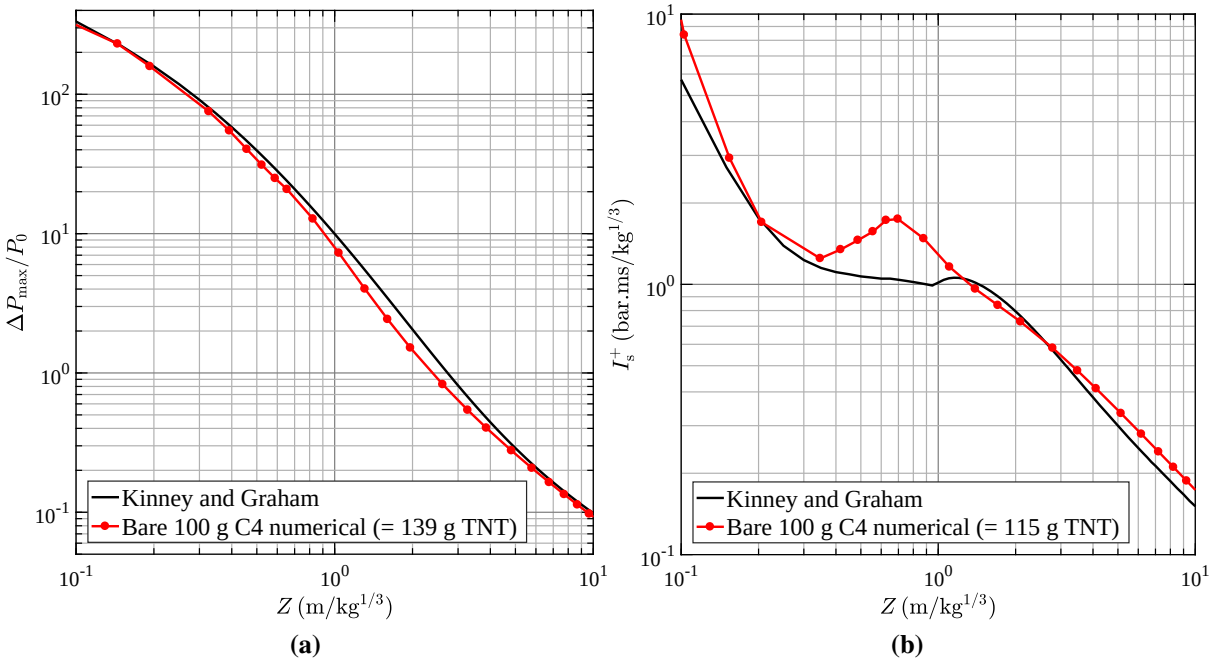

Fig. 4.1 Comparison between Kinney and Graham [16] database (dark full lines) for a conventional chemical explosive charge with energy release equivalent to 1 kg of TNT and calculated peak overpressures **(a)** and impulses **(b)** as a function of scaled distance Z, for a 100 g bare C-4 charge shown as red full lines with dots (equivalent to 139 g of TNT for peak overpressures and 115 g of TNT for positive-phase impulses).

the right (lower explosive mass). In comparison, calculated positive-phase impulses fall above the tabulated experimental values in the range with a maximal discrepancy of 68 % at $Z = 0.7$ m/kg$^{1/3}$, but slightly below in the region 1.5 m/kg$^{1/3} < Z < 2$ m/kg$^{1/3}$. Given the discrepancies, a relative study will be carried out in the paper. For the remainder of the presentation of results, the numerically calculated peak overpressures and impulses for the bare C-4 charge will define the baseline case.

4.3.2 Dispersal of granular media and liquids

In this section, computed peak overpressures and impulses generated in the air during explosive dispersal of either granular powders or liquids are reported and compared with the experimental data (reported in [2]). The calculated baseline case for a bare, or unmitigated, C-4 charge is also shown to quantify the attenuation of the pressure and impulse due to the presence of the inert material. In Figs. 4.2-4.4, blast properties for explosive charges surrounded by three different materials are investigated with various material to charge mass ratios M/C, including steel ($M/C = 55.06$), glass ($M/C = 6.50$ and $M/C = 46.85$) and water ($M/C = 32.21$). Properties of the materials (density, bulk density, particle size) and coefficients used in the model have been reported earlier in Table 4.1. The computed peak blast overpressures (shown as full lines with dots in the figures) are compared with experimental results for the overpressure obtained in two

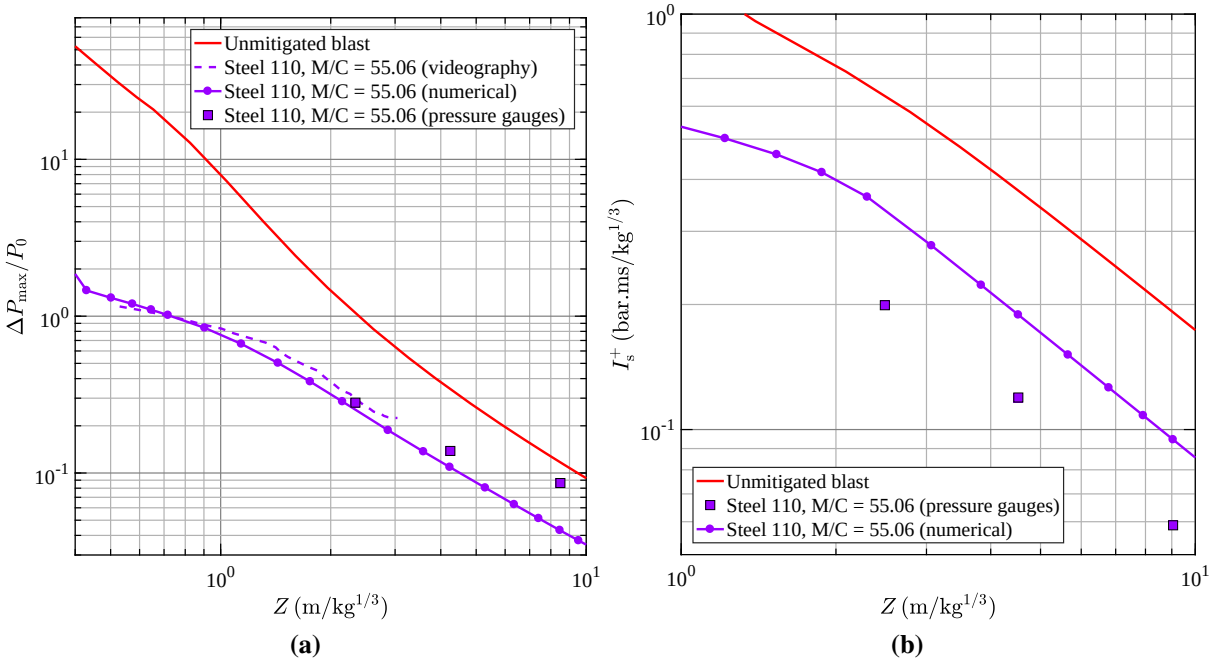

Fig. 4.2 Comparison between numerical calculations (full purple lines with dots) of peak overpressure **(a)** and impulse **(b)** for the explosive dispersal of 300 µm steel particles ($M/C =$ 55.06) with experimental data extracted either by videographic tracking of blast wave (dashed purple line) or direct pressure gauge measurements (square purple symbols). For comparison, the numerical calculations for a baseline, bare C-4 charge (solid red lines) are also shown.

different ways: i) tracking the blast wave trajectory to estimate the shock Mach number and hence inferring the shock overpressure with the Rankine-Hugoniot relation (dashed lines), or ii) by direct measurement of blast overpressure with side-on piezoelectric pressure gauges (square and diamond symbols) [2].

The calculated peak overpressure values generally agree with the experimental values within the error associated with the experimental results over the range of scaled distance simulated and mass ratios (see [2] for a discussion of the scatter in the experimental results and errors associated with the different measurement techniques). The maximal discrepancies in terms of peak pressure are 6 % for steel ($M/C = 55.06$, at $Z = 1.4$ m/kg$^{1/3}$) and 9 % for glass ($M/C =$ 46.85, at $Z = 1.6$ m/kg$^{1/3}$). Maximal discrepancies for water ($M/C = 32.21$, at $Z = 0.6$ m/kg$^{1/3}$) and glass ($M/C = 6.5$, at $Z = 0.7$ m/kg$^{1/3}$) are higher than the experimental estimated errors, i.e., respectively, 35 % and 55 %. Nevertheless, overall, the peak overpressure decays are reproduced by the numerical calculations for each material. Factors that are not accounted for in the model, which may contribute to the differences between the computed and experimental data, include the energy loss during deformation and fracture of the particles during particle compaction, and the relative velocity induced fragmentation and evaporation of water droplets.

With respect to the computed overpressure results for water, note the presence of a kink in the overpressure curve at a scaled distance $Z = 0.5$ m/kg$^{1/3}$ (a similar bend appears for the other materials at lower Z values). The physical mechanism responsible for this feature in

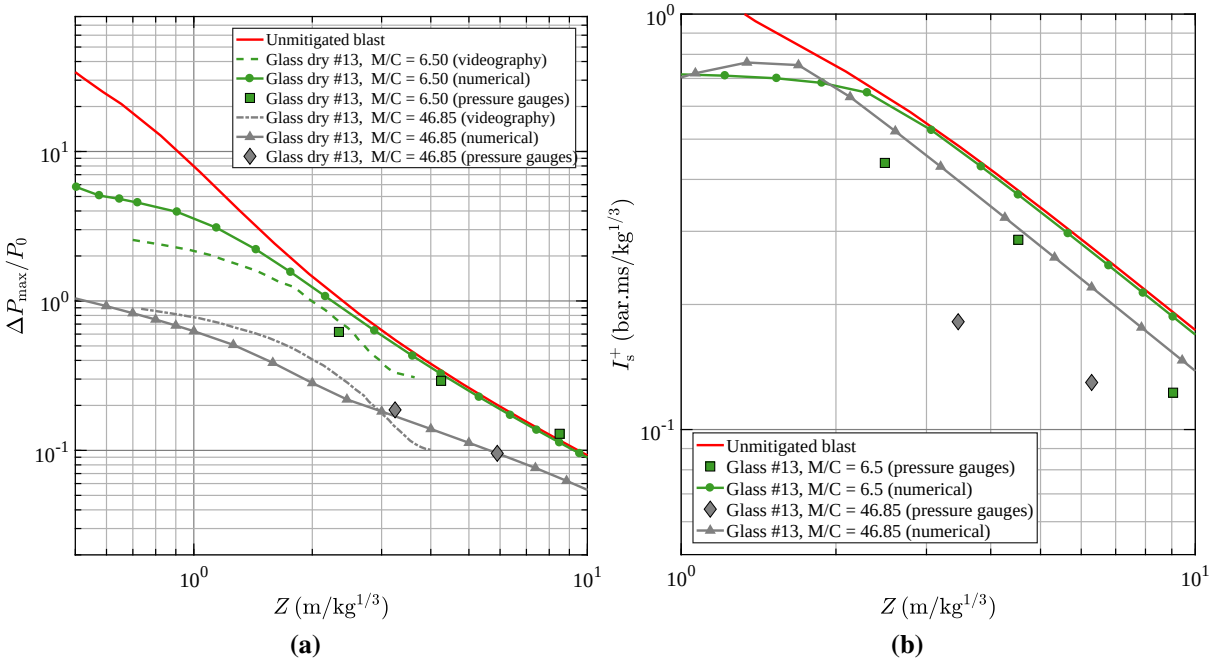

Fig. 4.3 Comparison between numerical calculations of peak overpressure **(a)** and impulse **(b)** with experimental data extracted either by videography or pressure gauges for the explosive dispersal of 50 µm glass particles with mass ratios $M/C = 6.5$ and $M/C = 46.85$.

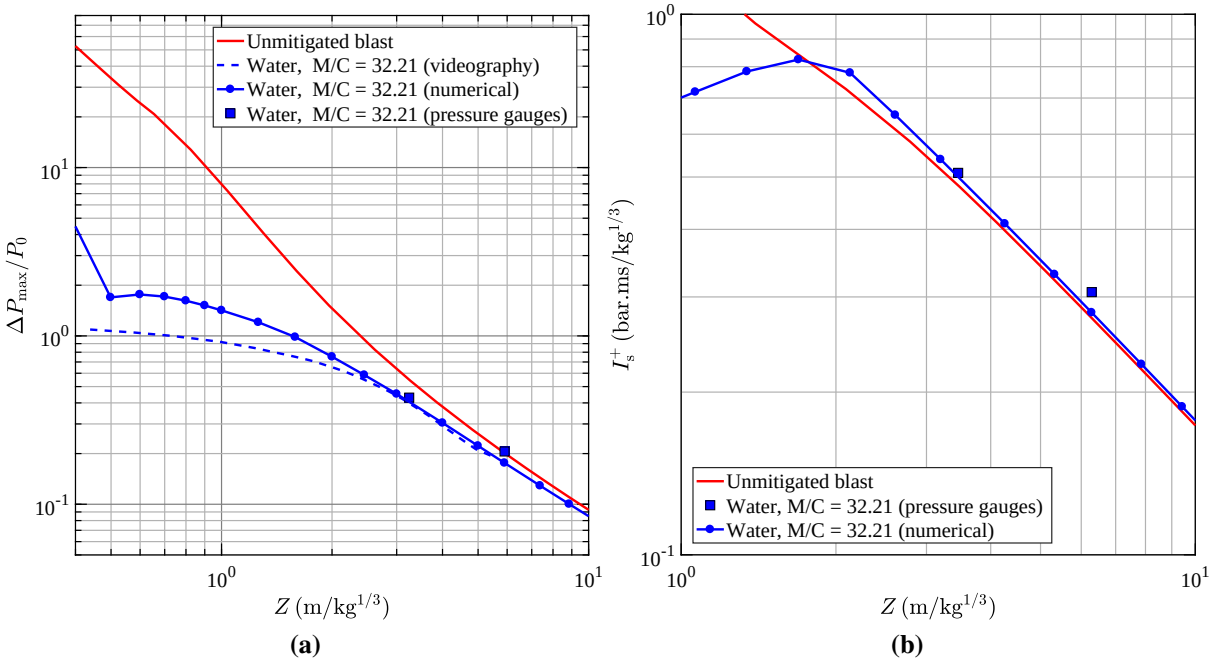

Fig. 4.4 Comparison between numerical calculations of peak overpressure **(a)** and impulse **(b)** with experimental data extracted either by videography or pressure gauges for the explosive dispersal of water with $M/C = 32.21$ (droplet sizes of 100 µm).

the overpressure curve will be discussed later (section 4.3.3). The presence of such a kink in the experimental data has not been observed, although experimental measurements of blast overpressure in the very near field, e.g., $Z < 0.5$ m/kg$^{1/3}$, is challenging since the blast wave is obscured by the detonation products at early times and pressure gauges are subject to particle impacts very close to the charge, which perturbs the blast pressure signal.

The calculated scaled positive-phase air impulse is also shown in comparison with experimental data from pressure gauges in Figs. 4.2-4.4. In general, the calculated air impulses exceed significantly the experimental measured values for particle dispersal (51 % - 61 % for steel, 36 % - 52 % for glass $M/C = 6.5$, 62 % - 105 % for glass $M/C = 46.85$), whereas they closely match the experimental results for water (maximum error of 8 %). The cause of the overestimate of the positive-phase blast impulse in comparison with the experimental data is not known, but the energy loss due to particle deformation and fracture, as well as the influence of particle clustering and jetting on the particle drag and energy transfer from the particles to the flow may contribute to this discrepancy. In the case of the explosive dispersal of water, it is also interesting to note that despite surrounding the explosive charge with a mass of water 30 times the mass of the explosive, the positive-phase impulse values are close to that of a bare C-4 charge in the far field ($Z > 4$ m/kg$^{1/3}$).

4.3.3 Parametric study

To gain more insight into the decay of the blast wave overpressure very near the charge, including the presence of the kink in Fig. 4.4, calculated results will be presented over a larger range of scaled distance Z, up to the location of the initial material layer. The effect of initial material parameters on the blast peak overpressure and positive-phase impulse, including the mass ratio M/C, initial particle, size and initial solid volume fraction is also presented in the following sections.

Effect of mitigant to charge mass ratio M/C

Three values of M/C, 1, 10 and 100 were chosen for a fixed mass of C-4 (C = 100 g), for steel and glass particles. For each value of M/C, the initial volume fraction of the powder is fixed at a nominal value of 0.6 with a particle size of 50 µm. As the solid volume fraction is fixed, for increasing masses of powder, the thickness of the powder layer increases and is indicated by dashed lines in Figs. 4.5 and 4.6. The thickness of the granular layer depends on the density of the material, since a denser material occupies less volume for the same mass of powder and particles are all assumed to be spherical.

For scaled distances greater than $Z = 0.4$ m/kg$^{1/3}$, the attenuation of the peak overpressure for both glass and steel increases with increasing M/C as expected with an attenuation of more than one order of magnitude for $M/C = 100$. For $Z < 0.4$ m/kg$^{1/3}$, this observation does not hold since, depending on the M/C ratio, the shock may still be propagating within the granular

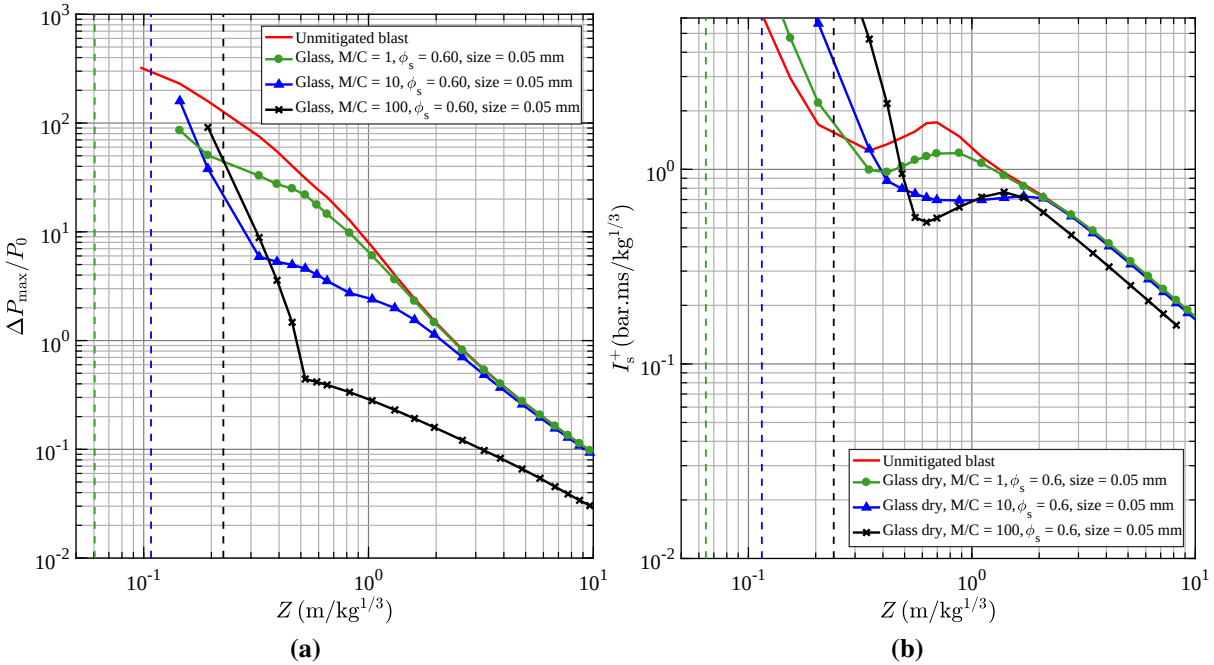

Fig. 4.5 Peak overpressures **(a)** and impulses **(b)** as a function of scaled distance for explosive dispersal of glass particles with mass ratios of $M/C = 1$, 10 and 100 ($\phi_s = 0.6$, particle size = 50 µm).

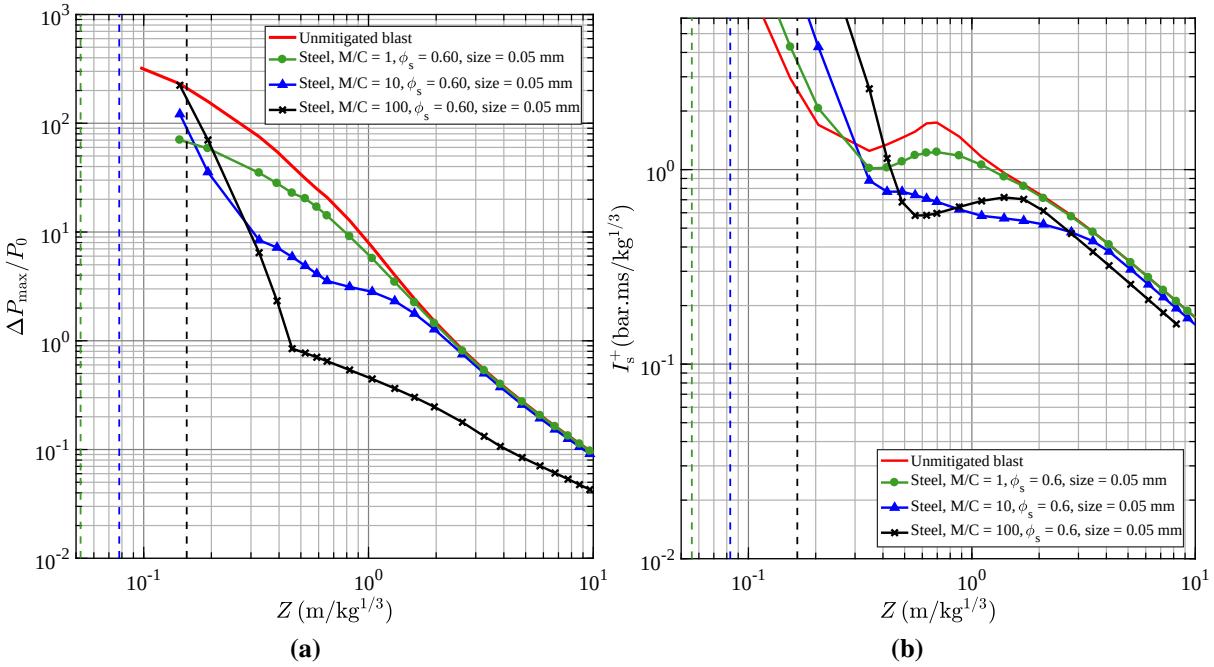

Fig. 4.6 Peak overpressures **(a)** and impulses **(b)** as a function of scaled distance for explosive dispersal of steel particles with mass ratios of $M/C = 1$, 10 and 100 ($\phi_s = 0.6$, particle size = 50 µm).

layer, and the particle acceleration phase is ongoing. At $Z = 1$ m/kg$^{1/3}$, for glass particles, the peak overpressure attenuation relative to that of a bare C4 charge is approximately 19 %, 69 %, 96 % for, respectively, $M/C = 1$, 10, 100. For steel particles, the attenuation is less than expected from the experiments [2] for $M/C = 10$, 100 with values of 64 % and 94 %. However, for $M/C = 1$, the attenuation is slightly higher with a value of 25 % (instead of 19 % for glass particles). Nevertheless, discrepancies between the peak blast overpressure mitigated by glass and steel particles at a fixed M/C and Z appear less compared to experimental data. For example, at $M/C = 100$ and $Z = 0.8$ m/kg$^{1/3}$, values of numerical peak overpressure are, respectively, 0.3 and 0.45 (difference of 0.15) for glass and steel, compared to 0.37 and 0.64 (difference of 0.27) estimated from Fig. 15 of [2]. Though, this analysis is cautionary given the experimental error bars.

For all materials, for scaled distances around $Z = 0.3$ m/kg$^{1/3}$ or $Z = 0.5$ m/kg$^{1/3}$, depending on the mass ratio, a kink appears in the peak overpressure curves, which is most pronounced for the largest M/C values. The kink separates a region of rapid pressure decay, for small scaled distances, from a region where the pressure decay is reduced and the peak overpressures approach values of an unmitigated charge. During the acceleration phase of the particles at early times, energy is extracted from the flow and the blast pressure drops rapidly. However, at some point the particles will reach their maximum velocity while the ambient flow velocity continues to decrease rapidly as the blast wave and flow expands spherically outwards. Depending on the inertia of the particles, there will be a period of time where the particles are moving faster than the ambient gas and will generate pressure perturbations to the local flow, or bow shocks if the relative flow velocity is supersonic. During this time the pressure disturbances will travel upstream and influence the pressure behind the blast wave, reducing the rate of blast pressure decay. The kink is also the location where the blast peak overpressure is attenuated the most. Due to the pressure recovery, the peak blast overpressure recovers to that of a bare charge, in the far field, after $Z = 3$ m/kg$^{1/3}$, for $M/C = 1$ and 10. Note that particle deformation, which accounts for irreversible energy losses in the compaction process, is not taken into account in the model and explains the pressure recovery to that of a bare charge for these mass ratios. Increasing the mass of particles, up to a mass ratio of 100, augments the energy absorption from the flow to the particle and delays the time of pressure recovery. Hence at this distance, the mitigated peak overpressure for $M/C = 100$ do not recovers totally the pressure of the unmitigated case, but will recovers further away from the charge. At $Z = 3$ m/kg$^{1/3}$, the peak blast overpressure attenuation (relative to that of a bare charge) for glass particles ($M/C = 100$) drops to 83 % (c.f. 75 % for steel particles).

The rate of decay of the blast overpressure is primarily dependent on the mass ratio M/C. Comparing the results for glass and steel particles at a specific mass ratio indicates that the dependence of blast overpressure on material properties is of secondary order, with more attenuation for glass particles than steel particles in the near field. Presumably the lower inertia and higher heat capacity of the glass particles contribute to this difference. However, at the lowest

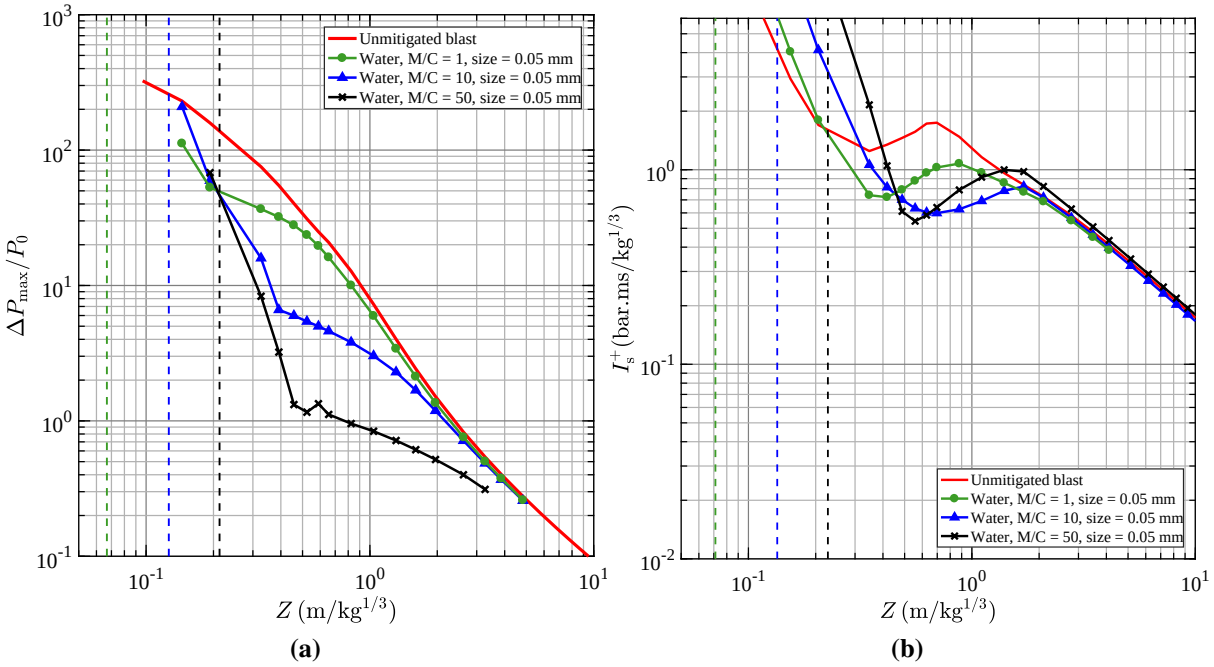

Fig. 4.7 Peak overpressures **(a)** and impulses **(b)** as a function of scaled distance for explosive dispersal of water with mass ratios of $M/C = 1$, 10 and 50 (droplet size = 50 µm).

mass ratio ($M/C = 1$), in the mid-to-far field ($Z > 1$ m/kg$^{1/3}$), steel particles can potentially reduce slightly more the blast peak overpressure. This depends on the motion of the particles, on the pressure disturbances created and how the particles are subjected to drag.

The same analysis is carried out with water but $M/C = 100$ has been replaced by $M/C = 50$. Droplet sizes are assumed to be 50 µm to compare with solid particles but no significant differences of mitigation effectiveness are observed between the liquid and the powders (Fig. 4.7). At $Z = 1$ m/kg$^{1/3}$, the peak blast overpressure attenuation is slightly less than for steel particles with, respectively, 18 %, 58 % and 88 % for $M/C = 1$, 10, 100. This is not consistent with experimental results which show lower mitigation rates for liquids and liquid/particle slurries (on average, solid powders outperform liquids by almost a factor of two at reducing the peak blast overpressure [2]). However, fragmentation of the water droplets after they are formed due to stripping at the high particle Weber numbers and subsequent evaporation of the fine droplets are not accounted for in the computations, which will influence the predictions for the water case at later times.

The behaviour of the scaled positive-phase impulse shown in the right plots of Figs. 4.5-4.7 also indicates that particle material properties have minimal influence on the impulse. The maximal impulse attenuation, for all the materials, takes place in the near field ($Z < 1$ m/kg$^{1/3}$), in the same region with the kink in the peak overpressure decay mentioned earlier. In this region, the positive-phase impulse mitigation, relative to that of a bare charge, for M/C going, respectively, from 1 to 100, are 32-69 % (glass), 35-66 % (steel), and 44-66 % (water). After $Z = 2$ m/kg$^{1/3}$, impulses for water at each M/C value are superimposed with the curve of an unmitigated charge

(at $M/C = 100$, water impulses are even higher), as observed experimentally [2]. For glass particles, in the same region, a similar behaviour is observed for $M/C = 1$ and 10. In the case of the explosive dispersal of steel particles, virtually no differences are observed with an unmitigated charge at $M/C = 1$. However, at $M/C = 10$, the impulse recovery takes place later than for glass particles, at around $Z = 4$ m/kg$^{1/3}$. At the same distance, at $M/C = 100$, values of impulses are still reduced by around 23 % for both types of solid particles compared to a bare charge. Differences in attenuation and recovery of impulses between the two types of solid particles are attributed to differences in heat capacity and density. Conversely, in the near field ($Z < 1$ m/kg$^{1/3}$), the vaporization is likely to contribute to the differences in mitigation performance. Specifically, the liquid may attenuate the blast impulse more, as compared to solid particles at $M/C = 1$. In the far field ($Z > 2$ m/kg$^{1/3}$), it is hypothesized that the motion of the vapour produced behind the blast front, during the explosive dispersal of water, will contribute to the total impulse recovery.

Effect of particle size

The influence of particle size on the decay of the peak blast wave overpressure is shown for glass (Fig. 4.8) and for steel (Fig. 4.9) for values of $M/C = 10$ and $\phi_s = 0.6$. In this case, the thickness of the granular layer is constant for the three curves. For glass particles, the particle size has little impact on the peak overpressure decay whereas for steel particles, the effect of particle size is more significant. In the very near field ($Z = 0.4$ m/kg$^{1/3}$), the shock attenuation is weakest for the largest steel particles (57 % for 5 mm particles), compared to the smallest particles (86 % for 0.05 mm particles). On the contrary, at the same distance, the differences of peak overpressure attenuation for glass particles are less, i.e, respectively, 85 % (largest particles) and 90 % (smallest particles). The poor mitigation performance for the largest particles is presumably a result of the large particle inertia and long time for the particles to accommodate to changes in the local flow velocity. Nevertheless, in the far field ($Z > 2$ m/kg$^{1/3}$), this trend is reversed and the smallest particles attenuate the peak overpressure the least. In the case of water (Fig. 4.10), differences of mitigation effectiveness are only evident in the mid-to-far field ($Z > 1$ m/kg$^{1/3}$). The mitigation performance varies from 15 % (smallest droplets, 0.5 mm) to 59 % (biggest droplets, 5 mm), at $Z = 2$ m/kg$^{1/3}$. Although the results in this regime are uncertain due to a lack of a droplet fragmentation model as noted earlier.

Similar trends are observed in Figs. 4.5-4.7 for the positive-phase impulses, except that discrepancies in mitigation are more apparent in the far field ($Z > 2$ m/kg$^{1/3}$) for glass particles, contrary to the near field ($Z < 1$ m/kg$^{1/3}$) for steel particles. Indeed, the impulse attenuation at $Z = 0.4$ m/kg$^{1/3}$ for glass particles is only between 25 % (5 mm particles) and 35 % (0.05 mm particles). In comparison, the attenuation for steel particles is between 0 % - 43 %, respectively, whereas at $Z = 4$ m/kg$^{1/3}$, the impulse mitigation becomes 47 % (c.f. 29 % for steel) for the largest particles (the blast impulse is effectively not attenuated by the smallest particles). The

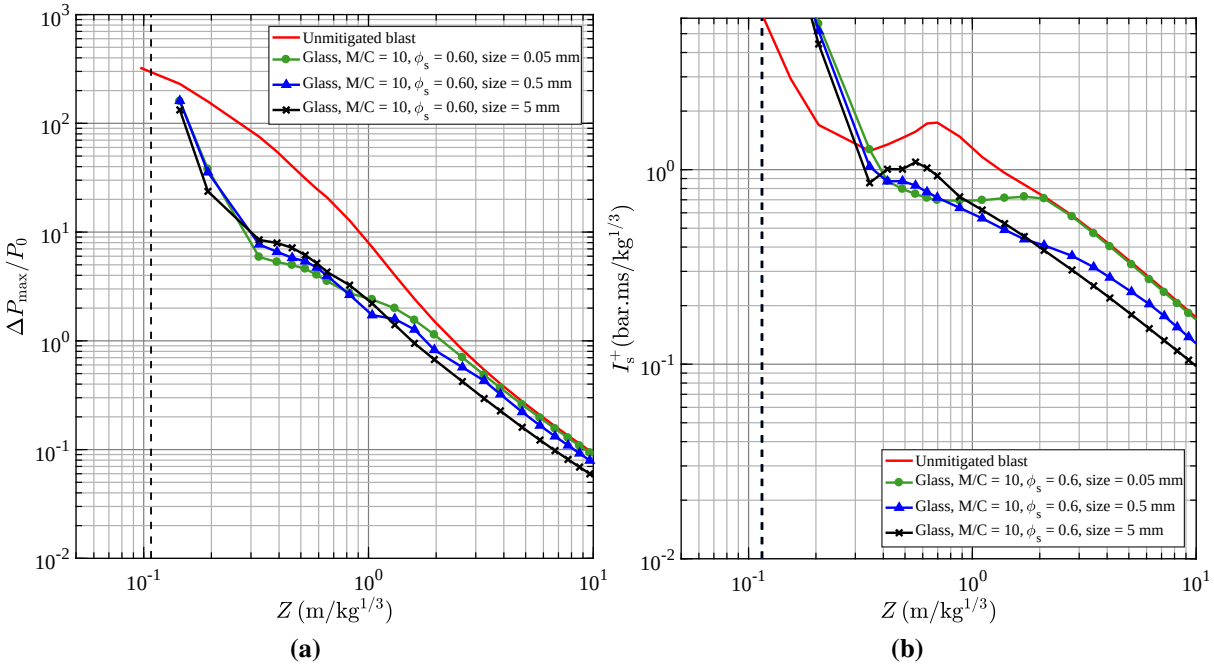

Fig. 4.8 Peak overpressures **(a)** and impulses **(b)** as a function of scaled distance for explosive dispersal of glass particles with particle sizes of 50 µm, 0.5 mm and 5 mm ($M/C = 10$, $\phi_s = 0.6$).

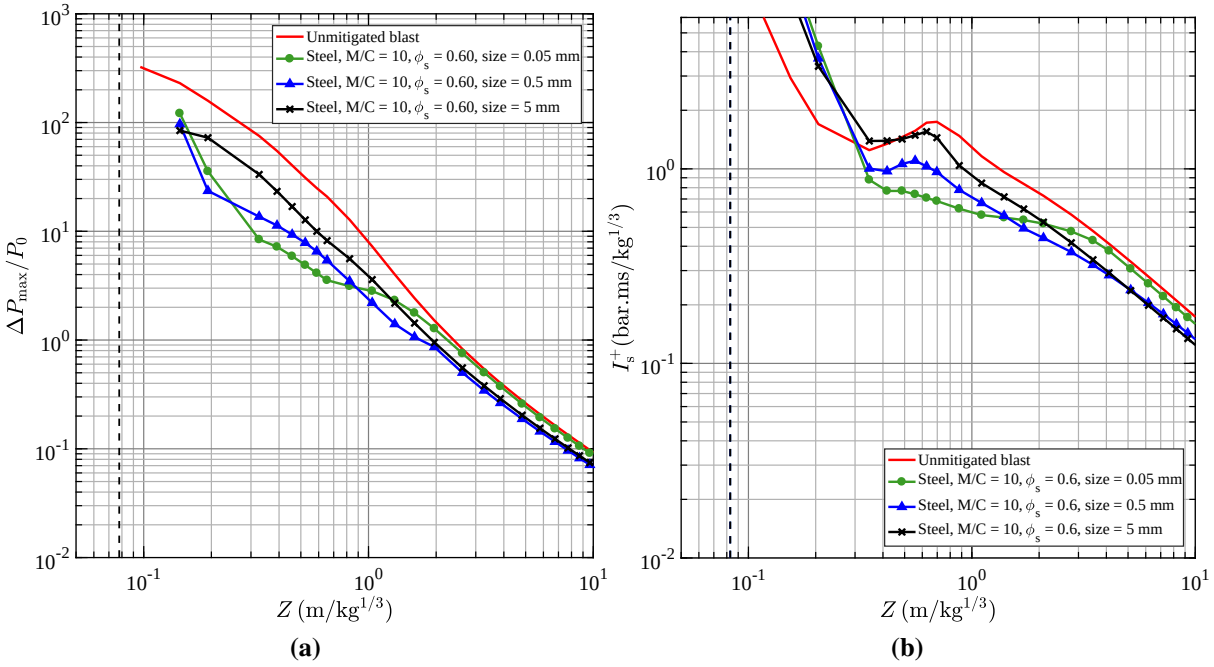

Fig. 4.9 Peak overpressures **(a)** and impulses **(b)**as a function of scaled distance for explosive dispersal of steel particles with particle sizes of 50 µm, 0.5 mm and 5 mm ($M/C = 10$, $\phi_s = 0.6$).

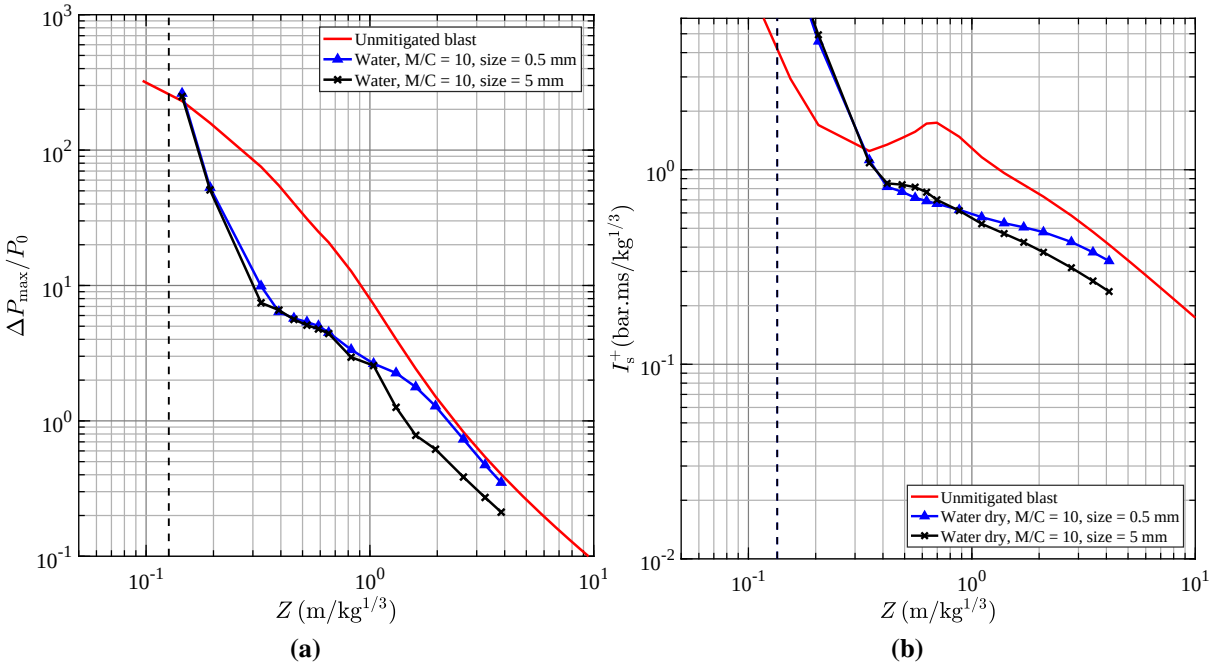

Fig. 4.10 Peak overpressures **(a)** and impulses **(b)**as a function of scaled distance for explosive dispersal of water with droplet sizes of 0.5 mm and 5 mm ($M/C = 10$).

effect of droplet size on impulse in the case of the explosive dispersal of water (Fig. 4.10) is more predominant in the same region as for peak overpressures, i.e., in the mid-to-far field, with an attenuation between 34 % (0.5 mm droplets) and 48 % (5 mm droplets) at $Z = 2$ m/kg$^{1/3}$.

In general, since smaller particles accommodate to the local flow velocity more rapidly than larger particles, energy is extracted more rapidly from the flow during particle acceleration and conversely given back to the flow more rapidly during particle deceleration. Hence, smaller particles tend to lead to more rapid decay of the blast pressure in the near field and greater pressure recovery in the far field. Since the size distribution of particles generated during explosive particle dispersal, in general, differs from the initial particle size due to particle compaction, deformation, and sintering effects, it is difficult to predict the effect of particle size without also addressing the details of the particle bed compaction and fracture processes. In any case, the effect of particle size appears to be a secondary effect compared with the effect of varying the mass ratio M/C.

Effect of initial solid volume fraction ϕ_s

The influence of the initial solid volume fraction for a constant mass ratio of $M/C = 10$ and particle size of 50 µm, on blast overpressure and impulse for glass particles is shown in Fig. 4.11. Three values of volume fraction, i.e., 0.50, 0.60, and 0.85, are investigated. Note that in this case the thickness of the granular powder layer decreases with increasing solid volume fraction. The dependence of peak overpressure on initial solid volume fraction is weak, with the highest solid fraction leading to slightly less blast pressure attenuation, as would be expected since with

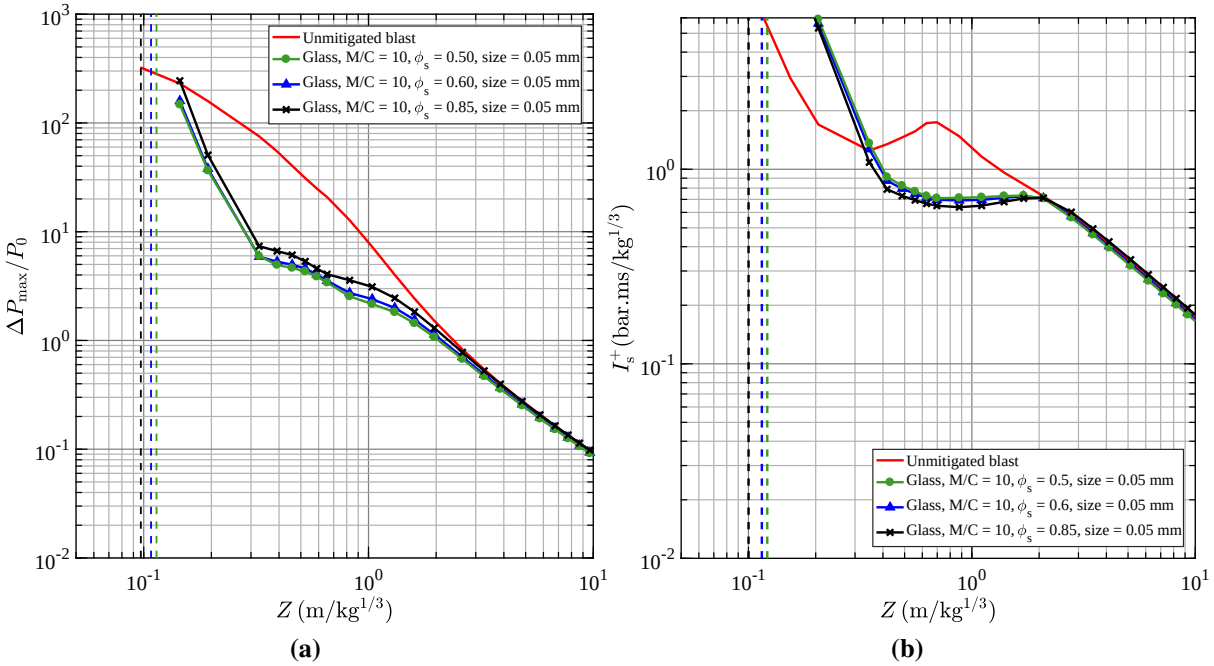

Fig. 4.11 Peak overpressures **(a)** and impulses **(b)** as a function of scaled distance for explosive dispersal of glass particles solid mass fractions of $\phi_s = 0.5$, 0.6 and 0.85 ($M/C = 10$, particle size = 50 µm).

a denser layer with a lower void fraction, less energy dissipation occurs upon compaction of the bed. The maximum discrepancy appears at $Z = 1$ m/kg$^{1/3}$ and the blast peak overpressure attenuation, relative to that of a bare charge, is between 57 % and 70 %. Conversely, the blast impulse attenuation at $Z = 0.7$ m/kg$^{1/3}$ varies from 59 % to 63 %. In the far field ($Z > 2$ m/kg$^{1/3}$), for both peak overpressure and impulse, all curves are superimposed on top of the unmitigated blast case. No significant changes were observed comparing the plots for glass and steel particles, and hence the results for steel particles are not shown.

4.3.4 Overpressure profiles

To elucidate the particle-blast interaction in more detail, it is instructive to compute pressure-time histories. Fig. 4.12 presents blast pressure histories for glass particles ($M/C = 10$, ϕ_s = 0.6, particle size 50 µm) at four different scaled distances as well as the results for an unmitigated charge. Solid volume fractions are also plotted to correlate the presence of the particles with the blast wave structure. At every distance, the arrival of the blast wave from a mitigated charge is delayed compared to an unmitigated blast as the blast travels at a lower speed. Moreover, by comparing mitigated overpressures with the baseline of a pure C-4 charge (dashed lines), mitigation efficiencies appear more substantial in the near-field.

With the addition of particles, the blast overpressure is reduced in the near field and hence the time for the blast wave to arrive at a given location is increased. At the farthest location ($Z = 3.27$ m/kg$^{1/3}$), the peak blast overpressure for the mitigated charge is essentially the same

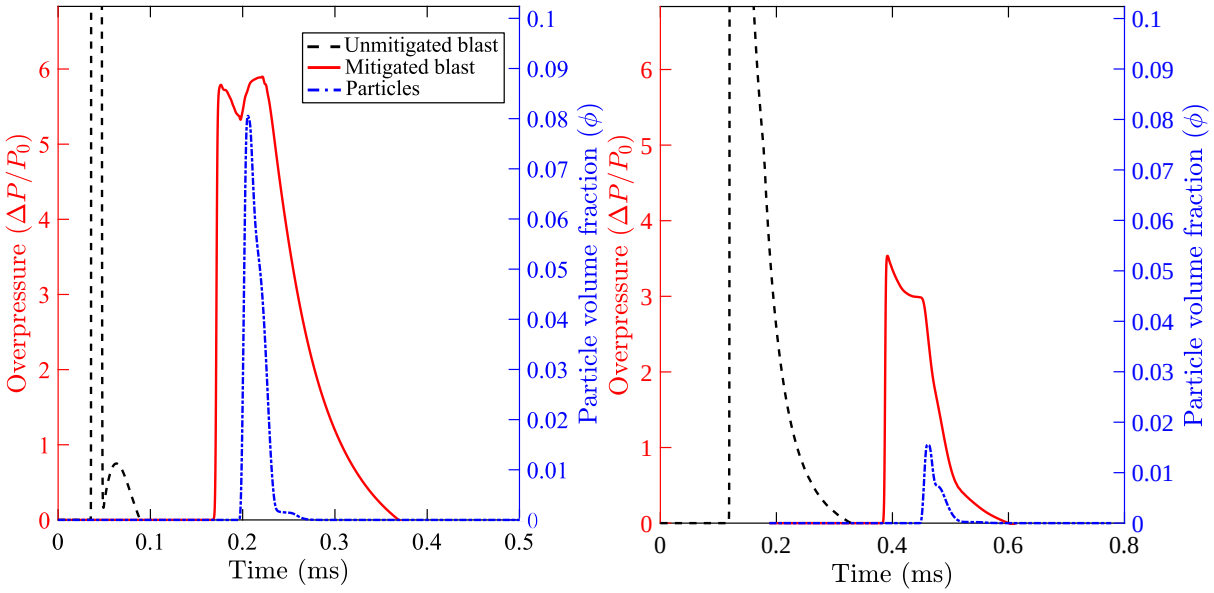

(a) $Z = 0.33$ m/kg$^{1/3}$ **(b)** $Z = 0.65$ m/kg$^{1/3}$

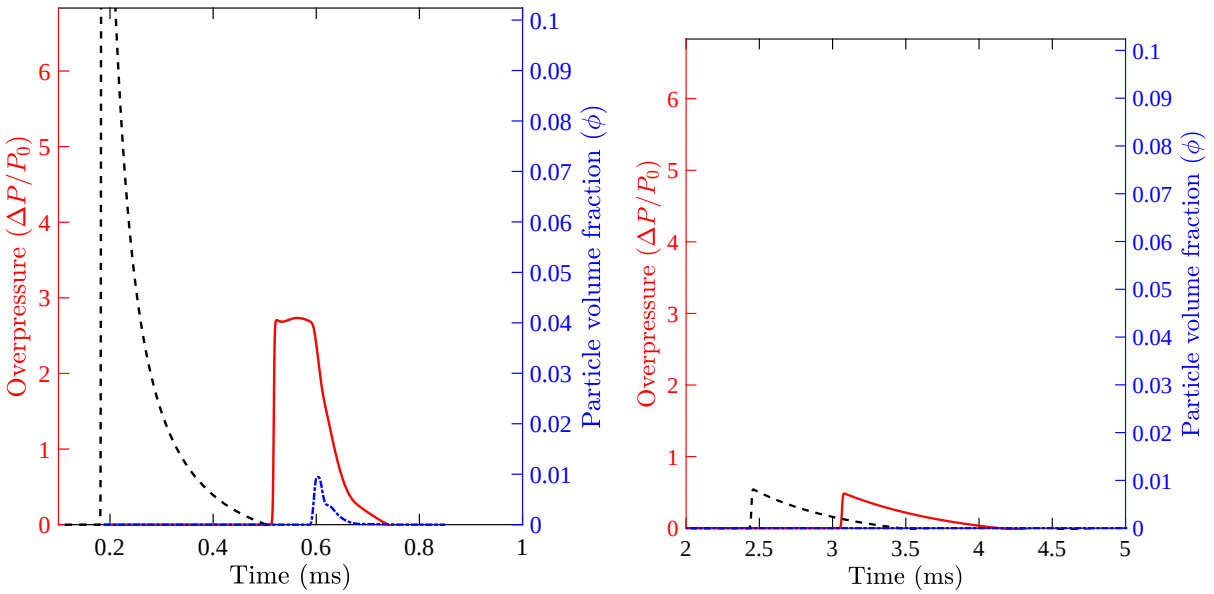

(c) $Z = 0.82$ m/kg$^{1/3}$ **(d)** $Z = 3.27$ m/kg$^{1/3}$

Fig. 4.12 Comparison of the blast pressure profile for a bare C-4 charge (dashed black lines) with that of the same charge surrounded with a layer of 50 µm glass particles ($M/C = 10$, $\phi_s = 0.6$) at scaled distances of **(a)** $Z = 0.33$ m/kg$^{1/3}$, **(b)** $Z = 0.65$ m/kg$^{1/3}$, **(c)** $Z = 0.82$ m/kg$^{1/3}$ and **(d)** $Z = 3.27$ m/kg$^{1/3}$ (red curves). The particle volume fraction is also shown (dotted blue curves) and appear to influence the blast overpressure (figure courtesy of [17]).

as for the bare C-4 charge, although the arrival time is longer. For the intermediate distances, the motion of the particles clearly has a strong influence on the shape of the pressure histories, particularly at the smallest distance where the particle number density is still relatively high and the pressure trace exhibits a double peak structure at a time that is coincident with the arrival of the particles. As the particle density falls with distance, the perturbation to the blast wave trace decays until the blast wave trace is essentially the same as that of the bare C-4 charge at a distance of $Z = 3.27$ m/kg$^{1/3}$. Notably, a comparison between Figs. 4.5 and 4.12, indicates that the particles influence the peak blast overpressure even if the particles do not follow closely behind the blast front. Indeed, from Fig. 4.12, the arrival time of the particles is delayed compared to the arrival time of the blast front for all the distances, although the peak overpressures are located after the kinks in Fig. 4.5 (phase of pressure recovery). This evidence supports the hypothesis of the creation of pressure disturbances by the particles that travel upstream in the disturbed flow which ultimately merge with the blast front [2]. At the third distance ($Z = 0.82$ m/kg$^{1/3}$), the blast overpressure exhibits a plateau. This plateau appears when the pressure disturbances created by the particles combined with the overpressure behind the shock are of the order of the peak overpressure value. This phenomenon is possible since the pressure disturbances decay more slowly than the peak overpressure due to the propagation in a hot, shocked medium, contrary to the blast front, which propagates in air at ambient temperature.

4.3.5 Time-distance trajectories of particles and blast wave

Bare C-4 charge

The blast trajectory, or scaled time of arrival plotted as a function of normalized distance, for the baseline case of a 100 g bare C-4 charge is shown in Fig. 4.13, superimposed with the logarithm of the air overpressure shown as a greyscale map. The thickness of the high-pressure region between the leading blast wave front and trailing edge of the blast wave structure increases with time as the trailing edge slows down and eventually begins to implode towards the centre at a scaled distance of about $Z = 0.59$ m/kg$^{1/3}$. This imploding wave eventually reflects at the origin generating a secondary outgoing shock, although the secondary shock is not visible due to the overpressure scaling chosen. A faint curved line within the high-pressure region represents the contact surface which reaches a maximum scaled radius of a little less than $Z = 0.8$ m/kg$^{1/3}$. Further details of the blast wave structure for this baseline case can be obtained by consulting the classical work of Brode [18].

Charges with glass particles

Fig. 4.14 shows a similar plot as in Fig. 4.13, except for the case of a 100 g C-4 charge surrounded with glass particles with $M/C = 1$ (50 µm particles, initial solid volume fraction $\phi_s = 0.6$). The blast wave trajectory for the baseline of a bare 100 g C-4 charge is also shown for comparison.

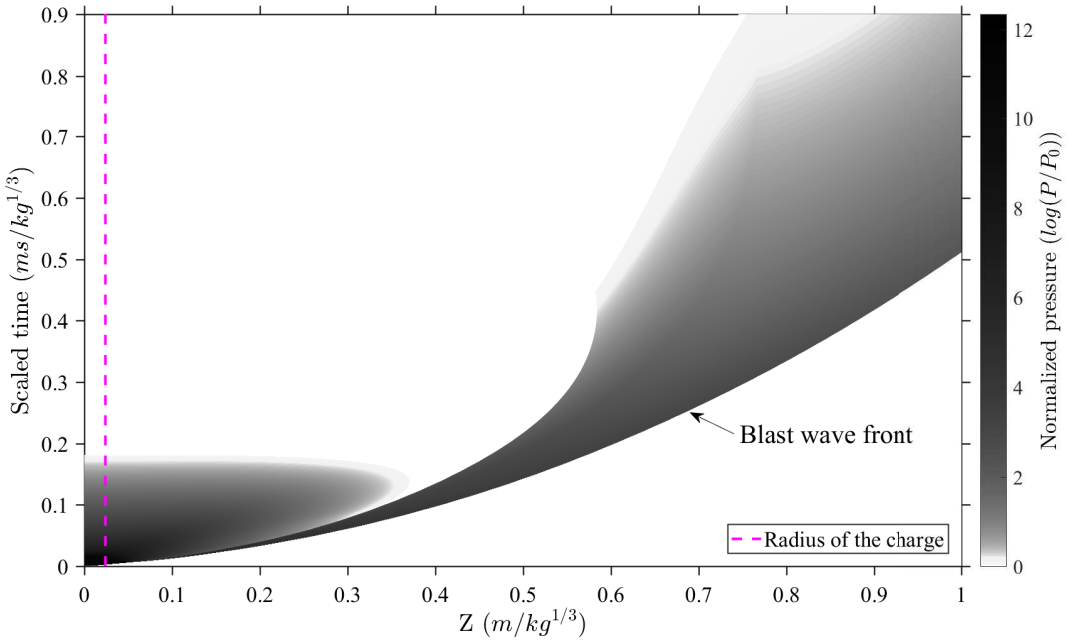

Fig. 4.13 Blast wave trajectory plotted on a scaled time-distance plot for a 100 g bare C-4 charge. Also shown on the plot is a grayscale mapping of the logarithm of the normalized pressure.

The location of the dispersed layer of glass particles as a function of time is indicated on the plot on the right by the coloured region, with the colour scale representing the logarithm of the interstitial gas pressure between particles, in a similar manner as the grayscale. The plot appearing on the left side of the figure shows only a grayscale map of the solid volume fraction, and not the gas pressure, for clarity. It is apparent that for these relatively small, light, glass particles, the particles catch up to the blast at a distance of about $Z = 0.4$ m/kg$^{1/3}$, then continue to follow closely behind the blast wave front, for this case of a small mass ratio. Although the solid volume fraction decreases as the particle cloud expands radially outwards, the particles remain within a narrow region in space and time.

If the mass ratio is increased to a value of $M/C = 10$, Fig. 4.15 shows that the blast wave velocity is reduced and the blast wave trajectory lags considerably behind the corresponding trajectory for an unmitigated, bare C-4 charge. Furthermore, the radial zone over which the particles are contained expands and the particle zone becomes more diffuse, as shown by the coloured region on the right of the figure, or the grayscale map of solid volume fraction shown on the left. The leading edge of the particle zone falls behind the blast wave front. Eventually the decay in the blast wave velocity will allow the particles to approach the blast wave, but this will occur at much further distances from the charge. The air overpressure in the region between the particle front and the blast wave remains relatively high, suggesting that the porous particle front acts effectively as a (porous) piston to generate pressure disturbances that propagate ahead into the shocked air region. These pressure disturbances travel faster than the leading shock front and ultimately merge with the blast wave, reducing the rate of decay of the blast wave

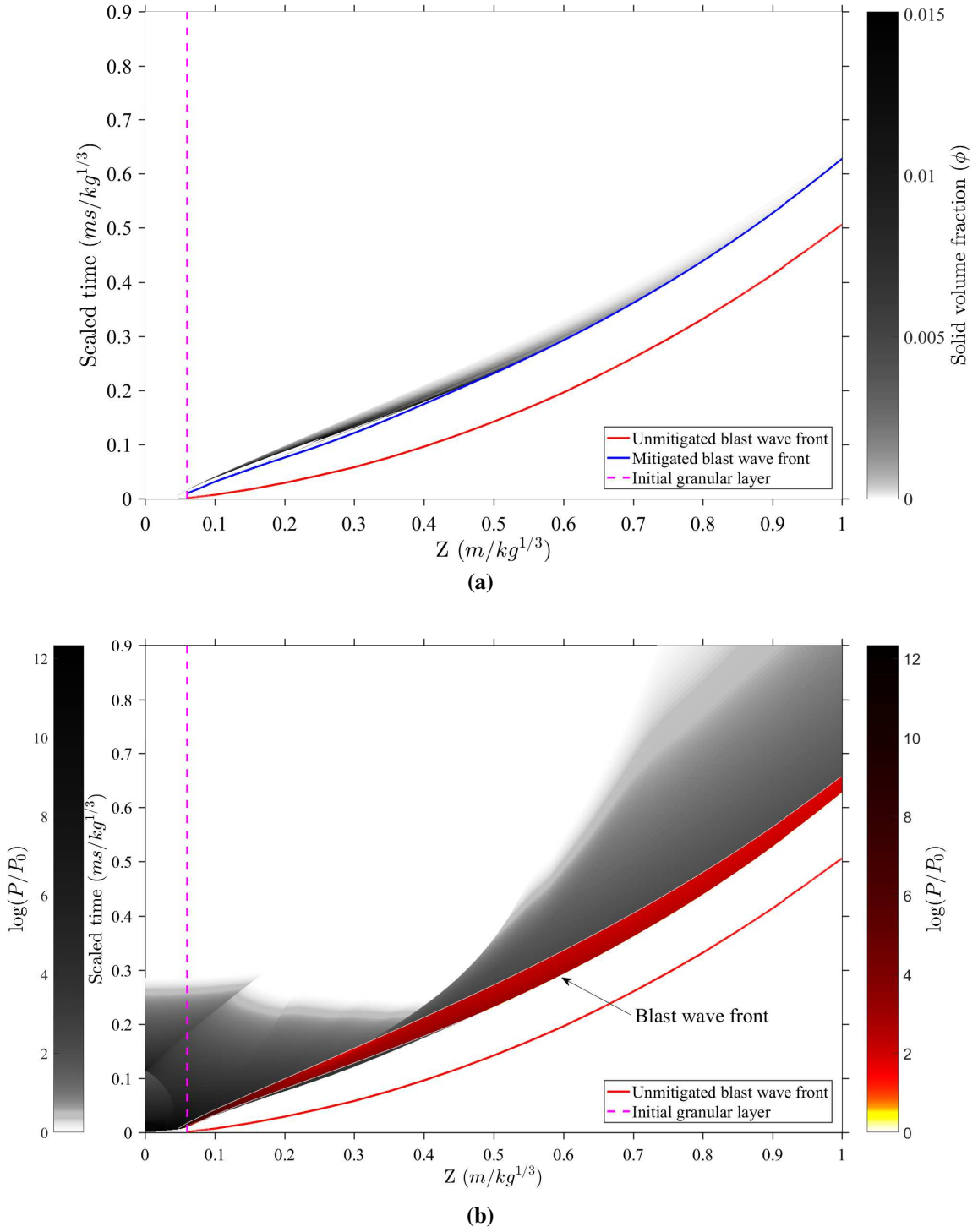

Fig. 4.14 The plot **(a)** shows trajectories of the blast wave (blue curve) and particles (shown as a grayscale map of solid volume fraction) on a scaled time-distance plot for the explosive dispersal of 50 µm glass particles, at $M/C = 1$, with initial solid fraction of $\phi_s = 0.6$. The blast trajectory for a 100 g bare C-4 charge (red curve) is shown for comparison. On **(b)**, the same information is shown, except that now the grayscale map corresponds to the logarithm of the scaled pressure. The location of the particles in time and space is indicated by the coloured region, with the colour mapping corresponding to the logarithm of the scaled pressure of the interstitial gas between the particles.

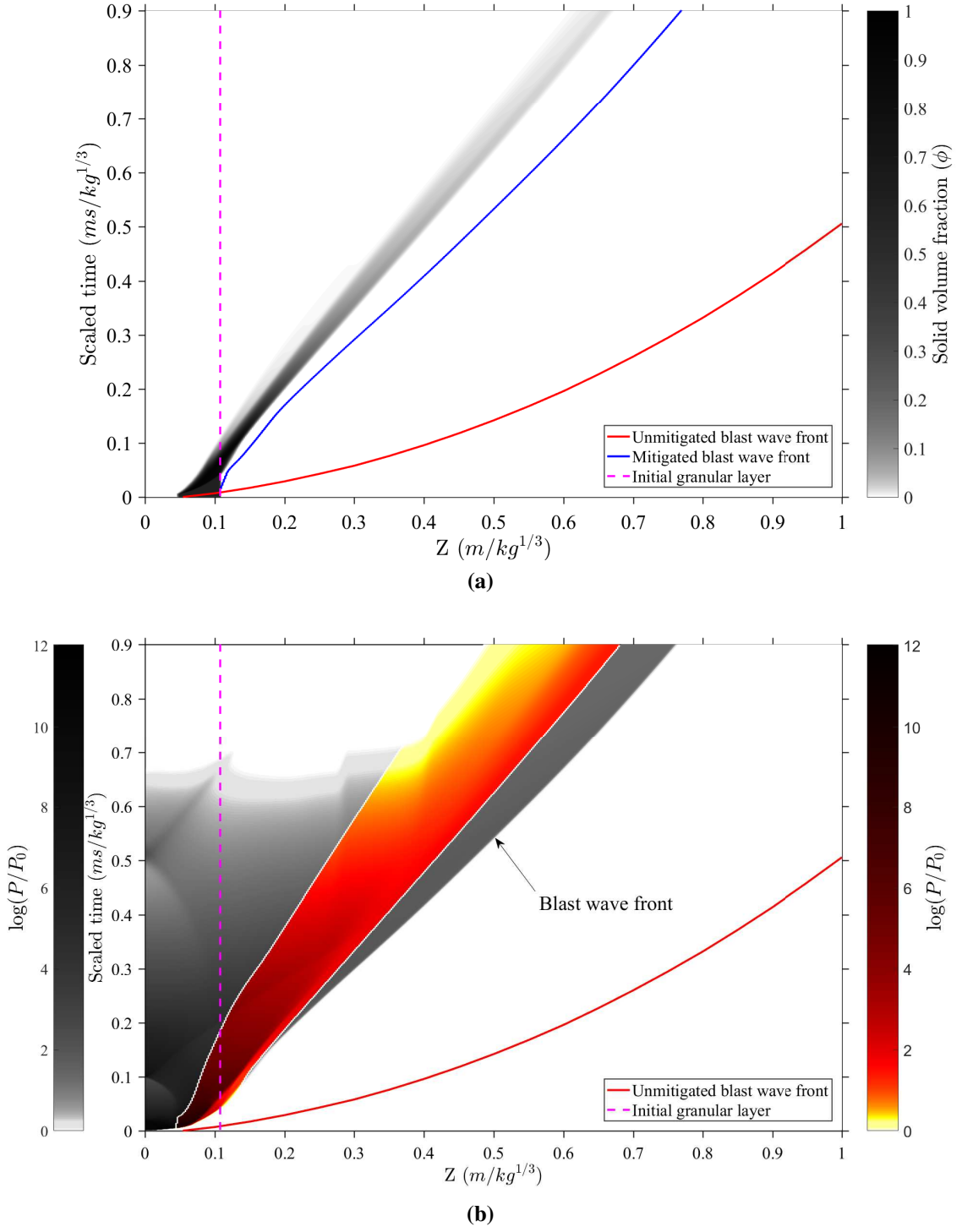

Fig. 4.15 Similar plots as shown in Fig. 4.14 but for the explosive dispersal of 50 µm glass particles with mass ratio $M/C = 10$ ($\phi_s = 0.6$).

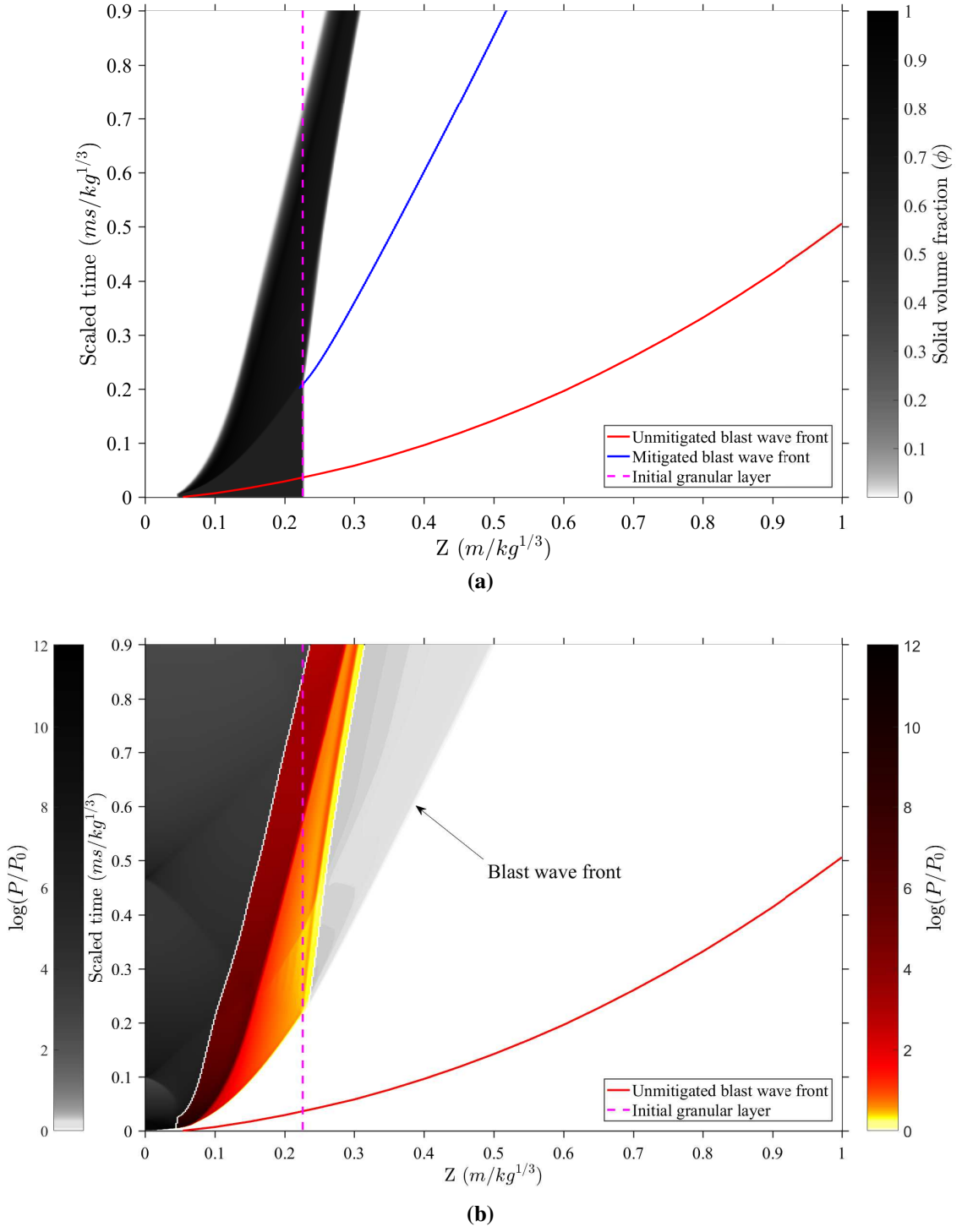

Fig. 4.16 Similar plots as shown in Fig. 4.14 but for the explosive dispersal of 50 µm glass particles with mass ratio $M/C = 100$ ($\phi_s = 0.6$).

overpressure, until the mitigated peak blast overpressure returns to the values of that of a bare charge.

The trends observed when increasing M/C from 1 to 10 are accentuated when the mass ratio is increased further to a value of 100, as shown in Fig. 4.16. Here the initial particle layer is considerably thicker due to the higher mass of glass and when the blast wave emerges from the particle layer, it immediately runs ahead of the particle front, which moves more slowly than for smaller mass ratios. With the slower expansion of the particle layer, the pressure in the detonation products takes a longer time to reduce in magnitude. Despite the lower velocity of the particle front, pressure disturbances, visible as gradations in the grayscale region between the particle front and blast wave, propagate ahead of the particle front into the shocked air region behind the blast wave. The region where the accumulation of these pressure disturbances begins to influence the blast wave propagation and reduce the rate of pressure decay occurs at scaled distances $Z > 0.5$ m/kg$^{1/3}$ (see Fig. 4.8), which is just beyond the region shown in Fig. 4.16.

Charges with steel particles

If the mass ratio is held constant at 100, but glass particles are replaced by steel particles, differences are seen. The change in the behaviour of the trajectories of the particles and blast wave are shown in Fig. 4.17. Due to the higher sound speed in the steel particles, the shock travels faster through the particles before transmitting a blast wave into the air. As the detonation products expand, they plough up the inner surface of the particle layer towards the outer surface, which is moving at a lower velocity. This has the result that the accumulated layer of particles, or accretion layer, has a noticeably smaller thickness than for glass particles. The gas pressure within the particle layer remains relatively low compared with the pressure in the detonation products. Pressure disturbances are again visible emanating forward from the front surface of the particle layer, and travelling at the sound speed in the shocked air. These pressure disturbances eventually catch up to the blast wave front, reducing the rate of decay of the peak blast wave overpressure.

Charges surrounded with a water layer

For the case of dispersal of a layer of water with a mass ratio of 100, the resulting trajectories are shown in Fig. 4.18. Contrary to the dispersal of solid powders, a spall layer is present which runs ahead of the accretion layer. The dynamics of the dispersal of a water layer is described more fully in previous publications [11], [19]. When the initial shock propagating through the water layer reaches the surface of the water layer, a blast wave is transmitted outwards and a rarefaction wave is created moving back through the shocked water. This expansion wave depressurizes the liquid causing cavitation, and generating a two-phase bubbly liquid zone between the accretion and spall layers. As the low pressures within the cavitation region cannot be plotted with the log pressure scaling, the pressure is set to zero in this region. Similarly as

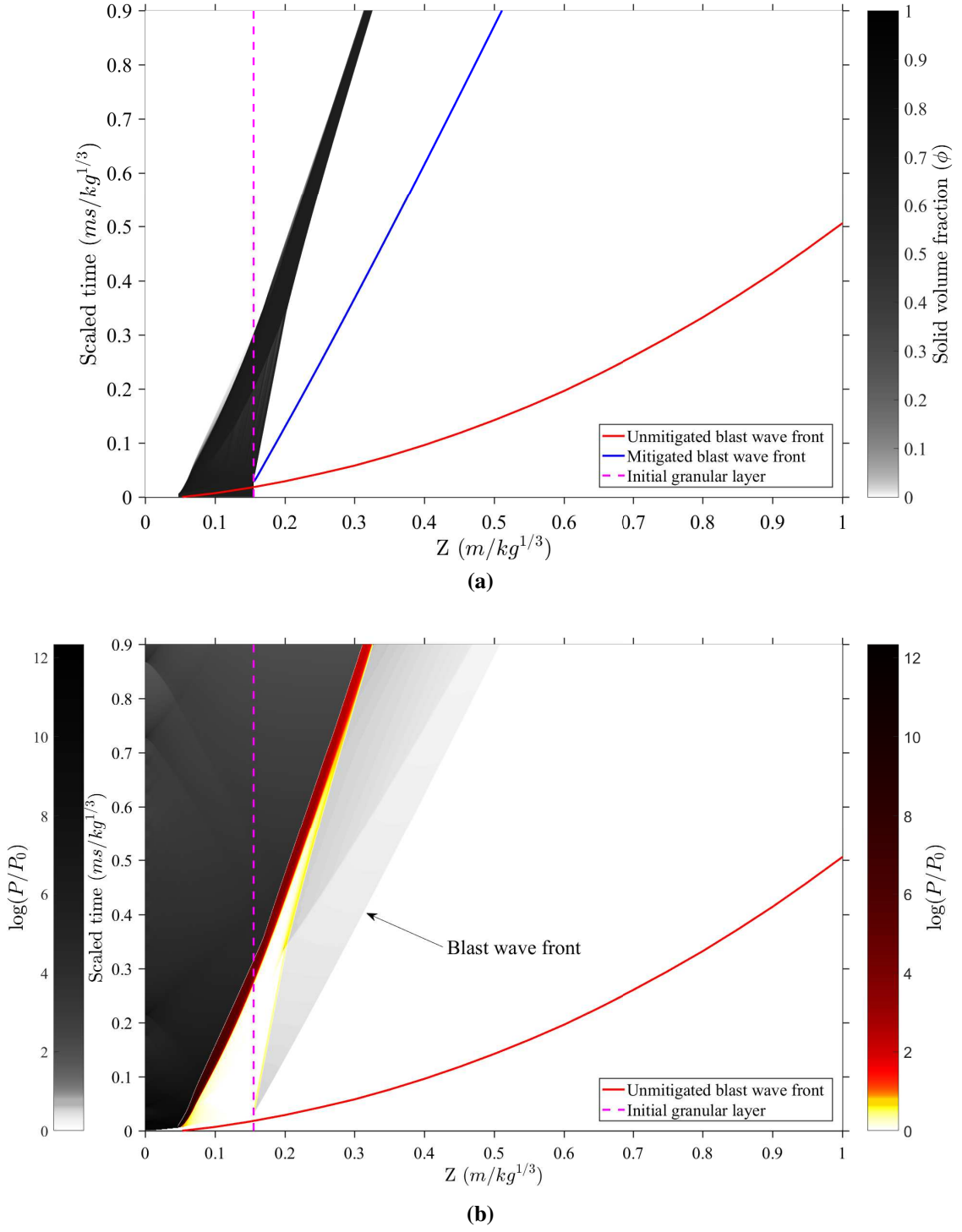

Fig. 4.17 Similar plots as shown in Fig. 4.14 but for the explosive dispersal of 50 μm steel particles with a mass ratio of $M/C = 100$ ($\phi_s = 0.6$).

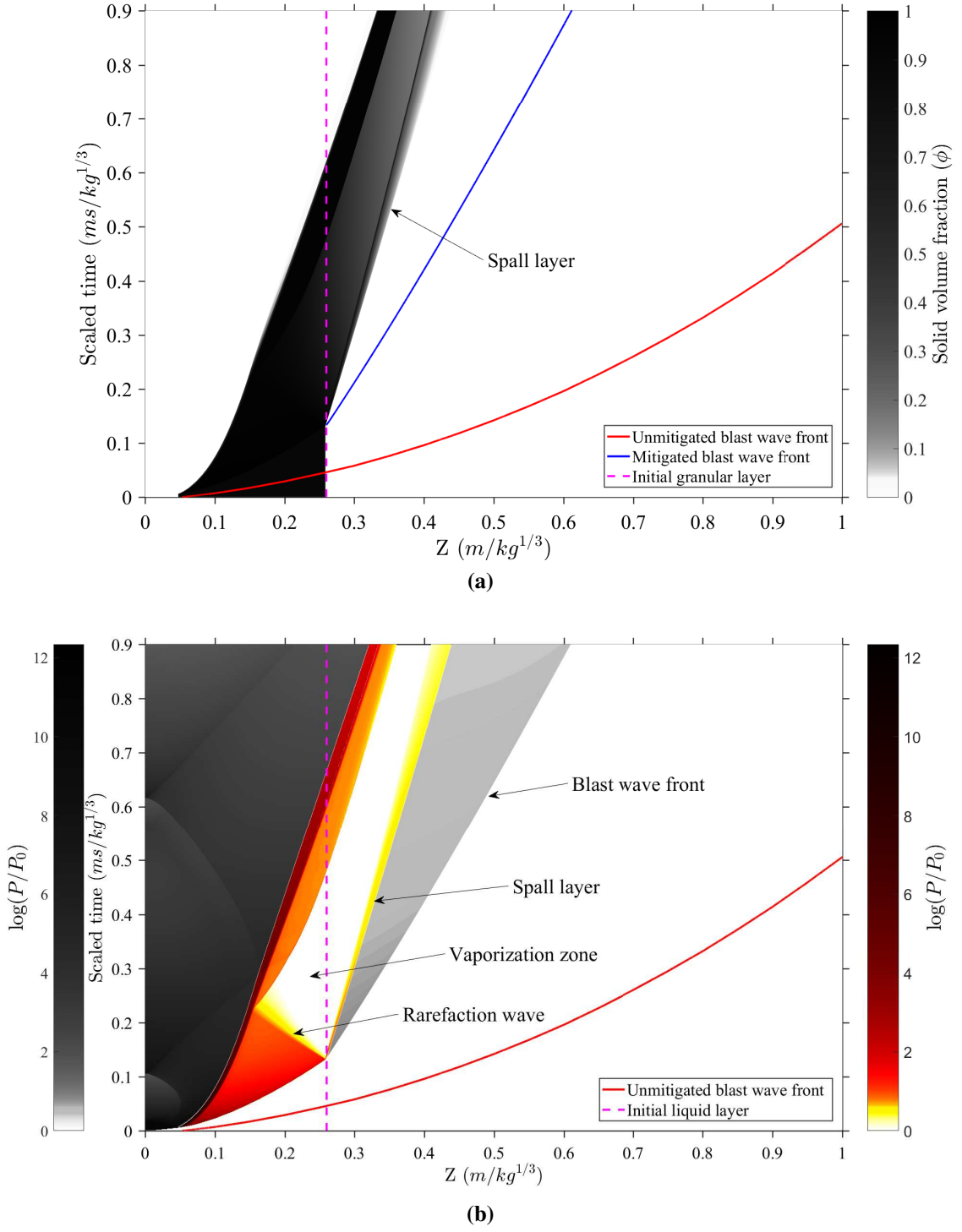

Fig. 4.18 Similar plots as shown in Fig. 4.14 but for the explosive dispersal of water with a mass ratio of $M/C = 100$.

for solid powders, pressure disturbances are visible emanating from the front of the liquid spall layer into the shock air region towards the leading blast wave front.

4.3.6 Momentum fluxes

Following the analysis of Frost [3], it is possible to compute the momentum fluxes of particles and the gas at different distances from the charge for the dispersal of glass particles (with $M/C = 100$, solid volume fraction $\phi_s = 0.6$, particle size = 50 μm). This analysis is relevant for assessing the impulse applied to a nearby structure. Momentum fluxes are defined as the product of the density of each phase multiplied by the square of the velocity of the phases ($\rho_p v_p^2$ for particles and $\rho_g v_g^2$ for the gas). Figure 4.19 shows the history of the momentum fluxes of the particles and air passing three different scaled distances ($Z = 0.2$ m/kg$^{1/3}$, 0.5 m/kg$^{1/3}$, and 1 m/kg$^{1/3}$) for glass at $M/C = 100$. For the two smallest scaled distances, the momentum flux of the particles has a higher peak value in comparison with the momentum flux of the air. The decay in the particle momentum flux with time is explained largely by the decrease in the particle number density and velocity as the cloud of particles expanding radially outwards is subjected to drag.

At $Z = 0.5$ m/kg$^{1/3}$, the location where a kink appears in the decay of the peak overpressure curve (Fig. 4.5), the peak value and the area below the curve for the momentum of the particles has decreased substantially and is on the order of the values for that of air. The particles are localized spatially, so the particle momentum flux at this distance is localized temporally, in contrast with the air which has a more distributed momentum flux. Finally, at $Z = 1$ m/kg$^{1/3}$, both peaks have reduced considerably and the integrated particle momentum flux is less than that of air due to the reduction in particle velocity from drag.

To find the total impulse applied to a structure from a blast-driven multiphase flow, it is necessary to integrate the force applied to the structure from three components, i.e., i) the force applied from the blast wave as it diffracts around the structure, ii) the drag force from the gas flow behind the blast wave as it moves around the structure, which is proportional to the drag coefficient and gas momentum flux, and iii) the force from particle impacts, which depends on the particle momentum flux and the coefficient of restitution associated with the particle collisions (see [3] for a discussion of the various contribution to impulse in a multiphase flow). The relative contribution to the total impulse from the particles and gas depends on the location from the charge. From Fig. 4.19, it is apparent that the momentum flux of the particles dominates the corresponding value for the gas in the very near field ($Z \leq 0.5$ m/kg$^{1/3}$), whereas the opposite holds true further away from the charge. Hence the impulse associated with the particle collisions dominates the impulse from the gas motion in the very near field, and vice versa after this distance.

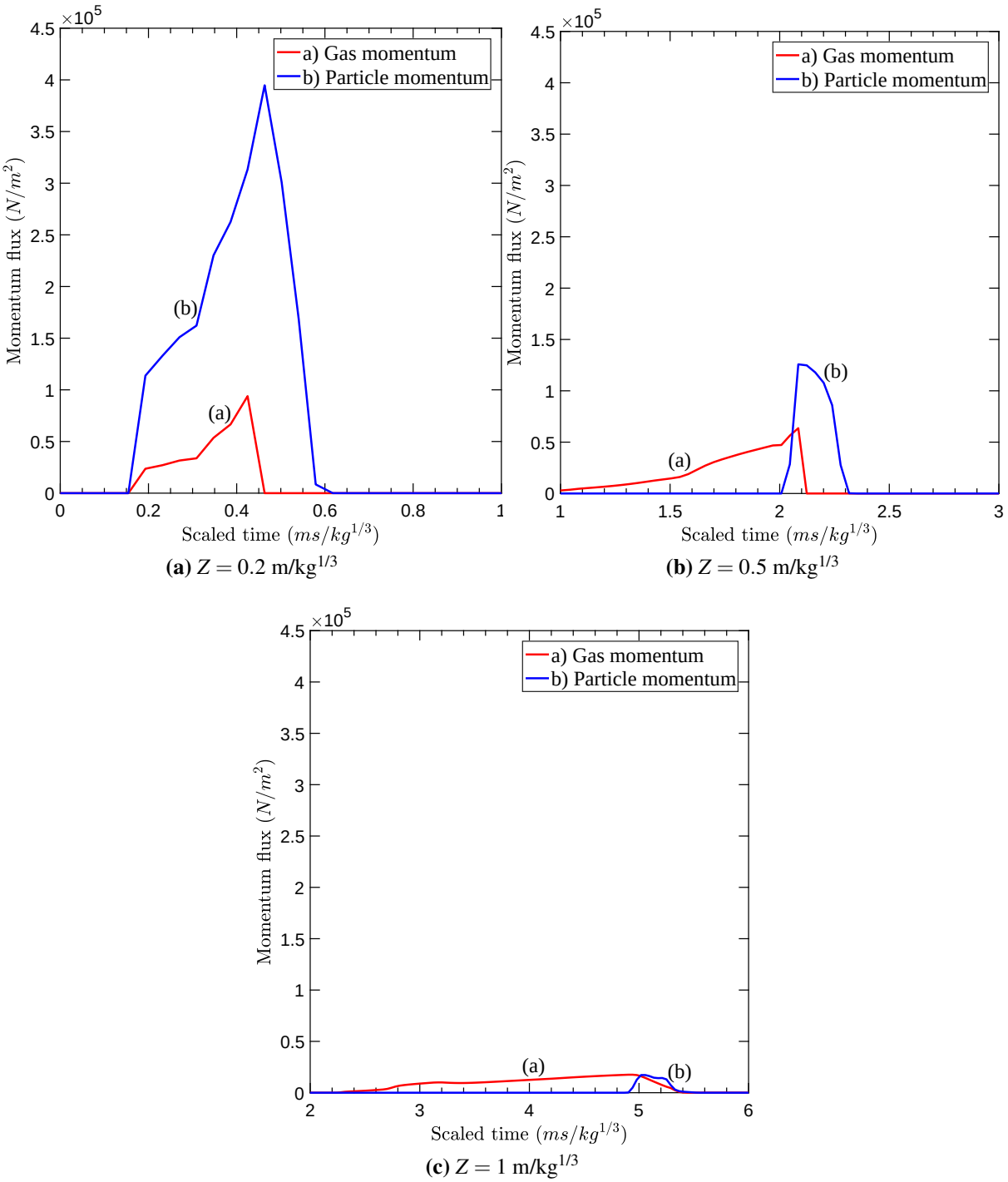

(a) $Z = 0.2$ m/kg$^{1/3}$ **(b)** $Z = 0.5$ m/kg$^{1/3}$

(c) $Z = 1$ m/kg$^{1/3}$

Fig. 4.19 Time history of the momentum flux of particles and air plotted as a function of scaled time for the explosive dispersal of 50 µm glass particles at scaled distances of **(a)** $Z = 0.2$ m/kg$^{1/3}$, **(b)** $Z = 0.5$ m/kg$^{1/3}$ and **(c)** $Z = 1$ m/kg$^{1/3}$ ($M/C = 100$, $\phi_s = 0.6$).

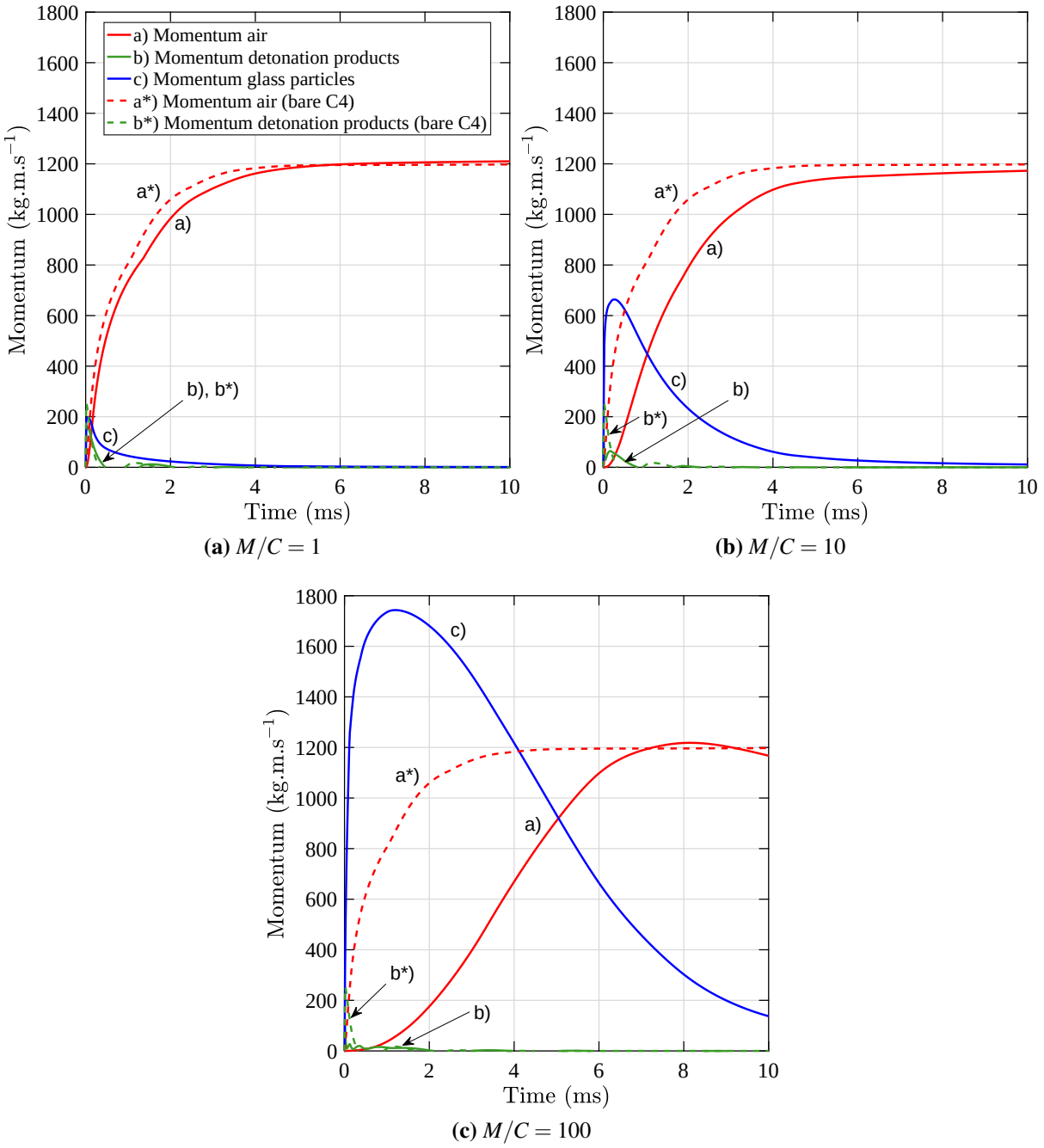

(a) $M/C = 1$ **(b)** $M/C = 10$

(c) $M/C = 100$

Fig. 4.20 Spatially-integrated momenta of the air, detonation products, and glass particles, as a function of time, for a 100 g bare C-4 charge (dashed lines) and for a charge surrounded by 50 µm glass particles ($\phi_s = 0.6$) with mass ratios of **(a)** $M/C = 1$, **(b)** $M/C = 10$ and **(c)** $M/C = 100$ (solid lines).

4.3.7 Spatially-integrated momenta

The dynamics of the interaction between the particles and the flow of the shocked gas behind the blast wave can be illustrated by considering the variation of the total momenta (integrated in space) of the particles, shocked air, and C-4 detonation products as a function of time. Figure 4.20 shows the history of the total momenta of the particles, air, and detonation products for the dispersal of glass particles for M/C values of 1, 10, and 100. Figure 4.21 shows expanded views of the early time of the same plots. Also shown in Figs. 4.20 and 4.21 is the history of the total air and product gas momenta for the baseline case of a bare C-4 charge.

For the smallest mass ratio ($M/C = 1$), the shock transmitted into the packed particle bed rapidly accelerates the particles to a maximum momentum in less than 100 µs. The particles then decelerate due to drag and the momentum of the shocked air increases as energy is transferred from the particles to the air. The deficit in the air momentum, compared with the bare C-4 case, is a result of the momentum transferred to the particles. However, this deficit completely recovers after about 5 ms, at which point the particle momentum has decayed nearly to zero.

When the mass ratio is increased from 1 by a factor of 10 or 100, the time for the particle momentum to reach a maximum increases from 0.1 ms to about 0.2 and 1 ms, for $M/C = 10$ and 100, respectively. The maximum particle momentum attained scales with $(M/C)^{0.47-0.52}$ (intermediate mass ratios M/C of 2, 3, 5, 15, 30, 50 have been simulated to establish this scaling law), consistent with Gurney theory, which predicts a dependence of $(M/C)^{1/2}$ [20]. The combined spatially-integrated momentum of both particles and the air are generally higher or equal than the momentum of an unmitigated charge and stay higher for a longer time with increasing M/C. Despite the increase in maximum particle momentum at the largest M/C value, the particle momentum eventually decreases leading to an increase in the gas momentum until it recovers to the same value as the baseline case at a time of about 7 ms, at which point the particles still have a significant, residual momentum. The time at which the particle and air momenta are exactly equal increases from about 0.15 ms to 1 ms to 5 ms, for $M/C = 1$, 10, and 100, respectively, which corresponds to a power law dependence on M/C of approximately $(M/C)^{0.76-0.84}$.

4.4 Conclusions

The explosive dispersal of a layer of granular material or liquid has been investigated computationally with a 1D multiphase hydrocode and compared with recent experimental results [2]. The computational results are consistent with the main experimental finding, i.e., that the mitigation of the blast wave overpressure by the surrounding inert material is primarily dependent on the mitigant to explosive mass ratio M/C, with the particle and bed properties playing a secondary role. Another salient observation from the experiments is that while the blast overpressure is reduced in the near-to-mid field (0.5 m/kg$^{1/3}$ $< Z <$ 2 m/kg$^{1/3}$), the rate of decay of the blast

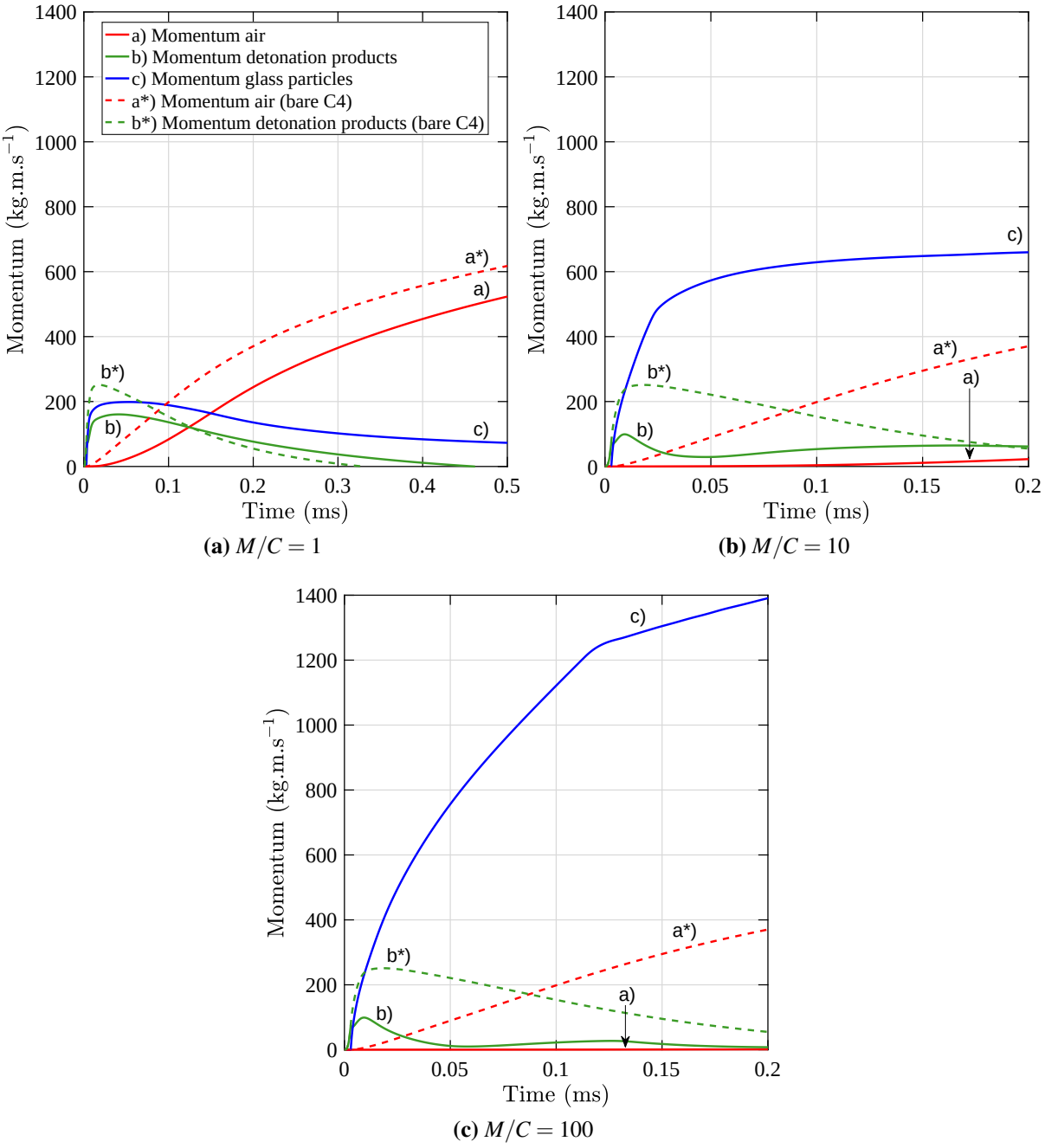

(a) $M/C = 1$ **(b)** $M/C = 10$

(c) $M/C = 100$

Fig. 4.21 Early time behaviour of the same momenta values shown in Fig. 4.20.

overpressure is reduced with distance and the overpressure nearly recovers to the value for a bare charge for small values of the mass ratio ($M/C < 10$), in the far field ($Z > 2$ m/kg$^{1/3}$). The hypothesis that the particles act as a porous piston and generate pressure disturbances which reach the blast wave front and slow the rate of pressure decay has been confirmed with the computations. In particular, by plotting the trajectories of the particles and blast wave as well as the gas pressure field on a time-distance plot, the pressure disturbances generated at the front of the expanding particle cloud can be visualized. Since these pressure perturbations move at the sound speed of the hot, shocked air behind the blast wave, they move faster than the blast wave and can eventually overtake the blast wave front.

The phase of pressure recovery follows the earlier phase when the particles accelerate and extract energy from the flow, reducing the blast overpressure in the very near field. The numerical simulations are useful for investigating the near-field phenomena which are not accessible experimentally [2]. The location of this transition, where the peak blast overpressure and positive-phase impulse exhibit the most reduction, as compared to a bare charge, appears in the region 0.3 m/kg$^{1/3} < Z <$ 0.6 m/kg$^{1/3}$, with the transition occurring at larger distances with increasing M/C.

While the blast wave decay for a mitigated charge is not strongly dependent on the particle properties, changes to the material properties lead to small systematic changes in the decay rate of the blast overpressure. For example, when the particle size and/or particle packing density is reduced, the particles accommodate more quickly to the ambient flow velocity. Hence during the particle acceleration phase at early times, energy is transferred more quickly to the particles by the flow and the rate of decay of the peak blast overpressure increases. Conversely, as the particles decelerate and transfer energy back to the flow, smaller particles lead to a more rapid recovery of the blast overpressure. A comparison between steel and glass particles indicates that the latter are more effective at reducing the peak blast overpressure and impulse. However, the discrepancies observed are less than that found experimentally [2].

The computational results for the blast wave overpressures for explosive dispersal of liquids or particles generally agreed with the experimental results, considering the degree of scatter in the experimental results, except in the near field (0.5 m/kg$^{1/3} < Z <$ 1 m/kg$^{1/3}$), for a mass ratio below around 30. On the contrary, in the far field ($Z > 2$ m/kg$^{1/3}$), impulses for glass and steel powders exceed experimental values. The differences are likely related to energy dissipation during particle deformation and fracture, or liquid droplet fragmentation, which are not captured in the computations. Surrounding an explosive charge with a layer of either particles or a liquid leads to a residual reduction of the peak blast overpressure in the far field ($Z > 2$ m/kg$^{1/3}$), especially at high M/C. Nevertheless, the effect on the positive-phase blast impulse differs for the two cases: particles lead to a reduction in blast impulse, whereas a liquid has virtually no effect on the blast impulse, in comparison with a bare explosive charge and that for all M/C. The independence of impulse on the presence of water for the explosive dispersal of water was reproduced by the computations. The impulse is an integrated measure of the blast overpressure,

and is dependent on the details of the flow field behind the blast wave. Hence, a more accurate prediction of the blast impulse will likely require a consideration of the particle deformation effects noted above, as well as the particle clustering and jetting that is characteristic of explosive particle dispersal.

Computations show that the momentum flux of the particles exceeds that of the gas in the very near field ($Z \leq 0.5$ m/kg$^{1/3}$) and hence the primary contribution to impulse to a structure in this region is from particle impacts. This observation, together with the tendency of the blast overpressure and impulse to recover in the far field when particles or liquids are explosively dispersed, are important factors that must be considered when attempting to mitigate the blast effects from a high-explosive charge at a given distance.

To extend the current work, refinements of the model are required to take into account the various mechanisms of energy dissipation (deformation, fracturing, cavitation, etc.) not modelled in the present study, as well as multidimensional effects. Investigation of the partition of kinetic and internal energy within the flow is helpful to quantify the energy transfer between the phases. Initial work in this direction is presented in another publication [21]. Another possible extension of the current work could be the investigation of the combined impulse from the particles and the blast applied to a structure. In addition, an analysis of the maximal radial extent of the particle cloud as a function of M/C and material properties is of interest to quantify the hazards associated with the explosive dispersal of particles.

Acknowledgements Assistance with the EDEN hydrocode calculations by Leo Crozes at Fluid Gravity Engineering is gratefully acknowledged as well as the Defense Threat Reduction Agency for funding under project HDTRA1-11-1-0014. The authors would also like to thank the three anonymous reviewers for their many constructive comments.

References

[1] R. M. Allen, D. J. Kirkpatrick, A.W. Longbottom, A. M. Milne, and N. K. Bourne. Experimental and numerical study of free-field blast mitigation. In *AIP Conference Proceedings*, volume 706, pages 823–826, 2004, doi:10.1063/1.1780363.

[2] Q. Pontalier, J. Loiseau, S. Goroshin, and D. L. Frost. Experimental investigation of blast mitigation and particle-blast interaction during the explosive dispersal of particles and liquids. *Shock Waves*, 28(3):489–511, 2018, doi:10.1007/s00193-018-0821-5.

[3] D. L. Frost, C. Ornthanalai, Z. Zarei, V. Tanguay, and F. Zhang. Particle momentum effects from the detonation of heterogeneous explosives. *Journal of Applied Physics*, 101(11):1–14, 2007, doi:10.1063/1.2743912.

[4] J. Loiseau, Q. Pontalier, A. M. Milne, S. Goroshin, and D. L. Frost. Terminal velocity of liquids and granular materials dispersed by a high explosive. *Shock Waves*, 28(3):473–487, 2018, doi:10.1007/s00193-018-0822-4.

[5] V. S. Lanovets, V. A. Levich, N. K. Rogov, Yu. V. Tunik, and K. N. Shamshev. Dispersion of the detonation products of a condensed explosive with solid inclusions. *Combustion, Explosion and Shock Waves*, 29(5):638–641, 1993, doi:10.1007/BF00783721.

[6] F. Zhang, D. L. Frost, P. A. Thibault, and S. B. Murray. Explosive dispersal of solid particles. *Shock Waves*, 10(6):431–443, 2001, doi:10.1007/PL00004050.

[7] Y. Ling, A. Haselbacher, and S. Balachandar. Importance of unsteady contributions to force and heating for particles in compressible flows. Part 2: Application to particle dispersal by blast waves. *International Journal of Multiphase Flow*, 37(9):1013–1025, 2011, doi:10.1016/j.ijmultiphaseflow.2011.07.002.

[8] E. J. Chang and K. Kailasanath. Shock wave interactions with particles and liquid fuel droplets. *Shock Waves*, 12(4):333–341, 2003, doi:10.1007/s00193-002-0170-1.

[9] Z. Zarei, D. L. Frost, and E. V. Timofeev. Numerical modelling of the entrainment of particles in inviscid supersonic flow. *Shock Waves*, 21(4):341–355, 2011, doi:10.1007/s00193-011-0311-5.

[10] K. Balakrishnan, D. V. Nance, and S. Menon. Simulation of impulse effects from explosive charges containing metal particles. *Shock Waves*, 20(3):217–239, 2010, doi:10.1007/s00193-010-0249-z.

[11] A. M. Milne, C. Parrish, and I. Worland. Dynamic fragmentation of blast mitigants. *Shock Waves*, 20:41–51, 2010, doi:10.1007/s00193-009-0235-5.

[12] D. L. Frost, Y. Grégoire, O. Petel, S. Goroshin, and F. Zhang. Particle jet formation during explosive dispersal of solid particles. *Physics of Fluids*, 24:091109, 2012, doi:10.1063/1.4751876.

[13] A. M. Milne, E. Floyd, A. W. Longbottom, and P. Taylor. Dynamic fragmentation of powders in spherical geometry. *Shock Waves*, 24(5):501–513, 2014, doi:10.1007/s00193-014-0511-x.

[14] K. Xue, L. Sun, and C. Bai. Formation mechanism of shock-induced particle jetting. *Physical Review E*, 94(2):022903, 2016, doi:10.1103/PhysRevE.94.022903.

[15] E. L. Lee, H. C. Hornig, and J. W. Kury. Adiabatic expansion of high explosive detonation products. Technical report, Lawrence Radiation Lab, University of California, Livermore, 1968, https://www.osti.gov/servlets/purl/4783904.

[16] G. F. Kinney and K. J. Graham. *Explosive shocks in air (Second edition)*. Springer, 1985, doi:10.1007/978-3-642-86682-1.

[17] Q. T. Pontalier, M. G. Lhoumeau, and D. L. Frost. Non-Ideal Blast Waves from Particle-Laden Explosives. In *31st International Symposium on Shock Waves*, Nagoya, Japan, 2017. doi:10.1007/978-3-319-91017-8_5.

[18] H. L. Brode. Blast wave from a spherical charge. *Physics of Fluids*, 2(1959):217–229, 1959, doi:10.1063/1.1705911.

[19] A. M. Milne, A. Longbottom, D. L. Frost, J. Loiseau, S. Goroshin, and O. Petel. Explosive fragmentation of liquids in spherical geometry. *Shock Waves*, 27:383–393, 2017, doi:10.1007/s00193-016-0671-y.

[20] R. W. Gurney. The initial velocities of fragments from bombs, shell and grenades. Tech. Rep. (45), US Army Ballistic Research Laboratory, Aberdeen Proving Ground, Maryland, USA, 1943, https://apps.dtic.mil/sti/pdfs/ADA800105.pdf.

[21] Q. Pontalier, M. Lhoumeau, and D. L. Frost. Blast wave mitigation in granular materials. *AIP Conference Proceedings*, 1979(1):110014, 2018, doi:10.1063/1.5044933.

Summary of Chapter 4

In Chapter 4, the blast wave overpressure generated by a C-4 charge surrounded by a packed bed of either glass particles, steel particles, or a bulk water layer, was investigated numerically in 1D. The numerical calculations were carried out with the EDEN hydrocode and were based on a two-phase model similar to that of Baer and Nunziatio [1]. The computational results were globally consistent with the main experimental findings of Chapter 3. Although the difference in the blast wave mitigation effectiveness between the bulk water layer and the granular powders was not as high as observed experimentally, the blast mitigation was primarily dependent on the mitigant to explosive mass ratio (M/C). Furthermore, the particle size and the bed properties played a secondary role, as observed in the experiments. These results confirmed that the heat and the momentum transfer from the detonation product gases to the material layer were primarily responsible for the blast wave attenuation. The M/C ratio was a parameter that encompassed both the thermal and the mechanical inertial aspects of the material layer. The relative importance of these two aspects on the blast wave attenuation was not presented in the previous chapter, but was analyzed in a complimentary study [2].

In this companion study, the transient partition in the total energy between kinetic and internal energy of the particles and gas was determined during the explosive dispersal process. This provided additional insight into the energy transfer processes between the particles and gas. After detonation of the charge, the shock transmitted into the material compacts and heats the interstitial air (for dry powder beds) or the water directly by shock heating. The material is also rapidly accelerated, with the resulting kinetic energy attained by the particles and air less than the increase in internal energy. The timescales for heat and momentum exchange depend primarily on the mass of material added and particle size, with longer timescales for high M/C ratios and with finer particles accommodating more rapidly to the ambient speed and velocity of the air.

In Chapter 4, for all the material layers and for all the M/C ratios tested, the blast mitigation effectiveness increased initially over a distance of 2-3 charge radii ($<$ 20 cm from the center of the C-4 charge). The augmentation of the blast mitigation effectiveness was mainly attributed to the transfer of energy from the detonation products to the material layer, via the contribution of the exchange terms in the numerical model (mostly drag and convective heat transfer). At a distance between 2-3 charge radii, the dispersed material reached thermal and mechanical

equilibrium with the surrounding gas. The exact location of this equilibrium point depended on the M/C ratio and on the material properties. Passing this equilibrium point, the sign of the exchange terms were reversed, and thus the direction of the energy transfer. In this region, the particles fed back their energy to the surrounding air and contributed to the reduction of the blast wave mitigation effectiveness with distance, as observed experimentally in Chapter 3. This so-called piston effect was later corroborated by other researchers [3–5] with a different numerical framework, suggesting that the phenomenon can be robustly predicted in hydrocode simulations.

Finally, the momentum fluxes of the gas and the particle phase were compared at different distances from the charge. In the vicinity of the initial charge, the momentum flux of the particles exceeded that of the gas. However, in the mid field the fluxes equalized as the particles slowed down due to aerodynamic drag. Ultimately, in the far field, the momentum flux of the gas exceeded that of the particles. This observation implies that mitigation systems should be adapted as a function of the distance from the explosion epicenter. In the case of an accidental explosion with blast wave generation and high-velocity fragment dispersion, an attenuation system consisting of a physical barrier in the near field and a blast wave attenuator in the far field would be optimal. Not only would the physical barrier prevent damage generated by the scattered materials, but it would also significantly reduce the influence of the porous piston effect that sustains the blast wave in the far field. Behind the barrier, the blast wave would lose energy as it propagates through the air and eventually encounters the attenuation system. The system must include compressible materials with a certain mass for practical and effective blast wave attenuation. The mass of the materials would increase the impedance mismatch at the air-layer interface and the heat/momentum transfer imparted to the material layer. In contrast, the compressible nature of the materials would increase the irreversible energy losses.

References

[1] M. R. Baer and J. W. Nunziato. A two-phase mixture theory for the deflagration-to-detonation transition (ddt) in reactive granular materials. *International Journal of Multiphase Flow*, 12(6):861–889, 1986, doi:10.1016/0301-9322(86)90033-9.

[2] Q. Pontalier, M. Lhoumeau, and D. L. Frost. Blast wave mitigation in granular materials. *AIP Conference Proceedings*, 1979(1):110014, 2018, doi:10.1063/1.5044933.

[3] Y. Sugiyama, T. Homae, T. Matsumura, and K. Wakabayashi. Numerical study on the attenuation effect on the blast wave of encircling a high explosive with granular media. *Journal of Applied Physics*, 127(16):164701, 2020, doi:10.1063/1.5143351.

[4] Y. Sugiyama, T. Homae, T. Matsumura, and K. Wakabayashi. Numerical study on the mitigation effect of glass particles filling a partially confined space on

a blast wave. *International Journal of Multiphase Flow*, 136:103546, 2021, doi:10.1016/j.ijmultiphaseflow.2020.103546.

[5] T. Tamba, Y. Sugiyama, K. Ohtani, and K. Wakabayashi. Comparison of blast mitigation performance between water layers and water droplets. *Shock Waves*, (0123456789), 2021, doi:10.1007/s00193-021-00990-3.

Part III

Preamble to Chapter 5

In part II, the blast wave pressure generated by heterogeneous explosive systems with stratified layers of material was thoroughly analyzed both experimentally and numerically. During the timescale of the blast wave propagation, the materials tested remained chemically inert and partially absorbed the energy of the detonation products. The energy transfer from the detonation products to the material layer resulted in the attenuation of the blast wave pressure in the near field. However, it was found that the dispersal of the material layer acted as a porous piston on the blast wave and contributed to the reduction of the blast mitigation effectiveness in the far field.

Embedding chemically reactive particles within a solid or liquid propellant or explosive is a common practice to increase the energy output of energetic materials. Metalized explosives have been historically used for military applications, with formulations optimized to enhance the blast strength or some other performance metric. In the modern context, metallized explosives are also used in the mining industry for rock blasting and to increase earthmoving capability. Metallized explosives can also be studied to understand how metals react chemically at extreme pressures, with different oxidizers. In Chapter 5, the blast wave pressure resulting from the detonation of metalized explosive charges at constant volume is investigated experimentally. The same diagnostics and experimental methodology as in part II are employed. The charges are comprised of a dilute suspension of aluminum or magnesium particles embedded within gelled and sensitized NM. This configuration is schematically depicted in Fig. 4.22. The results are compared with the same charges but with inert (glass) particles. Of primary interest for this study is to determine to what extent the metallic particles effectively release their chemical energy, and if the energy release is sufficiently rapid to contribute to the blast wave pressure. Of secondary interest, is to determine if the particle chemical energy release is sufficient to compensate for the reduction of explosive mass due to the addition of particles, as well as, the influence of the initial particle mass fraction and particle size on the resulting blast wave pressure. The contribution of the porous piston effect on the blast wave pressure, discussed in part II, is also investigated for charges with glass particles mixed with the gelled NM.

It is well known that metallic particles, and particularly aluminum particles, can react downstream of the detonation reaction zone. Experimental evidence from cylinder and flyer plate tests has shown that the energy released by the particles can enhance the acceleration of casings

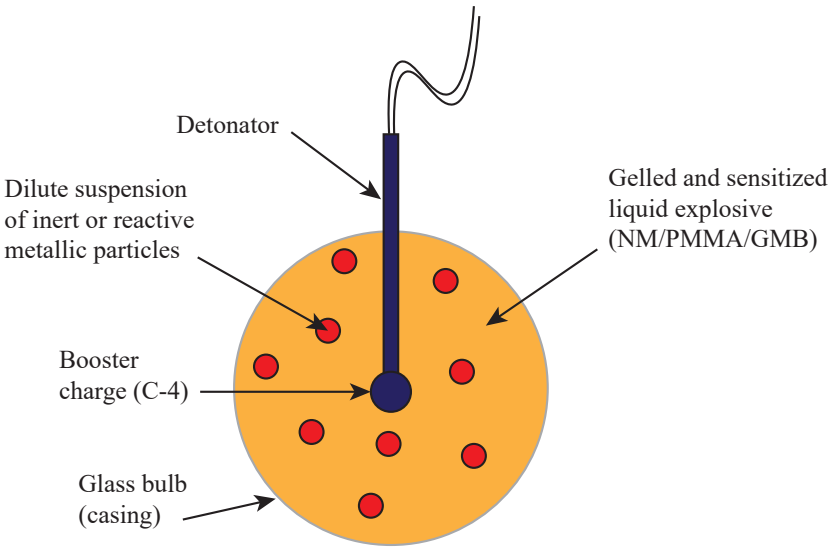

Fig. 4.22 In Chapter 5, the blast wave pressure generated by a dilute suspension ($\leq$ 50% by weight) of reactive metallic particles in a liquid explosive matrix is investigated. The liquid explosive (NM) is sensitized by a small fraction of glass microballoons (GMB) and initiated by a booster charge of C-4. The particles are homogeneously suspended and gelled in the liquid explosive with the addition of Polymethyl methacrylate (PMMA), a thermoplastic and transparent polymer.

and flyer plates. At the timescale of the detonation wave propagation, the particles do not have time to escape the detonation products due to their inertia. Hence, at this time, the particles react primarily anaerobically with oxidizers in the detonation products (primarily H_2O or CO_2 for most CHNO explosives). However, previous blast wave studies in the open literature have largely neglected the contribution of anaerobic reactions to the blast wave pressure enhancement. In these prior studies, only the energy release associated with aerobic reactions with the ambient air outside the fireball was assumed to contribute to the blast enhancement. Historically, particle reaction models that have been used were based on data from single particle experiments at ambient pressure, which depend on the particle surface area. In Chapter 5, it is of particular interest to determine if the experimental blast data implies some contribution of particle anaerobic reactions to the blast enhancement. Furthermore, determining the dependence of the blast enhancement on the particle size will shed some light on the validity of the historical particle reaction models. This chapter is comprised of a paper published in the *Shock Waves* journal.

Chapter 5

Blast enhancement from metalized explosives

Q. Pontalier, J. Loiseau, S. Goroshin, F. Zhang, and D. L. Frost, *Shock Waves*, 2021.
doi:10.1007/s00193-021-00994-z

Abstract

Experiments are carried out to determine the effects of particle size and mass loading on the free-field blast wave from spherical, constant volume metalized explosive charges. The charges are comprised of gelled nitromethane with uniformly embedded aluminum, magnesium, or glass particles. Particle sizes are varied over an order of magnitude with particle mass fractions up to 50%. Peak blast overpressures are directly measured within the fireball with piezoelectric pressure gauges and outside the fireball are inferred by tracking the velocity of the blast wave and using the Rankine-Hugoniot relation. With the addition of inert particles, the peak blast overpressure is initially mitigated, but then recovers in the far field. For charges with reactive particles, the particles react promptly with oxidizers in the detonation products, and release energy as early as within the first few hundred microseconds in all cases. The particle energy release enhances the peak blast overpressures in the far field by up to twice the values for a constant volume charge of the baseline homogenous explosive. By plotting the peak blast overpressure decay as a function of energy-scaled distance, it is inferred that at least half of the particle energy release contributes to the blast overpressure in the far field of higher mass loadings, and nearly all of the particle energy for a particle mass fraction of 10%. For aluminum, the blast augmentation is not a systematic function of particle size. This observation implies that conventional models for particle combustion that depend on particle surface area are not appropriate for describing the rapid aluminum reaction that occurs in the extreme conditions within the detonation products which influences the blast wave propagation.

Supplementary Information The online version contains supplementary material available at https://doi.org/10.1007/s00193-021-00994-z.

Keywords Blast wave enhancement · Al/Mg particles · Reaction timescales · Particle–blast interaction · Mass fraction · Particle size

5.1 Introduction

The addition of metallic particles to explosive formulations has been a common technique for enhancing the performance of conventional high explosives for over a century, going back to the study in 1899 by R. Escales [1] and the patent by Roth [2] in 1900. Blast enhancement studies with metalized explosives are based upon the fact that the volumetric energy release from metal reactions is generally larger than the base explosive itself, and the assumption that particle reaction may occur sufficiently rapidly to enhance the blast wave strength. It is assumed that for a constant volume charge, the energy release from the metal reaction more than compensates for the reduction in explosive mass with the particle addition, so that the overall energy output, and in turn the blast strength, are augmented.

Various reactive metals, such as aluminum, boron, magnesium, titanium, tungsten, and zirconium [3], have been added to explosives to enhance their performance. Aluminum is the most common metal used, due to the high heat of formation of condensed aluminum oxide, the low metal density, and relatively low cost. Energy release from the oxidation of the added metal particles can increase the blast overpressure and impulse, and hence such metalized explosives are often referred to as enhanced-blast explosives (EBX). Comprehensive reviews of such explosives have been prepared by Frost & Zhang [4], Trzciński & Maiz [5], and Türker [6]. So-called combined effects aluminized explosives (see [7] for a specific review) are formulated to enhance their metal-pushing performance as well as blast effects [8].

The addition of particles to an explosive influences the pressure history behind the blast wave produced in several ways. For inert particles, as they are accelerated by the expanding combustion products, and subsequently decelerate, the particles exchange momentum with the surrounding gas and perturb the local pressure field non-uniformly as the particles typically form particle jets or filaments [9]. This effect leads to a reduction in peak blast overpressure in the near field as the particles accelerate, and to a corresponding augmentation farther from the charge as the particles decelerate and return energy to the flow [10–13]. In the case of reactive particles, the contribution of the energy release from the particle reaction to the local pressure field is more complex. The coupling between the particle reaction and the blast wave pressure depends on the heat transfer rate between the particles and the surrounding gas [14], the oxidizing species present [15], the reaction rate of the particles, and the location of the energy deposition [16]. Other phenomena that may influence the strength of the blast wave from a metalized explosive include afterburning of the explosive detonation products [17, 18] or

afterburning of the reactive gases generated by particle combustion. Secondary fragmentation of partially-reacted particles due to relative flow, the interaction of reflected waves, or impact with nearby structure may also contribute to the blast overpressure augmentation.

Even after more than a century of research, the physical mechanisms associated with the particle reaction and the augmentation of the blast pressure remain poorly understood. One of the main outstanding issues for aluminized explosives is quantifying the fraction of the energy release from the aluminum reaction that occurs on the timescale of the detonation propagation (i.e., on the order of microseconds), relative to the fraction that occurs on the timescale of the blast wave propagation (i.e., on the order of milliseconds). From research into the propagation of detonations in metalized explosives, or the so-called detonics regime, there is a growing body of evidence that metal particles can react on microsecond timescales behind the detonation wave and contribute to the ability to accelerate a metal casing [19–28]. The early signs of metal reaction seem to appear regardless of the explosive formulations used. In particular, metallic particles were observed to react at microsecond timescales in RDX [19–21], RDX-ammonium perchlorate (AP) [22], HMX [23, 24], nitroguanidine (NG) and bis (2,2,2-trinitroethyl) nitramine (BTNEN) [24]. Early-time contribution of Al reaction was also observed in hydrogen-free compounds such as benzotrifuroxan (BTN) [25], carbon-free substances such as ammonium nitrate (AN) [26] or liquids such as nitromethane (NM) [27–29]. For example, Loiseau et al. [28] measured the ability of mixtures of aluminum with gelled NM to accelerate a flyer plate. They found for aluminum particles from 3.5–55 μm in diameter, that the detonation products delivered more energy to the flyer plate than the baseline explosive within 1–3 μs, and concluded that the aluminum reaction begins very close to the detonation sonic plane. In mixtures of NM and packed beds of aluminum particles, Kato et al. [29] observed a detonation pressure increase due to Al reaction about 2.5 μs behind the leading shock for 8 μm Al particles. Additional evidence that aluminum can react promptly is given by recent experimental results that a mixture consisting of fine aluminum particles mixed with water (with 10% added hydrogen peroxide) can support the propagation of a detonation wave [30, 31]. This implies that aluminum powder must be capable of reacting with water on a microsecond timescale to ensure that the propagation of the detonation front is self-sustained. Since the oxidizers present in the detonation products of common CHNO explosives consist primarily of water, with smaller amounts of carbon dioxide and carbon monoxide present, it is reasonable to assume that aluminum can react with the water in the products at the extreme conditions behind the detonation front or during the early stages of product expansion. Despite the evidence that aluminum can react on a microsecond timescale within detonation products, previous models for the propagation of blast waves from aluminized explosives have largely ignored this observation. Within the blast and shock wave community, it is often assumed that no particle reaction occurs during the detonics stage, and the particles then react with the combustion products and surrounding air on millisecond timescales, with the reaction rate assumed based on the wealth of single particle

combustion experimental results available at relatively low pressure and quiescent conditions (for example, see the particle reaction time correlations of Beckstead [32]).

Particle sizes used in aluminized explosives have ranged over 4 orders of magnitude, from 100's of nanometers to millimeters. Although nanometric aluminum particles were expected to react more rapidly than larger particles and contribute significantly to the blast strength, the predicted improvement in blast performance with adding nanoaluminum powder to an explosive has largely not been realized. Contributing factors to this include the difficulties in deagglomerating and dispersing nanopowder uniformly within an explosive, and the lower active aluminum content of the powder relative to larger particles due to the pre-existing oxide layer which represents a larger fraction of the overall mass. For particles in the micrometric range (e.g., 1-200 μm), previous studies showed little dependence of the particle size on the blast enhancement [15, 33, 34]. This is not consistent with most existing particle reaction models in which the reaction rate is determined by the amount of particle surface area available for reaction. We will return to this issue of the lack of dependence of particle size on blast performance and the implications for the particle reaction mechanism later in the discussion section.

Another parameter that influences the blast performance of aluminized explosives is the particle mass loading. As metal particles are mixed into an explosive, the explosive is diluted, reducing the mass fraction of explosive in the charge. However, the energy release from the reaction of the metal particles, which is larger on a volumetric basis than that of the explosive itself, partially compensates for the dilution effect. If the particle mass fraction is maximized, two other factors come into play. First, the resulting heterogeneous explosive will be highly fuel-rich and there will be insufficient oxidizer in the detonation products to fully react the metal. Secondly, the heat loss to the metal particles will reduce the temperature in of the products, and may inhibit or prevent the reaction of the particles altogether. In an earlier extensive series of experiments with packed beds of metal particles saturated with the liquid explosive sensitized nitromethane (the solid mass fraction varied from 76–80%, for aluminum particles larger than 8 μm), we observed a range of different particle reaction behaviours and blast effects, depending on the particle and charge size [4]. In many cases, the particles did not fully react, making it difficult to systematically determine the influence of particle size and mass loading on the blast enhancement from the metal particles. Similar effects were also observed by Trzciński & Maiz [5] for fully-dense nitromethane-particle mixtures.

In addition to the particle mass loading, another parameter that strongly influences the blast performance from metalized explosives is the scale of the charge, which governs the residence time of the particles within the hot detonation products before expansion cooling of the products may quench further particle reaction. From experimental results with kg-scale charges containing packed beds of magnesium particles saturated with nitromethane, a critical charge size for particle reaction was clearly observed, which depends on particle size [35]. The particle reaction behaviour and blast wave parameters will not be preserved with a change in scale. The importance of considering the scale in interpreting results regarding the effect of

particle size on blast enhancement in aluminized explosives has been pointed out by Peuker et al. [15] who carried out experiments with sub-gram quantities of aluminized explosive.

The trade off between dilution and enhanced energy density effects with the addition of particles suggests a critical mass fraction should exist that optimizes the explosive blast performance. The optimum mass fraction will depend on the type of reactive particle used as well as the nature of the explosive, and is best determined experimentally. To find the optimum particle mass loading with the nitromethane-particle system, it is necessary to gel the NM to enable the suspension of the particles. This technique was used by Loiseau et al. [28] and Trzciński et al. [36], who carried out experimental studies in which nitromethane was gelled with the addition of 4 wt% PMMA to allow a reduction in the particle loading. Trzciński et al. [36] investigated the effect of adding different fractions (15–60 wt%) of an Al-Mg alloy on the detonation properties and blast wave properties in a confined area from 200 g cylindrical charges. The highest peak overpressure and impulse values at 2 m from the charge were found for explosives with a particle mass fraction of 30%. The mean particle size was 63 μm.

In the present study, gelled nitromethane is also used as the base explosive, with various mass fractions of aluminum, magnesium or glass particles added. Of particular interest is the effect of varying the particle size as well as the mass fraction on the blast wave properties. The motivation of the work is to determine if the rapid (sub-millisecond timescale) reaction of aluminum in detonation products that has been observed in earlier detonics experiments can be shown experimentally to directly contribute to blast wave performance for charges with a prototypical scale (kg quantities) and a particle mass loading in a range that ensures uniform reaction of the particles. In the following sections, the experiments will first be described (section 5.2), followed by a description of the pressure gauge analysis and video data reduction procedure (section 5.3). Presentation and discussion of the experimental results are given, respectively, in section 5.4 and 5.5 before the conclusions (section 5.6). Additional results are given in the appendix.

5.2 Experimental overview

The baseline explosive charge utilized a thin-walled G40 light bulb for a casing (1–mm–thick, nominal dia of 12.7 cm), with the filament removed, and filled with nitromethane (NM). The NM was gelled to the consistency of liquid honey to suspend the particles by adding 4 wt% polymethyl methacrylate (PMMA), with 0.4 wt% of 3M K1 glass microballoons (GMB) added to sensitize the mixture. This explosive mixture was previously used in another study [28]. Various sized spherical aluminum powders (H-10, 13 μm dia; H-50, 54 μm dia; H-95, 114 μm dia; Valimet, Stockton, CA) were added at mass fractions ranging from 10–50%. Since the charge volume was constant at about 1 L, the fraction of gelled NM, as well as the Al mass fraction varied between trials. Tests were also carried out with spherical glass particles (+325/-170 mesh; 66 μm dia) to serve as a non-reactive particle case for comparison, as well

as a limited number of trials using spherical Mg powder (GRAN 17, 240 µm dia; Reade, PA). The charges were detonated by inserting a detonator (Reynolds RP-83) into a booster charge of 85.7–92.7 g (depending on the trial, see trial matrix in Table 5.1) of C-4 formed by hand, placed within a plastic sphere and held in place at the center of the charge with a glass tube through which the detonator was inserted. The charge was placed on the top of a wooden post, with a height of burst of 1.52 m (HOB $\approx$ 12 times the charge diameter). For each trial, the blast overpressure was recorded with three fast-response (1.5 µs risetime) piezoelectric pressure transducers mounted in lollipop-style gauges (dia 30 cm). The transducers were located at 1.0 m (PCB 113B26/PCB 113A31 depending of the trial), 1.5 m (PCB 113A31) and 2.0 m (PCB 113A31) from the charge, with the furthest gauge at almost 90° as shown schematically in Fig. 5.1. The gauge at 2.0 m is also visible behind the charge in Fig. 5.2. The distance of this gauge from the charge was chosen such that the ground-reflected wave arrived at the transducer location after the end of the positive phase of the blast wave signature so that the blast overpressure profile was not influenced by the reflected wave.

Table 5.1 Trial matrix. The baseline corresponds to the gelled NM + 0.4 wt% GMB + 4 wt% PMMA. P_0 and T_0 corresponds, respectively, to the atmospheric pressure and temperature.

Trial	Material	Particle mass fraction	Mean particle size (µm)	C4 booster mass (g)	Mass mixture (g)	P_0 (kPa)	T_0 (°C)
#0	Baseline	-	-	87.2	979.2	92.79	24
#1	H-10 Al	10%	13	88.9	1039.8	93.12	26
#2	H-10 Al	30%	13	92.2	1183.5	92.71	26
#3	H-10 Al	40%	13	91.3	1257	93.59	26
#4	H-50 Al	10%	54	87.6	1035.3	92.96	25
#5	H-50 Al	20%	54	90.8	1106.4	92.79	24
#6	H-50 Al	30%	54	88.89	1179.5	92.89	25
#7	H-50 Al	40%	54	87.7	1281.3	93.67	22
#8	H-50 Al	40%	54	86	1303.4	92.96	25
#9	H-95 Al	10%	114	90	1044.6	93.19	25
#10	H-95 Al	30%	114	85.7	1175.4	92.76	26
#11	H-95 Al	40%	114	92.2	1298.5	93.7	25
#12	H-95 Al	50%	114	87.7	1407	93.2	26
#13	Gran 17 Mg	10%	240	86	1024.6	92.94	21
#14	Gran 17 Mg	20%	240	91.7	1051.8	93.75	24
#15	Gran 17 Mg	30%	240	88.8	1085.7	92.92	23
#16	Gran 17 Mg	40%	240	88.6	1140.7	93.83	21
#17	Glass beads	10%	66	92.7	1038.5	93.21	23
#18	Glass beads	30%	66	87.4	1169.9	92.75	22
#19	Glass beads	50%	66	87.3	1378.5	93.19	22

The motion of the blast front was visualized using two Phantom 1610 high-speed video cameras recording at 16,000 frames/s (camera 1) and 35,000 frame/s (camera 2), respectively. The camera 1 operating at the slower speed had a higher resolution (1280 x 800 pixels) and was used for the analysis of the shock wave motion. This camera was offset to the left relative to the charge to provide the maximum field of view, as shown in Fig. 5.1 ($C'E$ = 1.67 m). The distance from the camera to the point C' shown in Fig. 5.1 was CC' = 34.50 m. The resulting absolute Euclidian distance from the camera to the charge was CE = 34.54 m. To enhance the visualization of the blast front, a zebra board (width of stripes is about 15 cm) was placed behind

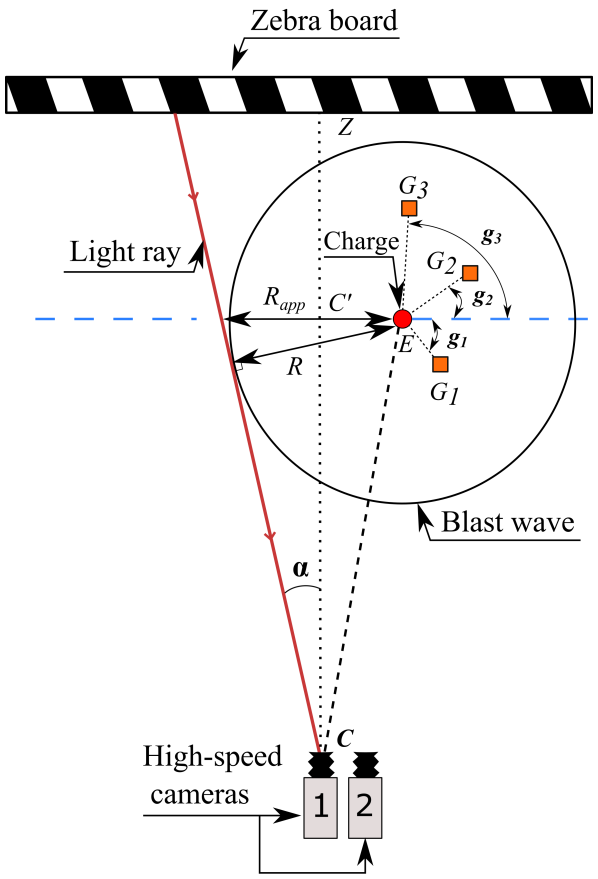

Fig. 5.1 Experimental overview (top view). The cameras were focused on the charge plane (dashed blue line). When the blast is viewed through a certain angle (α), the apparent blast radius (R_{app}) overestimates the actual blast radius (R). The optical axis of the camera 1 (CZ) is quasi perpendicular to the charge plane. The pressure gauges denoted G1 ($\sphericalangle g_1 = 54.1°$), G2 ($\sphericalangle g_2 = 53.8°$), G3 ($\sphericalangle g_3 = 88.4°$) are located, respectively, EG1 = 1.0 m, EG2 = 1.5 m, and EG3 = 2.0 m from the charge. Camera 2 was only used to visualize the fireball structures (section 5.4.1).

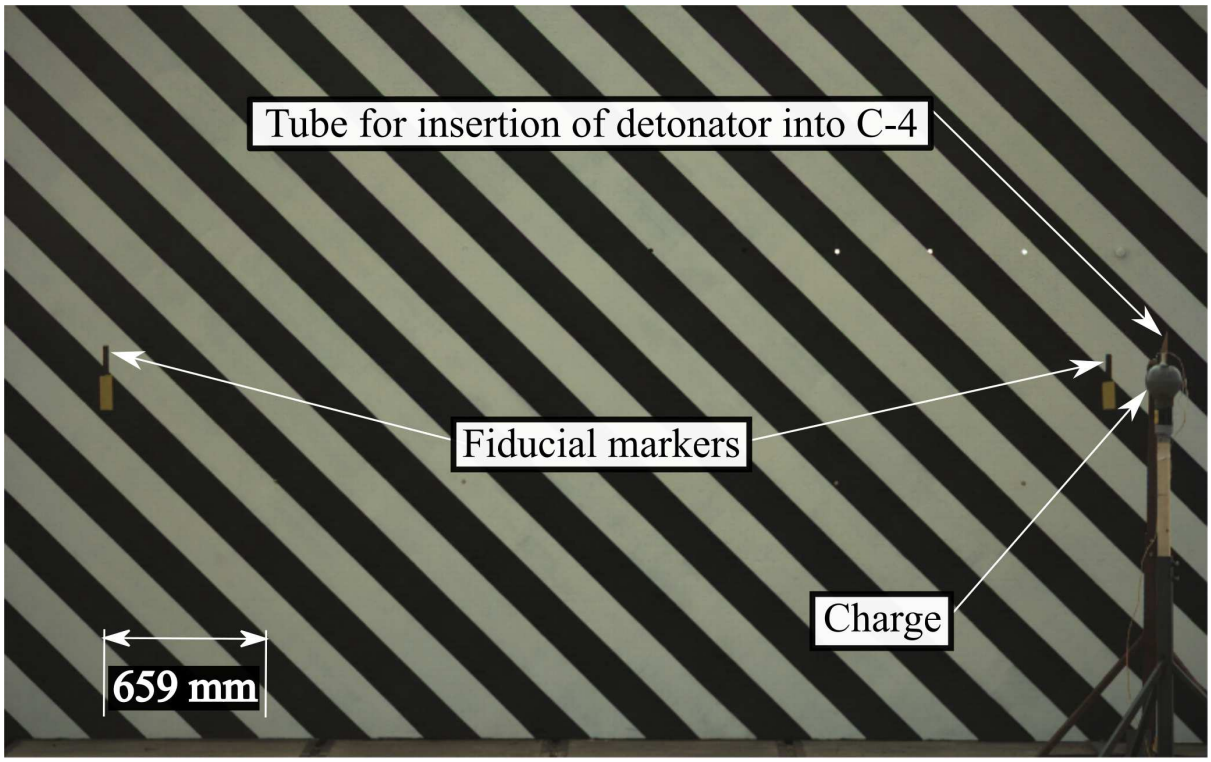

Fig. 5.2 Photograph of the experimental setup with zebra board backdrop (front view). The scale shown is in the plane of the zebra board.

the charge at a distance of $C'Z$ = 5.00 m, resulting in a distance of CZ = 39.50 m between the camera and the backdrop. The camera was focused on the plane of the charge center. Using the two black fiducial markers on the backdrop (shown on Fig. 5.2), spaced 3.95 m apart, for scaling, and with the camera resolution, the physical size of one pixel in the plane of the backdrop is estimated to be 3.7 mm. The corresponding size of a pixel in the plane of the charge, is calculated to be 3.2 mm ($= 3.7 \times \frac{CC'}{CZ}$). This value multiplied by the blast radius measured in pixels gives the value R_{app}. For all the trials, to increase again the field of view, the camera was rotated slightly to the left so that the charge center was just out of view to the right. Since the rotation angle is relatively small ($\approx 0.4^\circ$), the value of R_{app} is not expected to vary significantly and, consequently, no additional correction has been applied. Camera 2 was set to a resolution of 1152 x 400 pixels and was placed adjacent to camera 1 slightly to the right as shown in Fig. 5.1. This camera was used exclusively for the qualitative analysis of the fireball structures in section 5.4.1. Contrary to camera 1, the charge is in the field of view of camera 2. In total, 20 trials were conducted with, respectively, 1 trial with the baseline charge (95.6 wt% gelled NM + 4 wt% PMMA + 0.4 wt% GMB), 12 trials conducted with added aluminum powder (3 with H-10 Al, 5 with H-50 Al, 4 with H-95 Al), 4 with magnesium powder (GRAN 17 Mg), and 3 trials conducted with added spherical glass beads. A summary of the trials conducted is presented in Table 5.1 and the videos of selected trials are available online as supplementary materials.

5.3 Analysis methodology

In this section, the different methods for extracting the blast properties are described. Since the blast properties may depend on the actual distance from the charge, to avoid confusion with the terminology, we denote the near field as the region up to 2 m from the charge, the mid-field region 2–3 m from the charge, and the far-field region beyond 3 m from the charge.

5.3.1 Blast overpressure profiles from pressure gauges

The pressure-time histories were recorded by three transducers placed at 1.0 m, 1.5 m and 2.0 m from the charge. The transducers were located close enough to the charge that in most cases they were engulfed by the fireball, with the farthest transducer (at 2 m from the charge) typically near the maximum extent of the fireball. The non-uniform density field within the fireball, which is manifested by the conical jets that are visible projecting out of the fireball interface, leads to fluctuations in the pressure signals. Misalignment of the face of the lollipop gauge with the direction of travel of the blast wave can also generate expansion waves from the edge of the lollipop which influence the pressure recorded shortly after the pressure reaches a maximum. An example of the overpressure history (i.e., the pressure above atmospheric pressure, $\Delta P = P - P_0$) recorded at 2.0 m from the charge is shown in Fig. 5.3 for the trial with the charge containing 30 wt% of H-50 Al. The peak blast overpressure (ΔP_s) corresponds to the maximum overpressure value. Values of all peak overpressures at 2.0 m from the charge are included in the appendix (Tables 5.5 and 5.6). The blast time of arrival corresponds to the time separating the beginning of the oscillatory signal generated by the burst of the detonator (exactly correlated with time zero in Fig. 5.3) and the time of the maximum overpressure. Note that the previous definitions may introduce error in the estimation of the peak blast overpressure and blast arrival times, especially if the blast front is not associated with the maximum recorded overpressure. This scenario may happen if the gauges are misaligned with the direction of propagation of the blast wave. Both the secondary shock and the ground-reflected wave are evident on the pressure signal (the timing of the arrival of the ground-reflected shock can also be determined from the high-speed videos). The gauge located at 2.0 m is closest to the zebra board, although the reflected wave from the zebra board arrives at the gauge after a delay of 13.83 ms, which is not visible on the signal shown. The pressure profiles recorded within the fireball (at 1.0 m and 1.5 m from the charge) differ substantially from that of the (modified) Friedlander form [37], making it difficult to determine unambiguous values for the blast duration and peak overpressure. As a consequence, the trial-by-trial comparison of peak overpressure data is not considered at these distances. However, the blast times of arrival at 1.0 m are analyzed globally to evaluate the shortest aluminum reaction timescales. Due to the oscillatory nature of the pressure signal and the difficulty in choosing an unambiguous positive-phase blast duration, the calculated impulse values are not analyzed further.

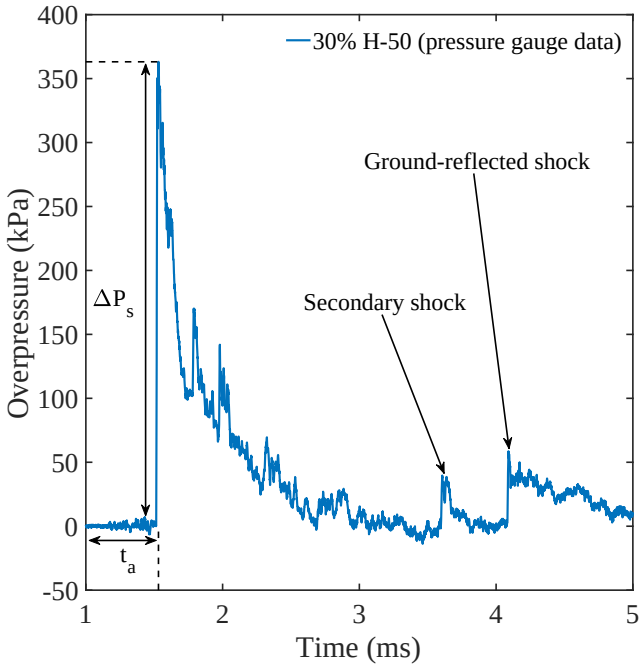

Fig. 5.3 Overpressure profile captured at 2.0 m from the charge in the case of a charge containing H-50 aluminum at a mass fraction of 30% (trial #6).

5.3.2 Video analysis

The blast front trajectories were determined through analysis of the high-speed videography images. To enhance the visibility of the blast wave, the function *find edges* was applied to the images using the open-source image processing software *ImageJ*. Since the vertical motion of the blast wave is perturbed by the flow of detonation products out of the tube holding the detonator, the blast front is tracked along a horizontal line emanating from the charge center. As the location of the blast front extracted from the images (R_{app}) overestimates the actual location (R) due to the parallax effect, a correction is implemented before calculating the blast velocity. The formula used to calculate the actual distance from the blast front to the charge center is given below:

$$R = R_{app} \times \frac{CC'}{\sqrt{R_{app}^2 + CE^2 - 2 \times R_{app} \times C'E}} \tag{5.1}$$

where $R < R_{app}$ is generally excepted when $R = R_{app} = C'E$. The blast trajectory with taking into account the parallax is plotted in Fig. 5.4. Note that the blast wave is not visible until it has propagated about 2 m due to the saturation of the video images from the luminosity of the fireball. Note also that data points are gathered by a group of 2 or 3, at regularly spaced intervals. These points are extracted when the blast front approaches the intersection of two consecutive stripes (shown in the background of Fig. 5.2), where the contrast is optimum. To determine the blast velocity, the blast trajectory is fitted by the monotonic fit of Kleine et al. [38] and then

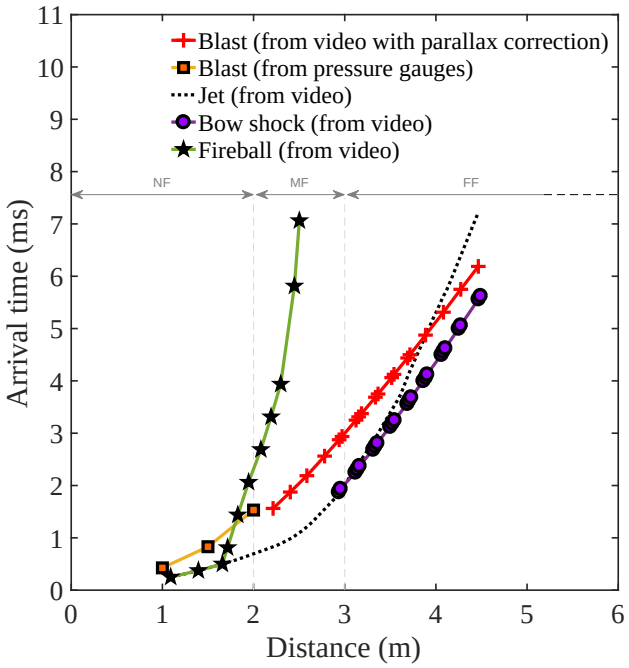

Fig. 5.4 Trajectories of the blast wave with the parallax correction for the case of a charge with 30 wt% of H-50 (trial #6) aluminum particles. Also shown are the blast arrival times obtained from the three pressure transducers as well as the trajectory of the bow shock that is driven by a jet of particles that is projected ahead of the blast front. The approximate trajectory of the maximum extent of the fireball is also plotted. The abbreviations NF, MF and FF correspond, respectively, to near field, mid field and far field.

differentiated. The parallax correction is relatively small, with a typical error in the velocity of about 2% (4% when converted into pressure), with the error highest when the blast wave is furthest from the charge. An approximate estimation of the trajectory of the maximum extent of the fireball is also plotted in Fig. 5.4. As mentioned previously, the first two gauges are engulfed in the fireball and the last gauge is typically very close to the contact surface.

The peak blast overpressure can be extracted by using the blast wave Mach number together with the Rankine-Hugoniot relation provided the local temperature and pressure are known. For each trial, the local temperature (ranging from 21–26°C) and atmospheric pressure (ranging from 92.71 to 93.83 kPa at an altitude of 700 m) were recorded (see Table 5.1) and used in the Rankine-Hugoniot relations. Further details of the method of determining the peak blast overpressure in this way can be found in an earlier publication [10]. Since the direct visualization of the blast front on the tracking line is not generally possible for distances from the charge less than 2.0 m, the peak blast overpressure is extrapolated in the near field by inferring the blast curvature, as shown in Fig. 5.5, for a direct comparison with gauge data. The results of this comparison are gathered in Table 5.7, in the appendix.

When extracting the blast wave trajectories, care must be taken to distinguish the actual blast front from the localized pressure disturbances (or bow shocks) created by the jets that are formed during the explosive event, as illustrated in Fig. 5.6. Due to the white color of these jet-like

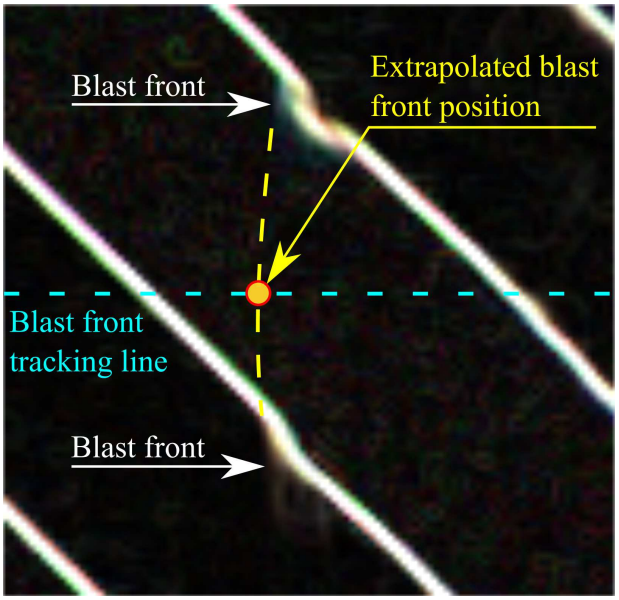

Fig. 5.5 Processed image with the *find edges* function showing the extrapolation method of the blast front in the near-to-mid field, on the blast front tracking line.

structures, they likely are comprised of agglomerated aluminum oxide particles or perhaps partially-reacted aluminum in the case of large initial solid mass loading. The bow shocks may be either ahead of or behind the blast front. Since the two features are not propagating at the same speed, one propagating in ambient air, the other one in the post-shocked medium, they ultimately merge after some time. In Fig. 5.4, trajectories of the jet and the bow shock visible ahead of the blast front are plotted. Initially separated in space, the blast front and the bow shock tend to converge while propagating outwards. On the contrary, the bow shocks tend to separate from the particle jets, due to aerodynamic drag with the surrounding atmosphere. The effect of the localized bow shocks on the peak blast overpressure has been discussed in previous publications [10, 11].

5.4 Results

5.4.1 Visualization of fireball expansion and blast propagation

To illustrate the dynamics of the fireball expansion and afterburning and the blast wave propagation, single frames from the video records of camera 2 have been extracted from a series of trials. Fig. 5.7 shows the images for the detonation of the baseline gelled nitromethane explosive. After about 0.5 ms, the fireball is highly luminous, but the processed image indicates that small-scale perturbations and jet-like structures are present on the fireball interface, likely due to action of the Rayleigh-Taylor (RT) instability. After 1 ms, the expansion has cooled the fireball gases and the interface between the detonation products and surrounding atmosphere

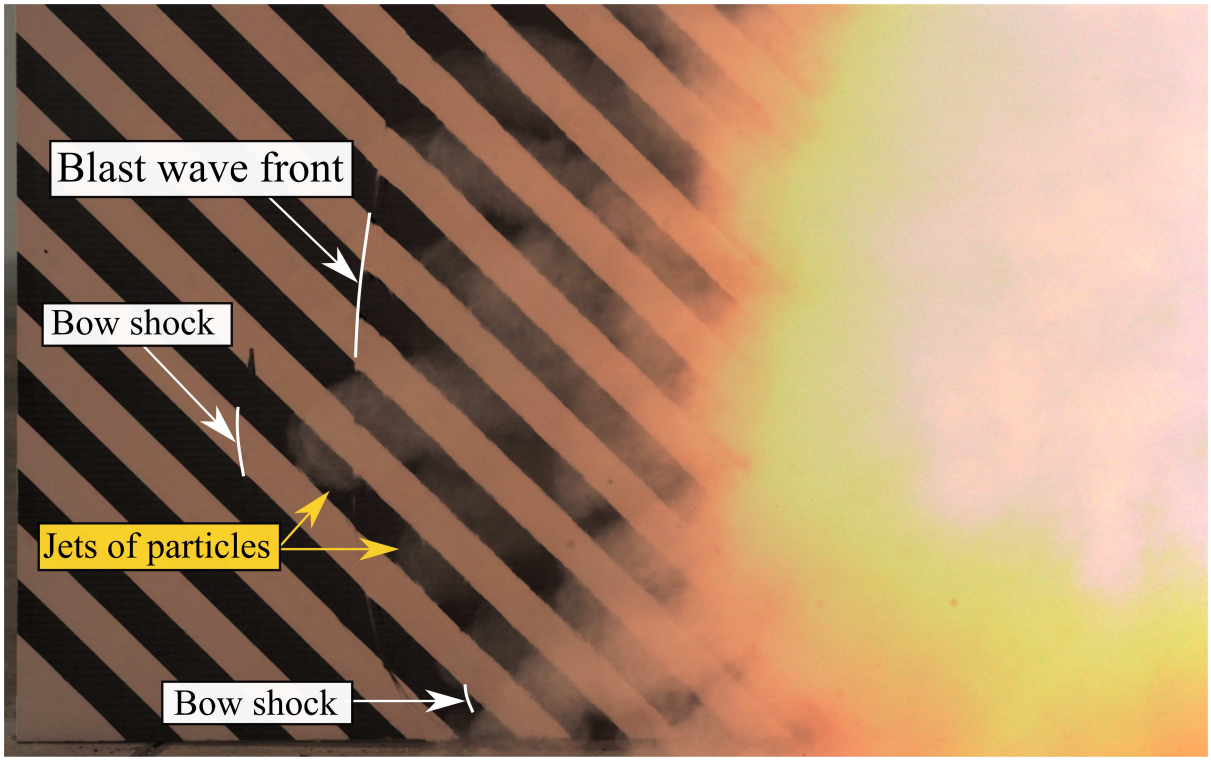

Fig. 5.6 Single frame from the video record of a test for a charge with 30 wt% of H-50 (trial #6) aluminum particles illustrating shock tracking against zebra board.

appears highly convoluted. The fireball continues to expand and cool until the secondary and the ground-reflected waves propagate up through the fireball, enhancing the mixing and afterburning of the products. The top interface of the highly luminous region in the image at 4 ms corresponds to the reflected wave that is propagating upwards at this time.

Fig. 5.8 shows the effect of adding 30 wt% of inert glass particles to the gelled nitromethane. The image taken at 0.314 ms shows the luminous fireball and the processed image indicates that conical jet-like structures are present, perhaps caused by entrainment of the glass particles into the RT perturbations. Fine streaks of particles are also present in this image near the fireball interface, which may be from the motion of the fine glass particles from the shattering of the glass lightbulb casing. At times of 1 ms and later, the fireball has expanded and cooled. The secondary and the ground-reflected waves do not induce significant afterburning of the soot from the NM products, due to the absorption of heat by the added inert glass.

Fig. 5.9 illustrates the fireball afterburning and blast wave propagation in the case of a charge with 30 wt% H-50 Al particles. Prominent conical particle jets form and project ahead of the primary blast front, which is only visible emerging from the fireball interface mixing region after about 2 ms. The fireball intensity does not diminish during the recording time of the video (10 ms), as the afterburning of the soot from the detonation products as well as energy release from the aluminum reaction continues to contribute to the fireball luminosity. The reader can refer to the videos available online for a dynamic visualization of Figs. 5.7, 5.8 and 5.9.

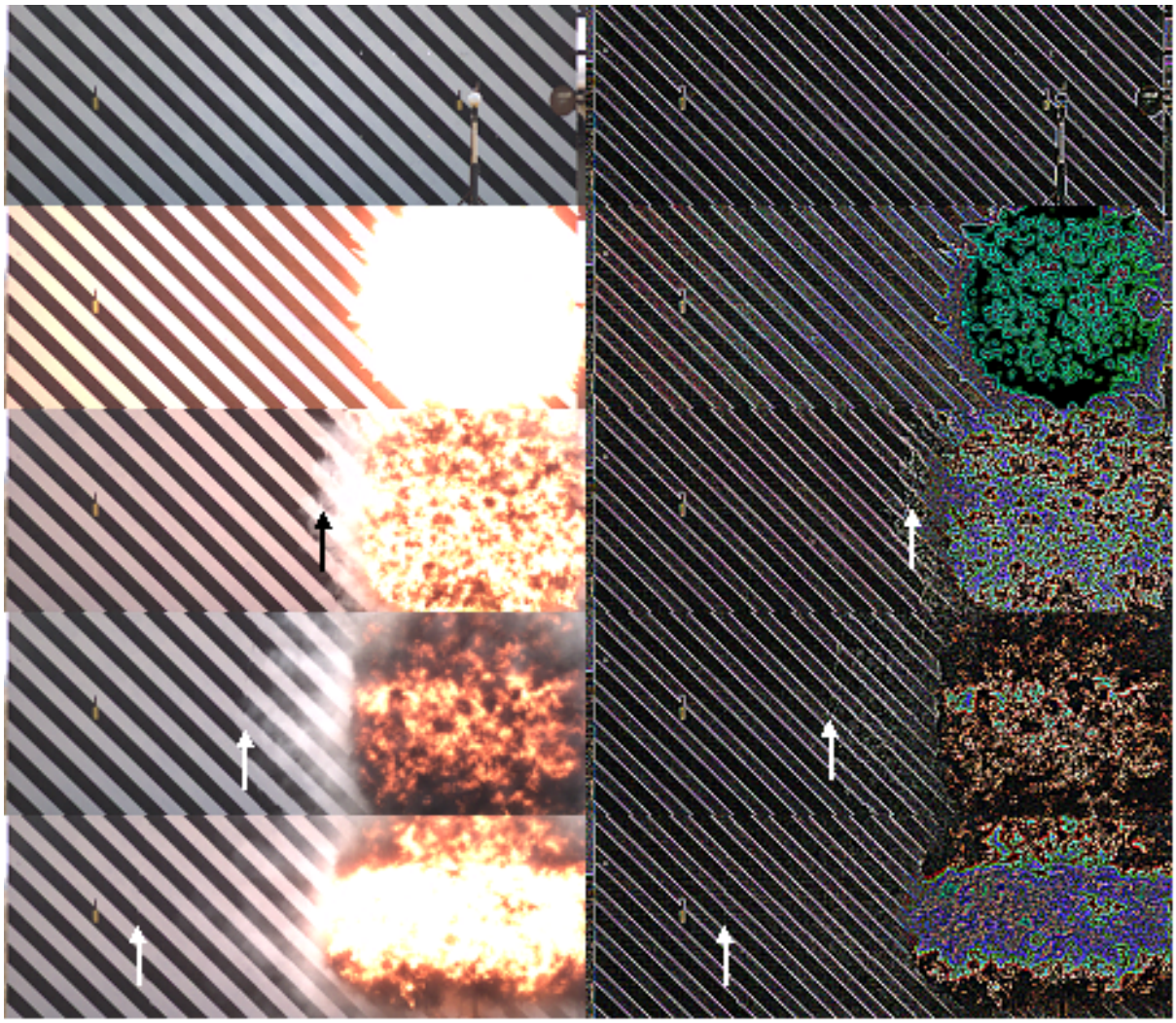

Fig. 5.7 Single frames from the video record of the detonation of a charge containing the baseline gelled nitromethane explosive (trial #0). Images on the left are the original video images and the images on the right are the same images, but after an edge Laplacian 5x5 filter has been applied to highlight the gradients in the image. Times for the image are (top to bottom): 0 ms, 0.514 ms, 1.000 ms, 2.000 ms, and 4.000 ms, respectively. The arrows indicate the locations of the blast wave.

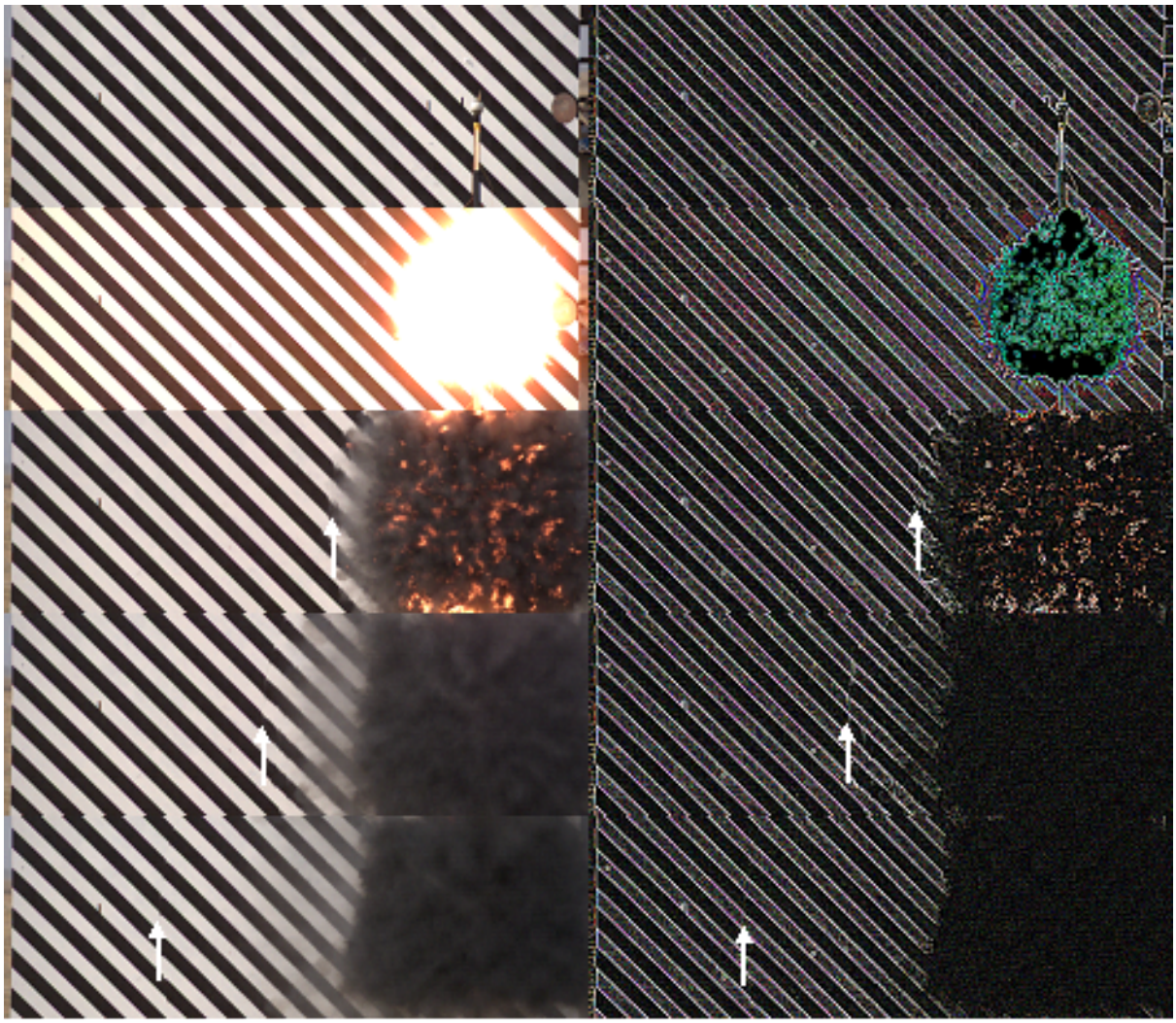

Fig. 5.8 Single frames from the video record of the detonation of a charge containing 30 wt% glass particles (trial #18). Similar to Fig. 5.7, the images on the left are the original video images and the same images are on the right, after an edge Laplacian 5x5 filter has been applied to highlight the gradients in the image. Times for the image are (top to bottom): 0 ms, 0.314 ms, 1.000 ms, 2.000 ms, and 4.000 ms, respectively. The arrows indicate the locations of the blast wave.

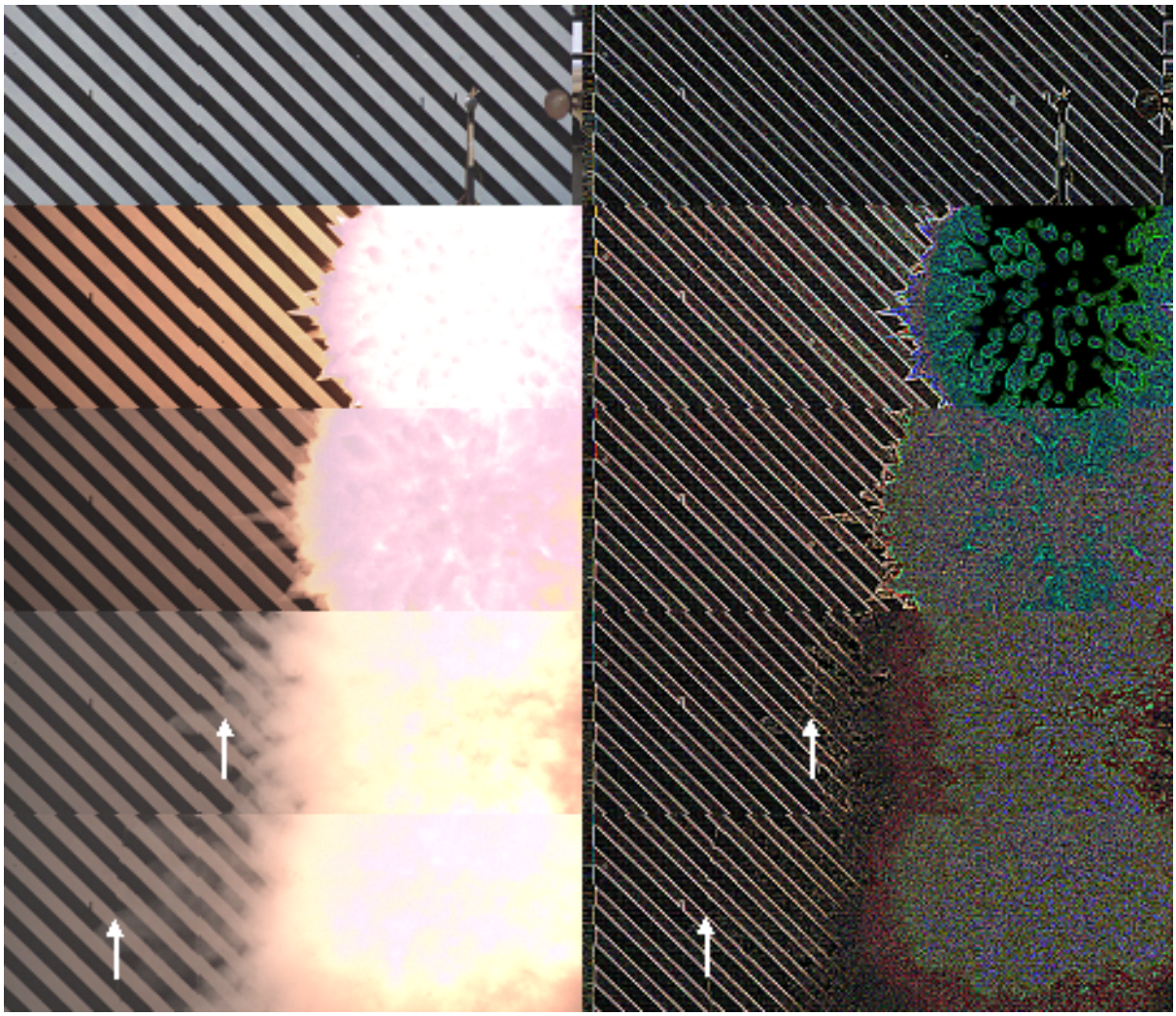

Fig. 5.9 Single frames from the video record of the detonation of a charge containing 30 wt% H-50 Al particles (trial #6). As in Figs. 5.7 and 5.8, the images on the left are the original video images and the images on the right have been processed with an edge Laplacian 5x5 filter to highlight the gradients in the image. Times for the image are (top to bottom): 0 ms, 0.657 ms, 1.000 ms, 2.029 ms, and 4.000 ms, respectively. The arrows indicate the locations the blast wave.

To illustrate the variation of luminosity between these three trials (#0, #6, #18), the spatially averaged pixel intensity ($\mathscr{L}$) is defined as:

$$\mathscr{L} = \frac{\sum_{i=1}^{i_{\max}} \sum_{j=1}^{j_{\max}} P_{i,j}}{N} \tag{5.2}$$

with $i_{\max} = 1280$, the number of pixels by width, $j_{\max} = 800$, the number of pixels by height, $N = i_{\max} \times j_{\max} = 1280 \times 800 = 1,024,000$ the total number of pixels in a frame and $P_{i,j}$, the intensity value of the pixel of coordinate (i, j) from the original 16-bits cine (Phantom format) files is plotted as a function of time, in Fig. 5.10. The cine file format is preferred to the RGB format to avoid correction of the pixel intensity value according to pixel color. For each trial, the intensity of the first image is subtracted from all the images so the $\mathscr{L}$ value is equal to 0 before detonation of the charge. The detonation time corresponds to the start of the sharp rise of the luminosity that saturates the camera. The integrated intensity decreases sharply after the detonation but increases again during the afterburning phase which occurs after the primary blast wave reflects off the ground, after about 2 ms. The value of $\mathscr{L}$ captured at a mass fraction of 30% H50-Al is significantly larger than that of the baseline. Conversely, adding the same mass fraction of glass particles reduces the luminosity considerably. Values of $\mathscr{L}$ can be even negative due to the soot formed that causes the video image to be darker than the initial image before the detonation. Note also the absence of an afterburning phase for the inert particles. The analysis of the spatially integrated luminescence presented here remains purely qualitative due to the numerous camera settings that influence the pixel intensity, such as the lens aperture, exposure time, and the Extreme Dynamic Range (EDR) setting, which is a feature of the operation of Phantom cameras that reduces the specific intensity of pixels that are approaching saturation.

5.4.2 Fireball expansion and blast propagation (pressure gauges and videography)

The relative position of the maximum extent of the luminous fireball and the shock wave for the three previous trials is shown in Fig. 5.11. Note that the maximum extent of the fireball is approximate and cannot be considered a precisely defined measurement since in cases where some of the pixels on the camera sensor are saturated, some charge leakage (or pixel bleed) between adjacent pixels can occur. The blast arrival times captured with the pressure gauges are also reported. In general, the blast time of arrival does not match perfectly with the blast time of arrival obtained with the videography analysis in the mid field. The discrepancy is explained by the fact that the pressure gauge at 2.0 m from the charge is not located within the field of view of camera 1 (see Fig. 5.1) and implies that the blast propagation is not isotropic. Nevertheless, the blast times of arrival obtained from videography measurements are offset to match the arrival time at the pressure gauge in the mid field (Fig. 5.11). As mentioned before, for the reactive

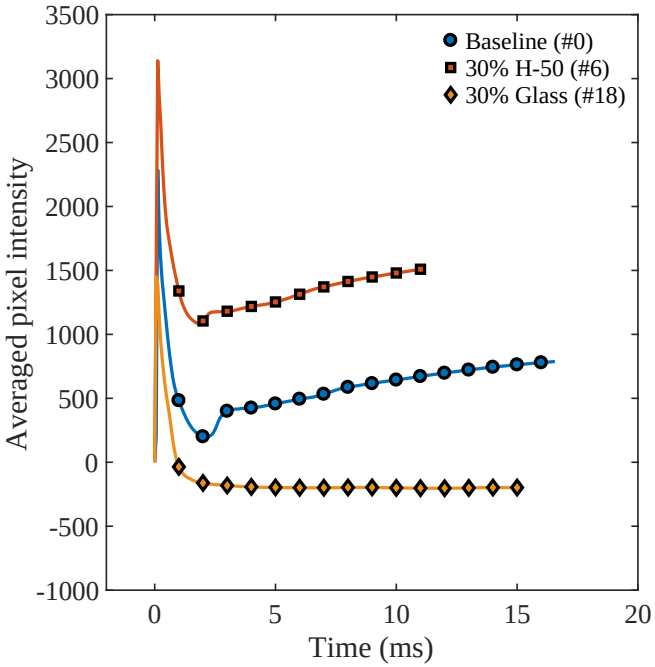

Fig. 5.10 Comparison of spatially-averaged pixel intensity ($\mathscr{L}$) as a function of time between the baseline explosive (trial #0) and with mixtures with 30 wt% H-50 (trial #6) and 30 wt% glass beads (trial #18).

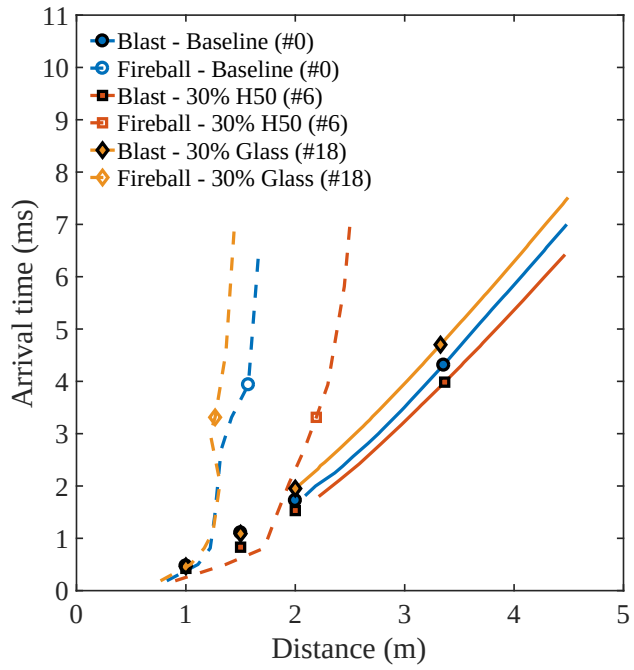

Fig. 5.11 Blast front and fireball trajectories plotted for the baseline explosive (trial #0) and with mixtures with 30 wt% H-50 (trial #6) and 30 wt% glass beads (trial #18).

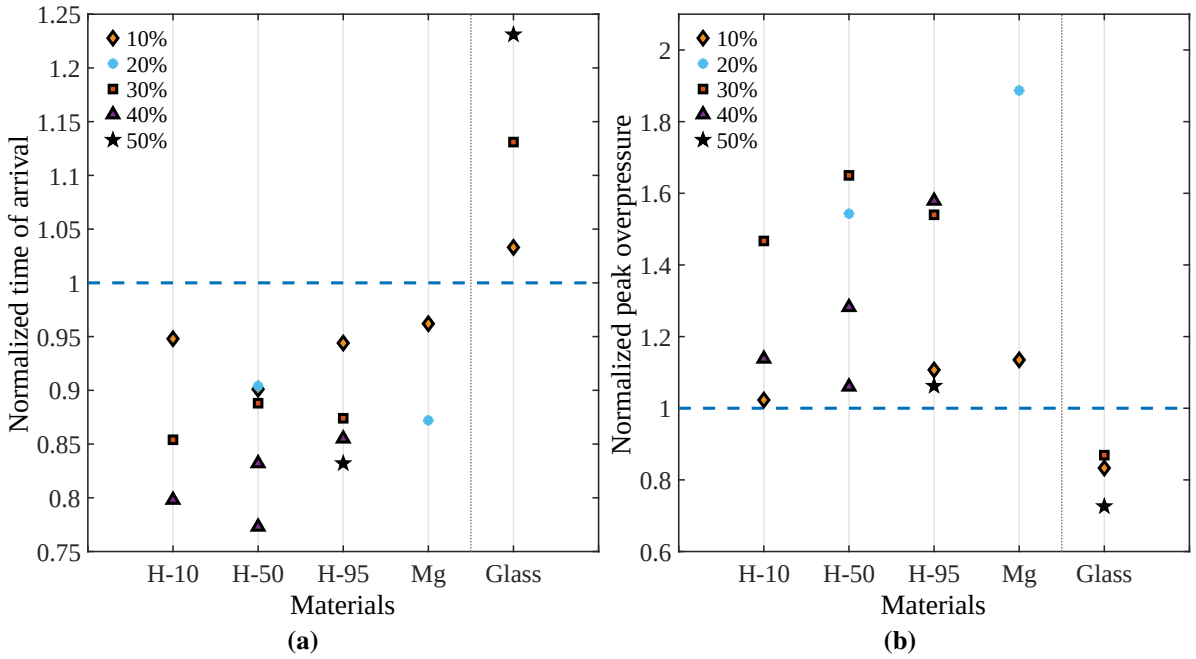

Fig. 5.12 (**a**) Effect of the mass fraction on the normalized blast times of arrival ($t_a/t_{a-baseline}$) calculated from pressure gauge data at 2.0 m from the charge and sorted by type of powders. The baseline value (gelled NM without particles) is represented by the horizontal dashed blue line. (**b**) Same plot but for the normalized peak blast overpressure ($\Delta P_s/\Delta P_{s-baseline}$).

case (30% H-50), the first two pressure gauges are engulfed in the fireball and the last gauge located typically very close to the fireball surface.

Analyzing the blast times of arrival is of interest to highlight the contribution of the particle reaction to the blast wave propagation. The energy deposited into the gas by the reaction of the particles may couple with the blast front and increase its velocity. Conversely, the absorption of the explosive energy by inert particles may reduce the energy available to support the blast, hence decreasing the blast velocity. Figure 5.11 indicates that the blast times of arrival are smaller for the trial with aluminum particles compared to the baseline from 0.426 ms (at 1.0 m) and more significantly from 0.830 ms (at 1.5 m). This suggests that the aluminum reaction contribute to increasing the blast velocity. Conversely, the blast time of arrival is higher when glass particles are added to the explosive mixture indicating that the addition of inert particles contributes to decreasing the blast velocity. A contraction of the fireball size after a few milliseconds due to rarefaction waves is visible for the inert case (30% glass) and for the baseline case, but not observed for the trial with aluminum. The comparison between the trajectories of the fireballs indicates that the fireballs generated by the aluminized explosives grow to a larger size than the fireballs generated with the baseline explosive. Conversely, the size of the fireball generated by the explosive diluted with inert particles tends to be smaller than that of the baseline explosive.

5.4.3 Blast time of arrival in the near-to-mid field (pressure gauges)

Figure 5.12a summarizes the times of arrival, for a given type of powder, at a distance of 2.0 m from the charge. Values of times of arrival for the different trials are normalized by the time of arrival for the baseline charge (i.e., $t_a/t_{a-baseline}$). The performance of the baseline is equal to 1 and is represented by the dashed blue line. When the explosive is diluted with glass particles, the blast times of arrival are systematically delayed compared to the baseline. The arrival times increase monotonically with the mass fraction by up to 23% of the baseline value at a mass fraction of 50%. Conversely, the addition of reactive (Al or Mg) particles in the gelled NM systematically reduces the blast times of arrival, for all trials tested, compared to the baseline case. The reduction of the arrival times is generally a monotonic function of the mass fraction. The addition of 20 wt% of magnesium particles reduces the blast time of arrival by 13% compared to the pure gelled NM. The addition of 40-50 wt% of aluminum particles typically reduces the blast time of arrival by 17%-23% compared to the baseline explosive depending on the powder considered. Figure 5.12a also indicates that the particle size of the aluminum particles has very little influence on the blast arrival times. Note the variation of the normalized arrival times between the repeated trials (H-50 particles at a mass fraction of 40%). This discrepancy suggests that the small variations of the normalized arrival times, when comparing the different aluminum particle sizes, are on the order of the stochastic variation of the experiments. The blast times of arrival for each trial, recorded by the pressure gauges, are presented in Tables 5.3 and 5.4 in the appendix.

5.4.4 Peak blast overpressures in the mid field (pressure gauge)

Similarly to Fig. 5.12a, the normalized peak blast overpressure values at the same distance are reported in Fig. 5.12b. The graph shows that the peak blast overpressures are systematically augmented for all charges tested with reactive materials and mitigated for all the charges tested with inert glass particles, compared to the baseline. Anomalously, the charge with 20 wt% magnesium particles outperforms all the other charges at enhancing the peak blast overpressures with an augmentation of 89% compared to the baseline, although data were not obtained for higher Mg mass loadings due to problems with the pressure sensors. For charges with aluminum particles, the highest performance was obtained at mass loadings of 30 wt% (H-10, H-50) or 40 wt% (H-95), with an augmentation of 47%-65% compared to the baseline value. This suggests that the peak blast overpressure enhancement does not change monotonically with the mass fraction, contrary to the blast arrival times. This lack of correlation between the arrival times and peak overpressure may be due to the error associated with the extraction method mentioned in section 5.3. Conversely, the addition of 50 wt% of glass particles in the gelled NM mitigates the peak overpressure by around 27%. As observed for the blast arrival times, the normalized peak blast overpressures show little dependence on the aluminum particle size excepted for a mass fraction of 40%. At this mass fraction, the normalized peak blast overpressures with H-95

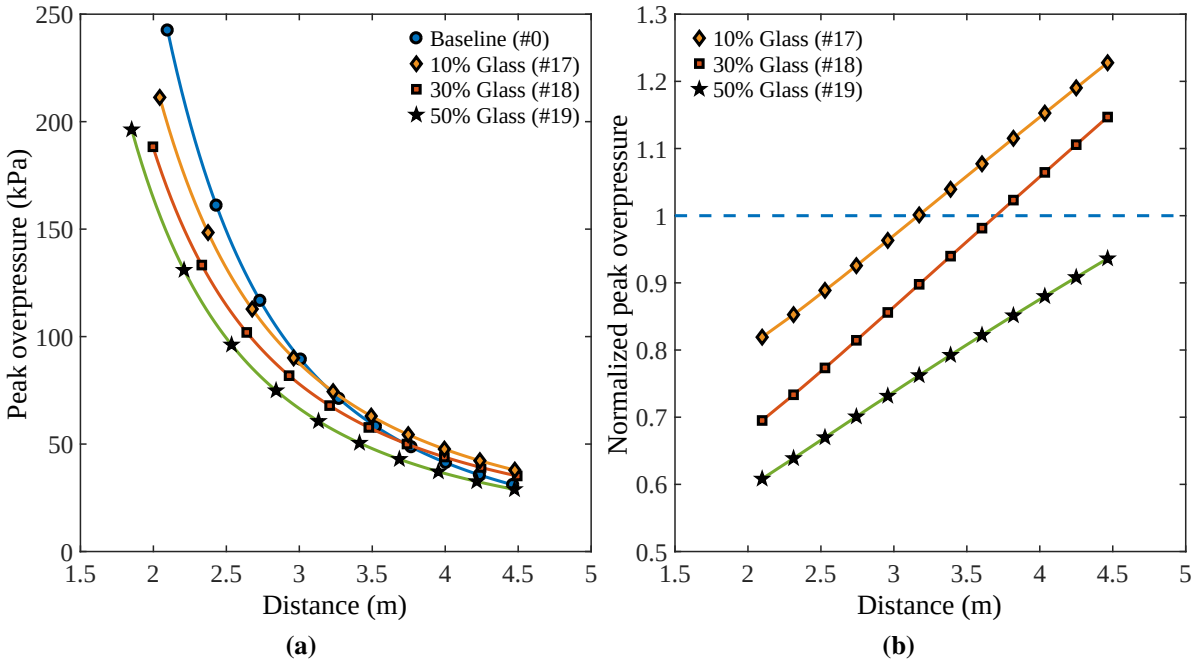

Fig. 5.13 (a) Effect of particle mass fraction on peak blast wave overpressure decays inferred from the blast wave trajectories, for glass (inert) particles. Each of the charges has about the same volume (1 L). The baseline charge (#0) contains only gelled NM with no particles. **(b)** Peak overpressure efficiencies relative to the baseline explosive (dashed blue line).

particles outperforms those obtained with H-10 particles by 44%. Nevertheless, this discrepancy is cautionary due to the stochastic variation between repeated trials (see the results for H-50 particles). All the peak overpressure values are presented in Tables 5.5 and 5.6 in the appendix.

5.4.5 Effect of particle material and mass loading on blast decay in the mid-to-far field (videography)

Figure 5.13a shows the decay of the peak blast overpressure with distance, in the mid-to-far field, for trials with glass particles, with various mass fractions of the additive powder. Note that the relative errors resulting mainly from the tracking of the blast front on the videos are typically of the order of the size of the data markers, and are consequently not shown. To highlight the performance, the normalized peak overpressures are also shown on Fig. 5.13b. As in Fig. 5.12, the performance of the baseline trial is equal to 1 and is represented by a blue dashed line. The peak blast overpressure decays for all the other materials are reported in the appendix in Figs. 5.19 and 5.20.

Adding the glass particles reduces the strength of the blast wave in the mid field, with the reduction in pressure increasing as more glass powder is added (by up to 37.5% at around 2 m). In the far field, the peak blast overpressure recovers almost to the same value as the base explosive charge for 50 wt% addition of glass and even exceeds the baseline case for 10 wt% and 30 wt% addition, by up to 22.8% even though the charges with added glass have a reduced

amount of explosive. This behaviour is consistent with the earlier results from Pontalier et al. [10–13], who attributed the near-field reduction in blast pressure to the energy transfer from the detonation products to the kinetic energy and heating of the inert particles, and the later time blast pressure recovery to the pressure perturbations induced by the particle-flow interactions.

With the addition of reactive particles, Fig. 5.14 shows that in all cases, the particle reaction enhances the strength of the blast wave over the baseline explosive, with the enhancement greatest in the far field. In the mid field, i.e., just outside the maximum fireball radius, the particle reaction counteracts the pressure reduction observed for inert particle addition, such that the peak blast overpressure is higher than that of the baseline case by between 5% (10 wt% H-95) and 27 % (40 wt% H-10) at around 2.2 m. Further from the charge, the combination of the particle reaction and the motion of the particles within the products sustains the peak blast overpressure at a higher level than for the homogeneous liquid explosive, so that the peak blast enhancement with the addition of reactive particles can attain a value of up to almost twice the baseline value (for 20 wt% Mg), at 4.5 m.

The effect of the mass fraction of added particles, for a given type of particle, on the blast overpressure decay is shown in Figs. 5.13 and 5.14. For the addition of glass particles, the attenuation of the blast wave overpressure increases monotonically with the mass fraction, as expected. Conversely, with added H-10 aluminum particles, the blast enhancement increases monotonically with the mass fraction. In the case of H-50 and H-95 particles, the blast enhancement depends on the location from the charge and is not necessarily a monotonic function of the mass fraction. In the far field, the maximum peak overpressure is attained at a mass fraction of 30-40% for H-50 and 50% for H-95. However, this assertion is subject to the scatter observed between the two repeated trials (40% H-50, trials #7 and #8). The results for Mg indicate that the blast enhancement is greatest for a particle mass fraction of 20%, at least in the far field. Note that for aluminum particles, the blast enhancement increases more rapidly when the mass fraction is high (30 - 50%) compared to low mass fractions (10 - 20%).

For aluminum particles, at a specific mass fraction of 30%, Fig. 5.15 shows that the peak blast overpressure exhibits no systematic dependence on particle size. The effects of particle size on blast overpressure at other mass fractions are shown in Fig. 5.20 in the appendix. The results for aluminum particles again do not show a systematic variation with particle size. In the mid field, the smallest aluminum particles yield slightly higher normalized peak overpressures for all mass fractions, whereas in the far field, the larger particles generate larger normalized overpressures at a mass fraction of 10% (after 3.5 m). However, at a mass fraction of 40%, H-10 Al particles yield the highest peak overpressure values in the far field. Fig. 5.20 also shows that with the addition of magnesium particles the normalized peak overpressures in the mid field are comparable to those for aluminum particles, but are lower than the aluminum values in the far field for mass fractions of 10 wt%, 30 wt% and 40 wt%, which is consistent with the smaller specific energy release from magnesium relative to aluminum. The comparison between the peak overpressure values at 2.0 meters from the charge, obtained with the pressure gauge or

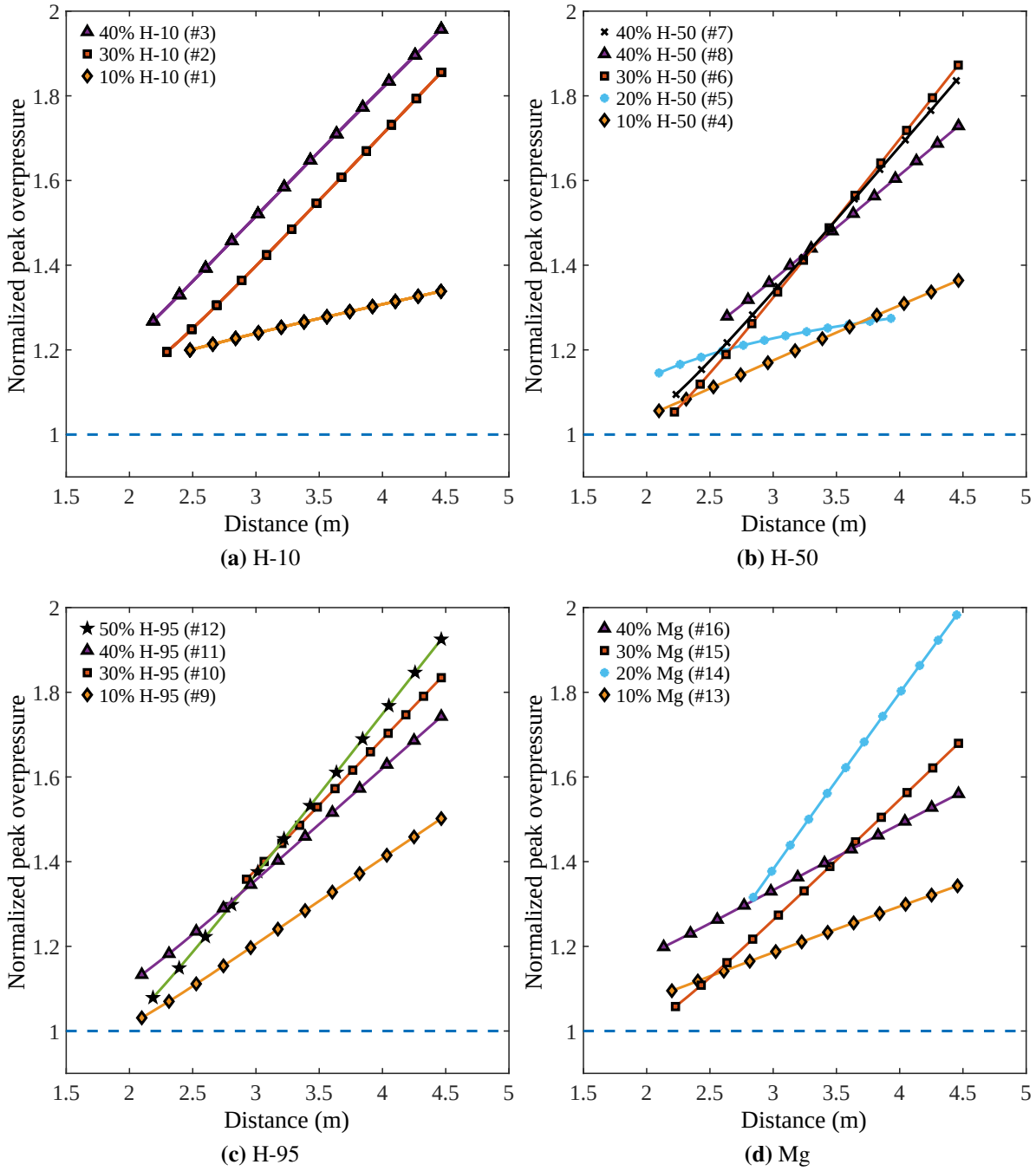

Fig. 5.14 Effect of the mass fraction on the peak overpressure efficiencies relative to the baseline explosive (dashed blue line) plotted for **(a)** H-10 Al, **(b)** H-50 Al, **(c)** H-95 Al and **(d)** GRAN 17 Mg.

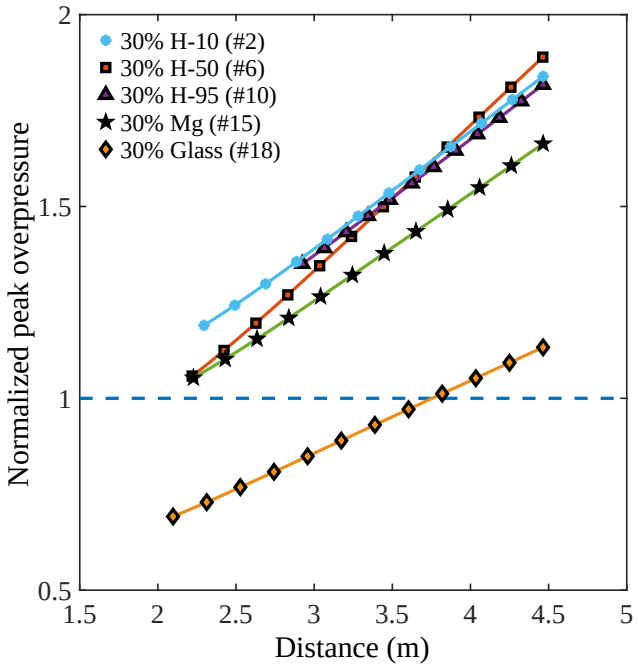

Fig. 5.15 Effect of material and particle size on the peak overpressure efficiencies relative to the baseline explosive (dashed blue line), for a particle mass fractions of 30%.

the videography analysis is shown in the appendix, in Table 5.7. The peak blast overpressure discrepancies between the two methods are not systematic. This observation suggests that the strength of the blast wave is not uniform in every direction.

5.5 Discussion

The results presented in this study show strong evidence of prompt reaction of the aluminum or magnesium particles embedded in the gelled NM mixture. The reactions are sufficiently exothermic to counteract the heat and momentum transfer from the detonation products to the particles, and contribute to enhancing the luminosity (see Fig. 5.10) and size (see Fig. 5.11) of the fireball, as well as the velocity and overpressure of the blast wave (see Fig. 5.12). Conversely, adding inert glass particles serves to absorb some of the explosive energy, which reduces the luminosity and size of the fireball as well as the velocity and overpressure of the blast wave, at least in the mid field. Farther from the charge, some of the kinetic energy of the particles is transferred back to the surrounding gas which leads to a recovery of the blast wave overpressure, in some cases to values above that of the baseline explosive alone (see Fig. 5.13). This blast recovery phenomenon, attributed to the pressure disturbances created by the particle-flow interactions, was described in previous work with explosive charges containing a variety of different embedded particles [10]. The contribution of these disturbances may also depend on the particle size. Small particles tend to adapt more quickly to the flow in comparison with larger particles, and hence transfer their energy to the flow more rapidly [11].

The influence of the energy release from the particles on the blast wave propagation depends on the location of the energy release. If the energy release occurs immediately behind the blast wave, the local increase in gas pressure will promptly enhance the blast overpressure. Even if the particle energy release occurs some distance behind the blast wave, the pressure disturbances generated can catch up to the blast wave in the mid or far field since the local sound speed behind the blast wave is increased due to the shock heating as well as the particle reaction. In general, with the addition of reactive particles, the blast wave peak overpressure increases linearly with distance from the charge, when normalized relative to the baseline explosive, due the effect noted above (see Fig. 5.14). Effectively, the particle reaction continues to contribute to augmenting the blast wave overpressure in the far field due to the continual arrival of pressure disturbances at the blast wave front.

In the near field within the fireball, the blast wave is not directly visible, but the motion of the blast wave can be tracked using signals from the pressure gauges that are engulfed by the fireball. For example, the times for the arrival of the blast wave at the first gauge, located 1.0 m from the charge, are reported in Table 5.2, and are less than for the baseline explosive, which is consistent with the higher blast wave speed noted above. From Fig. 5.11, it is evident that the combustion products fireball extends beyond this pressure gauge for the baseline explosive charge and eventually grows to a radius of about 1.5 m. Hence it is expected that when aluminum particles are added to the explosive, by the time that the blast wave reaches this first pressure gauge, the aluminum particles will have been exposed primarily to the oxidizers within the detonation products, which predominantly consist of water for charges with NM. The minimum observed arrival time is 353 μs, and hence the particles must have started to react before this time. Since the nearest pressure transducer is located 1 m from the charge, with the current diagnostics used, it is not possible to resolve the rate of energy release from the particles at earlier times than this.

It is of interest to consider the nature of this early-time reaction of aluminum with the water in the detonation products. This reaction produces molecular hydrogen gas which will contribute to inflating the size of the fireball. This hot hydrogen gas is highly reactive and it will react promptly when it mixes with the oxygen in the surrounding atmosphere at the contact surface between the detonation products and air. The rate of reaction of the hydrogen will be limited by the mixing rate with the surrounding atmosphere which in turn is influenced by the rate of growth of the perturbations that develop at the contact surface due to the Rayleigh-Taylor instability as the interface decelerates.

In Fig. 5.11, the growth of the radius of the fireball with added aluminum particles begins to separate from that of the baseline explosive as early as 200 μs. This may be due to the production of hydrogen and subsequent reaction with the surrounding air. After this time, the fireball continues to expand over several milliseconds. The reactions within the fireball, due to the particles as well as from residual soot from the baseline oxygen-deficient explosive, are also

Table 5.2 Blast times of arrival for all trials at 1.0 m from the charge indicating the early contribution of the energy release of Al/Mg particles to the blast wave.

Trial	Material	wt%	t_a (ms - 1.0 m)	$t_a/t_{a-baseline}$
#0	Baseline	-	0.474	**1.000**
#1	H-10 Al	10%	0.376	**0.793** $<$ **1**
#2	H-10 Al	30%	0.379	**0.800** $<$ **1**
#3	H-10 Al	40%	0.464	**0.978** $<$ **1**
#4	H-50 Al	10%	0.353	**0.745** $<$ **1**
#5	H-50 Al	20%	0.455	**0.960** $<$ **1**
#6	H-50 Al	30%	0.426	**0.899** $<$ **1**
#7	H-50 Al	40%	0.436	**0.919** $<$ **1**
#8	H-50 Al	40%	0.398	**0.840** $<$ **1**
#9	H-95 Al	10%	0.510	**1.075** $\approx$ **1**
#10	H-95 Al	30%	0.424	**0.893** $<$ **1**
#11	H-95 Al	40%	0.461	**0.972** $<$ **1**
#12	H-95 Al	50%	0.458	**0.965** $<$ **1**
#13	Gran 17 Mg	10%	0.447	**0.943** $<$ **1**
#14	Gran 17 Mg	20%	0.387	**0.816** $<$ **1**
#15	Gran 17 Mg	30%	0.431	**0.908** $<$ **1**
#16	Gran 17 Mg	40%	0.452	**0.953** $<$ **1**
#17	Glass beads	10%	0.488	**1.028**
#18	Glass beads	30%	0.465	**0.980**
#19	Glass beads	50%	0.617	**1.301**

enhanced by the mixing induced by the passage of the secondary and the ground-reflected blast waves after about 2 ms, which leads to an increase in fireball luminosity (see Fig. 5.10).

The oxygen balance of an explosive provides a measure of the availability of oxidizers for reacting with aluminum in the explosive decomposition products. Alternatively, equilibrium calculations can be carried out to estimate the amount of aluminum that could theoretically react within the detonation reaction zone as well as during adiabatic expansion of the products. Calculations were carried out using the equilibrium code CHEETAH 2.0 [39] to determine the maximum amount of aluminum that could potentially completely react with the products of the detonation of the gelled NM at the CJ detonation state as well as if the products were allowed to adiabatically expand to 1 atm. The result of these calculations with the BKWC library indicated that a maximum of 26 wt% of Al mixed with the gelled NM could potentially completely react by the end of the detonation zone assuming equilibrium conditions are attained. Furthermore, if the products are allowed to expand adiabatically to atmospheric pressure, additional reaction of Al is possible and in this case an initial mixture containing 36 wt% would result in complete reaction of the Al after expansion. If more species are allowed in the detonation products (JCZS library), the percentages go up to 39% and 63%, respectively. These values provide an upper bound for the amount of aluminum that could react with the detonation products without additional mixing with oxygen in the surrounding air. Due to the finite rates of aluminum oxidation and mixing, the actual amount of Al that could react in the products will be less.

An important observation from the present experimental results is that the blast enhancement with added aluminum particles does not systematically depend on particle size. Despite varying the particle size by one order of magnitude (or the surface area by two orders of magnitudes), the normalized blast overpressure was not significantly different for the various particle sizes, and in the far field the results did not vary systematically with particle size at the various mass loadings considered. In previous work, Peuker et al. [15] found negligible particle size effects for 3–40 μm aluminum particles on blast enhancement from small-scale aluminized explosive charges. These results suggest that conventional scaling laws for aluminum particle combustion based on surface area correlations that are derived from single particle experimental results at quiescent atmospheric conditions must be modified to describe the particle reaction within the extreme conditions within the detonation products at early times.

In the detonation reaction zone for condensed explosives, pressures are on the order of tens of GPas [14], with temperatures ranging from 3000-5000 K [40], and slip velocities above 1 km/s [41]. Under these extreme conditions, the particle reaction mechanism and transport properties are completely unknown. Within the detonation products, the density of the flow is initially of the same order as the density of the metallic particles such that extremely high heat transfer rates may be possible. In supercritical conditions, aluminum oxide dissolves in water [42], and hence the pre-existing oxide coating on aluminum particles provides no barrier against the dissolution of the particle and subsequent anaerobic reaction with the detonation products. Note that the reaction of the aluminum with the oxidizers in the detonation products

(primarily H_2O) is not coincident with the energy release from the reactions. The formation of some aluminum sub-oxides (e.g., AlO, Al_2O) is weakly exothermic, but the primary energy release is associated with the chemical condensation of the stable aluminum oxide Al_2O_3, which occurs only after a degree of expansion of the products has taken place.

In contrast with the lack of systematic dependence of blast performance on the particle size, the ratio of particle mass to the explosive mass does influence the blast enhancement. As the particle mass loading is increased for a fixed volume, the explosive is diluted. Initially, the energy release from the added particles overcomes this dilution effect, as the maximum energy release for complete oxidation of the particles is several times that of the energy release of the explosive itself (31.5 kJ/g for Al [4], 24.7 kJ/g for Mg [43] vs 6.4 kJ/g for NM [44]). Eventually, with a sufficiently high solid mass fraction, the heat and momentum losses to the particles will weaken the blast strength. This suggests that there exists an optimal particle loading for maximum blast strength, which will depend on both the particle and explosive properties. In the present experiments, the normalized peak overpressure is maximized for mass fractions between 30% and 50% for aluminum particles (see Fig. 5.14). The smallest mass loading (10%) consistently gave the smallest blast overpressures, and the overpressure augmentation increases with distance from the charge, possible due to the energy release from hydrogen gas as it mixes and rapidly burns with the surrounding air.

5.5.1 Energy-based blast overpressure scaling

To compare the blast wave overpressure decay with distance for explosive charges of different sizes, it is conventional to scale the distance with the mass of explosive (Hopkinson scaling [45, 46]), or the explosive energy release, which depends on the explosive mass. For a multi-component explosive, it appears to be more meaningful to scale the distance with a parameter that depends on the total energy release, or the sum of the energy released by each component, which in general will be different, rather than the total mass of the charge [4]. Using Bach & Lee's convention [47], we define a scaled distance R_0 (or explosive characteristic length), defined by the following expression:

$$R_0 = \left(\frac{E_{\text{total}}}{\rho_0 c_0^2 k_j} \right)^{\frac{1}{j+1}} \tag{5.3}$$

where ρ_0 and c_0^2 are, respectively, the density and the speed of sound of the blast propagating medium (atmospheric air in this case). j and k_j are geometrical factor set, respectively, at 2 and 4π for a 3D-spherical blast wave. If it is assumed that the ambient air is an ideal gas, the previous equation can be rewritten as following:

$$R_0 = \left(\frac{E_{\text{total}}}{4\pi\gamma P_0} \right)^{\frac{1}{3}} \tag{5.4}$$

where γ is the ratio of specific heats, taken to be 1.405 for air (in the mid-to-far field), and P_0 is the value of the atmospheric pressure, which changes from trial to trial. To account for the multiple sources of energy release, E_{total} is defined as the following:

$$E_{\text{total}} = m_{\text{NM}} \times q_{\text{NM}} + m_{\text{C4}} \times q_{\text{C4}} + \varepsilon \times m_{\text{me}} \times q_{\text{me}} \tag{5.5}$$

Here m (g) is the mass of each component. For m_{NM}, the mass of explosive is calculated without the 4.4 wt% inert additives (GMB + PMMA). Note that in the previous definition, the total energy E_{total} is assumed to be released instantaneously after the detonation. q is the energy release per unit mass of each component (kJ/g), and the last term refers to the energy release from the metal combustion, with the subscript "me" (or metal) corresponding to either Al or Mg, depending on the trial. The parameter ε, which may vary between 0 and 1, corresponds to the fraction of the energy released from the metal combustion that is assumed to contribute to supporting the blast wave propagation. Note that this ε value does not represent the amount of Al or Mg that reacts. Indeed, even if the timescale of particle energy release is short, it is not instantaneous, as assumed in Eq. (5.3). This finite timescale for the energy release implies that that the percentage of metal reacting is generally higher than the ε value. In the limit of long times for the energy release of the metal particles, ε will tend to zero, whereas for instantaneous and complete energy release ε will approach unity. Note that since the charges in the present investigation have a constant volume, the relative contribution of the base explosive and the particle reaction to the blast overpressure will change as the particle material or mass loading is changed. Values of energy release for complete combustion of the various components, i.e., q_{NM}, q_{C4}, q_{Al} and q_{Mg} are set, respectively, to 6.4 kJ/g [44], 6.7 kJ/g [48], 31.5 kJ/g [4] and 24.7 kJ/g [43]. Note that the values of heats of combustion for magnesium and aluminum particles are those for complete reactions with molecular oxygen. However, these values are equivalent to the total heat of combustion assuming that the particles first react primarily with water in the detonation products to form molecular hydrogen gas, followed by the combustion of the hydrogen with the oxygen present in air, i.e.,

$$q_{\text{Al}}(31.5\,\text{kJ/g}) \begin{cases} 2\,\text{Al(s)} + 3\,\text{H}_2\text{O(g)} \longrightarrow \text{Al}_2\text{O}_3\text{(s)} + 3\,\text{H}_2\text{(g)} \\ 3\,\text{H}_2\text{(g)} + 1.5\,\text{O}_2\text{(g)} \longrightarrow 3\,\text{H}_2\text{O(g)} \end{cases} \tag{5.6}$$

and

$$q_{\text{Mg}}(24.7\,\text{kJ/g}) \begin{cases} \text{Mg(s)} + \text{H}_2\text{O(g)} \longrightarrow \text{MgO(s)} + \text{H}_2\text{(g)} \\ \text{H}_2\text{(g)} + 0.5\,\text{O}_2\text{(g)} \longrightarrow \text{H}_2\text{O(g)} \end{cases} \tag{5.7}$$

If the two reactions given in each case above are added together, as expected the resulting reaction gives the direct oxidation of the metal with molecular oxygen to form the metal oxide. In the case of aluminum, complete oxidation of aluminum to Al_2O_3 releases an energy of 31.5 kJ/g. The two intermediate reactions given above release roughly equal amounts of energy. In

particular, the first reaction of aluminum with water releases 15.1 kJ/g, with the remainder of the energy released by the reaction of hydrogen gas. It should be reemphasized that the parameter ε introduced above corresponds to the fraction of the energy release that is assumed to contribute to the blast wave propagation, and cannot be directly related to the fraction of aluminum that reacts. For example, a value of ε of 0.5 could correspond roughly to either *half* of the aluminum present *fully* reacting, or *all* of the aluminum present reacting *only* with water to form hydrogen.

Water vapour is not the only oxidizer present in the detonation products of NM [49] but is the most prevalent. According to CHEETAH 2.0 (BKWC library), the detonation product gases of NM at the CJ detonation state are composed, by order of prevalence, of water (H_2O), carbon monoxide (CO), nitrogen (N_2), hydrogen (H_2) and carbon dioxide (CO_2). The quantity of water vapour exceeds the quantity of carbon monoxide by more than one order of magnitude. The Al/Mg particles could alternatively react with all the other oxidizers than water. In particular, previous publications have shown the possibility of metallic particles to react, at microsecond timescales, in hydrogen-free explosives, through other reaction pathways including reaction with CO_2 as an oxidizer [25]. This implies that early-time metal reaction can contribute to the blast strength through different reaction pathways and that for different explosive compositions. Nevertheless, the reaction timescales and pathways may influence the overall blast wave dynamics as well as the peak blast overpressure values. The q values presented in Eqs. 5.6 and 5.7 are the most energetic ones and do not change if the primary oxidizer is substituted. For instance, the Al reaction with CO_2 and the subsequent combustion of the produced CO with the O_2 of the air give the same value of energy release (q_{Al} = 31.5 kJ/g).

If the peak blast overpressure results for charges containing inert glass particles are plotted versus scaled distance, the results are shown in Fig. 5.16. Figure 5.16a shows the overpressure decay in dimensional coordinates (same as the plot in Fig. 5.13a). In Fig. 5.16b the results are shown versus non-dimensional distance R/R_0 (with $\varepsilon = 0$ in the definition of E_{total} (Eq. (5.5))). As expected, the curves collapse reasonably well, with small discrepancies with the baseline results apparent in the mid and far field, suggesting that scaling with the energy released by the explosive (both NM and C4) for a liquid explosive mixture diluted by inert particles is reasonable. In the scaled coordinates, the small reduction in overpressure with the addition of particles in the near field is accounted for by the energy lost to heating and accelerating the particles whereas the small overpressure excess in the far field, as noted earlier, is due to particle-gas interactions [10, 11]. This figure shows that the reduction in the blast performance for explosives with added inert particles is primarily due to the dilution effect.

In Fig. 5.17a, the blast overpressure decay for the addition of H-10 Al particles is shown with respect to dimensional distance. In the remainder of the plots, the results are shown plotted versus non-dimensional distance, in which different values of ε were assumed in the definition of scaled distance, to determine if the overpressure results collapse. The working assumption is that if the overpressure results collapse in the scaled coordinates, at a given distance, then the value of ε chosen represents the effective contribution of the total energy release by the particle

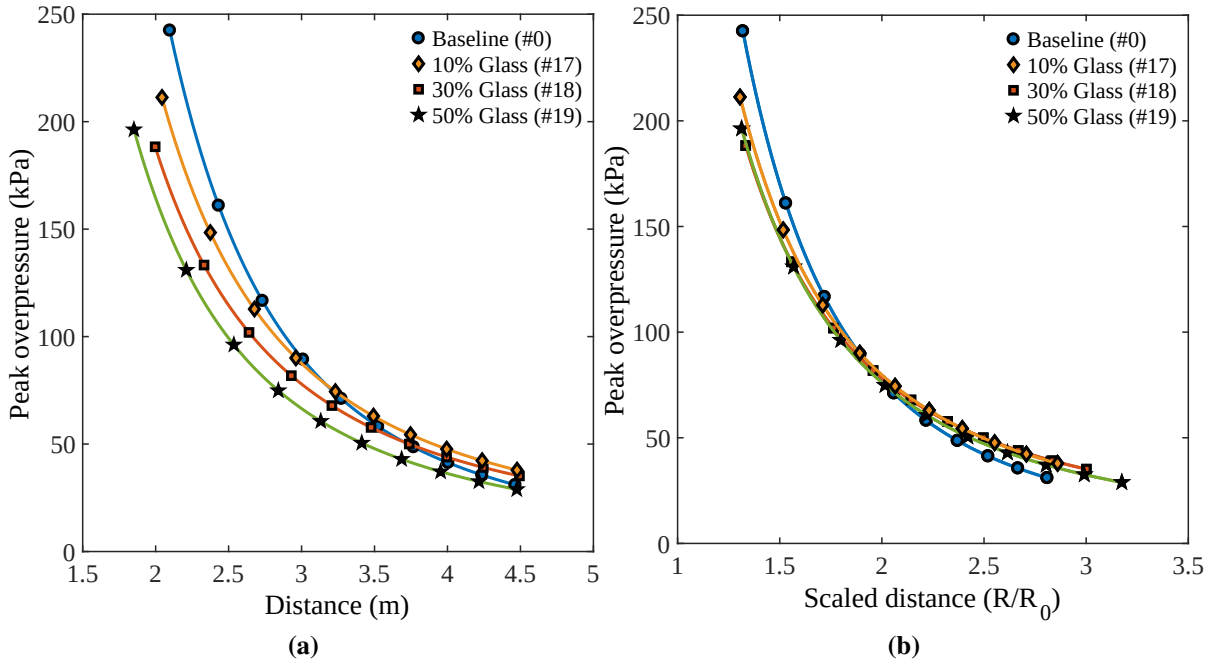

Fig. 5.16 Peak blast overpressure decays with distance for glass particles with **(a)** dimensional radius, and **(b)** with scaled distance, R/R_0, where R_0 accounts for the explosive energy only (NM+C4, $\varepsilon = 0$ in Eq. (5.5)).

reaction to the blast front. In Figs. 5.17b and 5.17c, the scaled distance is chosen assuming, respectively, no aluminum energy release ($\varepsilon = 0$) and that the full aluminum energy release contributes to the blast propagation ($\varepsilon = 1$). In both cases, the curves generally fail to collapse, indicating that these assumptions are not consistent with the experimental results. The sole exception to that is the assumption of complete energy release for a solid mass fraction of 10%, which results in the overpressure curve nearly overlapping the baseline explosive case in the far field (Fig. 5.17c). This suggests at this small mass fraction, that the energy release associated with complete oxidation of the aluminum powder contributes to the peak blast overpressure by the time the blast reaches the far field. The complete reaction of the particles in the detonation products is theoretically possible at this mass fraction, as demonstrated earlier with CHEETAH calculations. Figure 5.17d shows the blast overpressure results plotted with a scaling assuming 25% of the particle energy release contributes to the blast (i.e., $\varepsilon = 0.25$). The results collapse in the near field, at a distance near the edge of the fireball interface. At this distance, the particles will have reacted primarily with the detonation products, so one interpretation of the results is that one-half of aluminum particles fully react with water within the products and the energy release associated with this reaction contributes to the near field blast overpressure. In Fig. 5.17e, the results are plotted assuming that 50% of the particle energy release contributes to the blast strength. The results collapse in the far field, suggesting that additional energy is released, possibly due to reaction of the hydrogen produced, that contributes to strengthening the blast wave as it moves from the near field to the far field region.

A similar methodology is used to plot the results for H-50 and H-95 aluminum and for magnesium particles in Fig. 5.18, with values chosen for ε ranging from 0.15 and 0.5 for the aluminum particles and 0.3 and 0.65 for the magnesium particles. In the far field, for aluminum particles, with $\varepsilon = 0.5$, the curves for mass loadings of 40%-50% approach that of the baseline explosive, suggesting that the fraction of the particle energy release that has contributed to the blast wave overpressure by the far field approaches 50%. For smaller particle mass loadings (10%-30%), the scaled overpressure values actually exceed the baseline values, suggesting that at these mass loadings even more than half the particle energy release contributes to the blast wave. Note again that the energy that contributes to the blast does not reflect the real mass of reactive particles that react.

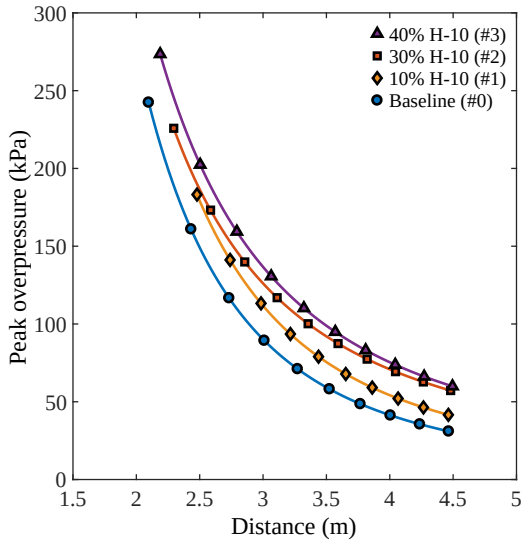

(a) H-10

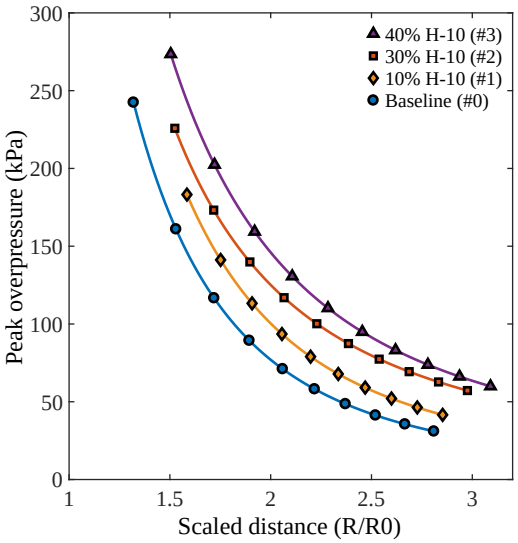

(b) H-10, $\varepsilon = 0$

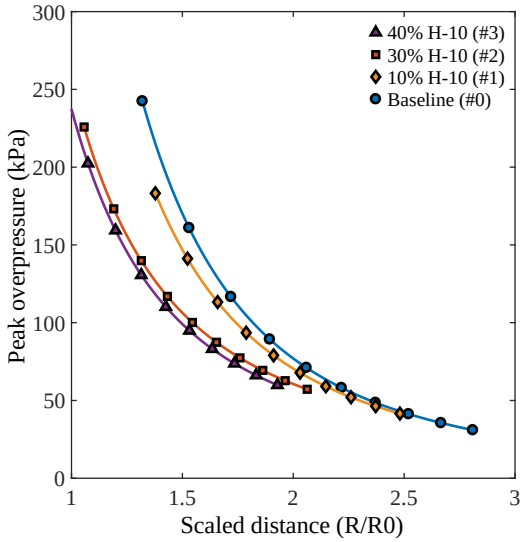

(c) H-10, $\varepsilon = 1$

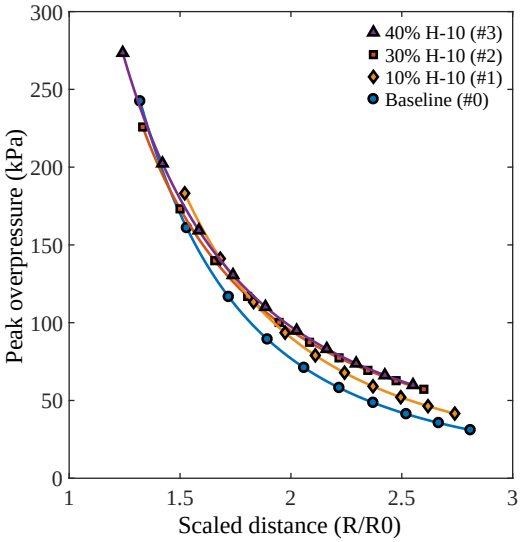

(d) H-10, $\varepsilon = 0.25$

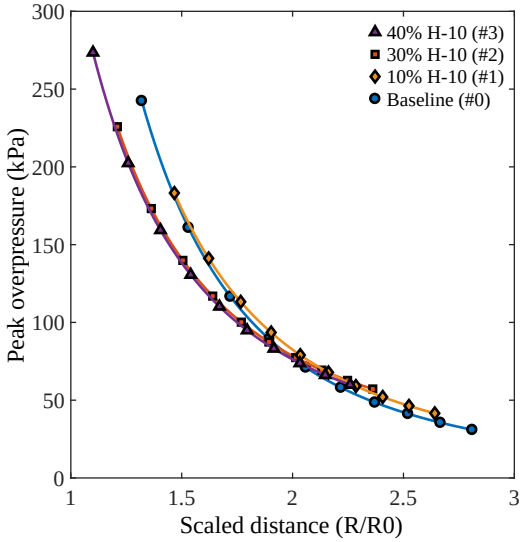

(e) H-10, $\varepsilon = 0.5$

Fig. 5.17 Peak blast overpressure decays with distance for H-10 aluminum particles with **(a)** actual radius or **(b)** scaled distance, R/R_0, where R_0 accounts for the explosive energy only (NM + C4, $\varepsilon = 0$ in Eq. (5.5)). **(c)** Peak blast overpressure decays with distance for H-10 aluminum particles assuming a full contribution of the Al chemical energy ($\varepsilon = 1$). **(d)** Peak blast overpressure decays with distance for H-10 aluminum particles assuming that 25% ($\varepsilon = 0.25$) of the Al chemical energy contribute to the blast front. **(e)** Peak blast overpressure decays with distance for H-10 aluminum particles assuming that 50% ($\varepsilon = 0.5$) of the Al chemical energy contribute to the blast front.

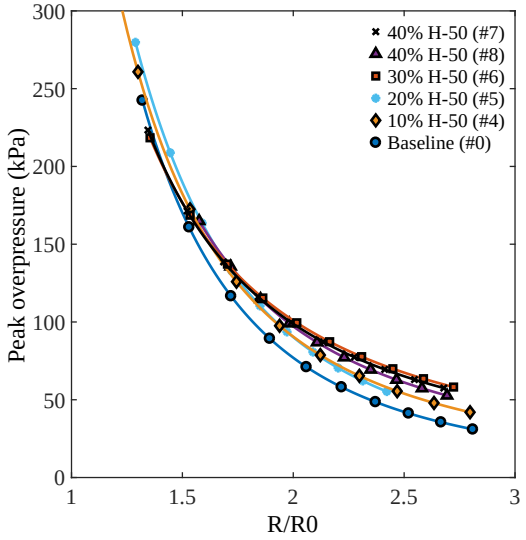

(a) H-50, $\varepsilon = 0.15$

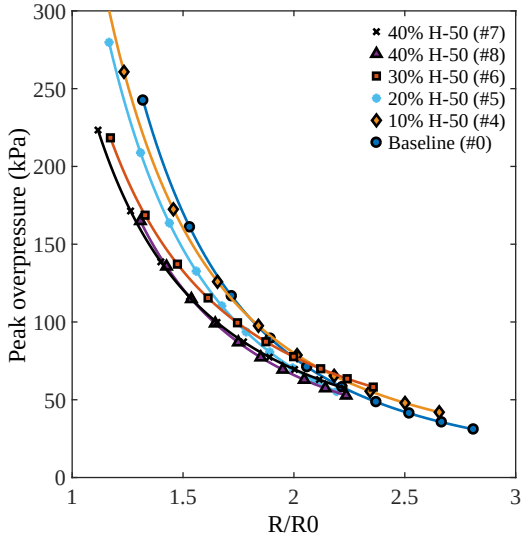

(b) H-50, $\varepsilon = 0.5$

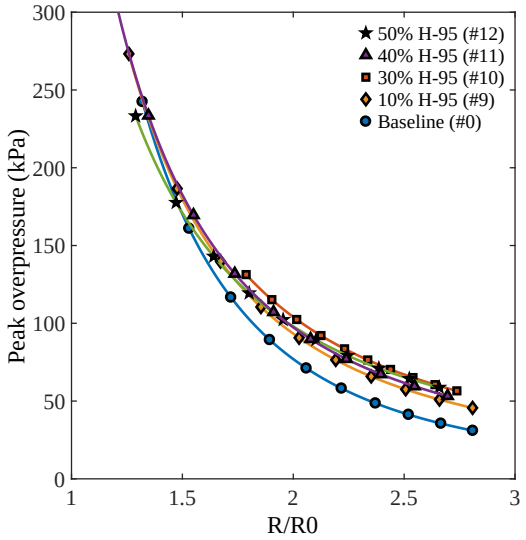

(c) H-95, $\varepsilon = 0.15$

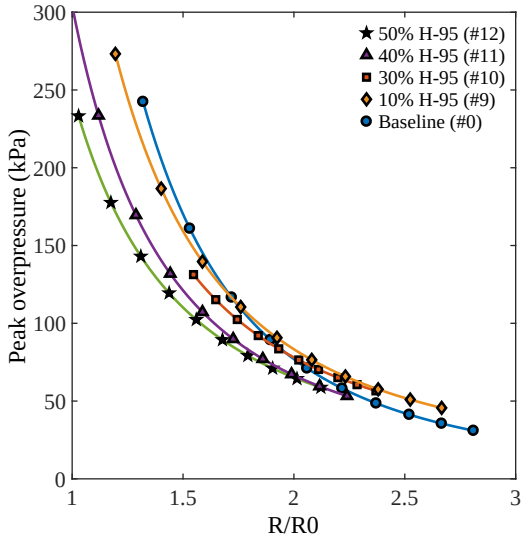

(d) H-95, $\varepsilon = 0.5$

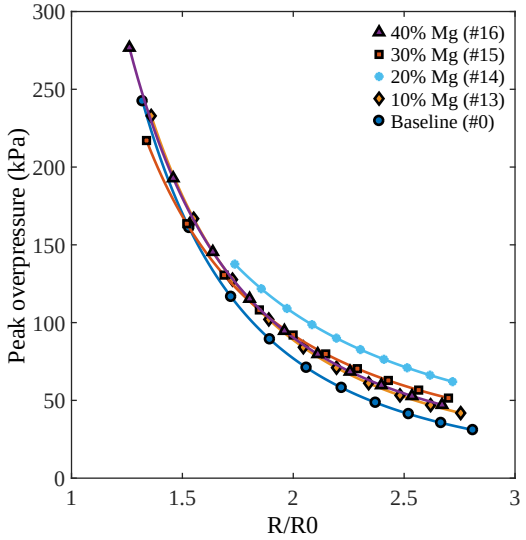

(e) Mg, $\varepsilon = 0.3$

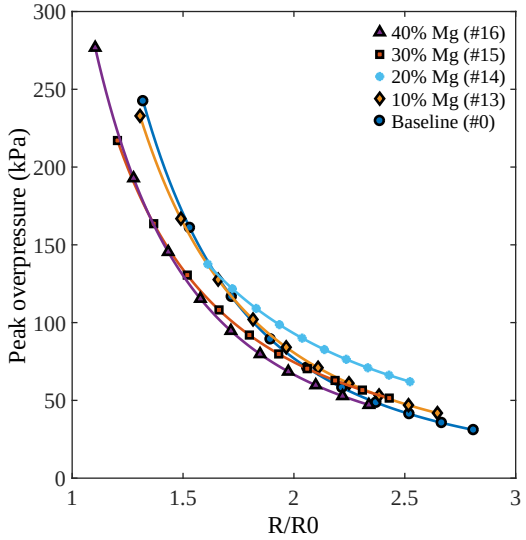

(f) Mg, $\varepsilon = 0.65$

Fig. 5.18 Same graphs as in Fig. 5.17 considering that **(a)** assuming that 15% ($\varepsilon = 0.15$) of the H-50 Al chemical energy contribute to the blast front **(b)** assuming that 50% ($\varepsilon = 0.5$) of the H-50 Al chemical energy contribute to the blast front **(c)** assuming that 15% ($\varepsilon = 0.15$) of the H-95 Al chemical energy contribute to the blast front **(d)** assuming that 50% ($\varepsilon = 0.5$) of the H-95 Al chemical energy contribute to the blast front **(e)** assuming that 30 % ($\varepsilon = 0.3$) of the Mg chemical energy contribute to the blast front **(f)** assuming that 65% ($\varepsilon = 0.65$) of the Mg chemical energy contribute to the blast front.

5.6 Conclusions

The effect of adding both inert (glass), and reactive (aluminum and magnesium) particles to gelled nitromethane on the performance of the blast wave generated by the detonation of the resulting heterogeneous explosive in constant volume charges was determined experimentally. The results were compared with the baseline case of the homogeneous explosive itself. Blast arrival times and peak blast overpressures in the near-to-mid field were analyzed from pressure gauge data. High-speed videography was used to infer the peak overpressure decays in the mid-to-far field. The main conclusions of this study are:

1. The addition of inert glass particles mitigates the peak blast overpressure by up to 38% in the mid field (i.e., just outside the maximum extent of the fireball), with the mitigation increasing with particle mass loading. When the peak blast overpressure is plotted as a function of non-dimensional distance accounting for the total energy release of the explosive, the blast decay results largely collapse, suggesting that the blast performance depends mainly on the explosive energy available. The addition of particles slightly attenuates the blast in the near field (due to heat and momentum transfer to the particles) and augments the blast in the far field (due to particle-flow interactions), consistent with previous results [10, 11].

2. Based on the reduced arrival time of the blast wave at the nearest pressure gauge with Al or Mg particles, relative to that of the baseline explosive, the energy release from the particles influences the blast wave propagation within about 300 μs of charge detonation in all cases. The peak blast overpressure was found to be increased by up to almost twice the baseline value in the far field. The best blast performance with aluminum particles was observed at a particle mass loading between 30% and 50% depending on the distance from the charge.

3. Although the Al particle size was varied over an order of magnitude, the blast enhancement effect was relatively insensitive to particle size. This suggests that the use of correlations for particle reaction time that depend monotonically on particle size are not sufficient to predict the blast performance. New particle reaction models are needed that are also consistent with the early metal reactions observed in metal acceleration experiments with metalized explosives.

4. By plotting the blast overpressure results versus an energy-scaled distance, and comparing the resulting overpressure decay with the baseline explosive, it is possible to gain insight into the degree to which the particle reaction contributes to the blast wave overpressure when the blast wave reaches various distances. The results for the metalized explosives containing aluminum or magnesium particles suggest that at a particle mass fraction of 10%, most of the energy release from the particle reaction has contributed to the blast

propagation by the far field, which here is defined as distances greater than 3 m from 1 L volume charges. At particle mass fractions of 30%-50%, more than half of the particle reaction energy contributes to the blast wave overpressure by the far field. The most probable reaction pathway for the aluminum in nitromethane consists of early sub-millisecond reaction of the aluminum with the water in the detonation products, releasing hydrogen, followed by combustion of the hydrogen with the surrounding air in the highly turbulent mixing zone near the fireball interface. Nevertheless, it is hypothesized that the possibility of the contribution to the blast of the early time metal energy release would also occur in hydrogen-free compounds through other reaction pathways.

The present results demonstrate that sub-millisecond energy release from the reaction of the metal particles with the water in the detonation products contributes to augmenting the blast strength. Additional experimental diagnostics very near the charge are needed to further resolve the rate of particle energy release at early times. Some insight into the partition of the particle energy release history between the detonics (microseconds), early expansion (100's microseconds), and later fireball expansion (millisecond) stages of the phenomena may be obtained by comparing hydrocode predictions of the blast decay with experimental results, assuming a parametric variation in the particle energy release rate, and efforts in this direction are currently underway [50].

Appendix

Tables 5.3 and 5.4 present the times of arrival captured with the pressure gauges at all distances from the charge (1.0 m, 1.5 m and 2.0 m). Table 5.3 is sorted by particle size whereas Table 5.4 is sorted by mass fraction. The same tables, but for the peak blast overpressures obtained at 2.0 m from the charge, are shown in Tables 5.5 and 5.6. These peak blast overpressures are compared with the peak overpressures obtained with the videography analysis at a distance of 2.0 from the charge in Table 5.7. Note that most of the time the blast front was not visible at this distance, at the same height as the charge. Consequently, the blast front position at 2.0 m from the charge was extrapolated by inferring the blast curvature as shown in Fig. 5.5. Discarding the non-reliable peak overpressure recorded for trial #4, the maximum discrepancy observed between the gauge measurements and the video analysis method is 42.2%. However, the discrepancies between the two methods are not similar for all trials tested suggesting that they are of a stochastic nature and not a systematic error resulting from the methodology employed. The discrepancies are explained by the fact that the blast is not tracked in the same directions around the charge (pressure gauges are not in the camera field of view as shown in Fig. 5.1). In other words, the blast propagation is not isotropic. Fig. 5.19 exhibits the peak blast overpressure decays obtained with the videography in the mid-to-far field for trials with aluminum and magnesium particles. The peak overpressure decays are also plotted in Figs. 5.20a, 5.20c, 5.20e at three specific

mass fractions (10%, 30%, and 40%) to illustrate the effect of the material and particle sizes. The normalized plots are also shown on Figs. 5.20b, 5.20d, 5.20f to highlight the performance. The trial videos corresponding to Figs. 5.7, 5.8, and 5.9 are available online as supplementary materials.

Table 5.3 Blast times of arrival for all trials at 1.0 m, 1.5 m and 2.0 m from the charge, captured with pressure transducers. At every distances, the arrival times are normalized by the baseline value ($t_a/t_{a-baseline}$) for comparison. Values of arrival times for two specific trials (trials #15 and #16), at 2.0 m, are not available due to record problems. At each distance, and for every types of particles, the most efficient trial at reducing (resp. augmenting) the blast arrival are highlighted in red (resp. blue).

Trial	Material	Mass fraction	t_a (ms - 1.0 m)	$t_a/t_{a-baseline}$	t_a (ms - 1.5 m)	$t_a/t_{a-baseline}$	t_a (ms - 2.0 m)	$t_a/t_{a-baseline}$
#0	Baseline	-	0.474	**1.000**	1.107	**1.000**	1.725	**1.000**
#1	H-10 Al	10%	0.376	**0.793**	1.099	**0.993**	1.635	**0.948**
#2	H-10 Al	30%	0.379	**0.800**	0.795	**0.718**	1.473	**0.854**
#3	H-10 Al	40%	0.464	**0.978**	0.753	**0.680**	1.377	**0.798**
#4	H-50 Al	10%	0.353	**0.745**	1.064	**0.961**	1.554	**0.901**
#5	H-50 Al	20%	0.455	**0.960**	0.836	**0.755**	1.559	**0.904**
#6	H-50 Al	30%	0.426	**0.899**	0.831	**0.750**	1.531	**0.888**
#7	H-50 Al	40%	0.436	**0.919**	0.782	**0.706**	1.436	**0.832**
#8	H-50 Al	40%	0.398	**0.840**	0.955	**0.862**	1.333	**0.773**
#9	H-95 Al	10%	0.510	**1.075**	0.930	**0.840**	1.629	**0.944**
#10	H-95 Al	30%	0.424	**0.893**	0.959	**0.866**	1.507	**0.874**
#11	H-95 Al	40%	0.461	**0.972**	0.727	**0.657**	1.475	**0.855**
#12	H-95 Al	50%	0.458	**0.965**	0.859	**0.776**	1.436	**0.832**
#13	Gran 17 Mg	10%	0.447	**0.943**	0.983	**0.888**	1.660	**0.962**
#14	Gran 17 Mg	20%	0.387	**0.816**	0.700	**0.632**	1.504	**0.872**
#15	Gran 17 Mg	30%	0.431	**0.908**	0.877	**0.792**	N.A.	**N.A.**
#16	Gran 17 Mg	40%	0.452	**0.953**	0.887	**0.801**	N.A.	**N.A.**
#17	Glass beads	10%	0.488	**1.028**	1.240	**1.120**	1.782	**1.033**
#18	Glass beads	30%	0.465	**0.980**	1.088	**0.983**	1.951	**1.131**
#19	Glass beads	50%	0.617	**1.301**	1.232	**1.113**	2.124	**1.231**

Table 5.4 Same table as Table 5.3 but reordered for comparison at a specific mass fraction.

Trial	Material	Mass fraction	t_a (ms - 1.0 m)	$t_a/t_{a-baseline}$	t_a (ms - 1.5 m)	$t_a/t_{a-baseline}$	t_a (ms - 2.0 m)	$t_a/t_{a-baseline}$
#0	Baseline	-	0.474	**1.000**	1.107	**1.000**	1.725	**1.000**
#1	H-10 Al	10%	0.376	**0.793**	1.099	**0.993**	1.635	**0.948**
#4	H-50 Al	10%	0.353	**0.745**	1.064	**0.961**	1.554	**0.901**
#9	H-95 Al	10%	0.510	**1.075**	0.930	**0.840**	1.629	**0.944**
#13	Gran 17 Mg	10%	0.447	**0.943**	0.983	**0.888**	1.660	**0.962**
#17	Glass beads	10%	0.488	**1.028**	1.240	**1.120**	1.782	**1.033**
#5	H-50 Al	20%	0.455	**0.960**	0.836	**0.755**	1.559	**0.904**
#14	Gran 17 Mg	20%	0.387	**0.816**	0.700	**0.632**	1.504	**0.872**
#2	H-10 Al	30%	0.379	**0.800**	0.795	**0.718**	1.473	**0.854**
#6	H-50 Al	30%	0.426	**0.899**	0.831	**0.750**	1.531	**0.888**
#10	H-95 Al	30%	0.424	**0.893**	0.959	**0.866**	1.507	**0.874**
#15	Gran 17 Mg	30%	0.431	**0.908**	0.877	**0.792**	N.A.	**N.A.**
#18	Glass beads	30%	0.465	**0.980**	1.088	**0.983**	1.951	**1.131**
#3	H-10 Al	40%	0.464	**0.978**	0.753	**0.680**	1.377	**0.798**
#7	H-50 Al	40%	0.436	**0.919**	0.782	**0.706**	1.436	**0.832**
#8	H-50 Al	40%	0.398	**0.840**	0.955	**0.862**	1.333	**0.773**
#11	H-95 Al	40%	0.461	**0.972**	0.727	**0.657**	1.475	**0.855**
#16	Gran 17 Mg	40%	0.452	**0.953**	0.887	**0.801**	N.A.	**N.A.**
#12	H-95 Al	50%	0.458	**0.965**	0.859	**0.776**	1.436	**0.832**
#19	Glass beads	50%	0.617	**1.301**	1.232	**1.113**	2.124	**1.231**

Table 5.5 Absolute peak overpressure (ΔP_s) values extracted from the pressure gauge at 2.0 from the charge for all the trials tested. Normalized peak overpressure values by the peak overpressure value of the baseline referred as normalized $\Delta P_s/\Delta P_{s-baseline}$ are also calculated. For every types of particles, the most efficient trial at enhancing (resp. mitigating) the peak blast overpressure are highlighted in red (resp. blue). The peak overpressure obtained for the trial #4 (10% H-50) is not considered as reliable.

Trial	Material	Particle mass fraction	Mean particle size (µm)	ΔP_s (2.0 m - gauge (kPa))	$\Delta P_s/\Delta P_{s-baseline}$
#0	Baseline	-	-	220.1	**1.000**
#1	H-10 Al	10%	13	225.2	**1.023**
#2	**H-10 Al**	**30%**	**13**	**322.9**	**1.467**
#3	H-10 Al	40%	13	250.5	**1.138**
#4	H-50 Al	10%	54	150.5 (not reliable)	**0.684**
#5	H-50 Al	20%	54	339.6	**1.543**
#6	**H-50 Al**	**30%**	**54**	**363.1**	**1.650**
#7	H-50 Al	40%	54	282.1	**1.282**
#8	H-50 Al	40%	54	233.3	**1.060**
#9	H-95 Al	10%	114	243.6	**1.107**
#10	H-95 Al	30%	114	339	**1.540**
#11	**H-95 Al**	**40%**	**114**	**347.6**	**1.579**
#12	H-95 Al	50%	114	233.8	**1.062**
#13	Gran 17 Mg	10%	240	249.9	**1.135**
#14	**Gran 17 Mg**	**20%**	**240**	**415.4**	**1.887**
#15	Gran 17 Mg	30%	240	N.A.	**N.A.**
#16	Gran 17 Mg	40%	240	N.A.	**N.A.**
#17	Glass beads	10%	66	183.3	**0.833**
#18	Glass beads	30%	66	191.3	**0.869**
#19	**Glass beads**	**50%**	**66**	**159.7**	**0.726**

Table 5.6 Same table as Table 5.5 but reordered for direct comparison at a specific particle mass fraction.

Trial	Material	Particle mass fraction	Mean particle size (μm)	ΔP_s (2.0 m - gauge (kPa))	$\boldsymbol{\Delta P_s / \Delta P_{s-baseline}}$
#0	Baseline	-	-	220.1	**1.000**
#1	H-10 Al	10%	13	225.2	**1.023**
#4	H-50 Al	10%	54	150.5 (not reliable)	**0.684**
#9	H-95 Al	10%	114	243.6	**1.107**
#13	**Gran 17 Mg**	**10%**	**240**	**249.9**	**1.135**
#17	Glass beads	10%	66	183.3	**0.833**
#5	H-50 Al	20%	54	339.6	**1.543**
#14	**Gran 17 Mg**	**20%**	**240**	**415.4**	**1.887**
#2	H-10 Al	30%	13	322.9	**1.467**
#6	**H-50 Al**	**30%**	**54**	**363.1**	**1.650**
#10	H-95 Al	30%	114	339	**1.540**
#15	Gran 17 Mg	30%	240	N.A.	**N.A.**
#18	Glass beads	30%	66	191.3	**0.869**
#3	H-10 Al	40%	13	250.5	**1.138**
#7	H-50 Al	40%	54	282.1	**1.282**
#8	H-50 Al	40%	54	233.3	**1.060**
#11	**H-95 Al**	**40%**	**114**	**347.6**	**1.579**
#16	Gran 17 Mg	40%	240	N.A.	**N.A.**
#12	**H-95 Al**	**50%**	**114**	**233.8**	**1.062**
#19	**Glass beads**	**50%**	**66**	**159.7**	**0.726**

Table 5.7 Comparison between peak overpressures at 2.0 from the charge obtained through videography or with pressure gauge measurements. *extp*: Peak overpressure values extrapolated by inferring the blast curvature as shown in Fig. 5.5, *sd*: Overpressure profile presenting a slight deviation from the modified Friedlander form, *id*: Overpressure profile presenting an important deviation from the modified Friedlander form, *R.E.*: Relative error between the two methods.

Trial	Material	Particle mass fraction	Mean particle size (µm)	ΔP_s (2.0 m - video (kPa))	ΔP_s (2.0 m - gauge (kPa))	***R.E. (%)***
#0	Baseline	-	-	276.2 (*extp*)	220.1	**25.5**
#1	H-10 Al	10%	13	320.3 (*extp*)	225.2 (*sd*)	**42.2**
#2	H-10 Al	30%	13	311.0 (*extp*)	322.9	**-3.7**
#3	H-10 Al	40%	13	335.4 (*extp*)	250.5 (*sd*)	**33.9**
#4	H-50 Al	10%	54	288.5	150.5 (*id* - (not reliable))	**91.7**
#5	H-50 Al	20%	54	313.0 (*extp*)	339.6	**-7.8**
#6	H-50 Al	30%	54	273.5 (*extp*)	363.1	**-24.7**
#7	H-50 Al	40%	54	285.8 (*extp*)	282.1 (*sd*)	**1.3**
#8	H-50 Al	40%	54	316.8 (*extp*)	233.3 (*sd*)	**35.8**
#9	H-95 Al	10%	114	280.5 (*extp*)	243.6	**15.1**
#10	H-95 Al	30%	114	308.1 (*extp*)	339.0 (*sd*)	**-9.1**
#11	H-95 Al	40%	114	307.5	347.6	**-11.5**
#12	H-95 Al	50%	114	281.9 (*extp*)	233.8	**20.6**
#13	Gran 17 Mg	10%	240	296.3 (*extp*)	249.9	**18.6**
#14	Gran 17 Mg	20%	240	267.6 (*extp*)	415.4 (*sd*)	**-35.6**
#15	Gran 17 Mg	30%	240	278.2 (*extp*)	N.A.	**N.A.**
#16	Gran 17 Mg	40%	240	325.6 (*extp*)	N.A.	**N.A.**
#17	Glass beads	10%	66	222.5 (*extp*)	183.3 (*sd*)	**21.4**
#18	Glass beads	30%	66	187.6	191.3	**-1.9**
#19	Glass beads	50%	66	164.3	159.7	**2.9**

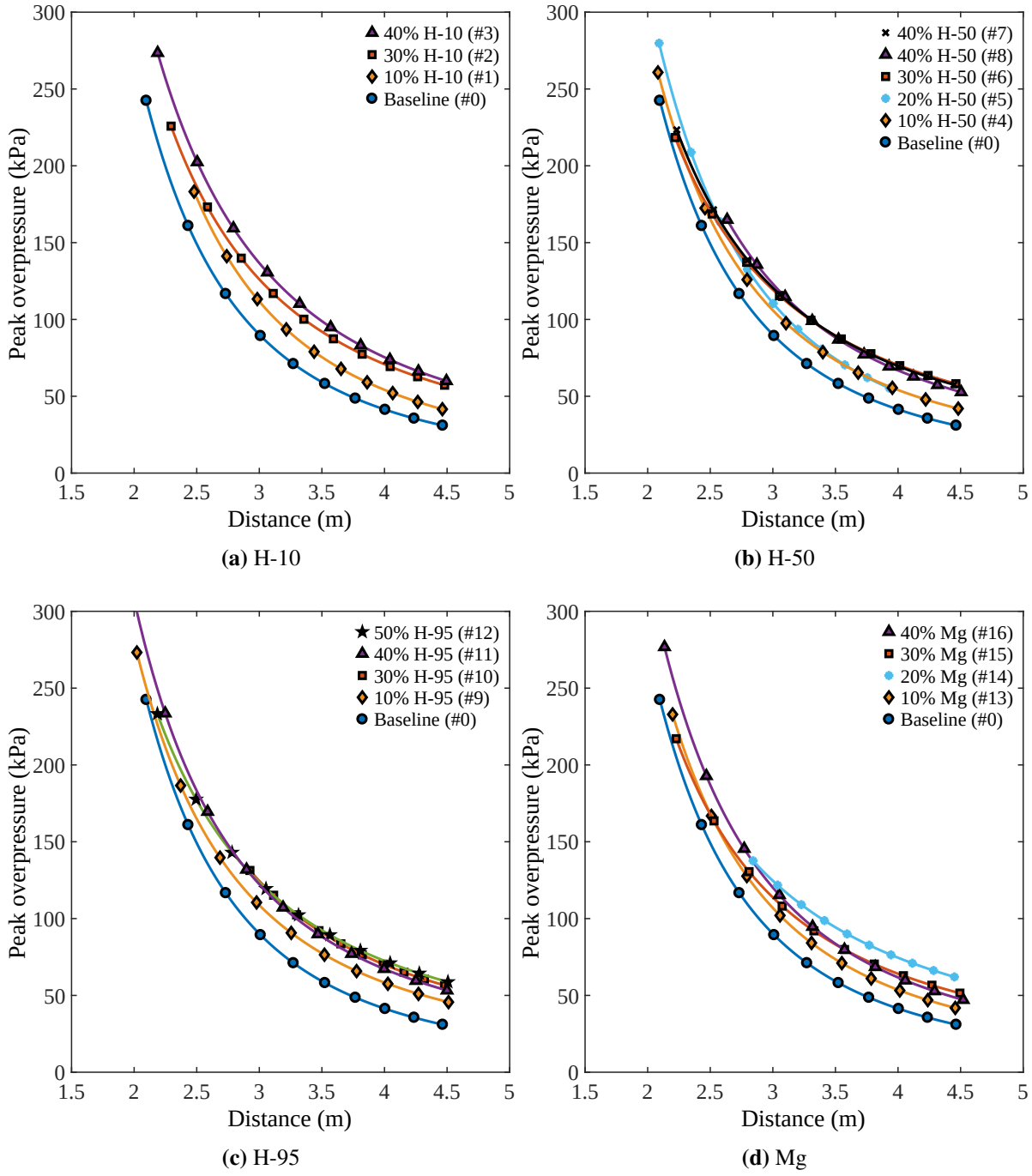

(a) H-10 **(b)** H-50

(c) H-95 **(d)** Mg

Fig. 5.19 Peak blast overpressure decays plotted in the mid-to-far field for trials with **(a)** H-10 Al, **(b)** H-50 Al, **(c)** H-95 Al and **(d)** Gran 17 Mg.

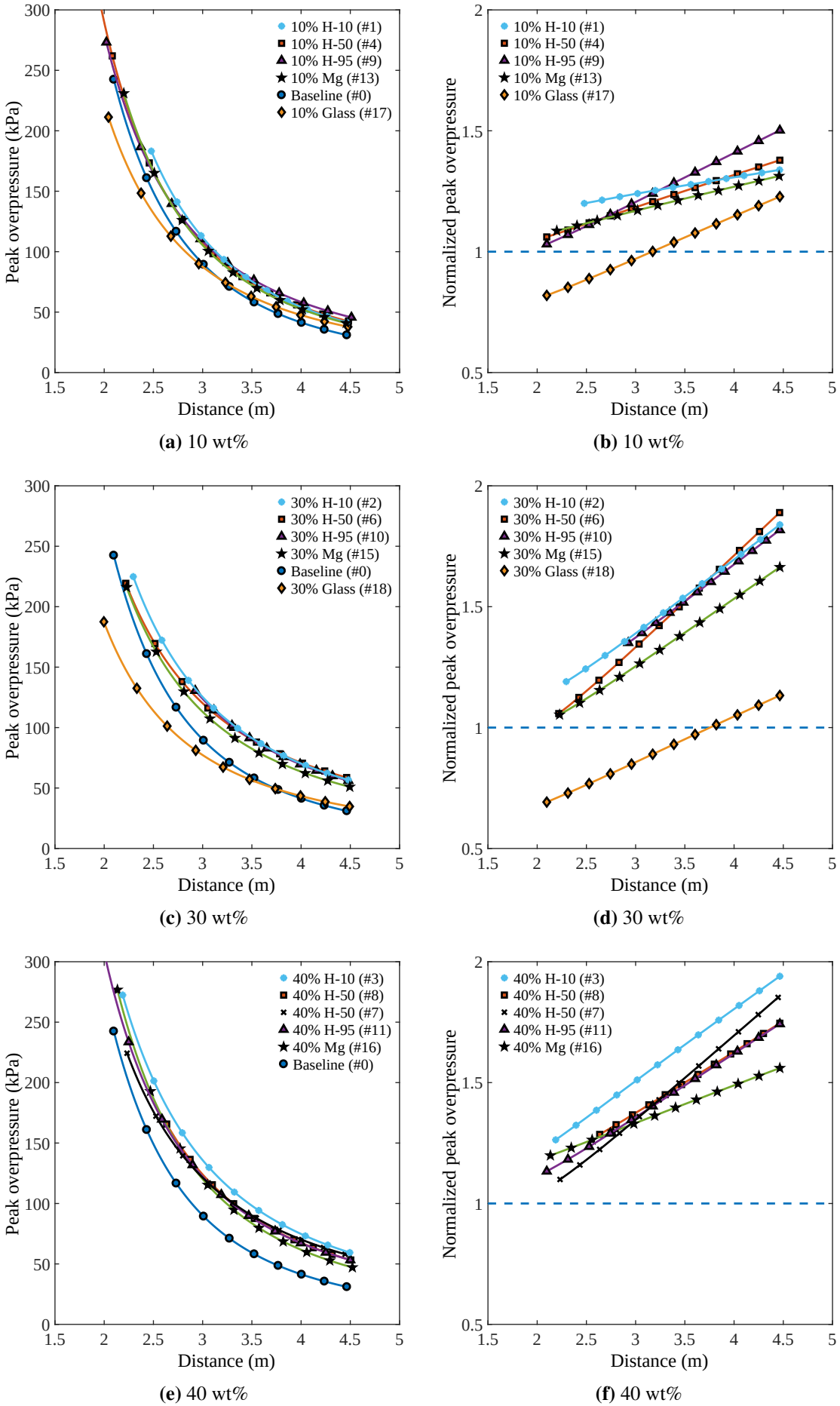

(a) 10 wt% **(b)** 10 wt%

(c) 30 wt% **(d)** 30 wt%

(e) 40 wt% **(f)** 40 wt%

Fig. 5.20 Effect of particle material and particle sizes on the peak blast overpressure decays with dimensional distance, for particle mass fractions of 10 wt%, 30 wt%, 40 wt%.

Acknowledgements The authors thank the field operation team at DRDC Suffield for assistance with setting up the experimental test site and S. Trebble for carrying out the high-speed video recording. The authors would like to thank A. Longbottom and A. Milne at Fluid Gravity Engineering for their valuable comments on the pressure gauge analysis. The authors would also like to thank the four anonymous reviewers for their many constructive comments.

Compliance with ethical standards

Conflict of Interest The authors declare that they have no conflict of interest.

References

[1] R. Escales. UK24377 (Patent), 1899.

[2] G. Roth. Performance of explosives (Patent), 1900.

[3] N. H. Yen and L. Y. Wang. Reactive metals in explosives. *Propellants, Explosives, Pyrotechnics*, 37(2):143–155, 2012, doi:10.1002/prep.200900050.

[4] D. L. Frost and F. Zhang. The nature of heterogeneous blast explosives. In *19th International Symposium on Military Aspects of Blast and Shock (MABS 19)*, Calgary, Canada, 2006.

[5] W. A. Trzciński and L. Maiz. Thermobaric and enhanced blast explosives - properties and testing methods. *Propellants, Explosives, Pyrotechnics*, 40(5):632–644, 2015, doi:10.1002/prep.201400281.

[6] L. Türker. Thermobaric and enhanced blast explosives (TBX and EBX). *Defence Technology*, 12(6):423–445, 2016, doi:10.1016/j.dt.2016.09.002.

[7] P. P. Vadhe, R. B. Pawar, R. K. Sinha, S. N. Asthana, and A. Subhananda Rao. Cast aluminized explosives (review). *Combustion, Explosion and Shock Waves*, 44(4):461–477, 2008, doi:10.1007/s10573-008-0073-2.

[8] C. Capellos, E. L. Baker, S. Nicolich, W. Balas, J. Pincay, and L. I. Stiel. Eigenvalue detonation of combined effects aluminized explosives. *AIP Conference Proceedings*, 955(2007):357–360, 2007, doi:10.1063/1.2833055.

[9] D. L. Frost. Heterogeneous/particle-laden blast waves. *Shock Waves*, 28(3):439–449, 2018, doi:10.1007/s00193-018-0825-1.

[10] Q. Pontalier, J. Loiseau, S. Goroshin, and D. L. Frost. Experimental investigation of blast mitigation and particle-blast interaction during the explosive dispersal of particles and liquids. *Shock Waves*, 28(3):489–511, 2018, doi:10.1007/s00193-018-0821-5.

[11] Q. Pontalier, M. Lhoumeau, A. Milne, A. Longbottom, and D. L. Frost. Numerical investigation of particle-blast interaction during explosive dispersal of liquids and granular materials. *Shock Waves*, 28(3):513–531, 2018, doi:10.1007/s00193-018-0820-6.

[12] Q. Pontalier, M. Lhoumeau, and D. L. Frost. Blast wave mitigation in granular materials. *AIP Conference Proceedings*, 1979(1):110014, 2018, doi:10.1063/1.5044933.

[13] J. Loiseau, Q. Pontalier, A. M. Milne, S. Goroshin, and D. L. Frost. Terminal velocity of liquids and granular materials dispersed by a high explosive. *Shock Waves*, 28(3):473–487, 2018, doi:10.1007/s00193-018-0822-4.

[14] R. C. Ripley, F . Zhang, and F-S. Lien. Acceleration and heating of metal particles in condensed matter detonation. *Proceedings of the Royal Society of London. Series A, Mathematical and Physical Sciences*, 468(February):1564–1590, 2012, doi:10.1098/rspa.2011.0595.

[15] J. M. Peuker, H. Krier, and N. Glumac. Particle size and gas environment effects on blast and overpressure enhancement in aluminized explosives. *Proceedings of the Combustion Institute*, 34(2):2205–2212, 2013, doi:10.1016/j.proci.2012.05.069.

[16] Z. Zarei and D. L. Frost. Simplified modeling of blast waves from metalized heterogeneous explosives. *Shock Waves*, 21(5):425–438, 2011, doi:10.1007/s00193-011-0316-0.

[17] K. Balakrishnan and S. Menon. On the role of ambient reactive particles in the mixing and afterburn behind explosive blast waves. *Combustion Science and Technology*, 182(2):186–214, 2010, doi:10.1080/00102200903341579.

[18] K. L. McNesby, B. E. Homan, J. J. Ritter, Z. Quine, R. Z. Ehlers, and B. A. McAndrew. Afterburn ignition delay and shock augmentation in fuel rich solid explosives. *Propellants, Explosives, Pyrotechnics*, 35(1):57–65, 2010, doi:10.1002/prep.200800084.

[19] J. Duan, C. Wu, F. J. An, and S. S. Liao. A quasi-analytical model of aluminized explosive products under strong constraint. *Advances in Mechanical Engineering*, 9(11):1–10, 2017, doi:10.1177/1687814017739511.

[20] X. Yuan, C. Wu, F. An, S. Liao, M. Zhou, Z. Shi, and D. Xue. A non-isentropic model of aluminized explosives involved with the reaction degree of aluminum powder for post-detonation burning behavior. *Physics of Fluids*, 32(2), 2020, doi:10.1063/1.5139692.

[21] X. Li, H. Pei, X. Zhang, and X. Zheng. Effect of aluminum particle size on the performance of aluminized explosives. *Propellants, Explosives, Pyrotechnics*, 45(5):807–813, 2020, doi:10.1002/prep.201900308.

[22] A. Lefrancois, G. Baudin, C. Le Gallic, P. Boyce, and J-P. Coudoing. Nanometric aluminum powder influence on the detonation efficiency of explosives. In *12th International Detonation Symposium*, San Diego, U.S.A., 2002.

[23] V. W. Manner, S. J. Pemberton, J. A. Gunderson, T. J. Herrera, J. M. Lloyd, P. J. Salazar, P. Rae, and B. C. Tappan. The role of aluminum in the detonation and post-detonation expansion of selected cast HMX-based explosives. *Propellants, Explosives, Pyrotechnics*, 37(2):198–206, 2012, doi:10.1002/prep.201100138.

[24] M. N. Makhov, M. F. Gogulya, A. Yu. Dolgoborodov, M. A. Brazhnikov, V. I. Arkhipov, and V. I. Pepekin. Acceleration ability and heat of explosive decomposition of aluminized explosives. *Combustion, Explosion and Shock Waves*, 40(4):458–466, 2004, doi:10.1023/B:CESW.0000033569.77449.d9.

[25] B. C. Tappan, L. G. Hill, V. W. Manner, S. J. Pemberton, M. A. Lieber, C. E. Johnson, and V. E. Sanders. Reactions of powdered aluminum with explosives that selectively form carbon dioxide or water as oxidizers. *International Journal of Energetic Materials and Chemical Propulsion*, 15(4):339–350, 2016, doi:10.1615/IntJEnergeticMaterialsChemProp.2017011503.

[26] D. L. Robbins, E. K. Anderson, M. U. Anderson, S. I. Jackson, and M. Short. Cylinder test characterization of an ammonium nitrate and aluminum powder explosive. *15thInternational Detonation Symposium*, 803:826–835, 2014.

[27] G. Baudin, A. Lefrancois, D. Bergues, J. Bigot, and Y. Champion. Combustion of nanophase aluminum in the detonation products of nitromethane and TNT. In *11th International Detonation Symposium*, Colorado, U.S.A., 1998.

[28] J. Loiseau, S. Goroshin, D. L. Frost, A. J. Higgins, and F. Zhang. Ability of metalized gelled nitromethane to accelerate a flyer plate. In *16th International Detonation Symposium*, Cambridge, U.S.A., 2018.

[29] Y. Kato, K. Murata, and S. Itoh. Detonation characteristics of packed beds of aluminum saturated with nitromethane. *Proceedings of the 13th International Detonation Symposium, IDS 2006*, pages 187–195, 2006.

[30] M. M. Schmitt, P. R. Bowden, B. C. Tappan, and D. Henneke. Steady-state shock-driven reactions in mixtures of nano-sized aluminum and dilute hydrogen peroxide. *Journal of Energetic Materials*, 36(3):266–277, 2018, doi:10.1080/07370652.2017.1376233.

[31] J. Loiseau, G. Chase, S. Goroshin, and D. L. Frost. Detonation and metal acceleration of aluminum-water mixtures. In *16th International Detonation Symposium*, Cambridge, U.S.A., 2018.

[32] M. W. Beckstead. Correlating aluminum burning times. *Combustion, Explosion and Shock Waves*, 41(5):533–546, 2005, doi:10.1007/s10573-005-0067-2.

[33] P. Brousseau, H. E. Dorsett, M. D. Cliff, and C. J. Anderson. Detonation properties of explosives containing nanometric aluminum powder. In *12th Internation Detonation Symposium*, pages 1–10, San Diego, U.S.A., 2002.

[34] L. Maiz and W. A. Trzciński. Detonation and combustion of new heterogeneous composite explosives containing aluminum particles. In *11th International armament conference on scientific aspects of armament and safety technology*, Ryn, Poland, 2016.

[35] D. L. Frost, F. Zhang, S. Murray, and S. McCahan. Critical conditions for ignition of metal particles in a condensed explosive. In *12th International Detonation Symposium*, pages 1–10, San Diego, CA, U.S.A.

[36] W. A. Trzciński, J. Paszula, and S. Grys. Detonation and blast wave characteristics of nitromethane mixed with particles of an aluminium - magnesium alloy. *Propellants, Explosives, Pyrotechnics*, 35(2):85–92, 2010, doi:10.1002/prep.200900041.

[37] J. M. Dewey. The shape of the blast wave: studies of the Friedlander equation. In *21st International Symposium on Military Aspects of Blast and Shock (MABS 21)*, pages 1–9, Jerusalem, Israel, 2010.

[38] H. Kleine, J. M. Dewey, K. Ohashi, T. Mizukaki, and K. Takayama. Studies of the TNT equivalence of silver azide charges. *Shock Waves*, 13(2):123–138, 2003, doi:10.1007/s00193-003-0204-3.

[39] L. E. Fried, W. M. Howard, and P. C. Souers. Cheetah 2.0 user's manual. Technical report, Lawrence Livermore National Laboratory, Livermore, CA, USA, 1998.

[40] M. H. Keshavarz. Detonation temperature of high explosives from structural parameters. *Journal of Hazardous Materials*, 137(3):1303–1308, 2006, doi:10.1016/j.jhazmat.2006.04.057.

[41] V. Tanguay, S. Goroshin, A. J. Higgins, and F. Zhang. Aluminum particle combustion in high-speed detonation products. *Combustion Science and Technology*, 181(4):670–693, mar 2009, doi:10.1080/00102200802643430.

[42] H. Weingärtner and E. U. Franck. Supercritical water as a solvent. *Angewandte Chemie - International Edition*, 44(18):2672–2692, 2005, doi:10.1002/anie.200462468.

[43] C. E. Holley and E. J. Huber. The heats of combustion of magnesium and aluminum. *Journal of the American Chemical Society*, 73(12):5577–5579, 1951, doi:10.1021/ja01156a020.

[44] P-A. Persson, R. Holmberg, and J. Lee. *Rock blasting and explosives engineering*. CRC Press, 1993, doi:10.1201/9780203740514.

[45] W. E. Baker. *Explosions in air*. University of Texas Press, Austin, 1973.

[46] G. F. Kinney and K. J. Graham. *Explosive shocks in air (Second edition)*. Springer, 1985, doi:10.1007/978-3-642-86682-1.

[47] G. G. Bach and J. H. S. Lee. An analytical solution for blast waves. *AIAA Journal*, 8(2):271–275, 1970, doi:10.2514/3.5655.

[48] B. M. Dobratz and P. C. Crawford. LLNL explosives handbook - Properties of chemical explosives and explosive simulants. Technical report, Lawrence Livermore National Laboratory (LLNL), Livermore, California, 1985, https://www.osti.gov/biblio/6530310-llnl-explosives-handbook-properties-chemical-explosives-explosives-explosive-simulants.

[49] J. Leadbetter, R. C. Ripley, F. Zhang, and D. L. Frost. Multiple energy scaling of blast waves from heterogeneous explosives. In *21st International Colloquium on the Dynamics of Explosions and Reactive Systems (ICDERS)*, Poitiers, France, 2007.

[50] Q. Pontalier, A. Longbottom, S. Cargill, C. Grapes, J. Loiseau, S. Goroshin, D. L. Frost, and F. Zhang. Numerical investigation of blast enhancement with metalized explosives. In *32nd International Symposium on Shock Waves*, pages 1–13, Singapore, 2019. doi:10.3850/978-981-11-2730-4_0323-cd.

Transition to Chapter 6

In the previous chapter, the peak blast wave overpressure resulting from the detonation of constant volume charges of gelled and sensitized NM, homogeneously mixed with a dilute suspension of particles, was investigated experimentally. The particles were made of either glass, aluminum or magnesium. Consistent with the results from part II, the addition of inert (glass) particles typically mitigated the blast wave in the near field. The attenuation was attributed to the transfer of heat and momentum from the explosive gases to the particles, and increased with more mass added. In the far field, the blast wave pressure recovered to that of the baseline explosive (gelled NM alone) pressure due to the porous piston effect, also discussed in part II. When the reactive metallic particles were added to the gelled NM, the exothermic reaction of the particles contributed to increasing the blast wave pressure by up to two times the value for the bare explosive alone. The blast enhancement was primarily dependent on the solid mass fraction, with generally a greater pressure augmentation for higher particle mass loading.

The energy released by the particles contributed to increasing the peak blast overpressure within a few hundred microseconds after detonation. This experimental result suggests that anaerobic particle reactions within the detonation products, on microsecond timescales, contribute to the augmentation of the blast pressure. This observation is not consistent with previous models that have assumed that the particles react only aerobically with the surrounding air outside of the fireball on millisecond timescales. The blast wave pressure enhancement was also not a systematic function of particle size. This result implies that conventional models for particle reaction that depend on particle surface area are not valid for describing the particle reaction that occurs in the high temperature and pressure environment within the detonation products. Finally, based on a scaling argument, it was hypothesized that at least 50% of the maximum possible particle energy release contributed to enhancing the blast wave pressure, for the highest particle mass fractions. For a mass fraction of 10%, the energetic contribution was closer to 100%. The previous experimental observations suggest that charges with dilute suspensions of metal particles are more effective than charges with a high mass fraction of particles (described in Chapter 2) to enhance the blast wave pressure. Therefore, enhanced blast explosives (EBX) systems must be adapted accordingly to increase performance.

The previous experimental results highlighted that the blast wave pressure wave was enhanced within at least a few hundred microseconds after detonation. However, with the diagnostics in

the current experimental setup, it is not possible to resolve the extent of particle reaction on timescales of microseconds or tens of microseconds. Moreover, the procedure of scaling the experimental blast wave pressure with various energy values was useful only to indicate the fraction of the particle energy that was released sufficiently rapidly to contribute to the peak blast overpressure. For particles that are reacting far from the blast front, if the reaction rate is too slow, the perturbation to the flow by the local energy release will not have time to reach the blast front and perturb the peak blast overpressure.

Given the uncertainties in modeling the reaction mechanisms and the reaction rate of metal particles in the extreme conditions of the detonation products, and lack of quantitative experimental data on early time particle reaction, the use of a simplified modeling approach seems appropriate. Hence, in Chapter 6, a modeling approach is considered in which the contribution of the particle reaction to the flow is determined by specifying two independent parameters, the fraction of the chemical energy of the particles that is released, and the timescale of the energy release. By varying these two parameters independently, we can then determine the sensitivity of the blast wave properties to the parameters. Similar to the computations presented in Chapter 4, the multiphase hydrocode EDEN is utilized in 1D. The first step was to validate the use of EDEN with inert glass particles embedded uniformly in the explosive. The simplified reaction model noted above was then implemented, with the particle reaction energy released added to the particle phase, which is then transferred to the surrounding gas by convective heat transfer. By varying the reaction time and energy release in the model until a best fit to the experimental data is obtained, insight into the contribution of the particle reaction to the blast enhancement is obtained. This chapter is comprised of a paper published in the proceedings of the 32nd International Symposium on Shock Wave (*ISSW32*), Singapore, 2019.

Chapter 6

Numerical investigation of blast enhancement with metalized explosives

Q. Pontalier, A. Longbottom, S. Cargill, C. Grapes, J. Loiseau, S. Goroshin, D. L. Frost, and F. Zhang, In *32nd International Symposium on Shock Waves*, Singapore, 2019.
doi:10.3850/978-981-11-2730-4_0323-cd

Abstract

Computations are carried out with a multiphase hydrocode to compare the strength of the blast wave generated by the detonation of an aluminized explosive consisting of gelled nitromethane embedded with spherical aluminum particles with the results of a recent experimental study [1]. Calculations for an explosive mixture containing inert glass particles are used to validate the two-phase model. A simplified model for the aluminum particle reaction specifies the reaction time and overall particle energy release as two independent parameters. Although the two parameters cannot be uniquely determined, the results indicate that a significant portion of the aluminum mass must react on the short timescale of the detonation propagation and early product expansion to reproduce the blast arrival time and overpressure in the near field observed experimentally. The blast strength is nearly independent of the particle size which implies that current reaction models for aluminum particles which depend on particle surface area are not appropriate.

6.1 Introduction

6.1.1 Background

Metal particles are commonly added to high explosives to either attenuate or augment the strength of the blast wave generated upon detonation of the explosive. In a recent thematic

issue of the Shock Waves Journal [2], a number of investigators have examined the effect of either embedding inert particles within an explosive or surrounding an explosive with a layer of inert particles on the subsequent multiphase flow field and blast wave structure. With inert particles, the peak overpressure of the blast wave is reduced in the near field as a portion of the thermal energy of the detonation product gases is transferred to kinetic and internal energy of the particles [3, 4]. The explosively-dispersed particles interact with the surrounding atmosphere through drag and generate local pressure disturbances. These pressure fluctuations catch up to and augment the strength of the leading blast wave further from the charge resulting in a recovery of the blast overpressure. In some cases, the peak blast overpressure returns to a value comparable to the baseline case of the explosive with no particles [5, 6].

6.1.2 Reactive particles

For the case of reactive particles, the particle reaction locally raises the temperature and pressure of the surrounding gases, which can lead to augmentation of the blast wave overpressure. The degree of pressure augmentation depends on the rate of particle reaction, the oxidizers available for reaction, the location of the energy release, as well as possible afterburning of the reaction products. While a variety of reactive metals have been added to explosives in the past [7], the most common type of metal particle added to explosives is aluminum due to the high energy release associated with aluminum oxidation and the relatively low metal density, and the focus of the present paper is on aluminized explosives.

A key issue is whether aluminum particles react to a significant extent on the timescale of the detonation propagation (i.e., $\sim$10's μs) within the detonation products, or if they react primarily on much longer, millisecond-timescales within the combustion products and surrounding air. Most previous researchers that have developed models for blast effects from aluminized explosives have assumed the particles react on a much longer (ms) timescale than that of the base explosive. However, there is a substantial body of experimental evidence that indicates that aluminum particles can react to a significant extent on a μs timescale with the products behind a detonation wavefront. This evidence includes detonation tests with aluminum/nitromethane mixtures by Murata and Kato [8] that showed a pressure rise several microseconds behind the detonation front. Cylinder and plate-pushing experiments with aluminum particles in various explosives support the conclusion that aluminum reactions occur as early as 2 μs after passage of the detonation front [9–11]. Furthermore, recent experiments have shown that a mixture consisting of fine aluminum particles mixed with water with 10% added hydrogen peroxide can detonate [12, 13]. This implies that aluminum powder must be capable of reacting with water on a microsecond timescale to support the propagation of the self-sustained detonation front. Since the oxidizers present in the detonation products of common CHNO explosives consist primarily of water, with smaller amounts of carbon dioxide and carbon monoxide present, it is reasonable to assume that aluminum can react with the water in the products at the extreme conditions

behind the detonation front, with pressures on the order of 10's GPa, and temperatures in the range of 3000–4000 K.

In a recent experimental study [1], the blast wave overpressure was determined for constant volume spherical charges containing gelled nitromethane mixed with various mass fractions of aluminum particles with three different sizes (13 μm, 54 μm, and 114 μm). The particles were observed to react promptly in all cases, with the peak blast overpressure enhanced by up to twice the peak overpressure of the baseline case of gelled NM alone. The highest blast overpressure enhancements were reached at mass fractions between 30% and 50%. The blast wave strength was relatively insensitive to particle size. By plotting the blast wave overpressure as a function of distance scaled with the total potential energy release of the explosive and particles, the blast wave decay collapses for the baseline case and for small (10%) aluminum mass loading, suggesting that at this mass loading the aluminum completely reacts on a timescale short enough to support the blast wave propagation.

The rate of particle reaction and the amount of energy released will influence the blast wave properties, including the blast arrival time at a given location and the pressure profile behind the leading blast front. In the present study, a simplified model for particle reaction is used in which the particle reaction time and energy release are specified as parameters. The subsequent blast wave propagation is computed using a multiphase hydrocode. The objective of the present work is to shed some light on the rate of energy release of the particles by comparing the predicted blast wave properties for various reaction parameters with the results of the recent experiments [1].

6.1.3 Summary of the experimental conditions and results

This section summarizes the main experimental conditions and findings of the study that serves as a basis for comparison with the numerical calculations. Details of the experimental procedure and the results of this study can be found in [1]. The field experiments were carried out to determine the effect of particle size and mass loading on the properties of the blast wave from constant volume spherical charges comprised of gelled nitromethane with uniformly embedded aluminum, magnesium, or glass particles. In each trial, the nitromethane was gelled to the consistency of liquid honey with the addition of 4 wt% PMMA. The appropriate mass of metal particles and 0.4 wt% of K1 microballoons, or GMB (added to sensitize the explosive), were then added and after further mixing the explosive mixture was then poured into a spherical glass casing (as shown in Fig. 6.1) and placed at the test site with a height of burst of 1.5 m. Detonation of the mixture was facilitated with a spherical C4 burster charge with a mass of approximately 90 g. The blast wave propagation was tracked using two high-speed videocameras, and the peak blast wave overpressure was determined from the blast wave velocity and utilizing the Rankine-Hugoniot relation. The pressure histories at three distances from the charge (1.0 m, 1.5 m and 2.0 m) were determined with fast-response piezoelectric pressure gauges. Three

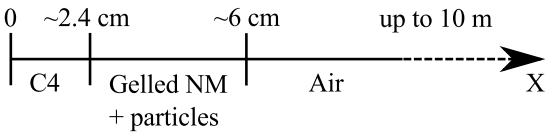

(a) (b)

Fig. 6.1 (a) Photograph of the experimental charge casing (nominal dia 12.7 cm; volume 1 L) in the process of being filled with the explosive mixture, with the central C4 burster charge visible. **(b)** Schematic showing the initial geometry for the 1D computations. The lengths of the C4 booster and the explosive mixture may vary slightly depending on the experimental masses recorded.

different sized spherical aluminum powders from Valimet (Stockton, CA) were tested (H-10, 13 μm; H-50, 54 μm; and H-95, 114 μm), with the particle loading ranging from 10%–50% by mass. The results with aluminized mixtures were compared with constant volume charges containing either the base gelled nitromethane explosive alone, or with mixtures containing inert spherical glass beads (66 μm dia). The addition of the inert particles mitigated the peak blast overpressure in the mid field by up to 38% and the positive-phase impulse by more than 30%, due to the energy expended to accelerate and heat the particles. Conversely, for charges with reactive particles, the particles reacted promptly in all cases, overcoming the losses and enhanced the peak blast overpressure by up to 80%. The blast enhancement with aluminum particles was relatively insensitive to particle diameter, despite a variation in particle size over an order of magnitude or two orders of magnitude in terms of surface area.

6.2 Numerical parameters

The numerical calculations were carried out with the EDEN multiphase hydrocode developed at Fluid Gravity Engineering Ltd. EDEN has been extensively validated in previous studies of reactive, multiphase flows, including modeling the propagation of complex blast waves [14], explosive-related phenomena such as the explosive dispersal of liquids and granular media ([15], and [16, 17], respectively), and afterburning effects [18].

Initial calculations were carried out in a 2D geometry, and the blast wave decay was compared with the results from 1D calculations. The magnitude of the positive-phase pressure region was similar in both cases at the locations of the pressure gauges, with the ground-reflected shock wave, resolved only in the 2D calculations, arriving at the pressure transducers only

after the end of the positive pressure phase. The comparison between the 1D and 2D results suggests that 2D hydrodynamic instabilities (e.g., Rayleigh-Taylor, Richtmyer-Meshkov), and the resulting enhanced mixing will only affect the afterburning phase and not the primary blast wave properties. Since these features are not the focus of this paper, further calculations were carried out in 1D for computational efficiency. The size of the computational domain must be large enough for a direct comparison with the experimental field of view (up to 5 m from the charge), with a simulation running time large enough (20 ms) to capture the positive-phase blast wave phase at the furthest distance from the charge. A photograph of the experimental charge during the filling process and the corresponding dimensions for the computations are shown in Fig.6.1. The lengths of the C4 booster and the explosive mixture were calculated using the experimental masses which implies that the total length may differ slightly from the bulb radius. The size of the domain goes from 0–10 m with a grid resolution 10,000 cells (or 1 cell/mm), sufficient to reach convergence. The pressure-time history is recorded every 0.5 m from 0–5 m for comparison with experimental data. Analysis of the video images [1] indicated that the pressure gauges located in the near field (at 1.0 m, and 1.5 m from the charge) were located within the maximum fireball radius and the signals were perturbed by the highly turbulent multiphase flow. Consequently, in the present study, the calculated overpressure histories will be compared only with the gauge located in the mid field (2.0 m), which is near to or just outside the maximum fireball radius. The computed decay of the peak blast overpressure is compared with experimental results obtained with the videography analysis in the mid-to-far field region (2.0–5.0 m). The computed blast arrival times are compared with the values extracted from each pressure gauge as well as from the video images.

6.3 Two-phase model and explosive equation of state (EOS)

In the two-phase model, the particle phase is distinct from the explosive phase. The particles are not resolved, but rather the particle phase represents a fraction of a numerical cell. In the two-phase model, particles are considered compressible (details of the compressible model can be found in a previous publication [6]), but when replaced with incompressible particles, no changes in the results were observed. In this model, the particle size is an input parameter and influences the timescales of heat and momentum transfer between the particles and the flow.

The explosive phase uses a reactive flow model with SESAME EOS for the reactants and products. Rates of reaction are fitted to take-over experiments [19]. Results with this EOS are compared with the JWL EOS in section 6.5.1. The SESAME EOS [20] is comprised of a library of tables accounting for the thermodynamic properties of materials (NM in this paper). The library includes tables of pressure and energy as a function of density and temperature. For the reactants this table is based on [21] while the products table is generated using CHEETAH 2.0 [22].

6.4 Particle reaction model

The particle reaction model utilized in the present study does not involve any chemistry, but simply specifies the rate and amount of energy release from the particle reaction. Energy is deposited into the particle phase at a constant rate over a specified time period (or burning time). The amount of energy deposited into the particles is controlled via the value of the heat of reaction (q). This value depends on the type of oxidizers present and the percentage of aluminum that is assumed to react, which we denote as ϕ. Complete oxidation of aluminum to Al_2O_3 corresponds to a value of $q = 31.5$ kJ/g. If the aluminum reacts within the combustion products (either on the detonation timescale $\sim$10's μs or during the early expansion of the products on timescales $\sim$100's μs), with water being the primary oxidizer, the energy released in the Al-water reaction is about half the total energy release (15.1 kJ/g). The rest of the energy release is associated with the complete reaction of the intermediary hydrogen gas liberated by this reaction with the surrounding air, which occurs in the product interface/air mixing zone on a timescale $\sim$ms. The particle phase does not lose mass and the energy is rapidly released into the flow by convective heat transfer. In summary, this simplified treatment of the particle reaction does not consider a particular reaction pathway, but only specifies the reaction timescale and amount of energy released over this time period.

6.5 Results

6.5.1 Gelled NM without particles (baseline)

Fig. 6.2 shows a comparison between the experimental measurements of the blast overpressure decay and the time-distance blast trajectory generated for a baseline charge containing only gelled nitromethane (95.6 wt% NM + 4 wt% PMMA + 0.4 wt% GMB) and the computational results obtained with the SESAME EOS for pure NM. A comparison with the overpressure profile at 2.0 m from the charge is shown in Fig. 6.3. The slope of the computed blast wave trajectory shown on the right in Fig. 6.2 agrees well with the experimental values. There is a small uncertainty in time zero from the video images due to the finite recording time of the videocamera, so the experimental blast trajectory was offset slightly to match the arrival time at the last point. The envelope of the overpressure history at 2.0 m shown in Fig. 6.3 is also well reproduced by the computations. From the plot on the left in Fig. 6.2, the computations slightly underpredict the peak blast pressure (as determined by blast wave tracking) in the near field and slightly overpredict the values in the far field. Factors that could contribute to this discrepancy include blast anisotropy due to heterogeneities within the explosive mixture and a slight offset in the centering of the C4 booster. Note that the pressure decay inferred by tracking the blast wave from the video records differs from the peak pressure from the transducer since the blast is not tracked in the same direction. Using the classical JWL EOS [23], with the constants for

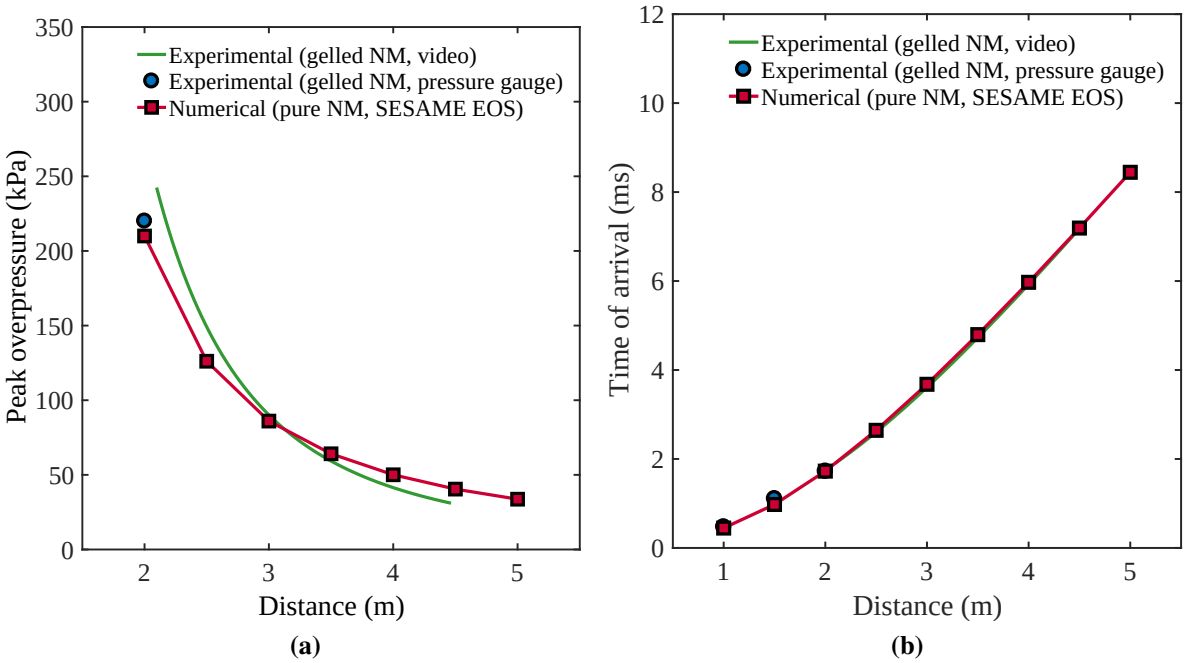

Fig. 6.2 (a) Comparison of the peak blast overpressure decay for pure gelled NM (95.6 wt% NM + 4 wt% PMMA + 0.4 wt% GMB), in the mid-to-far field, obtained either experimentally through videography analysis, pressure gauge measurement, or numerically. Numerically, the explosive is modelled using the SESAME EOS. **(b)** Time-distance trajectory plot of the blast wave motion.

pure NM obtained from the LLNL handbook [24], resulted in larger discrepancies with the experimental data. Consequently, the SESAME EOS is used to model the explosive phase for further calculations when particles are added in the explosive mixture.

6.5.2 Gelled NM with glass particles

To validate the two-phase model, it is of interest to perform calculations with inert glass particles embedded in the explosive. Fig. 6.4 shows the comparison between the experimental data and calculations using 66-µm glass particles (ρ_{glass} = 2.5 g/cm^3), at two different particle loadings (10% and 50%). The simulations reproduce the experimental results closely. An intermediate mass fraction of 30% was also tested and shows similar results. In all these figures, the particles are assumed compressible. Nevertheless, the results do not vary when the particles are assumed incompressible for mass loadings of 10% and 30% (the results collapse and are thus not included in the figures). As a result, in the next section, aluminum particles are considered to be incompressible to reduce the computational costs.

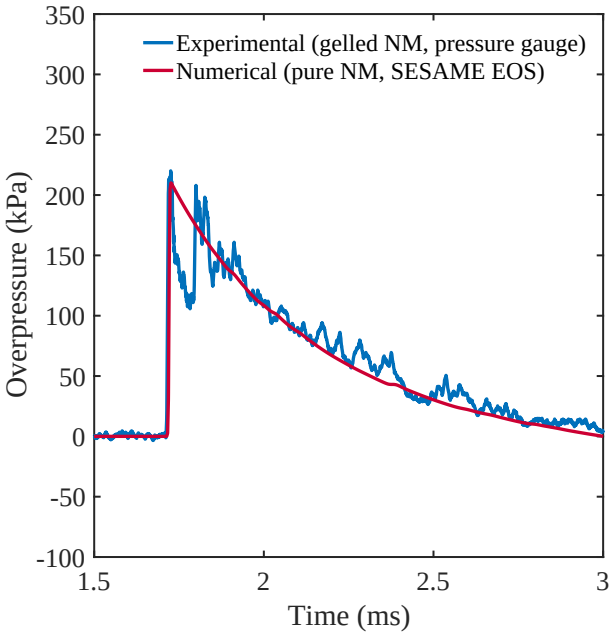

Fig. 6.3 Comparison between the experimental blast overpressure history at a distance of 2.0 m from the charge and the computational results for the pure gelled nitromethane mixture (95.6 wt% NM + 4 wt% PMMA + 0.4 wt% GMB).

6.5.3 Gelled NM with aluminum

For a given Al mass fraction and particle size, the parameters in the reaction model are the heat released from the particle reaction (which depends on the heat of reaction, or if we assume complete oxidation, the percentage of aluminum reacted) and the burning time. The primary objective of the computations is to determine how variations in these two parameters affects the subsequent blast wave propagation, including both the arrival time of the blast wave at a given location (or blast trajectory) and the decay of the peak blast wave overpressure with distance.

For illustration purposes, we will consider only a subset of the data, and particularly consider the experimental results for a mixture containing the largest particles tested, i.e., a mixture of 40 wt% H-95 Al and gelled NM. The experimental results for blast overpressure decay and the time-distance blast trajectory are shown on the left and right, respectively, in Fig. 6.5. The pressure history recorded with the pressure transducer at 2.0 m is shown in Fig. 6.6. Also shown in these figures are the computational results for two reaction scenarios. In the first, the particles are assumed to release their energy very rapidly, on the timescale of the detonation propagation (10 μs). In this case, it is assumed that $\phi = 55\%$ of the maximum particle energy is released. Although we do not specify the reaction pathway or the oxidizers explicitly, with this short reaction time, the particles are expected to react primarily with the detonation products of nitromethane, which consists primarily of water, with smaller amounts of carbon dioxide and carbon monoxide present. The second scenario assumes that 100% of the particle energy is

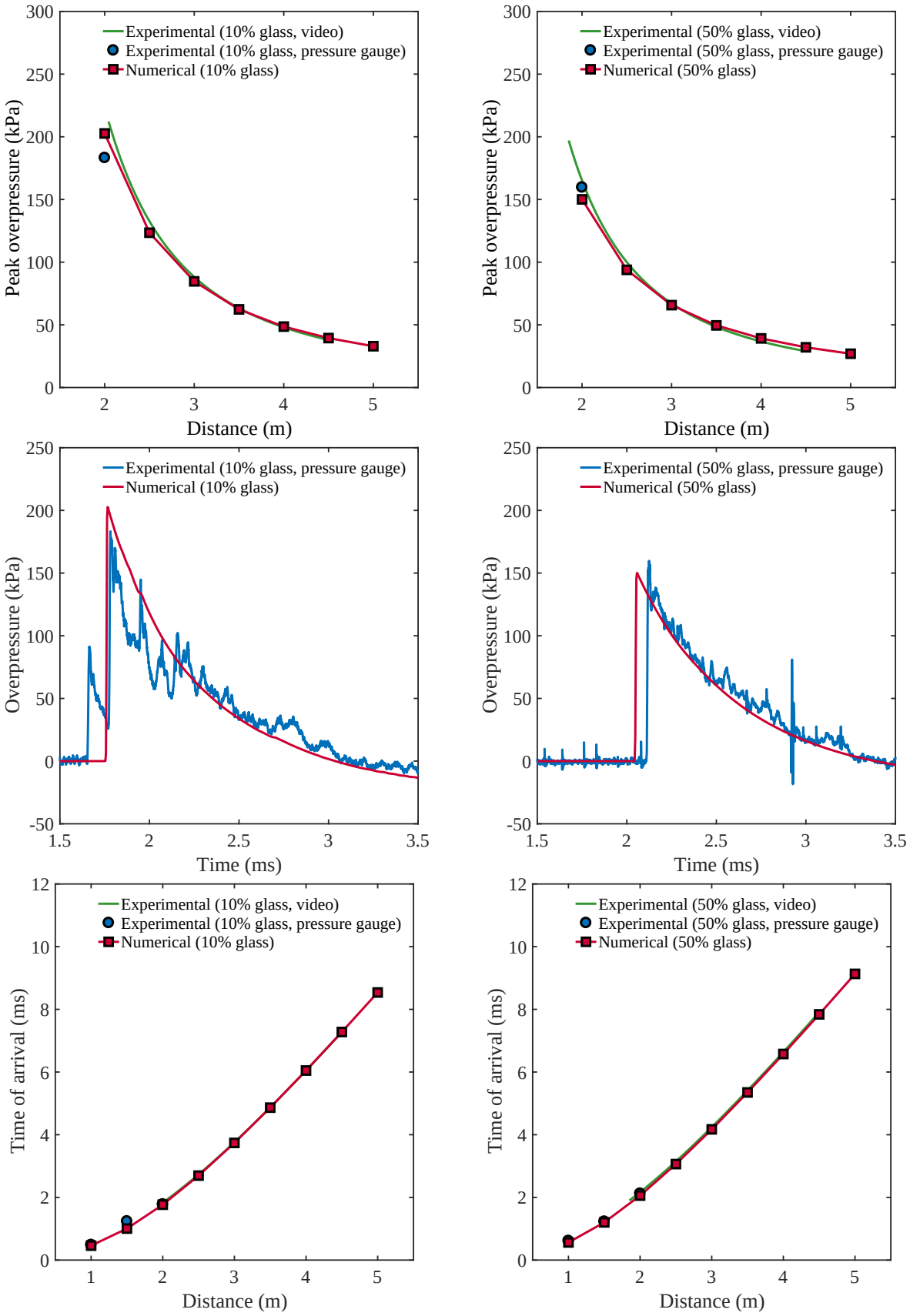

Fig. 6.4 Comparison between experimental data and numerical calculations for the gelled NM mixture with 66-µm glass particles embedded at mass fractions of 10% or 50%. For all these plots, the explosive phase is modeled using the SESAME EOS.

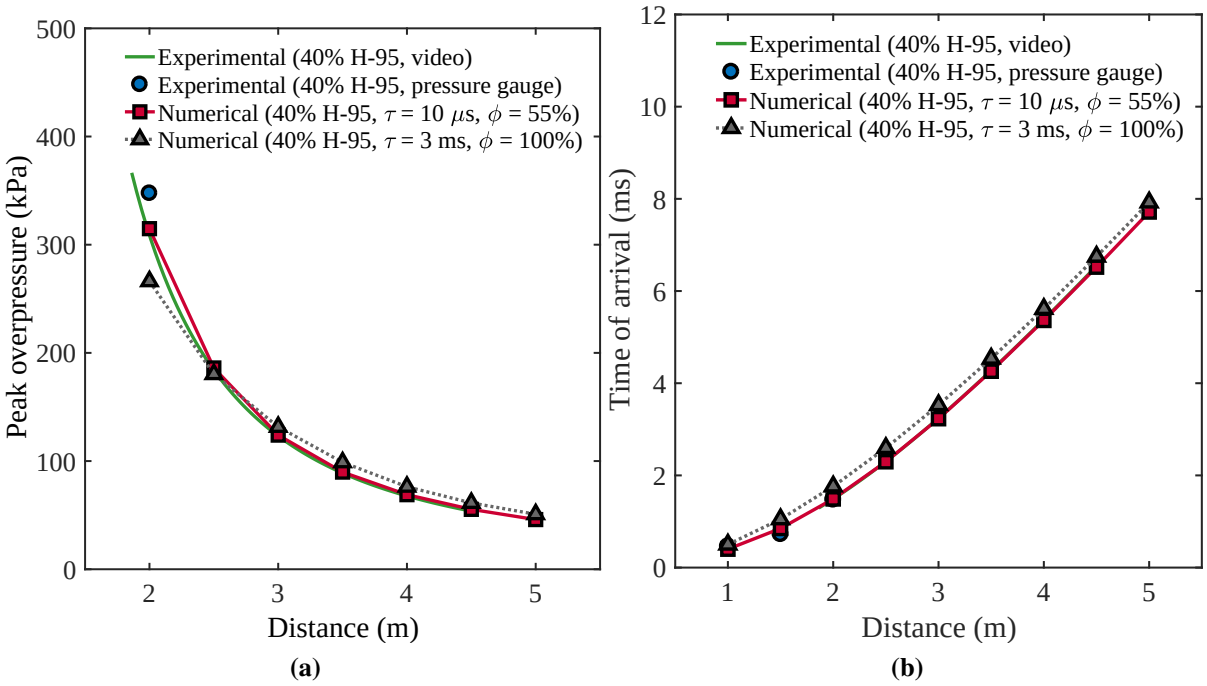

Fig. 6.5 Comparison of the computational and experimental results for **(a)** the blast wave overpressure decay with distance and **(b)** the time-distance blast wave trajectory for 40 wt% H-95 particles in gelled NM. For the computations, two different reaction rate scenarios are considered, one with a short reaction time and the other with a reaction time more than two orders of magnitude longer.

released, i.e., complete oxidation of the Al, but on a much longer timescale of 3 ms, which is the typical time for the fireball to reach its maximum extent.

From Fig. 6.6 it is apparent that with the assumption of the longer reaction time of 3 ms, even with the assumption of complete reaction of the Al, the arrival time is significantly overpredicted and the peak blast overpressure is underpredicted. In contrast, with the other scenario assuming rapid energy release of about half of the maximum particle energy, the computed arrival time and the pressure history agree well with the experimental measurements. This discrepancy in the predicted blast wave properties when asssuming a long reaction time is also reflected in the plots in Fig. 6.5. For example, from the blast trajectory plot in the right of Fig. 6.5, when the energy is assumed to be released on a millisecond timescale, the predicted blast wave trajectory lags behind the experiments which coincides with the predicted trajectory in the case of a smaller amount of energy being released more rapidly.

A comparison of experimental and computational results for the case with the same Al mass loading (40 wt%), but with the smallest particles, H-10 Al, yielded a similar result, i.e., the best fit with the experiments was obtained with the assumption of a short reaction time (10 µs) with 55 % of the total particle energy released. Furthermore, when the mass loading for the H-10 particle was reduced to 10%, the best fit for the computations was obtained when complete energy release (i.e., 100% oxidation) of the particles occurred over this short timescale.

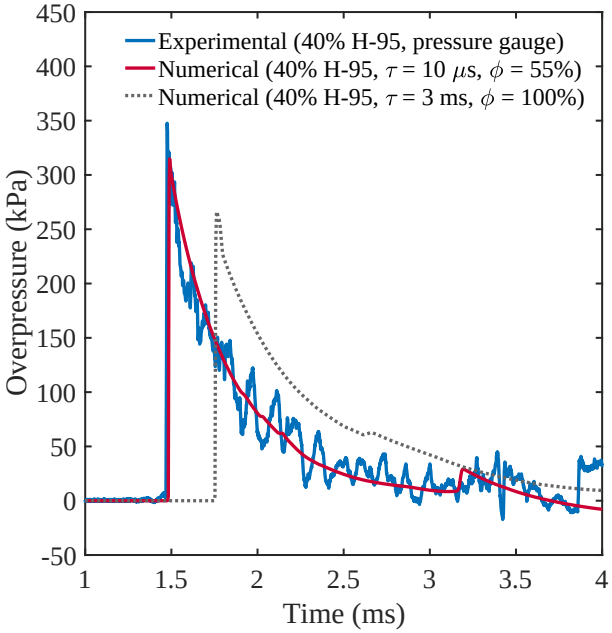

Fig. 6.6 Comparison between the experimental blast overpressure history recorded at 2.0 m from a charge containing 40 wt% H-95 in gelled NM and the computed overpressure history for the same mixture considering two different particle reaction rate scenarios.

6.6 Discussion

Currently the reaction mechanisms and timescales for Al particle reaction at the extreme conditions within the detonation products of a condensed explosive remain uncertain [9]. Even a rudimentary knowledge of the appropriate values for the transport of heat and mass at these conditions is lacking. This motivated the use of a simplified particle reaction model since it would not be possible to validate a detailed particle reaction model at detonation conditions given the lack of well-characterized data regarding condensed-phase kinetic rates in the flow behind the detonation front.

The oxygen balance of an explosive provides a measure of the availability of oxidizers for reacting with aluminum in the explosive decomposition products. Alternatively, equilibrium calculations can be carried out to estimate the amount of aluminum that could theoretically react within the detonation reaction zone as well as during adiabatic expansion of the products. Calculations were carried out using the equilibrium code CHEETAH 2.0 [22] to determine the maximum amount of aluminum that could potentially completely react with the products of the detonation of NM + 4 wt% PMMA at the CJ detonation state as well as if the products were allowed to adiabatically expand to 1 atm. The result of these calculations indicated that a maximum of 26 wt% of Al mixed with NM + 4 wt% PMMA could potentially completely react by the end of the detonation assuming equilibrium conditions are attained. Furthermore, if the products are allowed to expand adiabatically to atmospheric pressure, additional reaction of Al is possible and in this case an initial mixture containing 36 wt% would result in complete

reaction of the Al after expansion. These values provide an upper bound for the amount of aluminum that could react with the detonation products without additional mixing with oxygen in the surrounding air. Due to the finite rates of aluminum oxidation and mixing, the actual amount of Al that would react in the products will be less.

In previous extensive tests with charges containing packed beds of the same spherical Al particles used in the present investigation (H-10, H-50, and H-95), saturated with nitromethane, the Al mass fraction varied from 77–80 wt% [25]. In this case, the explosive mixtures are highly fuel-rich and complete combustion of the Al particles is only possible if the majority of the particles mix and react with the surrounding air. In these experiments, a variety of particle combustion modes were observed, including inert dispersal of particle jets followed by flame propagation through the particle filaments, particle ignition at localized hot spots within the particle cloud and subsequent flame propagation, or relatively uniform combustion of the particles throughout the particle cloud [25]. In the present experiments, particularly for the lower values of Al mass loading, there is a sufficient amount of oxidizer within the detonation products for complete combustion of the Al powder.

Using the experimental blast wave decay rates observed experimentally, together with hydrocode calculations and a simplified Al reaction model, it is not possible to conclusively determine uniquely the reaction rate and amount of energy release, since different combinations of reaction rate and amount of energy release will give similar blast wave profiles. However, the current computations suggest that at least a part of the Al must react rapidly, on a timescale consistent with the detonation propagation, for the blast wave arrival times to be consistent with the experimental results. Since blast wave propagation velocity may be influenced by disturbances from behind reaching the wave over some time, the use of blast data to validate possible reaction models of aluminized explosives is difficult. Furthermore, the visibility of a blast wave is limited at early times due to the intense luminosity generated by condensed explosives. A better test for determining the effect of early-time Al reaction in detonation products is flyer-plate experiments, where the effect of particle reaction on the flyer velocity may be determined on the μs timescale using standard optical techniques.

6.7 Conclusions

Computations with a multiphase hydrocode have been carried out to predict the dynamics of the blast wave generated by the detonation of a heterogeneous explosive consisting of particles embedded within gelled nitromethane, and compared with the results of a recent experimental series [1]. The computations were first compared with tests with the baseline explosive to guide the selection of the explosive EOS. Calculations were then carried out to predict the decay of the blast wave generated by the detonation of an explosive mixture containing various mass fractions of inert glass particles. These results agreed well with the blast decay observed experimentally, suggesting that the two-phase model captures the compressible hydrodynamics of the flow.

Computations were then carried out for charges containing various mass fractions of Al particles of various sizes. Given the uncertainties in how aluminum particles react within the extreme conditions that exist behind the detonation front in a condensed explosive, a simplified reaction model was used in which the particle reaction time and amount of energy release were independent parameters. Although the comparison of the calculations with the experimental observations cannot determine uniquely the burn time and fraction of the Al particles that react, it is apparent that a substantial fraction of the Al particles must react on a timescale of the detonation propagation and the early stages of the expansion of the detonation products to reproduce the arrival time and peak blast pressure observed experimentally in the near field. For low values of particle mass loading, it appears that it is likely that nearly all of the Al reacts on these early timescales.

The observation from the experiments that the strength of the blast wave generated, for a given Al mass fraction, is nearly independent of particle size over an order of magnitude indicates that existing models for particle reaction rate that are a function of particle surface area are not appropriate for Al particle reaction within detonation products.

To clarify the reaction pathways for Al particles in detonation products for improved simulation of reactive blast waves, it is critical to determine the extent of reaction in the first 20 volumes of expansion, which can only be done via the simulation of metal-acceleration experiments.

References

[1] Q. Pontalier, J. Loiseau, S. Goroshin, D.L. Frost, and F. Zhang. Effect of particle loading on the blast wave from a metalized explosive. In *The 25th International Symposium on Military Aspects of Blast and Shock (MABS 25)*, pages 1–20, The Hague, Netherlands, 2018.

[2] D. L. Frost. Heterogeneous/particle-laden blast waves. *Shock Waves*, 28(3):439–449, 2018, doi:10.1007/s00193-018-0825-1.

[3] J. Loiseau, Q. Pontalier, A. M. Milne, S. Goroshin, and D. L. Frost. Terminal velocity of liquids and granular materials dispersed by a high explosive. *Shock Waves*, 28(3):473–487, 2018, doi:10.1007/s00193-018-0822-4.

[4] Q. Pontalier, M. Lhoumeau, and D. L. Frost. Blast wave mitigation in granular materials. *AIP Conference Proceedings*, 1979(1):110014, 2018, doi:10.1063/1.5044933.

[5] Q. Pontalier, J. Loiseau, S. Goroshin, and D. L. Frost. Experimental investigation of blast mitigation and particle-blast interaction during the explosive dispersal of particles and liquids. *Shock Waves*, 28(3):489–511, 2018, doi:10.1007/s00193-018-0821-5.

[6] Q. Pontalier, M. Lhoumeau, A. Milne, A. Longbottom, and D. L. Frost. Numerical investigation of particle-blast interaction during explosive dispersal of liquids and granular materials. *Shock Waves*, 28(3):513–531, 2018, doi:10.1007/s00193-018-0820-6.

[7] N. H. Yen and L. Y. Wang. Reactive metals in explosives. *Propellants, Explosives, Pyrotechnics*, 37(2):143–155, 2012, doi:10.1002/prep.200900050.

[8] K. Murata and Y. Kato. Application of PVDF pressure gauge for pressure measurements of non-ideal explosives. *International Journal of the Society of Material Engineering for Resources*, 17(2):112–114, 2010, doi:10.5188/ijsmer.17.112.

[9] M. N. Makhov, M. F. Gogulya, A. Yu. Dolgoborodov, M. A. Brazhnikov, V. I. Arkhipov, and V. I. Pepekin. Acceleration ability and heat of explosive decomposition of aluminized explosives. *Combustion, Explosion and Shock Waves*, 40(4):458–466, 2004, doi:10.1023/B:CESW.0000033569.77449.d9.

[10] V. W. Manner, S. J. Pemberton, J. A. Gunderson, T. J. Herrera, J. M. Lloyd, P. J. Salazar, P. Rae, and B. C. Tappan. The role of aluminum in the detonation and post-detonation expansion of selected cast HMX-based explosives. *Propellants, Explosives, Pyrotechnics*, 37(2):198–206, 2012, doi:10.1002/prep.201100138.

[11] J. Loiseau, S. Goroshin, D. L. Frost, A. J. Higgins, and F. Zhang. Ability of metalized gelled nitromethane to accelerate a flyer plate. In *16th International Detonation Symposium*, Cambridge, U.S.A., 2018.

[12] M. M. Schmitt, P. R. Bowden, B. C. Tappan, and D. Henneke. Steady-state shock-driven reactions in mixtures of nano-sized aluminum and dilute hydrogen peroxide. *Journal of Energetic Materials*, 36(3):266–277, 2018, doi:10.1080/07370652.2017.1376233.

[13] J. Loiseau, G. Chase, S. Goroshin, and D. L. Frost. Detonation and metal acceleration of aluminum-water mixtures. In *16th International Detonation Symposium*, Cambridge, U.S.A., 2018.

[14] A. M. Milne, S. B. Cargill, and A. W. Longbottom. Modelling of complex blast. *International Journal of Protective Structures*, 7(3):325–339, 2016, doi:10.1177/2041419616661431.

[15] A. M. Milne, A. Longbottom, D. L. Frost, J. Loiseau, S. Goroshin, and O. Petel. Explosive fragmentation of liquids in spherical geometry. *Shock Waves*, 27:383–393, 2017, doi:10.1007/s00193-016-0671-y.

[16] A. M. Milne. Gurney analysis of porous shell. *Propellants, Explosives, Pyrotechnics*, 41(4):665–671, 2016, doi:10.1002/prep.201600016.

[17] A. M. Milne, E. Floyd, A. W. Longbottom, and P. Taylor. Dynamic fragmentation of powders in spherical geometry. *Shock Waves*, 24(5):501–513, 2014, doi:10.1007/s00193-014-0511-x.

[18] A. Longbottom, J. Verreault, S. Cargill, and A. Milne. Effect of different numerical methods on the modelling of TNT afterburn in internal explosions. In *25th International Symposium on Military Aspects of Blast and Shock (MABS 25)*, pages 1–18, The Hague, Netherlands, 2018.

[19] S. A. Sheffield, D. M. Dattelbaum, R. Engelke, R. R. Alcon, B. Crouzer, D. L. Robbins, D. B. Stahl, and R. L. Gustavsen. Homogeneous shock initiation process in neat and chemically sensitized nitromethane. In *13th International Detonation Symposium*, Norfolk, VA, U.S.A., 2006.

[20] Sesame: the Los Alamos National Laboratory equation of state database. Technical report, Los Alamos National Laboratory, https://permalink.lanl.gov/object/tr?what=info:lanl-repo/lareport/LA-UR-92-3407.

[21] M. E. Kipp and J. W. Nunziato. Numerical simulation of detonation failure in nitromethane. In *7th International Detonation Symposium*, Annapolis, MD, U.S.A., 1981.

[22] L. E. Fried, W. M. Howard, and P. C. Souers. Cheetah 2.0 user's manual. Technical report, Lawrence Livermore National Laboratory, Livermore, CA, USA, 1998.

[23] E. L. Lee, H. C. Hornig, and J. W. Kury. Adiabatic expansion of high explosive detonation products. Technical report, Lawrence Radiation Lab, University of California, Livermore, 1968, https://www.osti.gov/servlets/purl/4783904.

[24] B. M. Dobratz and P. C. Crawford. LLNL explosives handbook - Properties of chemical explosives and explosive simulants. Technical report, Lawrence Livermore National Laboratory (LLNL), Livermore, California, 1985, https://www.osti.gov/biblio/6530310-llnl-explosives-handbook-properties-chemical-explosives-explosives-explosive-simulants.

[25] D. L. Frost and F. Zhang. The nature of heterogeneous blast explosives. In *19th International Symposium on Military Aspects of Blast and Shock (MABS 19)*, Calgary, Canada, 2006.

Summary of Chapter 6

In Chapter 6, the blast wave overpressure produced by constant volume explosive charges, comprised of gelled NM with a dilute suspension of glass or aluminum particles, was investigated computationally with a 1D multiphase model. With added glass particles, the numerical calculations were based on the same two-phase model as in part II. The simulations reproduced the experimental blast wave overpressures well, for all three mass loadings tested. These results served to validate the hydrocode EDEN for modeling heterogeneous explosive systems with inert particles embedded. For aluminum particles, a simple reaction model was implemented, in which the energy released by the particles was transferred to the gas phase by convective heat transfer. The timescale and amount of energy release was systematically varied to reproduce the experimental blast wave overpressure. The amount of energy released was assumed to be a fraction of the maximum particle energy release, based on the total oxidation of aluminum with molecular oxygen. The results indicated that the aluminum particles must release their chemical energy within the first tens of microseconds after detonation, to reproduce the experimental blast wave overpressure. This observation reinforced the hypothesis in which the blast wave overpressure enhancement results primarily from anaerobic particle reactions, during the timescale of the detonation wave propagation. At this timescale, the particles do not have sufficient time to escape the detonation products due to their inertia. The blast enhancement was also independent of particle size, at a given mass fraction. Hence, the results of Chapter 6 have shown that existing particle reaction models at ambient pressure in which the reaction rate depends on the particle surface area, were inadequate to model the particle reaction that occurs in the high temperature and pressure environment within the detonation products and the blast wave pressure augmentation from metalized explosives.

Moreover, the computational results inferred that around 50% of the maximum particle energy release was transferred to the gas phase for higher particle mass loadings, whereas close to 100% of the maximum particle energy release was transferred for a solid loading of 10%. These energy values agreed well with the values obtained in Chapter 5 and suggest that all the energy released by the particles contributed to the peak blast wave overpressure enhancement. This observation also implied that aerobic reactions played a role in the blast enhancement. Furthermore, it was hypothesized that these aerobic reactions resulted primarily from molecular hydrogen, released when the aluminum particles reacted with water vapour within the detonation products,

reacting with the air in the turbulent mixing zone at the contact surface of the fireball. This reaction mechanism has not previously been proposed as the rate-limiting step for the coupling of the particle reactions from heterogeneous explosives to the enhancement of the blast wave. For mining explosives, the generation and combustion of this hydrogen could improve the earth-moving capability.

Part IV

Chapter 7

General conclusions

7.1 Synopsis of contributions

The objective of the research described in this thesis was to elucidate the mechanisms by which explosive dispersion of inert or reactive materials could influence the strength of a blast wave. The primary goal of this research was to contribute to the fundamental understanding of blast waves propagating in high-velocity multiphase flows. This thesis work was also motivated by the critical need to predict potential hazards to human life and buildings caused by the detonation of chemical explosives during industrial accidents, terrorist attacks, or energetic materials transportation (configuration 1, Part II). The results presented in this part could also be used to improve the design of blast wave mitigation systems. Conversely, the second configuration (part III) investigated the performance of metallized explosives with dilute particle suspensions. The results obtained have direct applications for the design of enhanced blasting explosives (EBX) for military and mining applications. They also contribute to advancing knowledge on the chemical reactions of metals to extreme pressures.

In the first part of the manuscript, a critical review of heterogeneous explosives systems with stratified material layers and embedded solid particles was presented. In the second part of the manuscript, the blast wave attenuation of a spherical high explosive charge surrounded by either a bulk liquid, wetted granular powders, or dry granular powders was investigated experimentally in the free field. The experimental results showed that dry granular powders performed much better than bulk liquids and saturated powders at mitigating the blast wave. The lower mitigation effectiveness of bulk liquids was a consequence of their poor compressibility. In comparison, compaction of dry powders and the subsequent collapse of interstitial air pores led to irreversible energy losses, resulting in more effective mitigation of the blast wave overpressure. Powders saturated with water behaved similarly to a bulk liquid with respect to the blast wave attenuation due to the stress-bearing capability of the interstitial water. The energy spent accelerating the materials also reduced the blast wave energy. Nevertheless, the high mass flux of material dispersed in jet-like structures posed significant hazards in the near field. In this

region, the supersonic particle jets could easily perforate the human body or cause damage to nearby structures. Moreover, these jets of material supported the blast wave overpressure and contributed to reducing the blast wave mitigation effectiveness with distance, even if the materials lagged at a noticeable distance behind the blast wave front. This effect resulted from the motion of the pressure disturbances driven by the jets, which merged with the blast front after travelling in the hot post-shocked medium. This jet-driven piston effect has never been characterized in the literature before, but contributes significantly to further understanding the dynamics of heterogeneous explosive systems. Including the pressure contribution of the dispersed materials to the blast wave complicates the design of mitigation systems but is essential to predict explosion hazards accurately. The jet velocity for dry granular powders was less than for wetted powders or bulk liquids, also attributed to losses due to compaction effects [1]. Consequently, systems with stratified layers of granular powders are preferable to systems with liquids/wetted powders to mitigate explosion hazards.

The numerical results showed that traditional two-phase models implemented in hydrocodes could reproduce the blast wave pressure decay trends with distance. This reproduction was only possible if momentum and energy exchanges were allowed between the material and the gaseous phase. Through a parametric analysis, the simulations confirmed that the mass of the mitigant normalized by the explosive mass was the primary parameter characterizing the blast wave attenuation, as observed experimentally. These results, coupled with those of a companion study [2] demonstrated that conversion of the chemical explosive energy into internal energy of the material layer was the main physical process responsible for the blast attenuation, especially for large masses of material. The size of the explosively-dispersed solid particles/liquid droplets had a weak influence on blast attenuation and was of secondary importance. More importantly, the calculations highlighted the contribution of the pressure disturbances to the blast wave hypothesized in the experimental study. This porous piston effect has been subsequently corroborated in recent numerical studies [3, 4]. The simulations also showed that the primary hazard in the near field ($Z < 1$ m/kg$^{1/3}$) was clearly associated with the impact of the dispersed material. However, the hazards due to material dispersal diminished in the mid-to-far field when the jets decelerated due to aerodynamic drag. Thus, the blast wave was the most dangerous explosive feature in this region. The combined experimental and numerical results for the explosive configuration with stratified layers of materials suggested that developing blast wave mitigation systems is a complex task and requires precise hazard assessments at specific distances from the explosion center.

In the third part of this thesis, the blast wave pressure resulting from the detonation of a liquid explosive, uniformly mixed with micrometric inert (glass) and chemically reactive particles (aluminum, magnesium), was investigated experimentally and computationally. As for explosive systems with stratified material layers, the blast wave was attenuated in the near field with added glass particles compared to that of the bare liquid explosive without particles. However, the mitigation effectiveness decreased with distance due to the aforementioned piston effect. The

prompt and exothermic metal reactions within the detonation products enhanced the blast wave pressure for added aluminum and magnesium particles. The particle energy release compensated largely for the reduction of explosive energy due to particle dilution and augmented the peak blast pressure by up to two times that for the neat explosive. The first signs of blast enhancement were observed a few hundred microseconds after detonation, inside the detonation products. Moreover, the blast enhancement was relatively insensitive to particle size. These observations suggest that previous reaction models based solely on particle reaction with ambient air and depending on particle surface area are inadequate to explain the blast enhancement in metalized explosives.

Numerical calculations were carried out using the same model as for part II but with the addition of a simple particle reaction model for aluminum. In this model, the metal reaction energy was dumped into the particle phase and then transferred to the gas phase by convective heat transfer. The particle energy release and the reaction timescales were parametrically varied to match the experimental blast wave pressures. As observed experimentally, the blast enhancement was insensitive to particle size. Moreover, the particles had to react within the first tens of microseconds to match the experimental results. At these timescales, the particles did not have time to escape the detonation products due to their inertia and thus, could not access the surrounding air. This observation further demonstrated that previous particle reaction models in blast enhancement studies that ignored particle reaction with detonation products and considered only particle reaction with air were invalid. However, the numerical results showed that some aerobic reactions (with air) contributed to the blast enhancement. The hypothetical scenario explaining these results for aluminum particles is the following. The aluminum particles react primarily with the oxidizer species within the detonation products under supercritical conditions. Under these conditions, the aluminide oxide layer coating the particle dissolves and is no longer a barrier to the reaction of the pure metal. The metal reacts with water vapour (the most prevalent oxidizer for many CHNO explosives) in the products to produce hydrogen and aluminum suboxides which eventually chemically condense to form the most stable oxide (i.e., Al_2O_3). The hydrogen mixes and burns with the oxygen in air, at the turbulent fireball interface, thus explaining the contribution of aerobic reactions to the blast enhancement. The results also indicated that, for initial particle mass fractions greater than 20%, at least half the maximum particle energy release had to be released sufficiently rapidly to contribute to the blast wave to reproduce the experimental blast wave pressures observed. Similar results were observed recently in the underwater detonation of metalized explosives [5]. Conversely, for a particle loading of 10%, the maximum energy had to be released on a timescale of about ten microseconds after detonation and coupled entirely to the blast wave front. This observation suggested that aluminum oxide condensation and hydrogen mixing/burning with the surrounding air occurred extremely rapidly, just behind the sonic detonation plane. The combined experimental and numerical results of part III contribute further to understanding the fundamentals of metal reaction at high pressures and to the field of explosive hazard predictions.

7.2 Directions for future research

Validation of numerical models requires well-characterized experimental data. Since heterogeneous explosive systems are intrinsically stochastic, it is well-known in the blast wave community that experimental blast wave overpressure and impulse results present a certain degree of variability [6]. Hence, the experiments in this thesis must be repeated to quantify the uncertainties more precisely and validate the numerical models with higher fidelity. For example, in the experiments of part II (Chapter 3), only one trial was repeated at a similar mass of mitigant to explosive (M/C) ratio. Hence, it was difficult to quantify the experimental variability of the peak blast wave overpressure and the positive-phase impulse. It is then of interest to repeat these experiments several times for a given material, at a specific M/C value. Conversely, the experiments of part III have been repeated several times[1] by Jason Loiseau and co-workers (RMC, Canada), and the reduction of the results are now under joint investigation. The replicated datasets could give additional information on the experimental variability and quantify the blast wave asymmetry. These new datasets could also provide additional information on the blast enhancement from explosive charges with magnesium particles. In this thesis, it was observed with a limited dataset that mixtures with 20 wt% of magnesium particles performed exceptionally well, but the results seemed anomalous and need to be confirmed with repeated trials.

The experimental setups could be adapted to further characterize the mitigation of explosions from charges with stratified material layers. For example, cantilever gauges could be used to characterize the particle load on a structure further as carried out previously by Frost and al. [7]. In the case of heterogeneous explosive systems with reactive embedded reactive particles (Chapter 5), an experimental device that would capture the dispersed particles a few microseconds after detonation (post-mortem analysis) would be beneficial. Once analyzed through a scanning electron microscope (SEM) and thermal analysis techniques (e.g., differential scanning calorimetry (DSC), thermogravimetric analysis (TGA)), the particles would reveal their true nature. If they are composed of metal oxide only, it would suggest that the pure metal has completely reacted within the detonation products. The results presented in this thesis indicated that aluminum particles need to react nearly completely for a mass loading of 10% to generate the blast pressures observed; thus, this case would be ideal for a preliminary investigation. In general, capturing condensed and gaseous products within the detonation products in a spatially- and temporally-resolved manner is extremely challenging to do experimentally. Nevertheless, some sort of direct *in-situ* sampling at early times within the fireball would provide the most direct evidence of the early time reaction history of the particles.

The results of Chapter 5 proved the energetic contribution of both anaerobic and aerobic metal reactions to the blast wave. The metallic particles were assumed to react chemically at microsecond timescales, predominantly with the water in the detonation products, to produce hydrogen. The contribution of aerobic reactions to the overall energy release was assumed to

[1] Personal communication with Jason Loiseau, July 2022

result from the rapid mixing and combustion of hydrogen with the surrounding air at the fireball interface. This hypothetical two-step reaction pathway could resolve the apparent paradox in the numerical results of Chapter 6. These results show better agreement with experimental data if the maximum metal chemical energy (based on the reaction of the particles with air) is assumed to be released in tens of microseconds. Most particles cannot access the surrounding air on this timescale due to their inertia and, thus, cannot react with the molecular oxygen in the air. This contradiction can be resolved if the total release of energy from the metal comes from a multi-step reaction pathway. For example, the proposed reaction pathway involving the reaction of the metal with water in the detonation products and the subsequent reaction of the hydrogen with the surrounding air releases the same amount of energy as the metal reacting with air alone. Nevertheless, this hypothetical reaction pathway has not been validated by direct experimental measurements in this thesis.

A possible experiment to evaluate the relative contribution of aerobic and anaerobic metal reactions to the blast wave energy would be to detonate a metalized explosive in an explosive chamber filled with an inert gas. Filling such a chamber with an inert gas would eliminate the possibility of aerobic reactions. Nitrogen is the most appropriate gas since air is composed primarily of 78% nitrogen, so the heat capacity of the gas (which can affect the blast wave pressure and propagation) would be relatively similar to that of the atmospheric air. Care should be taken to record the blast pressure far from the chamber walls to avoid perturbation of the blast wave by reflections. The alteration of the blast profile associated with these reflections would prevent a reliable comparison with the free-field experiments of this thesis. As suggested earlier, the detonation of an explosive charge of gelled nitromethane mixed with 10 wt% aluminum particles would be the ideal case for a preliminary study. If the blast wave pressure recorded in the nitrogen-filled chamber is about half the pressure of the same blast wave in the air (investigated in this thesis), then this would confirm that the total mass of particles burns anaerobically in the detonation products. Indeed, the reaction of the metal with water alone releases half of the total energy of the proposed reaction pathway, so the blast wave enhancement should be half that observed for the same blast in the air. This would also suggest that the remaining energy released by aerobic reactions in free-field air blast experiments is due to the combustion of gaseous species that can mix quickly with air. The nature and concentration of these species could then be determined by experimental detectors and reveal the presence of hydrogen.

On the analytical and numerical side, the energy partition between the blast, the fireball and the dispersed powders/liquids in heterogeneous explosive systems with a stratified layer of material should be investigated at various mass of mitigant to the explosive ratios (M/C). This analysis would be a natural extension of the work presented in Chapter 4 and in [2]. It would aim to modify the Fano-Fischer-Hutchinson equation (see section A.6.3 of Appendix A) initially developed for hard-cased charges.

Improving models and equations of states is undoubtedly of interest to increase the predictive capability of numerical simulations. To improve the accuracy of the two-fluid approach to model

heterogeneous explosive systems with stratified material layers, the equations of states and sub-grid models must be defined more accurately, and account for other dissipative phenomena such as liquid vaporization, particle fracturing, etc. For example, modeling compaction with a pressure-dependent yield strength to account for the deviatoric response of dry or wet powders [8–10], and the inclusion of constitutive models should provide more accurate predictions. In a mesoscale approach, resolving both the flow field and the particles/droplets, the influence of the formation of jets and particle-particle collisions on the resulting blast wave pressure could be explored. The mesoscale approach is now limited to studies in the near field [11] and thus neglects the far-field interaction between the particles and the blast wave. Nevertheless, there are current efforts with the computational community studying compressible, multiphase turbulence to carry out exascale computations of particle-laden flows[2] in both the near-and-far field of heterogeneous explosions. Turbulence effects were not modeled in the numerical simulations of this thesis but may have importance on the overall dynamics of the blast wave. A more turbulent flow generates more particle drag and better convective heat transfer. Therefore, the localization and magnitude of the porous piston effect observed in the numerical simulations could be modified by turbulence effects.

The numerical challenges for heterogeneous explosive systems with embedded reactive particles are also considerable. Since the physical/chemical mechanisms for the reaction of metal particles under the extreme conditions found in the detonation products are largely unknown, some numerical modellers resort to using a thermodynamic approach. In this approach, the pressure and temperature of the expanding products are evaluated through calibration of the equation of states with experimental data obtained at the detonics stage and then used in single-phase numerical models. However, these calibrations are appropriate for the first few expansion volumes of the products but generally lack accuracy for modelling the blast wave propagation over large distances. Hence, a full calibration encompassing the dynamics of these heterogeneous explosive systems at various timescales remains to be done. For two-phase models, an approach based on the particle energy release such as the one carried out in the present thesis, seems appropriate to bypass the uncertainties in the metal reaction, in the first instance. This approach is suitable for charges with dilute suspensions of particles ($\leq$ 60 wt%) since the energy spent to form and accelerate material is less compared to a configuration with a packed bed of particles. Hence, the particle energy release associated with exothermic reactions could be quantified more accurately. This approach could also be extended to different explosive formulations with other metals. As with the first configuration, consideration of turbulence effects would be beneficial in assessing the possibility of hydrogen mixing (produced by the reaction of metal particles with detonation products) with the surrounding air. The characteristic mixing time of hydrogen with air appears to be the limiting factor in the energy contribution of aerobic reactions to the blast wave. Therefore, comparison of mixing timescales with blast

[2] https://www.eng.ufl.edu/ccmt/, accessed August 10, 2022

enhancement timescales could provide information on the energetic coupling between hydrogen combustion and the blast wave.

7.3 Applications to other explosive systems and engineered solutions

The main objective of this thesis was to study the fundamental interactions between inert or reactive materials and the blast wave during an explosive dispersal event. In this thesis, the explosions were produced by the detonation of powerful chemical explosives, but several results obtained can be applied to other explosions, such as those resulting from natural events. For example, the porous piston effect described for the first configuration (Part II) could occur during volcanic eruptions. Rocks and ash dispersed at high velocities could generate pressure perturbations and modify the blast wave pressure decay with distance. Similarly, at astrophysical scales, the plasma ejected during supernova explosions could also influence the strength of the blast wave. For this specific problem, it would be interesting to evaluate the interaction between this piston effect and the magnetic effects resulting from the plasma motion.

The configuration studied in Part II consisted of a spherical charge containing a chemical explosive surrounded by a material layer. This simplified configuration was not intended to evaluate a particular blast wave attenuation system but rather to study the fundamental interactions between the blast wave and the material layer. The spherical geometry was convenient for designing the charge but also allowed for comparison with 1D simulations. The results obtained with this configuration suggest that i) dispersed materials reduce the blast wave pressure decay with distance (porous piston effect) and ii) blast wave attenuation systems should include some mass of compressible materials.

These two main results have practical applications. Consider the example of a terrorist car bombing. A car is filled with a certain amount of explosives that can be easily estimated (several hundreds to thousands of kilograms). The detonation of the explosive generates a blast wave, shatters the car and disperses the fragments into the air at supersonic speed. In this configuration, the blast wave pressure can be roughly estimated at different distances from the explosion center using traditional blast wave scaling laws. A typical mitigation system to protect nearby infrastructures would consist of a hard physical barrier located at a large stand-off distance from the structures but relatively close to the hypothetical explosion center (near field). This barrier would effectively stop the dispersed materials (car fragments) and help limit the influence of the porous piston effect on the blast wave. Behind the barrier, the blast wave would lose energy by propagating in the air. The blast wave will eventually encounter the blast attenuation system at a smaller stand-off distance from the structure.

The blast attenuation system must include a certain mass of compressible materials for effective mitigation. The material mass increases the impedance mismatch at the air-layer

interface and the heat/momentum transfer imparted to the material layer. Nevertheless, the material mass must be manageable to minimize the dispersion of additional fragments. On the other hand, the compressible nature of the materials would increase the irreversible energy losses. For the transportation of energetic materials, the type and mass of the blast mitigant must be carefully considered to achieve a practical yet efficient mitigation system. A large mass of mitigant would make the system too heavy for transportation. Moreover, the results of this thesis showed that the blast wave attenuation follows a weak power law of the M/C ratio (mass of mitigant normalized by the explosive mass). This result suggests that above a certain threshold ($M/C \sim 10 - 20$), blast wave attenuation systems would not benefit much from the addition of material. Adding extra mass also generates more scattered fragments, which can lead to additional hazards. The addition of compressible materials at a M/C ratio of about 10 is recommended for practical and luggable blast wave mitigation systems. An example of mitigation systems for energetic materials transportation is the "Fountain" system [12]. This system designed by Special Materials Corp (Russia) consists of a box for containing the explosive mass. The walls of the box are filled with a gelled water containing compressible foam balls. The walls are lined with a ballistic fabric to limit the dispersion of materials in case of detonation of the explosive. The "Fountain" system has been designed to carry up to 5 kg of TNT.

The configuration studied in Part III consisted of mixing metallic particles with a conventional explosive to enhance blast wave effects. It was shown that, unlike configurations with high particle mass loadings, the addition of particles at a lower mass fraction (< 50 wt%) to a conventional explosive generates greater blast wave effects. The design of enhanced blasting explosives (EBX) must therefore be adapted accordingly. The results in Part III also indicate that metal particles react on the microsecond scale in the detonation products to produce a significant volume of hydrogen. This hydrogen burns with air at the fireball interface. The combustion of this hydrogen could increase the blast wave impulses and improve the earth-moving capability of mining explosives.

Summary

- The interactions between the dispersed materials, the fireball and the blast wave generated by detonating a chemical high explosive were investigated in two configurations.
- (Config 1) Even if they initially mitigate the blast wave, the explosive dispersal of inert materials poses a serious threat to personnel and structures in the near field and contributes to sustaining the blast wave pressure in the far field.
- (Config 1) Granular powders were found to be more effective blast mitigants than liquids due to the compressibility of a porous layer.
- (Config 2) Micrometric metallic particles can react substantially at microsecond timescales and anaerobically with the chemical species inside the detonation products to enhance the blast wave pressure.
- (Config 2) The hydrogen production resulting from the anaerobic particle reactions could mix and burn with the hot air at the fireball interface, thus further contributing to the blast wave enhancement.
- (Config 2) The blast wave enhancement was insensitive to particle size. Hence, previous reaction models depending on the particle surface are inadequate to characterize metal reactions following the detonation of metalized explosives.

References

[1] J. Loiseau, Q. Pontalier, A. M. Milne, S. Goroshin, and D. L. Frost. Terminal velocity of liquids and granular materials dispersed by a high explosive. *Shock Waves*, 28(3):473–487, 2018, doi:10.1007/s00193-018-0822-4.

[2] Q. Pontalier, M. Lhoumeau, and D. L. Frost. Blast wave mitigation in granular materials. *AIP Conference Proceedings*, 1979(1):110014, 2018, doi:10.1063/1.5044933.

[3] Y. Sugiyama, T. Homae, T. Matsumura, and K. Wakabayashi. Numerical study on the attenuation effect on the blast wave of encircling a high explosive with granular media. *Journal of Applied Physics*, 127(16):164701, 2020, doi:10.1063/1.5143351.

[4] Y. Sugiyama, T. Homae, T. Matsumura, and K. Wakabayashi. Numerical study on the mitigation effect of glass particles filling a partially confined space on a blast wave. *International Journal of Multiphase Flow*, 136:103546, 2021, doi:10.1016/j.ijmultiphaseflow.2020.103546.

[5] A. G. Milne, A. M. Milne, A. Burn, A. Carr, and M. Thomson. A modelling approach for the analysis of underwater explosive performance trials. *Propellants, Explosives, Pyrotechnics*, 46(12):1825–1836, 2021, doi:10.1002/prep.202100154.

[6] D. G. Farrimond, S. E. Rigby, S. D. Clarke, and A. Tyas. Time of arrival as a diagnostic for far-field high explosive blast waves. *International Journal of Protective Structures*, 13(2):379–402, 2022, doi:10.1177/20414196211062923.

[7] D. L. Frost, C. Ornthanalai, Z. Zarei, V. Tanguay, and F. Zhang. Particle momentum effects from the detonation of heterogeneous explosives. *Journal of Applied Physics*, 101(11):1–14, 2007, doi:10.1063/1.2743912.

[8] M. A. Cooper, A. W. Sapp, S. Guo, and T. J. Vogler. Imaging perturbed shock propagation in powders. *Review of Scientific Instruments*, 91(025109), 2020, doi:10.1063/1.5131348.

[9] M. Hudspeth, J. Olles, A. Mandal, J. Williams, S. Root, and T. Vogler. Strength of porous α- SiO_2 in a shock loaded environment: Calibration via Richtmyer-Meshkov instability and validation via Mach lens. *Journal of Applied Physics*, 128(205901), 2020, doi:10.1063/5.0028026.

[10] T. J. Vogler and M. C. Hudspeth. Tamped Richtmyer–Meshkov instability experiments to probe high-pressure material strength. *Journal of Dynamic Behavior of Materials*, 7(2):262–278, 2021, doi:10.1007/s40870-020-00288-y.

[11] A. V. Marayikkottu and D. A. Levin. Influence of particle non-dilute effects on its dispersion in particle-laden blast wave systems. *Journal of Applied Physics*, 130(3):1–19, 2021, doi:10.1063/5.0047516.

[12] Blast inhibitors "Fountain", https://www.npo-sm.ru.

Appendix A

Homogeneous explosives and blast wave theory

A.1 Introduction to homogeneous explosives

Explosives are very powerful energetic materials that can self-oxidize if properly initiated. Homogeneous condensed explosives are mainly composed of four atomic elements, namely carbon (C), hydrogen (H), oxygen (O), nitrogen (N), sometimes with the addition of chlorine (Cl) and sulfur (S). Whereas a liquid explosive can be easily categorized as homogeneous since the variations of density inside the charge are negligible, solid explosives are often composed of an agglomeration of crystalline structures and thus variations of densities can be observed if the charge is examined at a sufficiently small scale. Nevertheless, these disparities in density are very small compared to the mean explosive density across the charge such that most conventional solid explosives can be referred to as homogeneous.

Homogeneous explosives have been thoroughly studied for more than a century by chemists and physicists, and they have developed various theories and models to characterize the performance of these explosives and their effects. In this chapter, a basic and succinct review of the characteristics of homogeneous explosives is presented. First, the chemical properties and parameters of explosive molecules are presented. Then the thermodynamic properties of the explosive materials, including the physics of the detonation wave propagating inside the explosive charge are discussed. The formation and the dynamics of blast wave propagation are described including a discussion of the scaling laws that characterize the properties of homogenous explosives. The numerical and experimental methods used to probe the detonation and blast wave properties of explosives are then reviewed. Finally, the ability of an explosive to accelerate casing fragments is briefly addressed as well as the effect of blast waves on structures.

A.2 Chemistry and thermodynamics of homogeneous explosives

A.2.1 Chemistry

Molecular structure

The properties of homogeneous explosives do not depend only on the number and type of atomic species present, but also on the molecular structure. The molecular structure of condensed-phase explosives can be either organic (with the presence of carbon) or inorganic (without the presence of carbon). The organic compounds can be further classified into either aromatic or aliphatic compounds. Aromatic compounds are composed mainly of a benzene ring (Fig. A.1), which is a cyclic molecule formed by CH elements and linked by single or double covalent bonds. Upon reaction, the bonds constituting the cycle break and release energy. The ring may be attached to additional molecular structures, called substituents, as for the trinitrotoluene (TNT) molecule (Fig. A.2). The substituents with oxygen atoms such as nitro groups (NO_2), act as oxidizers, whereas those without oxygen atoms like the methyl group (CH_3), contribute as fuel. Note that a substituent in some cases may act as fuel and oxidizer (e.g., nitramine (NHNO2)) whereas others may not act as fuel or oxidizer but contribute to the overall explosive energy release if the bonds of the substituent are broken (e.g., azides N_3).

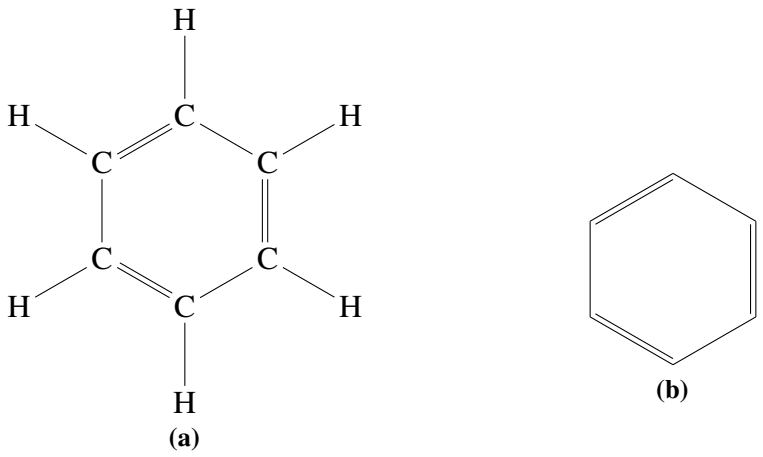

Fig. A.1 (a, b) Two representations of the benzene molecule. The benzene molecule is an aromatic and organic compound.

Aliphatic explosives, on the other hand, do not possess a benzene ring in their molecular structure, but can be cyclic like cyclotrimethylenetrinitramine (also referred to as "Royal Demolition Explosive" (RDX) or hexogen) (Fig. A.3). Aliphatic explosives may also have an open chain structure such as nitromethane (NM), presented in Fig. A.3 formed by a methyl and a nitro group.

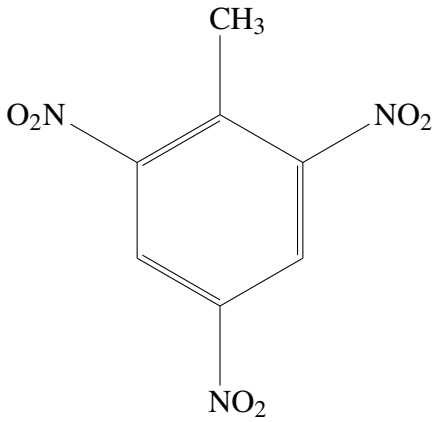

Fig. A.2 The trinitrotoluene (2,4,6-Trinitromethylbenzene or TNT) molecule formed by a benzene ring and three nitro and one methyl substituents is an organic aromatic explosive.

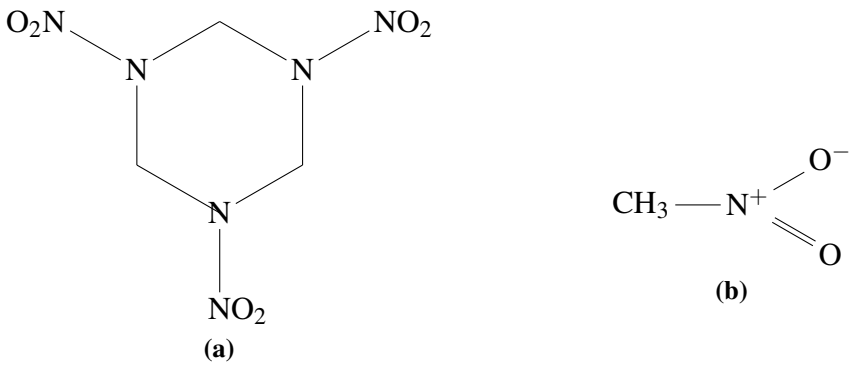

Fig. A.3 (a) Cyclotrimethylenetrinitramine or RDX is an explosive aliphatic organic compound despite being cyclic. RDX is the primary constituent of composition C-4 explosive **(b)** Nitromethane is an open chain aliphatic.

By contrast, ammonium nitrate (AN), which is responsible for the recent Beirut disaster, is an inorganic ionic compound (Fig. A.4).

Over the years, explosives have been classified according to their geometry and structure (monocylic, polycyclic, open chains, substitutions, etc.), as presented in [1]. Note that the characterization of homogeneous explosive properties is not straightforward. For instance, NM is more powerful than the TNT molecule even if the number of covalent bonds is less. RDX is much more powerful and sensitive to initiation than TNT despite having a relatively similar molecular structure [2]. Hence, predicting the properties of explosives requires a detailed chemical and quantum treatment which lies outside the scope of this work.

Additional substances can be added to explosives to modify their properties. For instance, sensitizers tend to decrease the energy necessary to initiate a detonation. Conversely, phlegmatizers tend to increase the energy necessary to initiate the explosion, which is particularly useful for explosive transportation and storage. Binders enable linking crystalline explosive molecules in a coherent macrostructure, whereas adding plasticizers make the explosive charge more malleable.

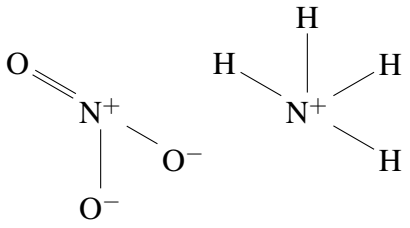

Fig. A.4 Ammonium nitrate is an inorganic ionic compound.

Reaction products hierarchy and oxygen balance

Upon reaction (oxidation) of a CHNO explosive, the chemical bonds of the explosive molecule are broken. This process releases energy and the magnitude of the energy release depends on the types of bonds. The elements resulting from the breaking of the bonds, rearrange and create new sub-molecular substances until the final oxidation state is reached. There is a specific order by which the atoms and molecules recombine, denoted the *reaction products hierarchy*, to form products in the final oxidation state. First, all nitrogen elements combine to form molecular nitrogen (N_2), then the oxygen atoms react with hydrogen to form water (H_2O). The oxygen elements that are not used to form H_2O then react with carbon to produce carbon monoxide (CO). If any oxygen atoms are left, the carbon monoxide oxidizes to form carbon dioxide (CO_2). Finally, after all the previous reactions, any remaining atomic oxygen combines to produce molecular oxygen (O_2). Any carbon and hydrogen atoms left remain in their elemental form. Note that the hierarchy presented here is valid for a rapid oxidation process, as observed in explosions of chemical explosives, but no longer applies for a slow degradation of the explosive molecule due to its interaction with the storage environment (thermal decomposition, etc.). The hierarchy is also modified after a certain degree of expansion of the explosive products [3], as will be seen in section A.4.1.

To obtain the most energy release from the explosive oxidation, the fuel-to-oxidizer ratio must be balanced (similar to the stoichiometric ratio in traditional flame combustion science) such that there is just enough oxygen to form the H_2O and the CO_2 without any O_2 left. When the fuel-to-oxidizer ratio is perfectly balanced, the explosive oxygen balance (or OB) is equal to 0. By contrast, if some O_2 remains at the end of the oxidation process, the explosive is called overoxidized and the oxygen balance is positive. Similarly, if some fuel is remaining (atoms or molecules with C and H, other than H_2O and CO_2) the explosive is called underoxidized and the oxygen balance is negative. For an explosive of chemical formula $C_xH_yN_wO_z$, the formula to calculate the OB, expressed in percentage of the excess mass of oxygen compared to the mass of the explosive compound is Eq. (A.7) [1]:

$$OB(\%) = 100 \times \frac{MW(O_2)}{MW_{\text{explosive}}} \times (z - 2x - \frac{y}{2}) \tag{A.1}$$

with MW corresponding to the molecular weight (or molecular mass).

The oxygen balance of an explosive is an important parameter to evaluate the concentration of species present in the products. The OB also assesses the possibility of secondary reaction with additional fuel/oxidizer in the surrounding medium where the explosive is reacted. For most explosive applications, it is beneficial for underoxidized explosive compounds to undergo secondary reactions of the remaining explosive fuel with the surrounding air. The visual sign of an underoxidized explosive in the field is the generation of products comprised of a dark sooty cloud indicating the presence of unoxidized carbon. The oxygen balance of AN, TNT, Composition C-4 (mix of RDX and other agents) and NM are reported in Table A.1.

Table A.1 Properties of selected explosives including ammonium nitrate (AN), trinitrotoluene (TNT), composition C-4 (C4) and nitromethane (NM), extracted from [4], [5] and [3]. OB indicates the explosive oxygen balance. The theoretical maximum densities (TMDs) are reported from measurements at ambient temperature (293 K). For solid explosives, the values of the detonation properties (VOD and P_{CJ}) are measured for explosive densities less than TMD. In these cases, the experimental densities (initial unreacted explosive density ρ_i) are reported below the velocity or the pressure value. The values for the heat of detonation ΔH_{det} reported from [5] are either calculated from thermodynamic relations or measured in a calorimeter. Consequently, for each explosive, a range of values is reported to account for the discrepancy between the two methods. C4 and NM are the only explosives used in this thesis and are boxed in red.

Explosive	**State**	**Color**	**Formula**	**TMD (g/cc)**	**VOD (m/s)**	$\boldsymbol{P_{CJ}}$ **(GPa)**	$\boldsymbol{\Delta H_f}$ **(kJ/mol)**	$\boldsymbol{\Delta H_{det}}$ **(MJ/kg)**
AN (inorganic)	Solid	Grayish -white	NH_4NO_3 (OB = + 20.0%)	1.72	2700 [4] (ρ_i = n. a.)	3.3 [4]	- 365.1 [5] - 359.6 [3]	1.60 [4]
TNT (aromatic)	Solid	Brownish	$C_7H_5N_3O_6$ (OB = - 73.9%)	1.65	6930 [5] (ρ_i = 1.64 g/cc)	21.0 - 22.3 [5] (ρ_i = 1.63 g/cc)	- 66.9 [5] - 54.4 [3]	4.27 - 5.90 [5] 5.07 [4]
C4 (aliphatic)	Solid (putty-like)	White	$C_{1.82}H_{3.54}N_{2.46}O_{2.51}$ (OB = - 46.4%)	1.67	8370 [5] (ρ_i = 1.66 g/cc)	25.7 [5] (ρ_i = 1.59 g/cc)	+ 13.9 [5] + 24.5 [3]	5.86 - 6.65 [5]
NM (open-chain aliphatic)	Liquid	Transparent yellow	CH_3NO_2 (OB = - 39.3%)	1.13	6350 [5] (ρ_i = 1.13 g/cc)	12.5 - 14.4 [5] (ρ_i = 1.13 g/cc)	-113 [5] - 81.8 [3]	4.44 - 6.78 [5] 4.54 [4]

A.2.2 Thermodynamics

As with all chemical compounds, explosives possess physical and thermodynamic properties. The knowledge of some properties is particularly useful for storage (fusion temperature T_{fus}, latent heat of fusion ΔH_{fus}, heat capacity c_p, solubility, etc.) but the determination of three parameters is particularly useful to determine explosion effects, namely the density, the heat of formation and the heat of reaction (or heat of detonation). For most explosives, increasing the initial explosive density increases the volumetric energy release, and thus the detonation pressure. The heat of formation of the explosive is the energy required to form the compound from its atomic constituents (at standard conditions). This parameter is particularly useful as an input parameter along with density in thermochemical codes as it will be seen in section A.5.1. Finally, the heat of reaction is the energy liberated (for exothermic reactions) or absorbed (for endothermic reactions) by the creation and rearrangement of molecular substances resulting from the oxidation of the explosive compound, at 298 K and 1 atm. The heat of reaction can be seen as the difference between the energy release by the breaking of the chemical bonds of the initial explosive macromolecule and the energy absorbed by the creation of sub-molecular substances. This energy difference is transferred to thermal or kinetic energy of the flow and may be calculated from the standard heat of formation (ΔH_f^0) of the initial explosive compound and its detonation products as follows (Eq. (A.2)):

$$\Delta H_{det}^0 = \Sigma \Delta H_{f-products}^0 - \Delta H_{f-explosive}^0 \tag{A.2}$$

For exothermic reactions, ΔH_{det}^0 is negative. Hence, the heat of detonation is maximized when ΔH_{det}^0 is the most negative, i.e., when $\Delta H_{f-products}^0$ is low and $\Delta H_{f-explosive}^0$ is high. Note that the heat of detonation calculated from Eq. (A.2) represents the maximum thermal energy liberated by the explosive. In reality, this energy is less due to changes in the reaction product hierarchy presented previously, and due to the higher entropy of the products (higher pressure and temperature) compared to that at standard conditions. Note also that the addition of materials (e.g., sensitizers, stabilizers, plasticizers) to the explosive molecule changes the overall chemical formula, oxygen balance and subsequently the value of ΔH_{det}^0. This is particularly true for comp C–4 as it will be seen in section A.3.4. Sometimes the heat of detonation is referred to as the heat of explosion. This terminology can be confusing since the heat of detonation does not include the secondary energy release of potential remaining excess fuel with the ambient atmosphere (i.e., afterburning effects). It is also of importance to emphasize that ΔH_{det}^0 solely encompasses the thermal aspects of the explosion energy and does not include the energetic contribution of the work produced by the expansion of the detonation products. The values of the heat of detonation for AN, TNT, Comp C-4 and NM are listed in Table A.1. The values of the heat of detonation for different explosive compounds can be found in numerous references [1, 3–5].

A.3 Detonation properties of conventional explosives

A.3.1 Deflagration and detonation waves

Deflagration is a rapid combustion wave associated with the reaction of a fuel/oxidizer mix, in the form of a flame which converts the reactants (fuel and oxidizer) into products. Energy is released by the breaking of the chemical bonds of the reactants and subsequent recombination to form the product species. This chemical energy is transferred into kinetic and internal energy of the products. Diffusion of mass and heat from the combustion zone to the medium ahead of the flame front causes it to ignite, thus propagating the flame, typically at rates of centimeter's to meter's per second. Besides combustible gases, deflagration waves are also observed in propellants such as black powder (mix of nitrate, charcoal and sulfur).

Detonation refers to a propagation wave in which the reaction of a gaseous mixture or a condensed phase energetic material is coupled with a leading shock wave. Contrary to deflagration waves, the reactants ahead of a detonation wave are undisturbed and chemical reactions occur behind the detonation front due to adiabatic compression of the reactants instead of heat transfer. Detonation waves also propagate at a much higher velocity (several thousands of meters per second) than deflagration waves. For ideal (not overdriven) and unidimensional detonation waves described by the Zel'dovich [6] - Neumann [7] - Döring [8] (ZND) theory, schematically depicted in Fig. A.5, the detonation front can be considered as a normal shock wave. Consequently, in the frame of reference of the detonation front, the flow is subsonic behind the shock but the temperature, pressure and density increase sharply in conformity with the Rankine [9] - Hugoniot [10] theory. The compression of the reactants by the normal shock triggers chemical reactions. However, although these reactions are fast (typically less than a microsecond), they are not instantaneous and need some time to release substantial energy. This induction time is the time required for the reactants to decompose and can be described by Arrhenius kinetics [11, 12]. In this induction zone, the values of pressure, temperature, density and velocity do not change significantly.

The induction zone is followed by a recombination zone with strong exothermicity where the dissociated reactants start to recombine to form the products. The energy release tends to increase the temperature and the products expand which decreases the pressure and density. The exothermic reactions and the thrust generated by the expansion wave in the reaction zone moves the flow towards the detonation front. The energy associated with this flow motion feeds the detonation wave and compensates for the heat losses through the reactants. Consequently, the detonation front moves at a constant speed (in the laboratory frame) provided that no other expansion waves penetrate the reaction zone. This constraint imposes that the flow in the reaction zone re-accelerates to sonic conditions (in the frame of the detonation front), to avoid the decay of the detonation wave. This condition is known as the Chapman-Jouguet (CJ) condition of a detonation wave. In the CJ, or sonic plane, chemical equilibrium is reached and the products

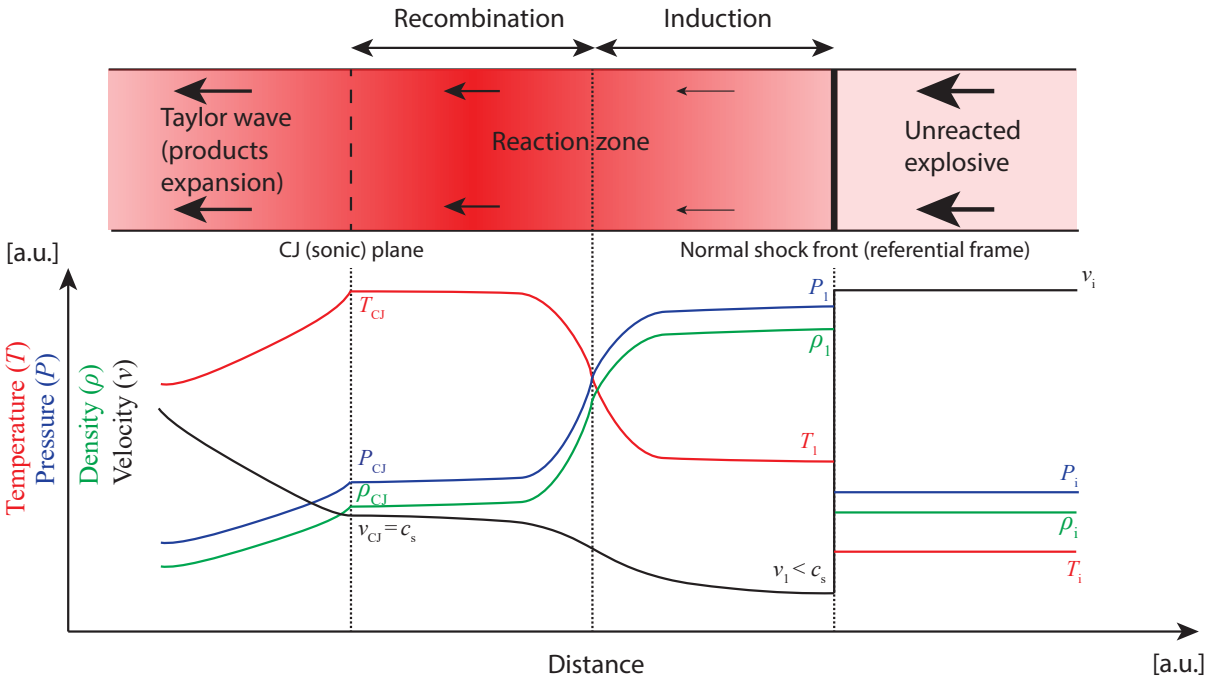

Fig. A.5 Structure of a detonation wave in the ZND model (adapted from [13]).

have reached their final oxidized state. At this point the pressure reaches ten's of GPa in the case of condensed explosives, and the temperature is about a few thousands of Kelvins. After the CJ plane, the reactants have been totally consumed and the products expand and do work on the surroundings, until they equilibrate with the atmospheric pressure. This expansion (also called the Taylor wave or post-detonation zone), reduces the pressure, temperature, and density. Since the energy is spent to push and heat the surrounding medium, the velocity of the gaseous products also slows down (in the laboratory frame). Note that the ideal ZND theory provides a unidimensional description of the detonation assuming a smooth planar detonation front but does not accurately describe the geometry of the detonation wave in three dimensions. In 3D, the detonation wave is composed of cellular structures due to the instability of the detonation wave and is best described by the Wood-Kirkwood (WK) theory [14]. However, the ZND theory is sufficient to understand detonation waves from the perspective of blast researchers since the knowledge of the velocity of the detonation (VOD) and the detonation pressure in the Chapman-Jouguet (sonic) plane P_{CJ} is sufficient to estimate the power of explosives and for blast applications. Nevertheless, these parameters may vary significantly with the detonation configuration (3D effects, shape of the charge, presence of casing, detonation curvature, etc.) and diverge from the values obtained from the ideal theory. For heterogeneous explosives (chapter 2), the addition of new materials in the explosive is often associated with a modification of the detonation properties and the properties of the air blast generated subsequently. Consequently detonation properties are best determined experimentally for a given experimental setup. Only

explosives that detonate, commonly referred as to high explosives (HE) are used in this thesis in order to produce strong blast waves.

A.3.2 Theoretical maximum density (TMD)

The theoretical maximum density (TMD) refers to the limit at which an explosive can be pressed before experiencing strong inter-molecular repulsion. Whereas pure liquid explosives can be considered to be at TMD, most solid explosives have a certain degree of porosity and are generally at $\sim 90\%$ TMD especially if they are mixed with other materials (binders, phelgmatizers, sensitizers, etc.). However this value is useful to calculate the maximum limit of the detonation properties (VOD, P_{CJ} and $\Delta H^0_{\mathrm{det}}$). The TMD can be calculated from the knowledge of the explosive molecular structure and follows a linear relationship with the hydrogen content of the substituted molecules [15, 16]. The coefficient of this relationship depends on many parameters including the state of the explosive (solid or liquid), the molecule symmetry and the nature of the substituents. The TMD is the default density of explosive compounds in thermochemical codes (section A.5.1).

A.3.3 Reaction-zone length, detonation failure, velocity of detonation (VOD) and detonation pressure (P_{CJ})

In section A.3.1, we saw that the detonation wave is comprised of a detonation front followed by a reaction zone. The size of the reaction zone is finite but is much smaller than the length of the Taylor wave. The reaction zone length depends on the explosive nature and its energy release but also on the initial explosive density ρ_i. In general, increasing ρ_i is associated with a decrease of the mean free path between reactant molecules speeding up their initiation and thus decreasing both the reaction zone length and reaction time. The reaction zone length may vary from sub-millimeter to centimeters in size [5], depending on the explosive nature and the initial density. The reaction zone length appears to be a key parameter controlling the propagation of the detonation wave. In particular, detonation waves with thick reaction zones are more prone to fail than detonation waves with thin reaction zones, since they are more susceptible to lateral expansion waves which may quench the reactions.

In the ZND theory, the explosive layer is considered to be infinitely thick such that heat losses from the sides of the detonation wave are non-existent. However, in reality, the explosive layer thickness is finite and is often surrounded by a casing. The most traditional configuration consists of an explosive charge pressed in a rigid cylinder. Tests to determine detonation velocity with such a cylindrical charge are referred to as rate stick tests. In tests with a charge of a given diameter, expansion waves that propagate inwards as the casing expands cool the reaction products, slowing the reaction rate. This causes the detonation front to become curved. If the expansion waves reach the center of the charge before the end of the reaction zone, the reactions

may be quenched, causing failure of the detonation wave propagation. The cylinder diameter at which the detonation wave extinguishes is called the failure diameter.

As for the calculation of the TMD in section A.3.2, the VOD at TMD can be determined from the chemical structure [17, 18] of the explosive molecule. However, in reality, the VOD depends on the initial unreacted explosive density. Hence, it is of interest to be able to estimate the VOD when the initial density is less than the TMD. The detonation velocity is well approximated to be a linear function of the density for most explosives. The velocity of detonation is also dependent on the initial temperature, type of casing and the geometry (curvature effects) [1]. The detonation pressure P_{CJ} is an important parameter to quantify the brisance ability of an explosive (ability to rupture a casing). P_{CJ} can be estimated using Eq. (A.3) [1]:

$$P_{\mathrm{CJ}} = \frac{\rho_i \times \mathrm{VOD}^2}{\gamma + 1} \tag{A.3}$$

where γ is the ratio of the specific heats of the detonation product gases which is approximately 3 for most conventional explosives. Since the VOD and thus P_{CJ} depend on numerous factors, they are best determined experimentally. Otherwise, thermochemical codes (section A.5.1) are useful to determine the VOD, P_{CJ} and $\Delta H^0_{\mathrm{det}}$ for a given explosive.

A.3.4 Properties of AN, C-4, TNT and NM

Several properties of the explosives listed below are also presented in Table A.1 with references.

AN

AN is white crystalline ionic compound, highly soluble in water and often used as a fertilizer in agriculture. AN is not a particularly efficient explosive since its detonation is very difficult to initiate (at ambient conditions), and tends to fail if the explosive layer is not thick enough (large failure diameter). In the case of the Beirut explosion, it was hypothesized that the moisture of the air transformed the AN into a rocky solid over the years, hence increasing significantly its detonability [19]. Then initiation of the AN by nearby pyrotechnics resulted in the explosion. The VOD and detonation pressure of AN are rather low (2700 m/s, P_{CJ} = 3.3 GPa) compared to most commercial explosives. Nevertheless, AN can be used as an oxidizer when mixed with a small amount of fuel oil (ANFO) [4]. The detonation properties of ANFO are much greater than AN alone.

TNT

TNT is a yellow solid. TNT has been widely used throughout history and is the reference explosive, in particular, to calculate the energy equivalence of explosions (section A.4.3). TNT is relatively insensitive to shock and friction which is useful for handling and storage. To be initiated TNT, must be shocked by a a booster explosive or a detonator. TNT has a relatively

high VOD and detonation pressure (VOD $\sim$ 6.9 km/s, $P_{CJ} > 20$ GPa), resulting in good brisance properties. TNT is particularly effective when mixed with other conventional explosives like AN (Amatol) or RDX (Composition B).

Composition C-4 (C4)

C-4 is a plastic high explosive primarily used by the U.S. army and is composed of a mix of 91% RDX as explosive agent, 5.3% of dioctyl sebacate (DOS) or dioctyl adipate (DOA) acting as a plasticizer, 2.1% polyisobutylene (PIB, a synthetic rubber) acting as a binder, and 1.6% of other substances such as a mineral oils. RDX ($C_3H_6N_6O_6$) is a common explosive used during WWII and has the texture of a white solid without taste or odour. The plasticizer serves to render the mixture malleable as a modeling clay which is useful to shape the explosive as desired. The binder holds the different components together. As for TNT, the C-4 explosive is remarkably stable and cannot be detonated unless shocked from a detonator. It cannot explode when set on fire or when dropped on the ground. The detonation velocity of C-4 is superior to TNT with about 8 km/s and its detonation pressure P_{CJ} closer to 25 GPa. The industrial production of C-4 also makes it affordable. The stability, the ability of C-4 to produce strong blast waves, and its relatively low cost makes it a good candidate for the present work.

Nitromethane (NM)

At ambient conditions, nitromethane (CH_3NO_2) is a liquid organic compound mostly used as a solvent in numerous industrial applications. NM is also used as a fuel, particularly in drag racing, primarily due to its oxygen content which enables it to burn with much less air compared to conventional gasoline, for a given mass of fuel. The explosive properties of nitromethane were identified in 1958 [20] during the explosion of a railroad tanker. NM alone is relatively insensitive and generally requires a sensitizer to detonate. During the accident of 1958, the sensitizing role was hypothesized to be played by shocked air bubbles entrained in the liquid. The collapse of these air bubbles was associated with the generation of hot-spots of high temperatures. Hence, a sensitized volume of NM shocked by a strong shock generally results in the detonation of the liquid. In chapter 5, NM will be sensitized by the collapse of very small hollow glass beads (glass microballons) following the same process as for air bubbles and the strong shock wave will be produced by a booster charge of C-4. The properties of the detonation of NM are lower than TNT and C-4 ($P_{CJ} \sim$ 13 GPa , VOD = 6350 m/s), but the liquid nature of NM enables the homogeneous mixing of additional elements which makes it a good candidate to study heterogeneous explosives with embedded particles (chapter5).

A.4 Blast wave theory

A.4.1 Detonation products, fireball and blast wave formation

In the previous section, we saw that the nature and concentration of the detonation products depend on the chemistry of the explosive compound, and on a particular reaction hierarchy at the CJ state (detonation condition). However, chemical equilibrium and subsequently the concentration of molecular species are strongly influenced by the thermodynamic state of the detonation products. In the Taylor wave, in the absence of any secondary reactions with the surrounding medium, the pressure and the temperature inside the detonation products drop substantially as the products expand and form a fireball. After a certain time (typically a few milliseconds for $\sim$ 1-kg charges), the thermodynamic state ultimately reaches ambient conditions (fireball condition). Consequently, at this stage, the chemical equilibrium has shifted from the CJ state and obeys a different product hierarchy. For example, at the CJ state for many explosives, the predominant oxidizer in the products is water vapour, whereas when the products expand to atmospheric conditions, the oxides of carbon have an increased mole fraction [3].

If some of the explosive reactants are left unoxidized after the CJ state, which is typically the case for explosives with a negative oxygen balance, they may react exothermically with the surrounding atmosphere. This process is referred to as *afterburning*. Note that the term *afterburning* denotes different physical processes depending on the timescales at which the phenomenon is observed. Whereas researchers working on the physics of the detonics stage refer to any chemical reactions occuring behind the detonation reaction zone (after the CJ plane on 10 – 100 microseconds timescale), researchers focusing on blast waves refer to the chemical reactions of the detonation products with the surrounding medium (air, in general) on millisecond timescales. This confusion in the terminology is exacerbated when additional reactive elements are added to the explosive mixture (chapters 2 and 5). Due to the difference in the product hierarchy, afterburning effects and the associated energy release may differ whether they occur at timescales of the detonation propagation or of the fireball dynamics.

The thermochemistry and the hydrodynamics of the products/fireball are also influenced by the different phases present in the explosive system. For homogeneous explosives, the fireball motion is particularly perturbed by the passage of shock waves. The formation of these shocks can be described as follows. When the detonation front reaches the outer layer of the explosive charge, the acoustic impedance mismatch at this interface (the density of the surrounding medium is generally much lower than the density of the explosive products) implies that a shock wave will be transmitted to the surrounding medium. The transmitted shock has a lower magnitude and propagates in a less dense medium so its velocity is also reduced. At the same time, the impedance mismatch at the interface results in a backwards propagation of a rarefaction wave from the interface to the origin of the explosion. This rarefaction wave contributes to further decreasing the pressure of the detonation products that are expanding. The transmitted shock that propagates outwards in the free field, is not supported by any pressure waves, and is thus also immediately followed by a release wave. However, the pressure reduction due to the

expansion of the products is much faster than the pressure reduction following the transmitted shock. The reconciliation of the pressure level is achieved by a secondary shock behind the transmitted shock which propagates backwards to the origin. When this converging shock wave reaches the origin, it reflects, forming a secondary shock that travels in the same direction as the transmitted shock. When reaching the interface between the products and the surrounding medium, which is further away than initially due to expansion of the gaseous products, the secondary shock is transmitted but with a lower velocity, as for the initial transmitted shock. At the same time, a third shock is created following the same process as for the secondary shock formation. This process is repeated until the explosion energy is entirely consumed, as shown in Fig. A.6. After each passage of a shock through the fireball interface (also called contact surface), the fireball interface is slightly perturbed outwards before experiencing an inward suction effect associated with the release waves. This alternating direction of the force at the interface results in an oscillation of the position of the fireball interface. Primary transmitted shocks that have traveled sufficiently far from the detonation products such that the pressure behind the front is no longer perturbed are commonly called *blast waves*. More details about the physics of the spherical blast problem can be found in the classic paper by Brode [21].

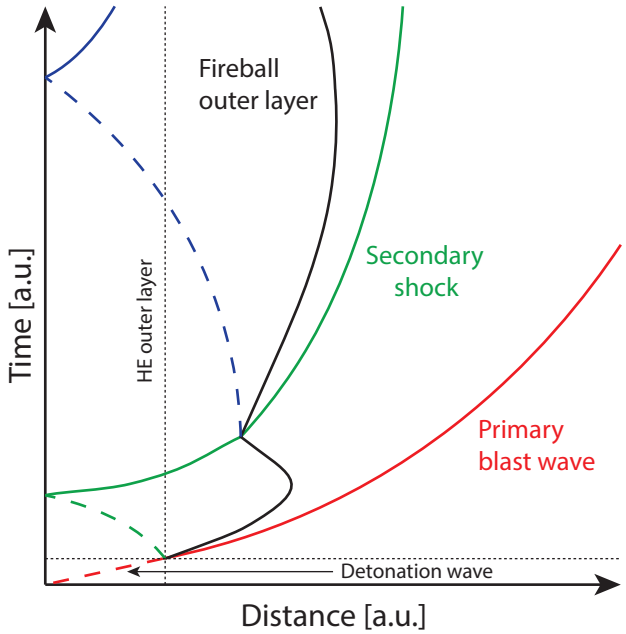

Fig. A.6 Formation of a blast wave and additional shocks from a spherical high explosive charge. The propagation of these shocks and their reflection at the fireball outer layer (contact surface) lead to a fireball oscillation (adapted from [21]).

Variations of the pressure and temperature inside the fireball associated with the dynamics of the different shocks and afterburning effects result in a highly turbulent flow and local modifications of the product hierarchy. The thermodynamic and chemical state of the products at different times and locations is difficult to predict analytically, and is better determined with numerical tools (section A.5). The perturbations of the hydrodynamics, thermodynamics and

chemistry of the fireball are more pronounced for heterogeneous explosive mixtures as was seen in chapter 5.

A.4.2 Blast wave profile

As seen in the previous section, in a free-field environment, the pressure of the flow behind the leading shock wave (or transmitted shock) produced by the detonation of the high explosive is not sustained contrary to a confined shock wave propagating in a shock tube. Consequently, the leading shock wave is followed immediately by a release wave that reduces the pressure of the flow just behind the shock front. Such a decaying shock wave has been denoted blast wave. At a given distance, the blast pressure decays quasi-exponentially with time immediately after the sharp hydrostatic pressure rise across the shock (P_s). Such a decay is often modeled by the modified Friedlander equation (Eq. (A.4)),

$$P(t) = P_s e^{-\alpha t}\left(1 - \frac{t}{t_d}\right) \tag{A.4}$$

which is a modified version of the Friedlander equation [22] with better accuracy for pressure peaks above two atmospheres. The modified version of the equation contains an additional term α, called the *wave form* parameter, in the exponential term. After a certain amount of time, commonly denoted the positive-phase duration time (t_d), the blast pressure falls below the ambient value. The regime of shock pressure above the ambient value is commonly called the "positive phase" (+), whereas the regime below the ambient value is referred to as the "negative phase" (-). A schematic of such a pressure profile is shown in Figure A.7. As shown on this figure the positive phase is more pronounced in magnitude but lasts for a shorter period of time than the negative phase. The positive phase is generally the most interesting phase for studying free-field air blast and only this phase is investigated in this thesis. The study of the negative phase is more relevant when investigating the interaction of blast loads with structures.

The blast temperature, the entropy and the particle velocity (the velocity of a virtual particle behind the blast front) also decline after reaching a peak [23, 24]. The density profile of blast waves is also similar to the pressure profile with the presence of a negative phase. However, the rate of decay and duration times are not necessarily the same between the different properties. Note that since the gas after the passage of the blast front is left in a state of radially decreasing entropy, no thermodynamic relations are available to derive the time-histories of these physical properties from pressure measurements. As a result, independent measurements are required [25].

The knowledge of two main blast wave characteristics are important to study free-field blast waves. The first property corresponds to the peak overpressure (ΔP_s) defined as the difference between the maximum blast pressure (P_s) (see Figure A.7) and the ambient atmospheric pressure (P_0). The second property, denoted the positive phase impulse I_s^+ (Eq. (A.5)),

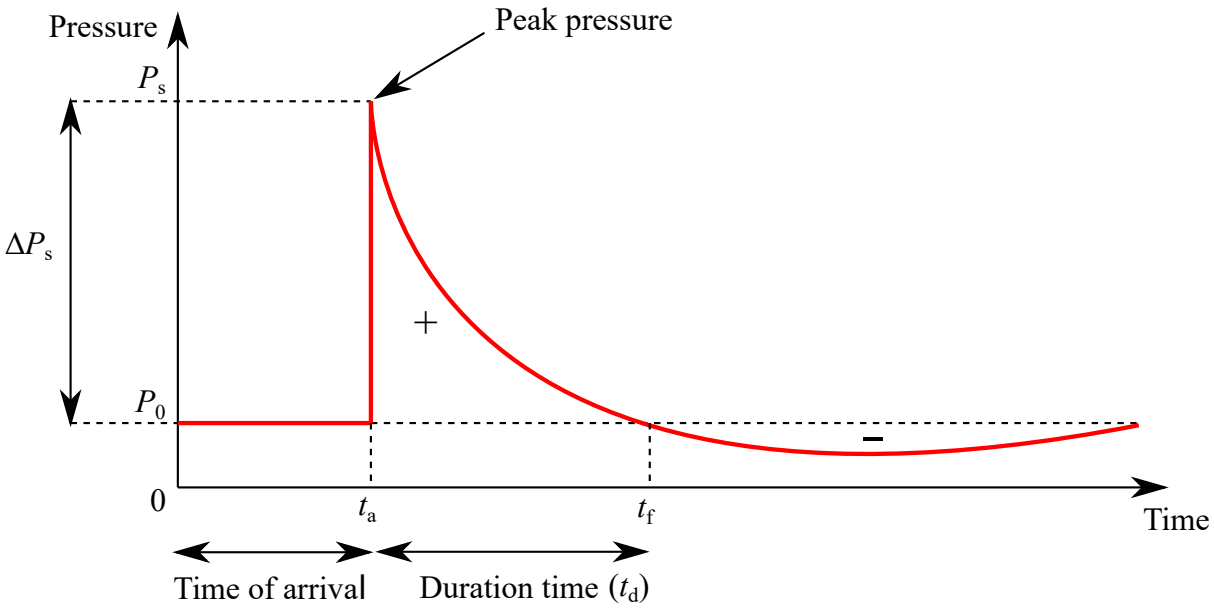

Fig. A.7 Typical blast pressure-time profile at a given distance from the charge.

$$I_s^+ = \int_{t_a}^{t_f} \Delta P_s(t)dt \tag{A.5}$$

has the dimension of a force-time product (per unit area) and is calculated by integration of the positive phase (+) of the blast pressure profile. The positive-phase impulse is an important parameter to evaluate the ability of the blast to cause damage. For instance, some systems may be able to withstand very high peak overpressures but may fail if a high level of pressure is sustained for a long duration. Hence both parameters must be considered when assessing the potential hazards of a blast wave.

A.4.3 Explosion energy and TNT equivalency

It is of interest for physicists and engineers to estimate the energy release of different explosives in order to quantify explosive effects and their destructive ability. Historically, TNT was defined as the reference for comparison of different explosive energies and 1 kg of TNT releases 4.184×10^6 Joules. For example, if an explosion event is deemed to be equivalent to 12 kg TNT, it means that the effective energy released is $12 \times 4.184 \times 10^6$ Joules. The Berthelot method [26] estimates the TNT equivalence of explosives considering that the energy release is partitioned between the work done by the expansion of the detonation product gases and the thermal energy of the explosion. The thermal energy is well approximated by the heat of explosion seen in section A.2.2. The expansion term is approximated by the volume of gas generated. Hence, the Berthelot method stipulates that the TNT equivalence of an explosive is proportional to the moles of gases (Δn) produced per mole of explosive, the molar heat of detonation (ΔH^0_{det}) and

inversely proportional to the molecular weight (MW) of the explosive squared (at detonation or fireball conditions) (Eq. (A.6)).

$$\text{TNT equivalent}\,(\%) = 840 \times \Delta n \times (-\Delta H^0_{\text{det}})/(MW)^2 \tag{A.6}$$

The coefficient 840 serves as a conversion factor to express the energy in TNT equivalence. Note that Eq. (A.6) is valid for chemical explosions but does not apply to nuclear explosions which generate no gaseous products. The advantage of the Berthelot method is its simplicity and that it requires only the knowledge of the chemistry of the explosive compound, the product hierarchy and the heat of detonation. On the contrary, the evaluation of the work done by thermodynamic means (solving the PV integral) may be tedious and requires several assumptions. The main drawback of the Berthelot method is the absence of secondary reactions of the detonation products with the surrounding atmosphere in the calculation of the energy released.

In practice, the TNT equivalence of an uncontrolled explosion from an unknown substance is best determined from the explosion effects. The most common method consists of correlating the blast time of arrival at different distances to establish the blast trajectory. The blast trajectory is then compared with the TNT reference and using scaling laws (see section A.4.5) the TNT equivalence can be determined. This method implies that the passage of the blast is recorded by videographic means. The videos are generally captured by CCTVs or by witnesses of the accidents. This method is inevitably associated with inaccuracies in the timing since the temporal resolution of CCTVs and smartphones are relatively small compared to the timescales of propagation of the blast wave over the field of view of the cameras (especially at short distances). Footage of the Beirut accident was analyzed by several researchers [27–29] and the TNT equivalence was evaluated to lie between 0.3 and 1.1 kilotons. This TNT equivalence was also confirmed by tracking the fireball motion [30, 31] or by analyzing seismic data [32].

In a controlled environment, the TNT equivalency is best determined by comparing not only the blast time of arrival, but also the peak blast overpressure and the blast impulse at different distances, recorded with pressure transducers and applying the same scaling laws. Note that since the timescale of energy release differs from one explosive to another, depending on the explosive thermochemistry, the TNT equivalence is not the same when extracted from peak pressure or impulse data. For the same reason, the TNT equivalence may vary at different distances from the charge. For instance, in the case of the Beirut accident, the TNT equivalence seemed to increase with distance [19] from 0.2 kilotons TNT at a distance of 85 m to 1.0 kilotons TNT at a distance of 1000 m. Once the TNT equivalence is known, it is possible to define a relative effectiveness factor (ε) to compare with the power of conventional explosives. The effectiveness factor of the reference TNT is set to 1. Explosives that are more powerful than TNT have $\varepsilon > 1$ whereas explosives less powerful have $\varepsilon < 1$. Since the TNT equivalence differs depending on the extraction method, the experimental conditions (explosive configuration and shape, mass, initial density, propagation medium of the blast wave, etc.) and the rate at

which the explosion dissipate its energy (endothermic reactions, heat transfer, acceleration of materials, etc.), ε is often presented as a range of values rather than a unique value. For instance, $\varepsilon = 0.3 - 1.1$ for AN evaluated from the Beirut explosion. For C-4, $\varepsilon = 1.16 - 1.47$ [33] when estimated from peak pressure data and $\varepsilon = 1.12 - 1.18$ [33] when estimated from impulse data with the lowest ε values for the farthest distances, contrary to AN. Contrary to other conventional explosives, the ε values for NM have not thoroughly been investigated, perhaps because they differ according to the concentration of sensitizer in the liquid explosive. However, a mean value of 1.10 seems to be an appropriate value.

The main advantage offered by the determination of the TNT equivalence and the effectiveness factor from explosion effects is the integration of additional energetic contributions to the overall explosion energy release. Whereas the Berthelot method includes the sole contribution of the oxidation and expansion of the explosive, explosion effects include secondary energy release from afterburning effects, shock reflections and take into account the nature of the surrounding medium which may influence the rate at which the explosive energy is dissipated. Nevertheless, the TNT equivalence using explosion effects cannot be a reliable metric to estimate the total explosion energy since it takes only into account the energy partition allocated to the effects considered (blast, fireball, seismisc waves, acceleration of materials, etc.). In order to evaluate precisely the total explosion energy at a given distance and time one must be able to know the energy partition between the explosion features which is difficult to do in practice.

A.4.4 Rankine-Hugoniot relations for blast waves

The Rankine [9] – Hugoniot [10] relations express the relationship between state variables across the discontinuity formed by a shock wave in one dimension. Using the principles of mass, momentum and energy conservation, the jump conditions of the state variables can be derived across such a shock. The pressure ratio across a normal shock can be written as Eq. (A.7)

$$\frac{P}{P_0} = \frac{2\gamma}{\gamma+1} M_a^2 - \frac{\gamma-1}{\gamma+1} \tag{A.7}$$

where M_a is the Mach number. The previous equation assumes that the shock propagates adiabatically in an inviscid, calorically perfect gas (γ is constant) and that the shock is infinitely thin. For a fully formed blast wave, the blast pressure calculated by Eq. (A.7) is generally a good approximation provided that the degree of blast curvature is relatively small which is generally the case in the mid-to-far field. If the blast propagates into atmospheric air, the value of γ is 1.4. However, when the blast propagates inside the detonation products (in the near field), the degree of blast curvature may be important and the value of γ diverges from that of air. As a consequence, care must be taken when extracting the blast pressure from Rankine-Hugoniot relations in this region. In chapters 3 and 5, the Mach number is estimated by inferring the blast trajectory using videographic means and the pressure ratio is calculated assuming that the blast propagates into atmospheric air ($\gamma = 1.4$).

A.4.5 Scaling laws

Point blast solution

From 1941, Sir Geoffrey Taylor started to work on the estimation of the effects of a potential bomb, using nuclear fission as a source of energy. He was particularly interested to know if such a bomb which could be considered as releasing energy from a infinitely small source would produce similar effects as those observed by conventional (chemical) explosives that produce work via expansion of the gaseous products. He carried out a theoretical analysis and found a relation between the radius of the blast wave (point blast solution) and appropriate physical parameters. Later, Sedov carried out a theoretical analysis of blast waves and found the results obtained by Taylor using dimensional analysis [34]. The similarity solution developed, referred to now as the Taylor-Sedov strong blast solution, is given by

$$R(t) = \eta_s(\gamma) \left(\frac{Et^2}{\rho_0} \right)^{1/5} \tag{A.8}$$

which expresses the radius (R) of a blast wave as a function of time (t), the density of the background fluid (ρ_0), the energy (E) generated in the explosion, and a constant (η_s) of order unity (Eq. (A.8)).

On July 16th, 1945, less than a month before the Hiroshima and the Nagasaki bombing, the U.S. Army proceeded to carry out the *Trinity* test, their first trial of a nuclear weapon. In 1947, two years later after the end of the World War II, the U.S. Army decided to declassify and release the photographs of the *Trinity* test captured by J. E. Mack showing the fireball expansion of the nuclear explosion. However, even if the estimation of the explosive energy and the details of the experiments were still kept secret, the U.S. Army inadvertently reported the frame timing and length scale on each of the photographs.

In 1950, Taylor published two articles [35, 36]. In the first paper, he reported the details of his theoretical analysis of the point blast solution [35]. In the second paper [36], he compared his point blast solution with the empirical correlation derived from the tracking of the blast trajectory (using the time and scale reported on the photographs) and found a good agreement. He also estimated that the value of η_s was close to unity but depended on the ratio of the specific heats (γ). Depending on the value of γ, he found that the TNT equivalence of the nuclear explosion could be between 16.8 and 23.7 kilotons of TNT. The latter estimation (23.7 kilotons of TNT) neglecting the radiation effects (ionizing or thermal), but taking into account the dependence of the air heat capacity with temperature, is relatively close to the modern accepted value of 21 kilotons [37].

The scaling law of Eq. (A.8) is well verified for very strong blast waves such as those produced by exploding stars (supernovae) or for all nuclear tests carried out subsequently to the *Trinity* experiment, but is not accurate for blast waves resulting from the detonation of a high-explosive charge. This divergence lies in the difference in the physical processes of energy release between

the two disparate explosions. In the case of the nuclear explosion, a significant part of the total energy is expanded ($\sim$ 35% of the total energy [38]) to heat the surrounding air in the vicinity of the explosion center to extremely high temperatures, and does not contribute to the blast wave. In comparison, the temperature of the detonation products of high explosives is much lower. Furthermore, a lot of energy is also lost by ionizing radiation ($\sim$ 15% of the total energy [38]) and only $\sim$ 50% of the total energy remains to support the blast wave [38]. Taylor concluded that without the contribution of the thermal energy and the ionizing radiation, nuclear explosions would be *"only half as efficient, as a blast-producer, as a high explosive releasing the same amount of energy"*.

Hopkinson-Cranz scaling (1915)

Earlier, before and after World War I, Hopkinson (1915) and Cranz (1926) also developed independently a similarity solution for chemical and conventional explosives. They found that the peak blast pressure generated by an explosive of mass W at a distance R from the explosion center would be equal to the peak blast pressure of a blast wave generated by the same explosive of mass $\alpha^3 W$ at a distance αR. They hypothesized that the blast pressure depends only on the explosive energy available and on the density of the blast propagating medium, thus α must depend on these two parameters. The explosive energy was converted to mass of explosive in TNT equivalent as seen in section A.4.3. On the other hand, the role of density could be neglected since the blast effects are compared in the same atmospheric conditions. Consequently, $\alpha = W^{-1/3}$ for 1 TNT unit and they introduced the concept of scaled distance Z also called cube-root scaling (Eq. (A.9)),

$$Z(\mathrm{m.kg}^{-1/3}) = \frac{R(\mathrm{m})}{W^{1/3}} = \frac{R(\mathrm{m})}{(C(\mathrm{kg}) \times \varepsilon)^{1/3}} \tag{A.9}$$

which is the ratio of the actual distance from the charge (R) to the explosive charge mass converted to an equivalent TNT mass (W) to the power one third, i.e., the actual charge mass (C) is multiplied by a relative effectiveness factor (ε) which depends on the nature of the explosive as defined in section A.4.3. As for the distance, the other blast properties (I_s^+, t_a and t_d) must be scaled as shown in Table A.2 [3].

In the sixties, Kingery [39, 40], and Kinney and Graham [3] extensively studied the effects of blast waves originated from nuclear explosions as well as detonations of chemical explosives in spherical or hemispherical configurations. Using numerous experimental and numerical data, they correlated the blast properties over a large range of scaled distances as shown in Fig. A.8 (red curves plotted from data extracted in [3] for the peak blast overpressure and the positive-phase impulse). These correlations based on the detonation of 1 kg of TNT contain, in principle, all the information to predict the blast properties at any distance, for any type of explosive (provided that the effectiveness factor is known) and of any mass. Note, however, that since the TNT equivalence of different explosives may vary with distance, as mentioned in

Table A.2 Actual and scaled blast parameters given for the same peak overpressure value [3].

For the same peak overpressure (P_s)	Actual	Scaled
Explosive mass (TNT equivalent unit)	W	$\alpha^3 W = 1$
Distance	R	$\alpha R = \frac{R}{W^{1/3}}$
Arrival time	t_a	$\alpha t_a = \frac{t_a}{W^{1/3}}$
Duration time	t_d	$\alpha t_d = \frac{t_d}{W^{1/3}}$
Positive-phase impulse	I_s^+	$\alpha_s I^+ = \frac{I_s^+}{W^{1/3}}$

section A.4.3, some degree of scattering is present even if no error bars were reported in [3]. The peak overpressures for the chemical explosions decreases monotonically with the scaled distance whereas the positive-phase impulse seems to plateau around $Z = 1$ m/kg$^{1/3}$. This is due to the effect of the secondary shock that perturbs the pressure decay behind the primary blast front.

In Fig. A.8, the black-dashed lines represent the decay of the same blast parameters, but for an unrealistically small nuclear explosion (based on a TNT equivalence of 1 kg) computed from the Taylor-Sedov solution. At small scaled distances, P_s/P_0 for nuclear explosions outperforms the values for the chemical explosions. This is due to the fact that the thermal radiation of nuclear explosions tends to preheat the medium ahead of the blast, thus enhancing the blast velocity and pressure compared to chemical explosions. However, after a certain distance, the effect of the work energy produced by the detonation products of chemical explosions becomes apparent and the blast produced is more powerful than that of the nuclear explosion. Ultimately, in the far-field, the decay rate of the peak pressure becomes similar for both explosions even if the values for the nuclear explosion remains lower due to the dissociation and ionization of the air. The same behaviour is apparent for I_s^+ but with the transition operating at larger distances. This is due to the fact that at the distance of the transition for P_s/P_0, the tail of the positive phase still benefits from the pre-heating effect. Hence, the distance at which I_s^+ no longer experiences this preheat effect is displaced further away from the charge. Note that the comparison between chemical and nuclear explosions based on 1 kg TNT remains qualitative and cannot be considered quantitatively accurate since the smallest nuclear test was performed for a TNT equivalence exceeding several kilotons.

Since the experimental data presented in this manuscript were obtained at similar atmospheric conditions, the scaled distance presented is Eq. (A.9) is used to analyze the data and compare the blast produced by different charges. Note that Eq. (A.9) can also be reversed to extract the

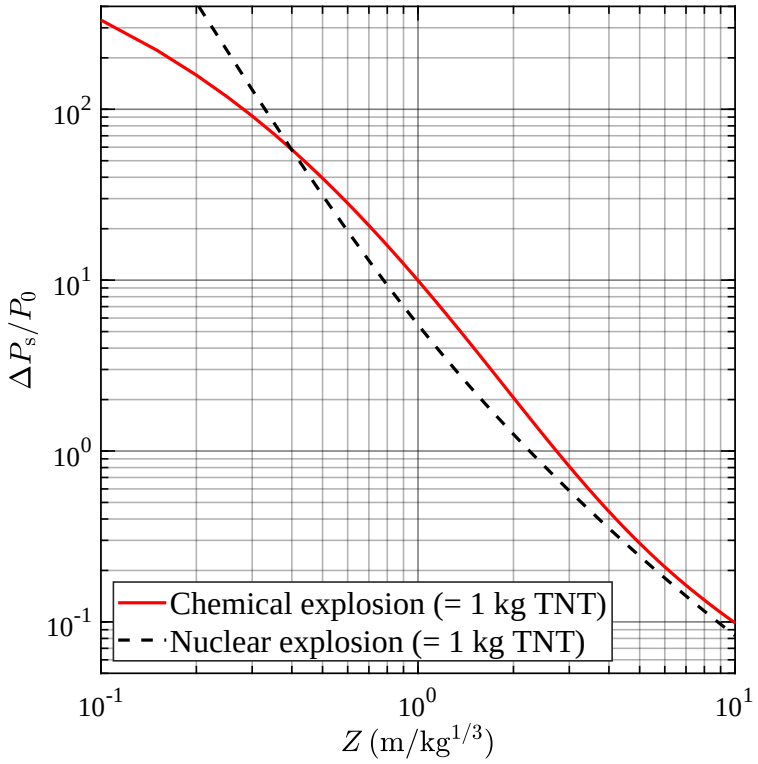

(a)

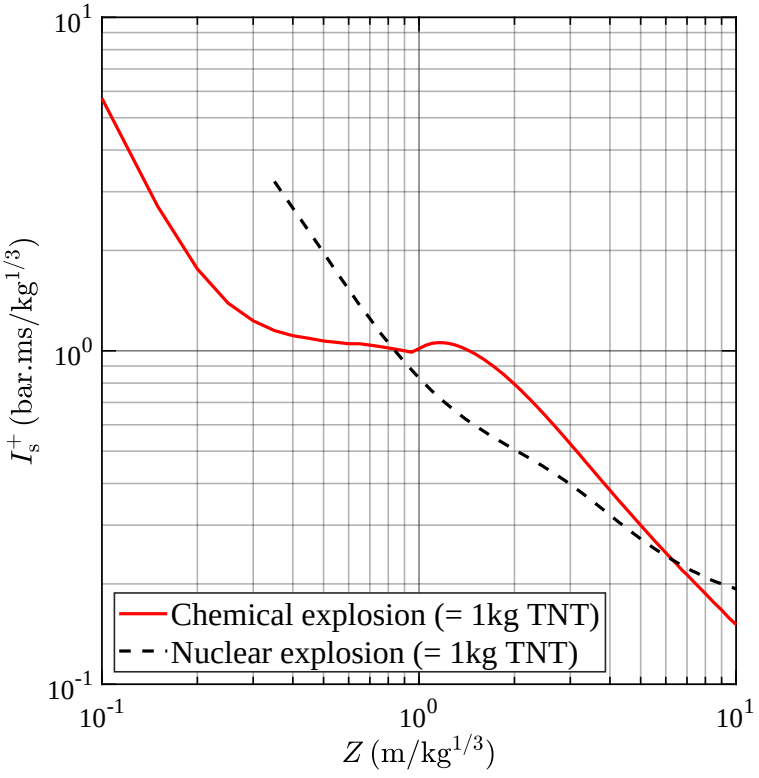

(b)

Fig. A.8 Peak overpressures **(a)** and impulses **(b)** as a function of scaled distance for chemical and nuclear explosions based on a TNT equivalent of 1 kg [3].

TNT equivalence of an unknown explosion providing that the blast properties are known, as mentioned in section A.4.3 .

Sachs scaling (1944)

Sachs in 1944 [41] generalized the Hopkinson–Cranz scaling law to include the properties of the ambient atmosphere, mainly to compare the effects of blast waves at different altitudes. Increasing the altitude within the troposphere is associated with a decrease of the air pressure, density, temperature and speed of sound. Hence, for a given altitude, the magnitude of the blast will be lower than that of the same blast wave propagating at sea level since the pressure ratio across the blast front is dependent on the speed of sound through the Mach number in Eq. (A.7). Consequently, the scaled distance of Sachs can be written as follows (Eq. (A.10)):

$$Z(\mathrm{m.kg}^{-1/3}) = \frac{R(\mathrm{m})P_0^{1/3}}{W^{1/3}} \tag{A.10}$$

Note that the Hopkinson scaling law can be considered to be a limiting case of Sachs scaling if the atmosphere conditions are invariant. Baker et al. [42] has thoroughly reviewed the validity of the Hopkinson-Sachs scaling laws and has discussed the range of distances from the charge and explosive energies for which the scaling principles remain valid. More recently, in 2021, a new scaling law based on the blast propagating medium density, sound speed, explosive energy and time was proposed by Wei & Hargather [43]. This scaling offers the possibility to compare the blast magnitude in condensed-phase media (e.g., underwater blasts) via the introduction of the sound speed as a controlling parameter. Nevertheless, since for each set of experiments considered in this thesis the explosive trials were performed at the same altitude, the Hopkinson scaling law is used to analyze data throughout the manuscript.

A.4.6 Unconfined versus confined explosions

The effects of explosions have been historically determined through experimental tests. These tests were either carried out in the field (unconfined explosions) or in a confined area such as houses, buildings or bunkers. Whereas unconfined explosions were mainly used to study the fundamental physical processes associated with explosions and establish scaling laws, explosions within confined spaces were investigated to determine the destructive power of explosives on building structures and to predict damage associated with accidental or deliberate explosions. Currently, due to the limited access to large-scale facilities in the world allowing field tests, many scientists resort to carrying out explosive tests within a confined facilities such as blast chambers.

When an explosive is detonated inside a dedicated chamber, the blast produced reflects off the walls of the chambers and diffract around nearby objects. These reflections cause perturbations to the pressure signals such that the pressure profile can be very different from that of a free-field

air-blast. After some time, the pressure inside the chamber reaches equilibrium at a value above atmospheric pressure commonly refers to as the quasi-static pressure (QSP), assuming that the chamber is closed and hence the pressure cannot be relieved. The presence of multiple wave reflections that interact with the fireball interface can strongly perturb the overall dynamics of the explosion by inducing turbulent mixing of the detonation products with the surrounding air and initiation of secondary reactions within the fireball, for either homogeneous or heterogeneous explosives (Chapter 2). Additionally, a change of the initial placement of the charge relative to the chamber walls will alter the wave dynamics and may give very different results. For all these reasons, care must be taken when extrapolating or interpreting air-blast data. In the present manuscript, the blast wave data are obtained solely in free-field tests and the results cannot be readily applied to confined geometries.

A.5 Modeling explosions

Modeling and predicting the characteristics of explosives and their effects is crucial to estimate their efficiency or their potential hazards. It is also of interest to develop numerical tools to evaluate the effects of new explosive compositions to avoid the costs of expensive experimental trials. In this section, thermochemical codes and associated equations of states (EOS) used to predict the detonation parameters are reviewed in section A.5.1. More details are provided regarding the well-established equilibrium code Cheetah 2.0 (section A.5.2), which is used in this thesis. Then the EOS used in this thesis to simulate the behavior of homogenous explosives are presented in section A.5.3. Finally, the numerical frameworks used to simulate the propagation of the blast wave are presented in section A.5.4.

A.5.1 Thermochemical codes and detonation parameters

Principle

The goal of using thermochemical codes for HE is to find the detonation parameters assuming mechanical and chemical equilibrium at the CJ state, and to compute the various state variables (P, V, ρ, T) at different stages of the detonation product expansion. Numerous thermochemical codes have been developed worldwide from the 70's and differ by their interfaces, the methods employed to find the detonation parameters, or by the number of chemical species assumed in the calculations. Many of the thermochemical codes are relatively similar, but have been developed independently by scientists from different countries. Table A.3 summarizes a subset of the different thermochemical codes and the equations of state utilized.

Table A.3 A few examples of thermochemical codes and associated EOS used to calculate the detonation properties.

Code	Country	Equations of State
RUBY [44] (1962), TIGER [45] (1974)	U.S.A	Virial expansion, BKW
TDS [46] (1986)	U.S.S.R	BKWR(R) (originally) - KLRR
EXPLO5 (1991) [47]	Czech Republic	BKW
CHEETAH (2.0) (1994) [48]	U.S.A.	BKWC (originally) - JCZS
CARTE (1998) [49]	France	KLRR
SIAME (2016) [50]	France	BKWC, BKWS, BKWG

Equations of states (EOS)

To predict the detonation parameters, the thermochemical codes must account for the behavior of the different species at different thermochemical states. Hence, it is crucial for scientists to develop accurate EOS for the gaseous and the condensed phases present in the detonation products. Several EOS have been proposed to simulate the gaseous phase, with the Virial, the Becker-Kistiakowsky-Wilson (BKW), and the Jacobs-Cowperthwaite-Zwisler (JCZ) EOS [51] remaining the most widely used in thermochemical codes. All these three EOS are in fact improvements of the perfect gas law and account for the molecular interactions occurring at high pressures. They are either semi-empirically or theoretically derived and differ by the description of the interaction term. For instance, in the Virial equation, interactions are assumed to be central forces that are a function of the distance to the barycenter between two molecules. The ratio $\frac{PV}{nRT}$ is expressed as a Taylor series of power of $\frac{1}{V}$. The coefficients of the series are normally dependent on the temperature, but can be assumed to be independent if the molecules behave as rigid spheres and collide elastically. The Virial equation is generally valid to simulate detonation products at moderate pressures (for deflagrative explosive or for a gaseous detonation) but fail to predict the behavior of products resulting from the detonation of a condensed-phase explosive, especially at high pressures and densities.

The BKW is a semi-empirically derived EOS originally proposed to simulate the behavior of nitrogen at high densities [52]. This EOS assumes that the molecules are not only subject to attractive forces, but also to repulsive forces and introduces the molar volume (covolume) of each gaseous species which can be theoretically calculated from the estimation of the lengths of the covalent bonds of the explosive molecule [53]. However, this EOS fails to predict accurate detonation velocities when using the theoretical covolumes. As consequence, the covolumes and the other parameters of the EOS are generally calibrated to fit experimental data. The different calibrations lead to the production of several distinct libraries with a specific set of fitting parameters. For instance, the BKWR library [54] was obtained using 10 explosives with 13 product species. Conversely, the BKWS library [55, 56] was calibrated using 61 gaseous species, 62 explosives at 111 initial densities, 107 VODs and 67 P_{CJ} values. Finally, the BKWC library [57] used the energy of the detonation products as an additional parameter. The

parameters were calibrated using 32 explosives including 5 non-ideal mixtures, 32 VODs, 30 P_{CJ} values and 132 detonation energies. The detonation characteristics using the BKWC EOS are generally in better agreement with experimental data compared to the other libraries. On the contrary, the formulation of the JCZ EOS is based on the theory of intermolecular potentials. This EOS assumes that the density of the gaseous products at very high pressures approaches that of solid density such that the molecular interaction can be proportional to higher powers of the intermolecular distances (Lennard-Jones potentials $\propto r^{-6}$, $\propto r^{-12}$ [58, 59]). The main advantage of the JCZ EOS over the BKW EOS is that it is based on theory and does not rely on experimentally calibrated parameters. For a large number of species, the thermodynamic state of the gaseous mixture can be derived by solving the intermolecular potentials using perturbation theories. The KLRR theory [60] proved its efficiency at solving the thermodynamic properties of condensed-phase explosives.

When the explosive balance is negative, the modeling of the detonation products is further complicated by the presence of condensed species. The nature and the phases of the condensed species has an influence on the detonation properties. For instance, Greneir et al. [61] reported that the presence of carbon in either a graphite form or a diamond form led to a discrepancy of up to 10% of the VOD and up to 20% for the detonation pressure. The treatment of these condensed phase species can be achieved either by adjusting the parameters obtained for the gaseous species (the BKWC library contains 3 additional parameters to account for the presence of carbon in a solid state), or by developing a new EOS. A literature review on these EOS can be found in [62]. Note that the accuracy of EOS for either gaseous or condensed species depends on the range of pressure considered. It is generally difficult to find accurate EOS parameters to fit experimental data from 10's GPa to 100 kPa. As a consequence, an EOS that is valid at the detonics stage would probably not be accurate for a large expansion volume of the detonation products, and may not result in reasonable blast pressure predictions.

A.5.2 Cheetah 2.0

Cheetah 2.0 [48] is a thermochemical code that solves the thermodynamic equations between the product species to find equilibrium at a given pressure and temperature. As for many thermochemical codes, Cheetah 2.0 attempts to minimize the Gibbs free energy by balancing chemical potentials while ensuring the conservation of the number of moles of the different species. As such, Cheetah 2.0 does not explicitly consider the actual reaction pathways between the products species, but balances the chemical potentials over a high number of artificial decomposition reactions. The number of elements is given by the chemical formula of the explosive compound, while the different species are listed in a library (BKWR, BKWS, BKWC, etc.). Cheetah 2.0 is an extension of the TIGER code [45] and includes a wider reactant library, a new set of parameters for the BKW EOS (BKWC), a friendlier interface and new algorithmic improvements [63]. Cheetah 2.0 evolved from the primary version of Cheetah (mainly based on

the Chapman-Jouget theory) by including a kinetic feature based on the Wood and Kirkwood theory [14] to account for detonation waves with long reaction zones and time-dependent phenomena.

Cheetah is often used to evaluate performance of propellants or explosives. The output files of Cheetah 2.0 gives the values of the VOD, P_{CJ}, ΔH^0_{det} as well as the mechanical and the total detonation energy of the detonation products. The PV relation is also fit with the JWL EOS (see section A.5.3). These output values are of interest since they can be reported in computational fluid dynamic (CFD) codes or hydrocodes used to model air-blast phenomena. Note that despite being at its ninth version, only Cheetah 2.0 is available for non-US institutions explaining its use in this thesis. For a given explosive compound, the input values are the chemical formula, ρ_i and ΔH^0_f. While it is relatively obvious that ΔH^0_f of different explosive compounds are different, isomeric forms of the same explosive molecule also have different values of ΔH^0_f. However, the variations of the detonation parameters as a function of ΔH^0_f are weak compared to the influence of the density. Note that the detonation characteristics calculated with Cheetah assumes an infinite explosive diameter (ideal detonation). Hence, even if Cheetah predicts experimental values with an accuracy of less than 5% for homogeneous explosive charges with large diameters, the discrepancy generally increases if the diameter is reduced. Cheetah also generally fails at predicting detonation parameters for non-ideal or heterogeneous explosives as was seen in Chapter 2.

A.5.3 EOS used to model homogeneous explosives in this thesis

The JWL EOS

The Jones-Wilkins-Lee (JWL) EOS [64] is by far the most common EOS used to simulate macroscopically the expansion of the detonation products. Sometimes it is also employed to simulate the reactants. The pressure as a function of the expansion volume and volumetric energy is defined in Eq. (A.11):

$$P(\tilde{V},E) = A\left[1-\frac{\omega}{r_1\tilde{V}}\right]e^{-r_1\tilde{V}} + B\left[1-\frac{\omega}{r_2\tilde{V}}\right]e^{-r_2\tilde{V}} + \frac{\omega E}{\tilde{V}} \tag{A.11}$$

where A, B, r_1, r_2 and ω are constant parameters. A and B have a dimension of a pressure whereas r_1, r_2 and ω are dimensionless. For validity, these parameters are subjected to the constraints that $r_1 > r_2 > 0$ and $\omega > 0$. When used for the detonation products, the JWL EOS must also follow the constraint $A > B > 0$ whereas for the reactants $A > -B > 0$. $\tilde{V} = \frac{V}{V_0}$ is the ratio of the normalized expanded volume (V) by the initial (unreacted) explosive volume (V_0) and E corresponds to the state-dependent internal explosion energy. E can be interpreted as the detonation energy per unit of the initial (and not the actual expanded) volume. Note that the JWL EOS is considered as a partial EOS since there is no temperature dependence in its formulation. The JWL EOS generally gives good agreement in the high-pressure regime following the early

expansion of the products, but may fail to predict accurately the pressure values in low-pressure regimes. Historically, the parameters of the JWL EOS were determined experimentally by fitting the *PV* relation of the detonation products obtained with data from cylinder expansion or flyer plate tests (see section A.6.1), or as an output EOS from thermochemical calculations. The JWL EOS can be then implemented in CFD/hydrocodes to simulate blast effects. In this thesis, the JWL EOS is used to model C-4, with parameters extracted from the LNLL handbook [5].

The SESAME EOS

The SESAME library is a tabular EOS and includes tables of pressure and energy as a function of density and temperature. One advantage of a tabular EOS is that it enables one to bypass the implementation of an EOS with a complex analytic form in CFD codes. In general, the tables of the SESAME library are generated using a variety of EOS rather than a unique EOS for a given material. However, the nature of these EOS are confidential and are not shared without approval. Nevertheless, the SESAME documentation [65] indicates that the thermal contribution of electrons and ions is included in the calculation of thermodynamic data, as well as the effects of vaporization, melting and shear. The SESAME library gathers a large number of materials (> 150), including elemental metals, alloys, polymers and high explosives. Data are listed from pressures of 10^{-6} up to 10^{4} g/cc (astrophysical densities) and energies up to 10^{5} eV . The tables for NM were provided by Fluid Gravity Engineering (FGE) and are used in this thesis.

A.5.4 Numerical frameworks for blast modeling

Thermochemical codes are very useful tools to evaluate the parameters of the detonation and the associated explosive energy release, but provide no information on the blast propagation and its properties. This is why thermochemical codes must be used in combination with numerical codes that predict the hydrodynamics of compressible flows. Typical CFD codes are appropriate to simulate air-blast phenomena. These codes are based on the Finite Element Method (FEM) or the Finite Volume Method (FVM) and follow the basic laws of mass, momentum and energy conservation. Since air in high-speed flows is compressible, the Eulerian equations are solved. Typical commercial codes include BLASTX, CTH, FEFLO, FOIL, SHARC, Air3D and SHOCK. Additional codes including DYNA3D [66], LS-DYNA [67], AUTODYN [68] and ABAQUS [69] offer the possibility to investigate the blast load on a structure. The numerical methods pertaining to these multiphase, multi-material flows will be described in chapter 2.

A.6 Experimental characterization of explosives and their effects

The determination of the explosive properties and their effects were historically determined experimentally. In section A.6.1, the diagnostics used to probe the detonation properties are briefly reviewed, whereas the diagnostics used to probe the explosion effects, and particularly those used in this work, are reviewed in section A.6.2.

A.6.1 Experimental characterization of detonation properties of explosives

The experimental determination of detonation properties of explosives is of interest for i) determining the particular performance metric of interest (e.g., stability, brisance, power, energy release etc.) or ii) providing data for validating numerical models. The detonation velocity is generally the easiest parameter to measure. For example, one technique to measure the detonation velocity is to use piezoelectric shock pins (or probes that generate a short from passage of the detonation wave, such as twisted wire pairs) placed at regular distances along the explosive layer. These pins generate an electrical charge when impacted which can be converted to a transient voltage signal. With multiple shock pins, the time of arrival of the detonation wave and hence the detonation velocity can be determined. The detonation velocity can alternatively be determined using optical methods [2]. A common technique for investigating the expansion of the detonation products is the so-called cylinder test. The tested explosive is placed within a cylindrical tube and detonated. After the detonation, the expansion of the products accelerates the cylinder wall outwards. The motion of the wall is then recorded with a high-speed video camera and the trajectory and the velocity can be determined. Using the assumption that the detonation products expand isentropically, the pressure-volume relation can be derived. The PV relation can be subsequently fitted with the JWL EOS and the parameters of the fit can be used in numerical codes. The detonation pressure P_{CJ} can be determined using various gauges, such as a Polyvinylidene Fluoride (PVDF) gauge [70], and the energy of detonation with calorimetric tests [71]. Nevertheless, the experimental determination of these parameters lies outside the scope of this thesis.

A.6.2 Experimental characterization of blast and explosion properties

Pressure gauge

A common diagnostic tool to investigate the blast properties is the piezoelectric pressure gauge. Such gauges are transducers that convert the hydrodynamic pressure into an electrical signal. When a pressure wave penetrates the sensor, the pressure is first converted into mechanical stress on a diaphragm (generally made of Invar) it as shown on Fig. A.9. The stress is transferred

to a quartz crystal which generates an electric charge proportional to the force exerted. The generation of the electric charges result from the creation of electrical dipoles associated with the compression of hexagonal structures formed by silicon and oxygen atoms inside the quartz crystal. The pressure gauge is typically used in combination with an amplifier to convert the signal into a voltage that can be read by an oscilloscope or a data acquisition system.

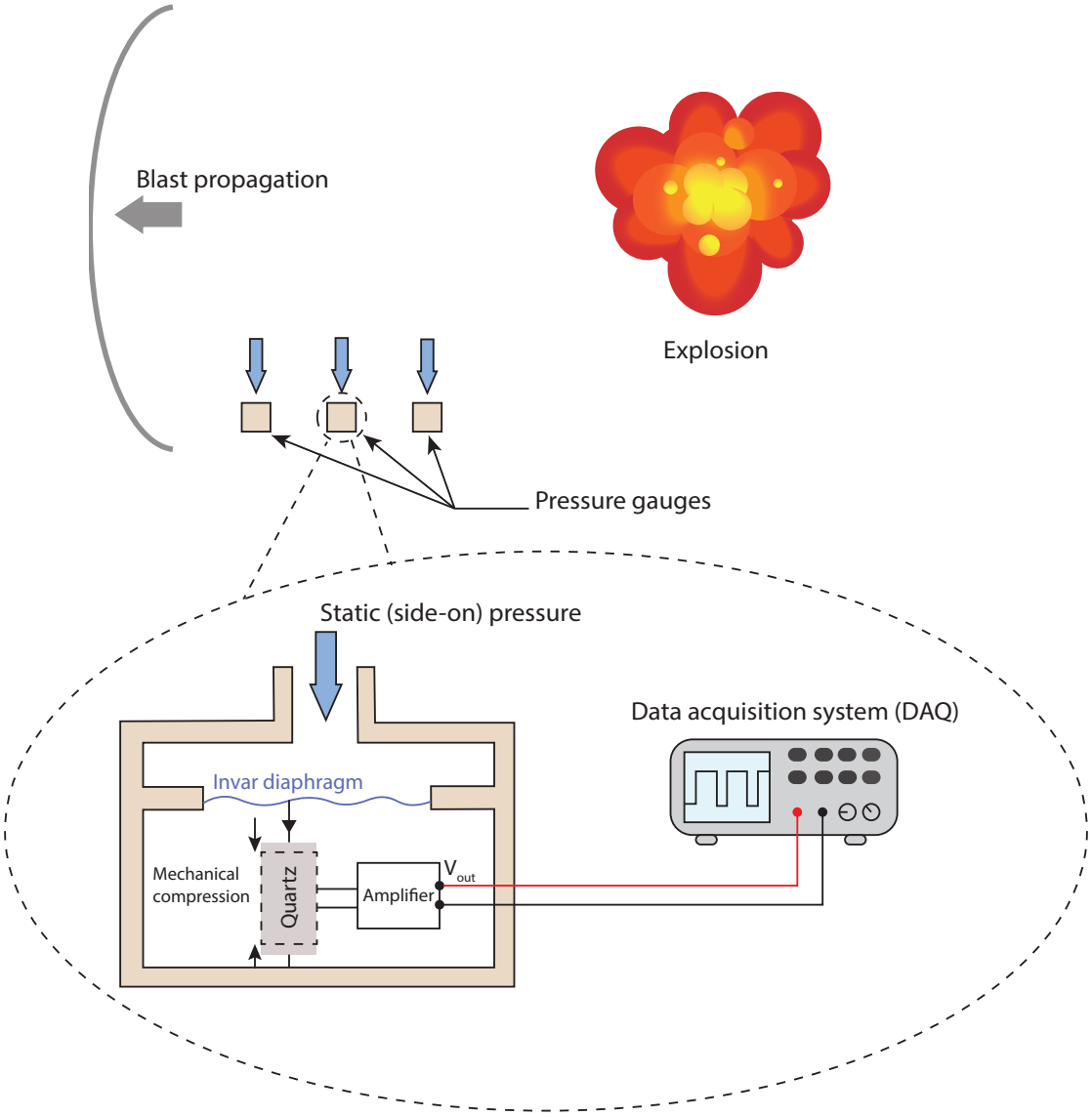

Fig. A.9 Top view of the correct position of the pressure gauges and details of their operating mechanism (adapted from [72]).

Piezoelectric pressure gauges are good at measuring rapid changes of pressure but are not useful for measuring static pressures over long times. Due to the internal resistance of the sensor, and dissipation of the electrical current by the Joule effect, the output signal will eventually fall to zero, even in the presence of an applied pressure on the diaphragm. For this reason, dynamic pressure gauges are used to measure the overpressure (or the pressure above ambient conditions) and they are calibrated to read 0 Pa at atmospheric pressure. They also must be

carefully calibrated to determine the sensitivity, or conversion of voltage to pressure. The high frequency piezoelectric pressure gauges used in the present thesis (e.g., 113B series gauges from PCB Piezotronics) have a resonant frequency above 500 kHz and a rise time on the order of 1 microsecond. Although the gauge materials (Invar and quartz) have low thermal expansion coefficients, the gauge signals can be influenced by high temperatures, such as within a fireball. In this case, the thermal effects can be minimized for short times by coating the gauge face with a protective layer (e.g., of silicone). Near-field blast pressure signals can be influenced by wave reflections (e.g., from gauge stands) so that blast overpressure data are often fit to a Friedlander form (Eq. (A.4)).

The orientation of the face of a pressure gauge is also important to record accurate blast pressure profiles. Since blast profiles represent the static pressure (or the pressure associated with the sole random molecular agitation), the top of the sensor must be aligned with the direction of the flow. On the contrary, if the sensor is facing the blast front, the recorded pressure is first that of the reflected overpressure, which is much higher than the static pressure. The reflected overpressure represents the molecular agitation resulting from the random motion of the molecules perturbed by both the incident wave and the reflected wave from the sensor plus the orderly movement of the molecules associated with the bulk motion of the fluid (dynamic pressure). However, depending on how the gauge is mounted, after a few microseconds rarefaction waves (caused by the diffraction of the reflected shock around the transducer) reach the sensor and relieve the pressure such that the pressure recorded by the sensor corresponds to the total (or stagnation) pressure. In this thesis manuscript, all the occurrences of the word "pressure" refer to the static pressure and the concepts of total and reflected pressures are not considered further.

High-speed video imaging

High-speed video cameras are an essential tool to characterize explosions. Qualitatively, these cameras can capture the dynamics and the luminosity of the fireball and the potential dispersal of material. Moreover, cameras may also capture the motion of the blast wave front providing that it can be resolved visually. The high density gradients between the undisturbed air ahead of the blast and the disturbed air behind, are associated with a high gradient in the refractive indices between the two media. This variation of the optical refractive index distorts the light rays traveling in the vicinity of the blast front, enabling the visualization of a sharp interface corresponding to the blast front as shown in Fig. A.10. At laboratory scale, to study weaker blast waves resulting from smaller explosive charges, it is necessary to use schlieren photography to enhance the contrast of the blast front [73]. Nevertheless, at larger scale, it is difficult to implement this technique in the field due to the scale of the required optics and the high power needed for the light source.

Fig. A.10 Fireball from the detonation of an explosively dispersed cloud of metal particles and fuel droplets. Photograph taken at DRDC Suffield, Alberta, Canada (cover picture of *Shock Waves* journal, Vol. 28, No. 3, 2018). The variation of the air refractive index due to the passage of the blast wave enables the visualization of the blast front.

By tracking the blast wave front trajectory and using the Rankine-Hugoniot relations as defined in section A.4.4, it is also possible to estimate quantitatively the pressure jump across the shock (peak blast pressure). This method is described in detail in chapter 3 and is used for all the experiments reported in this thesis. On the contrary, extracting the pressure gradients behind the blast front is not straightforward. Analytically, since the flow behind the blast front is not isentropic, it is not possible to extract the pressure using traditional thermodynamic relations. In practice, it is necessary to measure independently several physical parameters to characterize the flow [74]. For small-scale explosions, Biss & McNesby [75] attempted to map the pressure field behind the blast front using schlieren photography by mapping the density field. Density gradients in the videos were evaluated using various mathematical algorithms. Combined with the assumption of a temperature field decaying linearly at each stand-off distance from the explosion center, they were able to reproduce the experimental pressure profiles relatively accurately and calculate the positive-phase blast impulses. However, this methodology is difficult to implement at large-scale and is not used in the present work.

The validity of the Rankine-Hugoniot relations to determine the peak blast overpressure from videography records depends on the assumptions that the blast front is sufficiently thin, and that the degree of shock curvature is small compared to the scale of the measuring instrument. The first assumption is generally verified for well-formed blast waves (the shock front thickness is

of order a few mean free paths between gaseous molecules). The second assumption is also verified provided that the spatial resolution of the high-speed video camera is sufficiently high, such that the blast front appears as a normal shock on the pixel considered. Currently, with the advancement of modern camera technology, it is relatively easy for laboratories to acquire high-speed video cameras with a spatial resolution of a few hundred thousands pixels, sufficient to acquire data for most experiments. Note that the temporal resolution of these cameras is also an important factor to consider. Considering that blast waves can travel at a speed of a few kilometers per second, especially in the near field, it is important to have a sufficient framing rate to resolve the dynamics of the explosion. Moreover, obtaining a high temporal resolution is an important factor to reduce the error bars associated with the estimation of the blast velocity and peak pressure as was seen in Chapter 3. In practice, due to the limitation of the camera memory, these cameras offer a trade-off between spatial and temporal resolution. Hence, the camera settings (framing rate, field of view, frame duration and so on) must be chosen with care and optimized for each experiment.

Other diagnostics

Thermocouples It is also of interest to measure the temperature behind the blast front or within the fireball, to estimate the thermal load of an explosion. Thermocouples are generally used to evaluate the temperature of gaseous products by exploiting the *Seebeck effect* [76]. This effect, also called thermoelectric effect, consists of generating a electric current by joining two different metals maintained at different temperatures.

The main drawback of thermocouples is their slow response time, especially when thermal conditions vary rapidly which is typically the case for gaseous products within the highly turbulent flow of the fireball. In addition, the spatial heterogeneity of the temperature field demands many measurements at different locations to get an estimation of the average temperature within this medium. Some of the drawbacks of using thermocouples for determining fireball temperatures can be overcome by two different analysis techniques: i) considering local extrema in the signals, when the thermocouple temperature is instantaneously equal to the local gas temperature, and ii) reconstructing the transient gas temperature by using multiple co-located thermocouples with different time constants [77].

Spectroscopy Fast-response optical diagnostics, such as time-integrated spectrometers and pyrometers, are useful to record the transient radiation emitted by a fireball and hence to infer the temperature of the condensed species within the detonation products. In general, the condensed products can be considered as gray emitters which means that their spectrum depends only on temperature and follows Planck's law [78]. However, the emissivity (effectiveness of a species in emitting energy as thermal radiation) of a gray body is dependent on the wavelength such that the estimation of the temperature cannot be inferred by measuring only the radiance at

one wavelength. Hence, the determination of the ratio of the radiant fluxes at two wavelengths (two-color pyrometer) is the minimum needed to infer the temperature of the fireball [79]. Three (or more) color pyrometers are often used to assess the dependence of emissivity on the wavelength.

Spectroscopic studies have highlighted important physical processes that occur during the detonation of HE. One important phenomenon highlighted by spectroscopic instrumentation is the presence of a thin and extremely hot region in the air, at the contact surface immediately behind the shock breakout with the detonation products. The temperatures in this region can reach up to 6000 K [79] for NM charges. In comparison, Brode [21] predicted a temperature of approximately 9000 K for TNT. These temperatures are, in fact, close to those estimated by the Rankine-Hugoniot theory for a high Mach number normal shock wave, ($M_a \sim 13 - 18$) which is consistent with the blast wave velocity in the very near field. On the contrary, inside the detonation products, the gas temperature are still high but lower than the shocked air layer due to the higher density and molecular weight, as well as the pressure reduction associated with the release wave, and following expansion of the products.

However, fireballs of HE are generally optically thick and the spectrum and temperature of the condensed species can only be probed in the outer few centimeters of the fireball using emission spectroscopy [80]. In addition, optical instrumentation are fragile and require significant time to set up in the field. For all these reasons, spectroscopic measurements were not used in the present work, although they have been used extensively in the past in our research group [79].

Other diagnostics Other experimental apparatus can be used to extract other explosion properties such as the particle velocity or the flow density but lie outside the scope of this thesis. The interested reader can refer to [23, 24, 74]

A.6.3 Casing effects and acceleration of fragments

Fragmentation of casings

When a explosive is detonated, the sudden increase in pressure generally fragments and shatters the casing encompassing the explosive. This is particularly true for brisant explosives with high detonation velocities and pressures. The detonation wave will transmit into the casing and generate stress by reverberating within the casing. Subsequently, the expansion of the detonation products causes the casing to deform plastically. At some point, the casing will fracture and tensile relief waves propagate to the sides of the fracture region. N. F. Mott [81] theorized that the size distribution of the fragments (and thus the number of fragments) could be determined from the competition between the strain rate and rate of tensile relief inside the casing. Further theories evaluated fragment sizes as a function of a hypothesized critical expansion velocity [82]. Estimating the number of fragments dispersed by an explosion and their velocities is of interest to quantify explosion hazards.

Gurney theory and the Fano-Fischer equation

In 1943, R. W. Gurney derived a model to predict the fragment velocities generated by the rupture of spherical and cylindrical metal cases by a high-explosive core [83]. A brief summary of the assumptions made by Gurney and the main steps of the derivation are presented in [84]. Currently, Gurney's methodology continues to be the primary analytic technique to estimate the terminal velocity of explosively accelerated materials, especially for those dispersed by homogeneous explosive systems. However, for certain heterogeneous systems, Gurney's equations fail to predict the velocity of the dispersed materials and corrections must be applied to recover the correct velocities as analyzed in [84].

In principle, the energy spent to accelerate hard casings diminishes the energy available to support the blast wave. The reduction in energy available to the blast wave must be considered relative to the total mass of material that is accelerated. This simple reasoning lead Fano in 1944 [85] and Fisher in 1953 to attempt to predict analytically the energy partition between the blast and the accelerated materials as a function of the total explosive energy and mass of materials, based on the work of Gurney. In 2011, Hutchinson [86–88] revisited the work of Fano and Fisher, and revealed that their derivations were, in fact, inconsistent with the Gurney model and did not correlate well with all experimental data. He concluded that his derivations were best suited to estimate the energy partition between the two phases. Note that whereas the Gurney model is widely used to predict the acceleration of materials and has been extensively validated, the validity of the Fano-Fischer-Hutchinson equations to determine the energy partition between the blast and the fragments remains elusive, especially for materials that are able to convert energy into internal energy via compaction, deformation, fracturing, etc.

A.6.4 A note on explosion effects on a structure

Explosions effects pose serious hazards for building structures. Over the last few decades, the response of structures to blast loads has been extensively investigated [89], to address the consequences of uncontrolled explosions from industrial accidents, and the growing occurrence of terrorist attacks. Contrary to popular belief, most of the casualties resulting from the detonation of explosives near a building are not due to the primary energy release of the explosive through thermal or blast loads. Rather, they are more related to the failure of the structures, including the shattering of glass windows as well as complete building collapse. For instance, the simultaneous terrorist attacks against the U.S. embassies in Nairobi, Tanzania and Dar es Salaam, on the 7^{th} of August 1998, lead to the death of 223 people mostly caused by the collapse of a nearby building, and more than 4500 persons were injured mainly due to lacerations by flying glass fragments [89].

Quantifying the blast pressure load on a building and the subsequent failure is far more complex than quantifying the blast propagating in air (incident pressure). When a blast wave reaches the face of a building, the blast reflects back, causing a significant increase in the

pressure exerted on the wall. In an ideal-linear case where the air molecules would move and bounce freely, the increase of pressure would be two times the incident pressure. But due to the non-linearity of strong shock waves, as those associated with the detonation of high explosives, the motion of the reflected molecules are obstructed by the continuous motion of the air molecules from the incident blast. This obstruction lead to much higher reflected pressures than that of the incident pressure. Reflected pressures are also dependent on the angle of incidence of the primary blast with the wall. For an incidence degree of 0° (i.e., when the blast wave is perpendicular to the wall), the reflected pressure is maximum. The pressure generally decreases monotonically with the angle of incidence, except for the $40^\circ - 55^\circ$ region, where the pressure suddenly increases again due to the formation of a Mach stem. The analysis of the blast load on a building is further complicated by the diffraction of the primary blast wave around the structure, causing a different pressure force of the side and rear walls, by the pressure associated with the motion of the air molecules behind the blast front (dynamic or drag pressure) and clearing effects [90]. Moreover, the pressures associated with the negative blast phase, even if lower than those associated with the positive pressure phase, may cause the collapse of the structure already damaged by the effects of the positive pressure phase. Finally, the characterization of the damage to a structure subjected to a blast load would not be possible without a complete knowledge of the material properties and response to various constraints.

Nevertheless, the characterization of a blast load on a structure is clearly outside the scope of this thesis, which is focused rather on the quantification of the air-blast incident pressure and positive-phase for heterogeneous explosives systems.

Summary

- Conventional explosives are mainly composed of four elements (C, H, N, O) and detonations products are composed of molecules based on these elements.
- Composition C-4 (C4) and sensitized nitromethane (NM) are used as explosives in this work.
- The blast wave properties of homogeneous explosives obey a cube root scaling law.
- The blast pressure can be measured by pressure transducers or inferred from videography data using Rankine-Hugoniot relations.
- Thermochemical codes and equations of states (EOS), such as Cheetah 2.0 and the JWL EOS, can be used in combination to model the detonation properties of homogeneous explosives with a good accuracy.

References

[1] P. W. Cooper. *Explosives engineering*. Wiley-VCH, wiley-vch edition, 1996.

[2] R. Chéret. *Detonation of condensed explosives*. Springer-Verlag New York, Inc., 1993, doi:10.1007/978-1-4613-9284-2.

[3] G. F. Kinney and K. J. Graham. *Explosive shocks in air (Second edition)*. Springer, 1985, doi:10.1007/978-3-642-86682-1.

[4] N. Kubota. *Propellants and explosives: thermochemical aspects of combustion*. Wiley-VCH Verlag GmbH & Co. KGaA, 2015, doi:10.1002/9783527693481.

[5] B. M. Dobratz and P. C. Crawford. LLNL explosives handbook - Properties of chemical explosives and explosive simulants. Technical report, Lawrence Livermore National Laboratory (LLNL), Livermore, California, 1985, https://www.osti.gov/biblio/6530310-llnl-explosives-handbook-properties-chemical-explosives-explosives-explosive-simulants.

[6] Y. B. Zeldovich. *On the theory of the propagation of detonation in gaseous systems*. 1950.

[7] J. Von Neumann. Theory of detonation waves. Technical report, Technical report OSRD-549, National Defense Research Committee, 1942, https://apps.dtic.mil/sti/citations/ADB967734.

[8] W. Döring. Über den Detonationsvorgang in Gasen. *Annalen der Physik*, 435(6-7):421–436, 1943, doi:10.1002/andp.19434350605.

[9] W. Rankine. On the thermodynamic theory of waves of finite longitudinal disturbances. *Philosophical Transactions of the Royal Society of London*, 160:277–288, 1870, doi:10.1098/rstl.1870.0015.

[10] P-H. Hugoniot. Mémoire sur la propagation des mouvements dans les corps et spécialement dans les gaz parfaits (deuxième partie). *Journal de l'École Polytechnique*, 58(Print.):1–125, 1889.

[11] S. Arrhenius. Über die dissociationswärme und den einfluss der temperatur auf den dissociationsgrad der elektrolyte. *Zeitschrift für Physikalische Chemie*, 4:96 – 116, 1889, doi:doi.org/10.1515/zpch-1889-0408.

[12] S. Arrhenius. Über die reaktionsgeschwindigkeit bei der inversion von rohrzucker durch säuren. *Zeitschrift für Physikalische Chemie*, 4, 1889, doi:10.1515/zpch-1889-0416.

[13] S. Boulal. *Comportements dynamiques de la détonation dans des compositions gazeuses non-uniformes*. PhD thesis, École National Supérieure de Mécanique et d'Aéronautique, 2017, https://tel.archives-ouvertes.fr/tel-01508647.

[14] W. W. Wood and J. G. Kirkwood. Diameter effect in condensed explosives. The relation between velocity and radius of curvature of the detonation wave. *The Journal of Chemical Physics*, 22(11):1920–1924, 1954, doi:10.1063/1.1739940.

[15] L. E. Eremenko. Interrelationship between density and structure in an explosive. In *Proceedings of the 11th symposium on explosives and pyrotechnics*, Philadelphia, U.S.A., 1981.

[16] L. E. Eremenko. Density calculation of aromatic crystals using their structure. In *Proceedings of the 8th International Pyrotechnics Symposium*, Colorado, U.S.A., 1982.

[17] L. R. Rothstein. Predicting high explosive detonation velocities from their composition and structure. *Propellants, Explosives, Pyrotechnics*, 4(4):56–60, 1979, doi:10.1002/prep.19790040305.

[18] L. R. Rothstein. Predicting high explosive detonation velocities from their composition and structure (II). *Propellants, Explosives, Pyrotechnics*, 6(4):91–93, 1981, doi:10.1002/prep.19810060402.

[19] J. M. Dewey. The TNT and ANFO equivalences of the Beirut explosion. *Shock Waves*, 31(1):95–99, 2021, doi:10.1007/s00193-021-00992-1.

[20] Interstate commerce Commission. Railroad accident investigation. Accident near Mt Pulaski. Technical report, Illinois central railroad company, 1958, https://rosap.ntl.bts.gov/view/dot/45483.

[21] H. L. Brode. Blast wave from a spherical charge. *Physics of Fluids*, 2(1959):217–229, 1959, doi:10.1063/1.1705911.

[22] J. M. Dewey. The shape of the blast wave: studies of the Friedlander equation. In *21st International Symposium on Military Aspects of Blast and Shock (MABS 21)*, pages 1–9, Jerusalem, Israel, 2010.

[23] C. E. Needham. *Blast waves*. Springer, 2010, doi:10.1007/978-3-642-05288-0.

[24] C. E. Needham. *Blast waves (second edition)*. Springer, Cham, 2 edition, 2018, doi:10.1007/978-3-319-65382-2.

[25] J. M. Dewey. The Julius Meszaros lecture - 53 years of blast wave research - A personal history. In *21st Military Aspects of Blast and Shock (MABS)*, pages 1 – 11, Jerusalem, Israel, 2010.

[26] M. Berthelot. *Explosives and their power*. London: J.Murray, Print., 1892.

[27] S. E. Rigby, T. J. Lodge, S. Alotaibi, A. D. Barr, S. D. Clarke, G. S. Langdon, and A. Tyas. Preliminary yield estimation of the 2020 Beirut explosion using video footage from social media. *Shock Waves*, 30(6):671–675, 2020, doi:10.1007/s00193-020-00970-z.

[28] C. Stennett, S. Gaulter, and J. Akhavan. An estimate of the TNT-equivalent net explosive quantity (NEQ) of the Beirut port explosion using publicly-available tools and data. *Propellants, Explosives, Pyrotechnics*, 45(11):1675–1679, 2020, doi:10.1002/prep.202000227.

[29] H. J. Pasman, C. Fouchier, S. Park, N. Quddus, and D. Laboureur. Beirut ammonium nitrate explosion: are not we really learning anything? *Process Safety Progress*, 39(4), 2020, doi:10.1002/prs.12203.

[30] C. J. Aouad, W. Chemissany, P. Mazzali, Y. Temsah, and A. Jahami. Beirut explosion: TNT equivalence from the fireball evolution in the first 170 milliseconds. *Shock Waves*, 2021, doi:10.1007/s00193-021-01031-9.

[31] J. S. Díaz. Explosion analysis from images: Trinity and Beirut. *European Journal of Physics*, 42(3), 2021, doi:10.1088/1361-6404/abe131.

[32] C. Pilger, P. Gaebler, P. Hupe, A. C. Kalia, F. M. Schneider, A. Steinberg, H. Sudhaus, and L. Ceranna. Yield estimation of the 2020 Beirut explosion using open access waveform and remote sensing data. *Scientific Reports*, 11(1):1–14, 2021, doi:10.1038/s41598-021-93690-y.

[33] D. Bogosian, M. Yokota, and S. Rigby. TNT equivalence of C-4 and PE4: A review of traditional sources and recent data. In *24th International Symposium on Military Aspects of Blast and Shock (MABS 24)*, pages 1–15, 2016.

[34] L. I. Sedov. *Similarity and dimensional methods in mechanics*. Academic Press, 1959, doi:10.1016/B978-1-4832-0088-0.50008-6.

[35] G. Taylor. The formation of a blast wave by a very intense explosion. I. Theoretical discussion. *Proceedings of the Royal Society. Series A. Mathematical, Physical and Engineering Sciences*, 201(1065):159–174, 1950, doi:10.1098/rspa.1950.0049.

[36] G. Taylor. The formation of a blast wave by a very intense explosion. II. The Atomic explosion of 1945. *Proceedings of the Royal Society of London. Series A. Mathematical and Physical Sciences*, 201(1065):175–186, 1950, doi:10.1098/rspa.1950.0050.

[37] Fact sheet: operation TRINITY. Technical report, Defense Threat Reduction Agency (DTRA), 2014, https://web.archive.org/web/20141125082310/http://www.dtra.mil/docs/documents-ntpr-factsheets/trinity—2014.pdf?sfvrsn=0.

[38] S. Glasstone and P. J. Dolan. The effects of nuclear weapons. Technical report, 1977, https://www.deepspace.ucsb.edu/wp-content/uploads/2013/01/Effects-of-Nuclear-Weapons-1977-3rd-edition-complete.pdf.

[39] C. N. Kingery and B. F. Pannill. Peak overpressure versus scaled distance for TNT surface bursts (hemispherical charge). Technical report, BRL, Aberdeen Proving Ground, Maryland, USA, 1964, https://apps.dtic.mil/sti/pdfs/AD0443102.pdf.

[40] C. N. Kingery. Air blast parameters versus distance for hemispherical TNT surface bursts. Technical report, BRL, Aberdeen Proving Ground, Maryland, USA, 1966, https://apps.dtic.mil/sti/pdfs/AD0811673.pdf.

[41] R. G. Sachs. The dependence of blast on ambient pressure and temperature. Technical report, Ballistic Research Laboratories, Aberdeen Proving Ground, Maryland, USA, 1944, https://apps.dtic.mil/sti/pdfs/ADA800535.pdf.

[42] W. E. Baker, P. S. Westine, and F. T. Dodge. *Similarity methods in engineering dynamics: theory and practice of scale modeling*. Elsevier, 1991.

[43] T. Wei and M. J. Hargather. A new blast wave scaling. *Shock Waves*, 31(3):231–238, 2021, doi:10.1007/s00193-021-01012-y.

[44] H. B. Levine and R. E. Sharples. Operator's manual for RUBY. Technical report, Lawrence Radiation Laboratory, 1962, https://catalog.hathitrust.org/Record/007293219.

[45] M. Cowperthwaite and W. H Zwisler. TIGER computer program documentation. Technical report, Standford Research Institute, Menlo Park, CA, U.S.A., 1974, https://apps.dtic.mil/sti/pdfs/ADA002791.pdf.

[46] S. A. Gubin, V. V. Odintsov, and V. I. Pepekin. Thermodynamic calculation of ideal and nonideal detonation. *Combustion, Explosion and Shock Waves*, 23:446–454, 1987, doi:10.1007/BF00749306.

[47] M. Sućeska. Calculation of the detonation properties of C-H-N-O explosives. *Propellants, Explosives, Pyrotechnics*, 16(5):197–202, 1991, doi:10.1002/prep.19910160409.

[48] L. E. Fried, W. M. Howard, and P. C. Souers. Cheetah 2.0 user's manual. Technical report, Lawrence Livermore National Laboratory, Livermore, CA, USA, 1998.

[49] F. Charlet, M. L. Turkel, J. F. Danel, and L. Kazandjian. Evaluation of various theoretical equations of state used in calculation of detonation properties. *Journal of Applied Physics*, 84(8):4227–4238, 1998, doi:10.1063/1.368640.

[50] M. Genetier and G. Baudin. SIAME version 1, notice physique. Technical report, CEA Gramat, 2016.

[51] M. Cowperthwaite and W. K. Zwisler. The JCZ equations of state for detonation products and their incorporation into the TIGER code. In *Proceedings of the 6th Symposium (International) on Detonation*, pages 162–170, Coronado, CA, U.S.A., 1976.

[52] V. R. Becker. Eine zustandslgleichungfur strichstoff bei grossen dichten. *Zeitschrift fur Physik*, 4:393 – 409, 1921, doi:10.1007/BF01332504.

[53] C. L. Mader. *Numerical modeling of explosives and propellants*. CRC press, 2007.

[54] M. Finger, E. Lee, F. H. Helm, B. Hayes, H. Hornig, R. McGuire, M. Kahara, and M. Guidry. The effect of elemental composition on the detonation behavior of explosives. In *Proceedings of the 6th International Detonation Symposium*, page 710, San Diego, CA, U.S.A., 1976.

[55] M. L. Hobbs and M. R. Baer. Nonideal thermoequilibrium calculations using a large product species data base. *Shock Waves*, 2(3):177–187, 1992, doi:10.1007/BF01414640.

[56] M. L. Hobbs and M. R. Baer. Calibrating the BKW-EOS with a large product species database and measured C-J properties. *10th International Detonation Symposium*, (January 1992):414–423, 1992.

[57] L. Fried and P. C. Souers. BKWC: An empirical BKW parametrization based on cylinder test data. *Propellants, Explosives, Pyrotechnics*, 21(4):215–223, 1996, doi:10.1002/prep.19960210411.

[58] J. E. Jones. On the determination of molecular fields.—I. From the variation of the viscosity of a gas with temperature. *Proceedings of the Royal Society of London. Series A*, 106(738):441–462, 1924, doi:10.1098/rspa.1924.0081.

[59] J. E. Jones. On the determination of molecular fields. — II. From the equation of state of a gas. *Proceedings of the Royal Society of London. Series A*, 106(738):463 – 477, 1924, doi:10.1098/rspa.1924.0082.

[60] H. S. Kang, C. S. Lee, T. Ree, and F. H. Ree. A perturbation theory of classical equilibrium fluids. *The Journal of Chemical Physics*, 82(1):414–423, 1985, doi:10.1063/1.448762.

[61] N. R. Greiner, D. S. Phillips, J. D. Johnson, and F. Volk. Diamonds in detonation soot. *Nature*, 333(6172):440–442, 1988, doi:10.1038/333440a0.

[62] S. Poeuf. *Équations d'état des produits de détonation des explosifs solides*. PhD thesis, Ecole Nationale Supérieure de Mécanique et d'Aérotechique (ENSMA), 2018, https://tel.archives-ouvertes.fr/tel-01955764.

[63] J. P. Lu. Evaluation of the thermochemical code - CHEETAH 2.0 for modelling explosives performance. Technical report, DSTO, 2001, https://apps.dtic.mil/sti/pdfs/ADA396687.pdf.

[64] E. L. Lee, H. C. Hornig, and J. W. Kury. Adiabatic expansion of high explosive detonation products. Technical report, Lawrence Radiation Lab, University of California, Livermore, 1968, https://www.osti.gov/servlets/purl/4783904.

[65] Sesame: the Los Alamos National Laboratory equation of state database. Technical report, Los Alamos National Laboratory, https://permalink.lanl.gov/object/tr?what=info:lanl-repo/lareport/LA-UR-92-3407.

[66] J. O. Hallquist and R. G. Whirley. DYNA3D user's manual. Technical report, Lawrence Livermore National Laboratory, 1989, https://www.osti.gov/servlets/purl/5920559.

[67] https://www.ansys.com/fr-fr/products/structures/ansys-ls-dyna.

[68] https://www.ansys.com/fr-fr/products/structures/ansys-autodyn.

[69] https://www.keonys.com/logiciels-simulations/abaqus-solution-simulation-dassault-systemes/.

[70] R. V. Hodges, L. E. McCoy, and J. R. Toolson. Polyvinylidene Fluoride (PVDF) gauges for measurement of output pressure of small ordnance devices. *Propellants, Explosives, Pyrotechnics*, 25(1):13–18, 2000, doi:10.1002/(SICI)1521-4087(200001)25:1<13::AID-PREP13>3.0.CO;2-R.

[71] D. L. Ornellas, J. H. Carpenter, and S. R. Gunn. Detonation calorimeter and results obtained with pentaerythritol tetranitrate (PETN). *Review of Scientific Instruments*, 37(7):907–912, 1966, doi:10.1063/1.1720361.

[72] https://www.avnet.com/wps/portal/abacus/solutions/technologies/sensors/pressure-sensors/core-technologies/piezoelectric/.

[73] G. S. Settles. *Schlieren and shadowgraph techniques*. Springer, Berlin, Heidelberg, 2001, doi:10.1007/978-3-642-56640-0.

[74] J. M. Dewey. Measurement of the physical properties of blast waves. In Ozer Igra and Friedrich Seiler, editors, *Experimental methods of shock wave research*, chapter Part I, pages 53–87. Springer, 2016, doi:10.1007/978-3-319-23745-9.

[75] M. M. Biss and K. L. McNesby. Optically measured explosive impulse. *Experiments in Fluids*, 55(6), 2014, doi:10.1007/s00348-014-1749-x.

[76] T. J. Seebeck. Ueber die magnetische polarisation der metalle und erze durch temperatur-differenz. *Annalen der Physik und Chemie*, 6, 1826, doi:10.1002/andp.18260820102.

[77] D. L. Frost, J. M. Clemenson, S. Goroshin, F. Zhang, and M. Soo. Thermocouple temperature measurements in metalized explosive fireballs. *Propellants, Explosives, Pyrotechnics*, 46(6):899–911, 2021, doi:10.1002/prep.202000328.

[78] M. Planck. *The theory of heat radiation*. P. Blakiston's Son & Co, 1914.

[79] S. Goroshin, D. L. Frost, J. Levine, A. Yoshinaka, and F. Zhang. Optical pyrometry of fireballs of metalized explosives. *Propellants, Explosives, Pyrotechnics*, 31(3):169–181, 2006, doi:10.1002/prep.200600024.

[80] J. M. Peuker, P. Lynch, H. Krier, and N. Glumac. Optical depth measurements of fireballs from aluminized high explosives. *Optics and Lasers in Engineering*, 47(9):1009–1015, 2009, doi:10.1016/j.optlaseng.2009.04.011.

[81] N. F. Mott. Fragmentation of shell cases. *Proceedings of the Royal Society A: Mathematical, Physical and Engineering Sciences*, 189(1018):300–308, 1947, doi:10.1098/rspa.1947.0042.

[82] J. S. Rinehart and J. Pearson. *Metals under impulsive loading*. Dover Publications Inc, 1954.

[83] R. W. Gurney. The initial velocities of fragments from bombs, shell and grenades. Tech. Rep. (45), US Army Ballistic Research Laboratory, Aberdeen Proving Ground, Maryland, USA, 1943, https://apps.dtic.mil/sti/pdfs/ADA800105.pdf.

[84] J. Loiseau, Q. Pontalier, A. M. Milne, S. Goroshin, and D. L. Frost. Terminal velocity of liquids and granular materials dispersed by a high explosive. *Shock Waves*, 28(3):473–487, 2018, doi:10.1007/s00193-018-0822-4.

[85] U. Fano. Methods for computing data on the terminal ballistics of bombs - II estimation of the air blast. Technical report, Aberdeen Proving Ground, Maryland USA, 1944.

[86] M. D. Hutchinson. Replacing the equations of Fano and Fisher for cased charge blast equivalence – I ductile casings. *Propellants, Explosives, Pyrotechnics*, 36(4):310–313, 2011, doi:10.1002/prep.201000167.

[87] M. D. Hutchinson. Replacing the equations of Fano and Fisher for cased charge blast impulse - II fracture strain method. *Propellants, Explosives, Pyrotechnics*, 37(5):605–608, 2012, doi:10.1002/prep.201200047.

[88] M. D. Hutchinson. Replacing the equations of Fano and Fisher for cased charge blast impulse – III yield stress method. *Propellants, Explosives, Pyrotechnics*, 39(4):586–589, 2014, doi:10.1002/prep.201300173.

[89] D. O. Dusenberry, editor. *Handbook for blast-resistant design of buildings*. John Wiley & Sons, Inc, 2010, doi:10.1002/9780470549070.

[90] S. E. Rigby. *Blast wave clearing effects on finite-sized targets subjected to explosive loads*. PhD thesis, University of Sheffield, 2014, http://etheses.whiterose.ac.uk/6735/.

Appendix B

EDEN hydrocode

EDEN[1] [1] is a commercial hydrocode developed by Fluid Gravity Engineering (FGE)[2] and designed to simulate high-speed multiphase flows. A hydrocode is a subclass of CFD codes specifically dedicated to the modeling of very high speed shocks and impacts. FGE is a highly specialized scientific consultancy company based in the UK with two offices (St Andrews, Scotland, and Emsworth, England). This company mainly specializes in developing numerical models to answer specific questions addressed by customers from different sectors, including space, maritime, oil, and gas companies. Scientists at FGE have a long expertise in modeling aero-thermal problems such as those associated with the entry of the Schiaparelli probe into the Martian atmosphere or with explosions and reactive flows generated by chemical high explosives.

The modeling of heterogeneous explosive systems in EDEN is based on a two-phase fluid approach. It follows an Eulerian-Eulerian strategy where the gas and particle phases are continua advected through a fixed mesh. The model is based on a formulation similar to that of Baer & Nunziato [2] where separate sets of conservation equations determine the evolution of the gas and particle phases. The model and the equation of states were employed and validated in numerous studies devoted to the formation of jets [3, 4], the detonation of conical [5] and cylindrical charges [6], explosive afterburning effects [7, 8], the blast wave mitigation [7, 9], aluminized explosives [10–12], the acceleration of porous shells [13] or underwater explosions [14]. The equations for the different phases are based on the compressible Euler equations (without external forces) but include global exchange terms that are intended to simulate the interactions between the phases. The phases are assumed to interact through nozzling, drag, and convective heat transfer. The governing equations are listed in the Appendix of [15]. The assumptions for the models that were employed in Chapter 4 and Chapter 6 are listed below:

In Chapter 4,

[1] Note that the name EDEN is not an acronym, but rather refers to one of the local golf courses in St. Andrews, Fife, Scotland. EDEN also refers to one of Fife's two principal rivers.

[2] http://www.fluidgravity.co.uk/fgewebsite/

- C-4 was modeled by a *programmed burn* function where the explosive reactants were modeled by an ideal gas law and the detonation products by the Jones-Wilkins-Lee (JWL) equation of state (EOS) [16]. Parameters of the JWL EOS were those of the LLNL handbook [17].
- The surrounding air is assumed to be an ideal gas.
- Viscous and turbulence effects are neglected (Euler equations).
- The effects of flow diffraction around the particles and particle-particle collisions are neglected.
- The formation of jets is not captured in the 1D simulations. Before detonation, granular powders and bulk liquids are assumed to be represented by homogeneously packed layers of solid particles or liquid droplets of finite size. As such, the fracturing of the compacted shell for solid powders, or the formation of nucleation sites for liquids described in Chapter 2 are not modeled.
- For granular powders, the compaction energy was assumed not to be recovered upon expansion of the particle bed. This key assumption was validated in a previous study [3] comparing experimental particle radius-time data with 1D numerical simulations.
- Vaporization of the liquids is not modeled.
- There is no mass exchange between the particles and the surrounding gas.

In Chapter 6, the same assumptions were made with several exceptions and additions.

- The C-4 booster was also modeled by the *programmed burn* function, but NM was modeled by the Sesame tabular EOS [18] due to a better match with experimental data. The Sesame EOS was used previously in EDEN to model the afterburning effects of TNT [8].
- The effects of radiation were neglected in the particle reaction modeling.
- The reaction energy was deposited into the particle phase only at a constant rate, and over a specified time defined as an input parameter. The amount of energy deposited was also an input parameter. This energy was subsequently released into the surrounding flow, primarily by drag and convective heat transfer.
- The reaction energy was dumped into the particle phase with no delay time as soon as processed by the detonation wave.

References

[1] Development team EDEN. EDEN user manual. Technical Report 12, Fluid Gravity Engineering (FGE), St, Andrews, Scotland, 2011.

[2] M. R. Baer and J. W. Nunziato. A two-phase mixture theory for the deflagration-to-detonation transition (ddt) in reactive granular materials. *International Journal of Multiphase Flow*, 12(6):861–889, 1986, doi:10.1016/0301-9322(86)90033-9.

[3] A. M. Milne, E. Floyd, A. W. Longbottom, and P. Taylor. Dynamic fragmentation of powders in spherical geometry. *Shock Waves*, 24(5):501–513, 2014, doi:10.1007/s00193-014-0511-x.

[4] A. M. Milne, A. Longbottom, D. L. Frost, J. Loiseau, S. Goroshin, and O. Petel. Explosive fragmentation of liquids in spherical geometry. *Shock Waves*, 27:383–393, 2017, doi:10.1007/s00193-016-0671-y.

[5] D. L. Frost, J-F. Ruel, Z. Zarei, S. Goroshin, Y. Grégoire, F. Zhang, A. Milne, and A. Longbottom. Explosive formation of coherent particle jets. *Journal of Physics: Conference Series*, (500), 2014, doi:10.1088/1742-6596/500/11/112026.

[6] D. L. Frost, J. Loiseau, S. Goroshin, F. Zhang, A. Milne, and A. Longbottom. Fracture of explosively compacted aluminum particles in a cylinder. *Journal of Physics: Conference Series*, pages 1–7, 2015, doi:doi.org/10.1063/1.4971701.

[7] A. M. Milne, S. B. Cargill, and A. W. Longbottom. Modelling of complex blast. *International Journal of Protective Structures*, 7(3):325–339, 2016, doi:10.1177/2041419616661431.

[8] A. Longbottom, J. Verreault, S. Cargill, and A. Milne. Effect of different numerical methods on the modelling of TNT afterburn in internal explosions. In *25th International Symposium on Military Aspects of Blast and Shock (MABS 25)*, pages 1–18, The Hague, Netherlands, 2018.

[9] R. M. Allen, D. J. Kirkpatrick, A.W. Longbottom, A. M. Milne, and N. K. Bourne. Experimental and numerical study of free-field blast mitigation. In *AIP Conference Proceedings*, volume 706, pages 823–826, 2004, doi:10.1063/1.1780363.

[10] A. M. Milne, K. Bennett, and A. W. Longbottom. Modelling of a suite of aluminised explosives experiments. *Proceedings of the 14th International Detonation Symposium*, pages 51–60, 2010.

[11] A. M. Milne, A. W. Longbottom, D. J. Evans, P. J. Haskins, M. D. Cook, and R. I. Briggs. The Burning Rate of Aluminium Particles in Nitromethane in Cylinder Tests. *12th International Symposium on Detonation*, pages 895–900, 2002.

[12] Q. Pontalier, J. Loiseau, A. Longbottom, and D. L. Frost. Simulating the propulsive capability of explosives loaded with inert and reactive materials. *AIP Conference Proceedings*, 2272, 2020, doi:10.1063/12.0000829.

[13] A. M. Milne. Gurney analysis of porous shell. *Propellants, Explosives, Pyrotechnics*, 41(4):665–671, 2016, doi:10.1002/prep.201600016.

[14] A. G. Milne, A. M. Milne, A. Burn, A. Carr, and M. Thomson. A modelling approach for the analysis of underwater explosive performance trials. *Propellants, Explosives, Pyrotechnics*, 46(12):1825–1836, 2021, doi:10.1002/prep.202100154.

[15] A. M. Milne, C. Parrish, and I. Worland. Dynamic fragmentation of blast mitigants. *Shock Waves*, 20:41–51, 2010, doi:10.1007/s00193-009-0235-5.

[16] E. L. Lee, H. C. Hornig, and J. W. Kury. Adiabatic expansion of high explosive detonation products. Technical report, Lawrence Radiation Lab, University of California, Livermore, 1968, https://www.osti.gov/servlets/purl/4783904.

[17] B. M. Dobratz and P. C. Crawford. LLNL explosives handbook - Properties of chemical explosives and explosive simulants. Technical report, Lawrence Livermore National Laboratory (LLNL), Livermore, California, 1985, https://www.osti.gov/biblio/6530310-llnl-explosives-handbook-properties-chemical-explosives-explosives-explosive-simulants.

[18] Sesame: the Los Alamos National Laboratory equation of state database. Technical report, Los Alamos National Laboratory, https://permalink.lanl.gov/object/tr?what=info:lanl-repo/lareport/LA-UR-92-3407.

Appendix C

Experimental investigation of blast mitigation and particle-blast interaction during the explosive dispersal of particles and liquids (supplementary materials)

These supplementary materials complement the results of Chapter 3. The materials include all the peak blast overpressures values obtained by the videography method (Figs. C.1–C.21) and the peak blast overpressures obtained by the fast-response pressure transducers (Tables C.1–C.8). The positive-phase impulses are also reported at the various distances from the charge center (Tables C.9–C.16). Peak overpressures as a function of M/C and the comparison between materials in the mid field are given in Figs. C.22–C.25. Finally, the trial matrix reporting all the trials tested, is reported at the end (Tables C.17–C.18).

Videos corresponding to the images shown in Figs. 1 and 25 in the paper have also been uploaded. The two videos corresponding to Fig. 1 illustrate examples of jet formation during the explosive dispersal of particles (silicon carbide) and a liquid (glycerol). The videos corresponding to the images in Fig. 25 include both the original high-speed videos as well as versions of the video processed to accentuate the visibility of the blast waves by subtracting consecutive video frames. To illustrate the sequence of image processing steps and fitting to the blast wave shown in Fig. 4 of the paper, a video has been uploaded, corresponding to the dispersal of Chronital steel.

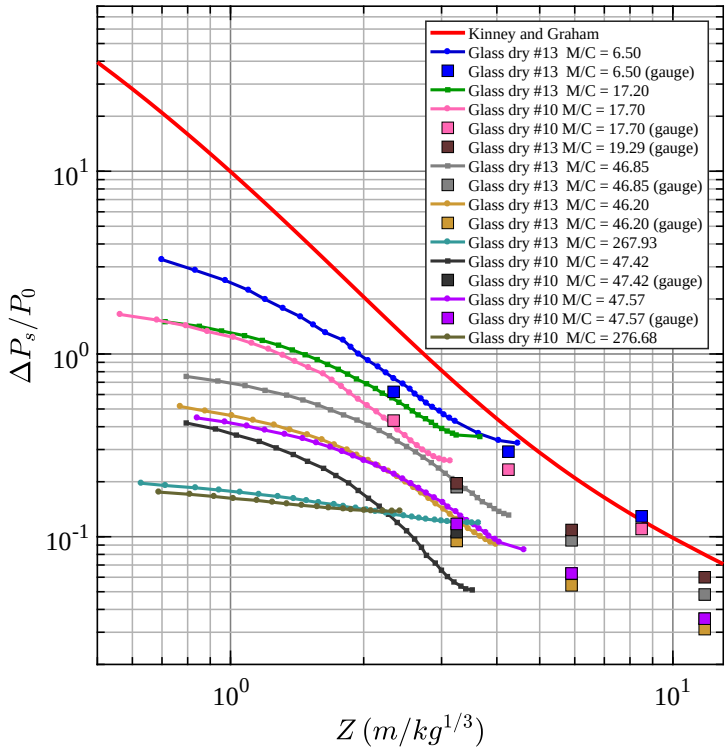

Fig. C.1 Peak overpressure as a function of Z for dry glass.

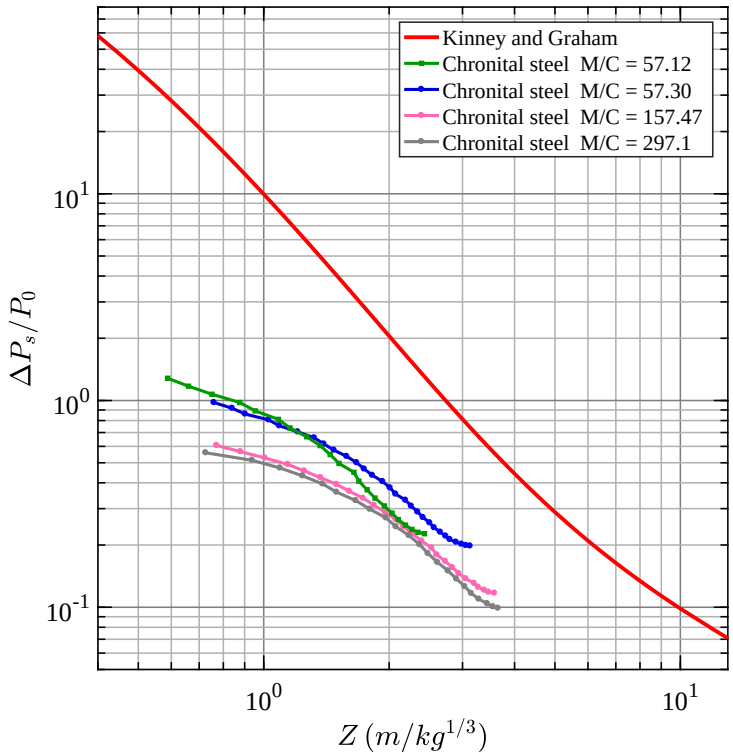

Fig. C.2 Peak overpressure as a function of Z for chronital steel.

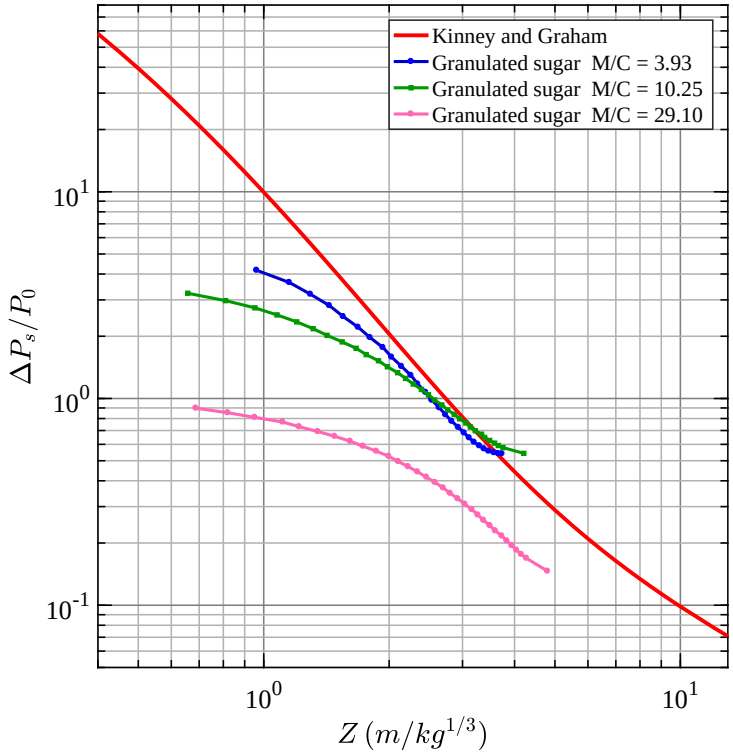

Fig. C.3 Peak overpressure as a function of Z for granulated sugar.

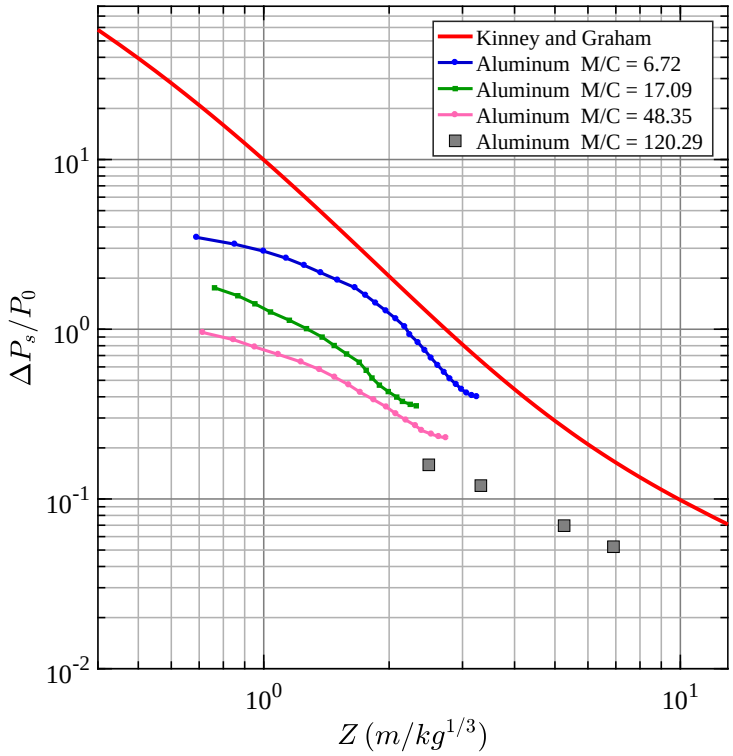

Fig. C.4 Peak overpressure as a function of Z for aluminum.

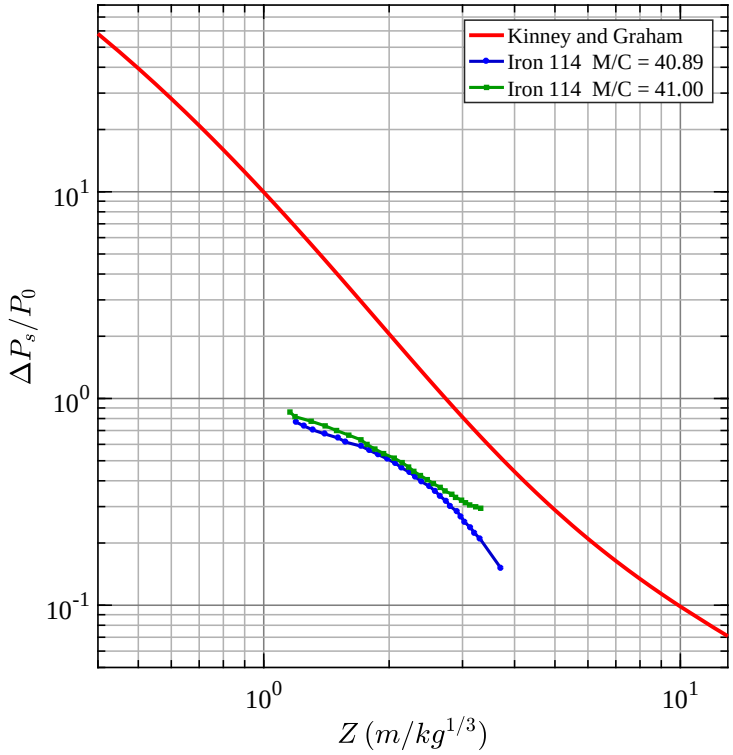

Fig. C.5 Peak overpressure as a function of Z for iron.

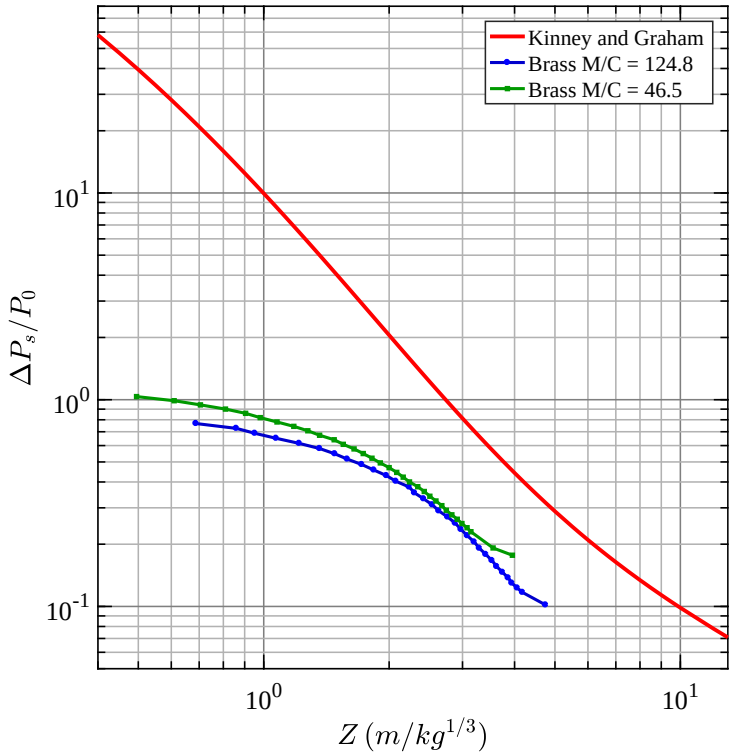

Fig. C.6 Peak overpressure as a function of Z for brass.

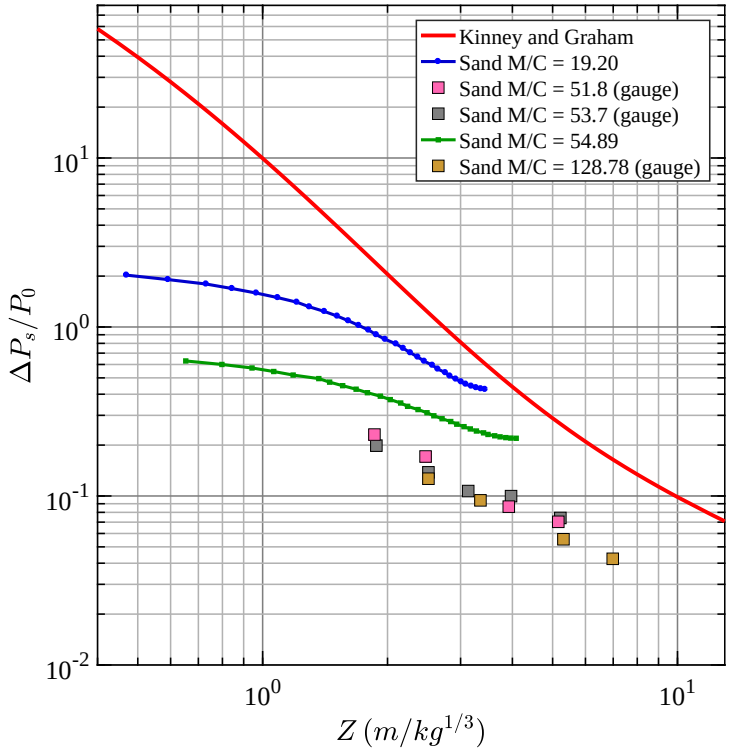

Fig. C.7 Peak overpressure as a function of Z for sand.

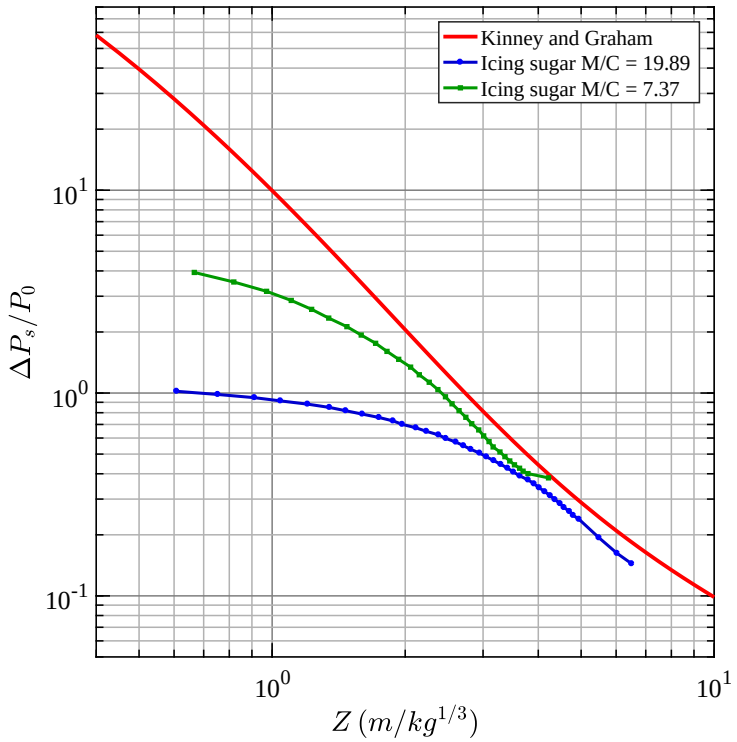

Fig. C.8 Peak overpressure as a function of Z for icing sugar.

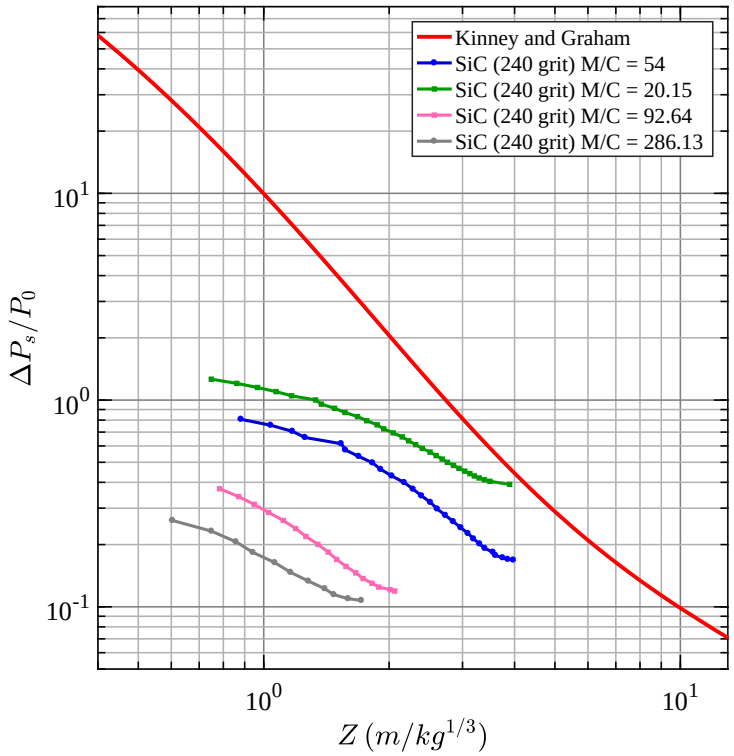

Fig. C.9 Peak overpressure as a function of Z for silicon carbide.

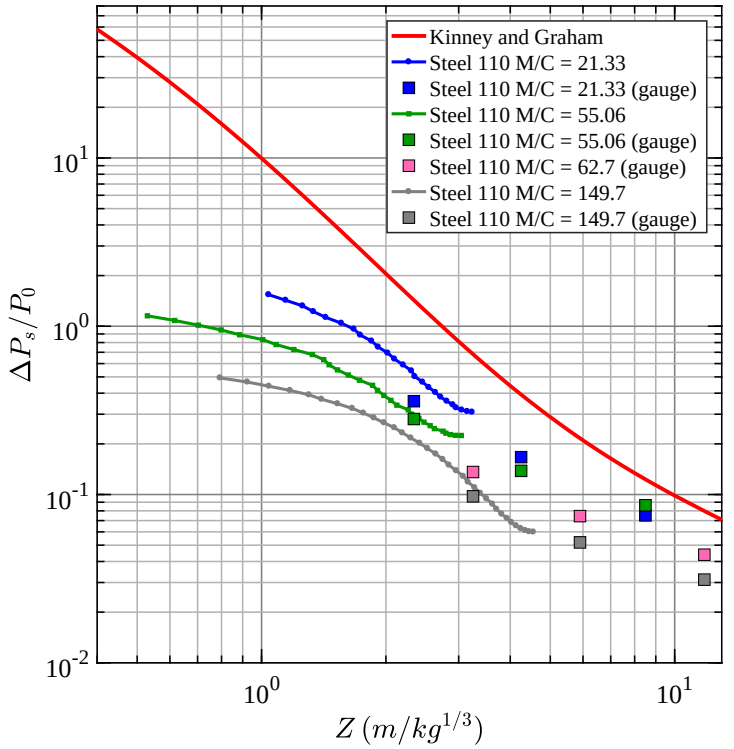

Fig. C.10 Peak overpressure as a function of Z for steel 110.

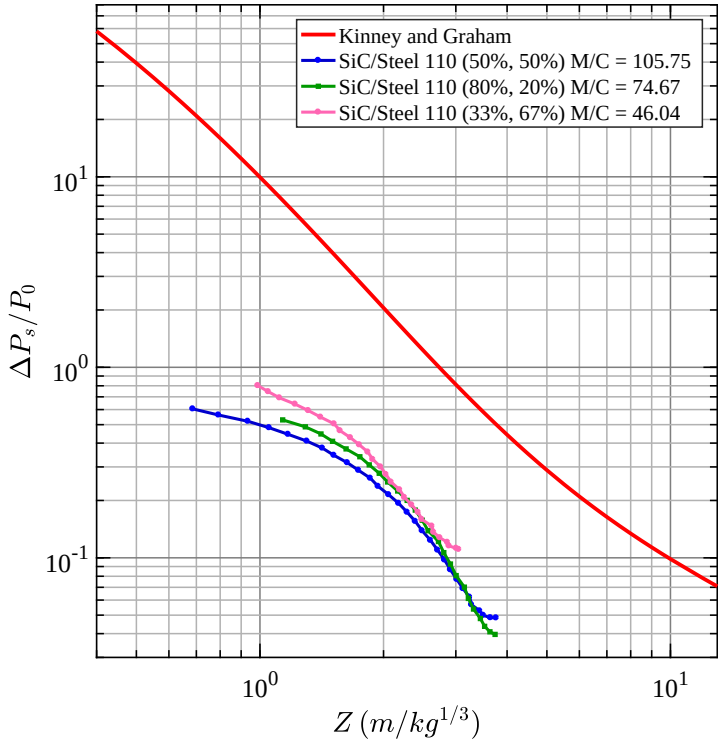

Fig. C.11 Peak overpressure as a function of Z for silicon carbide mixed with steel 110.

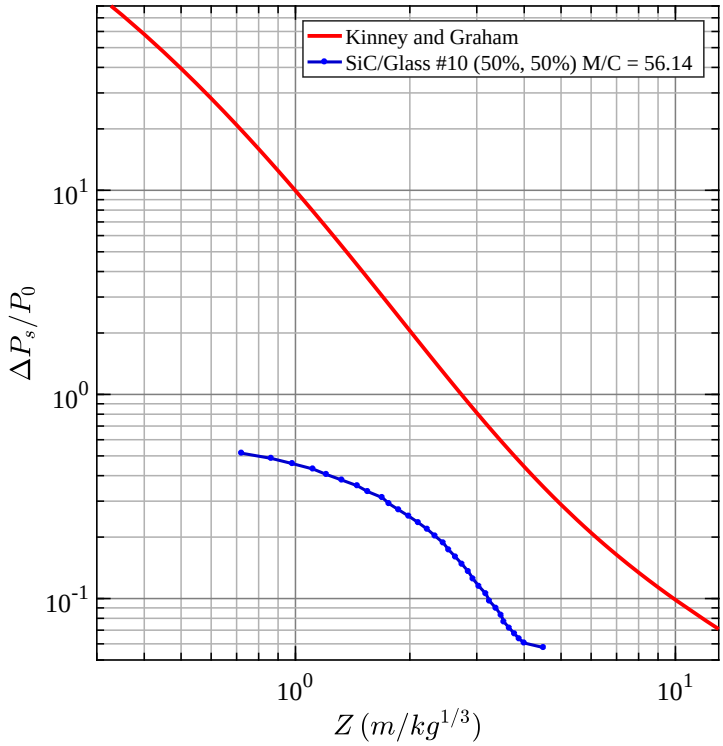

Fig. C.12 Peak overpressure as a function of Z for SiC/glass # 10.

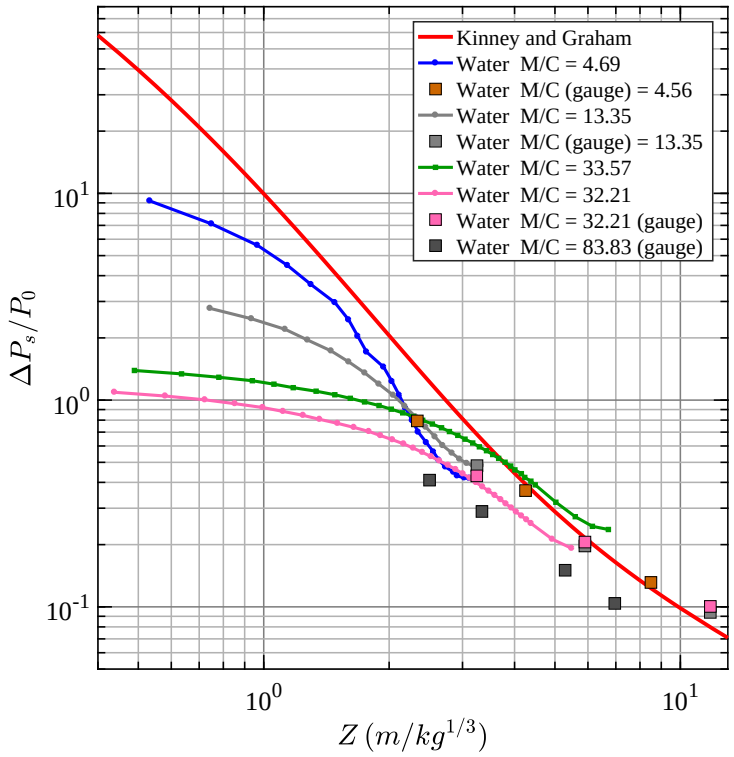

Fig. C.13 Peak overpressure as a function of Z for water.

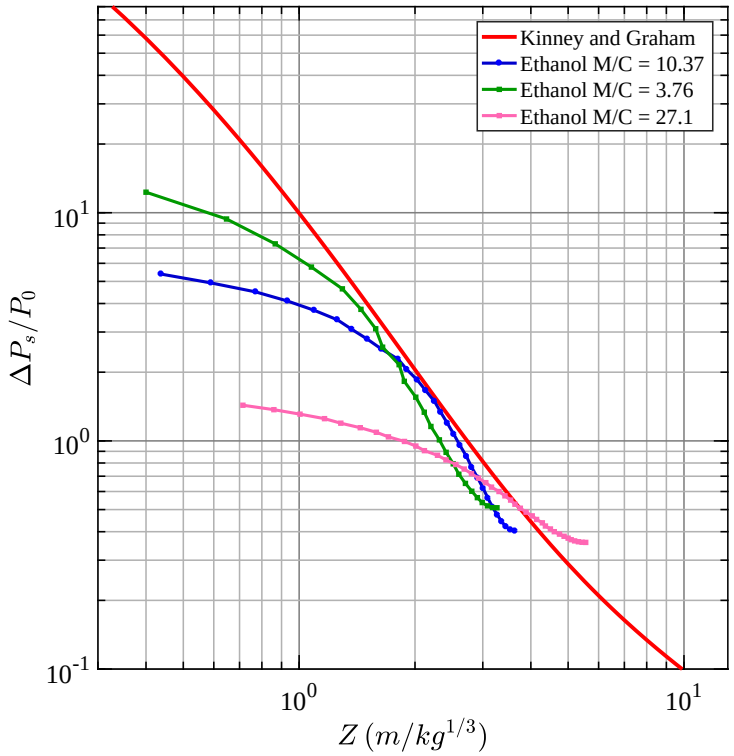

Fig. C.14 Peak overpressure as a function of Z for ethanol.

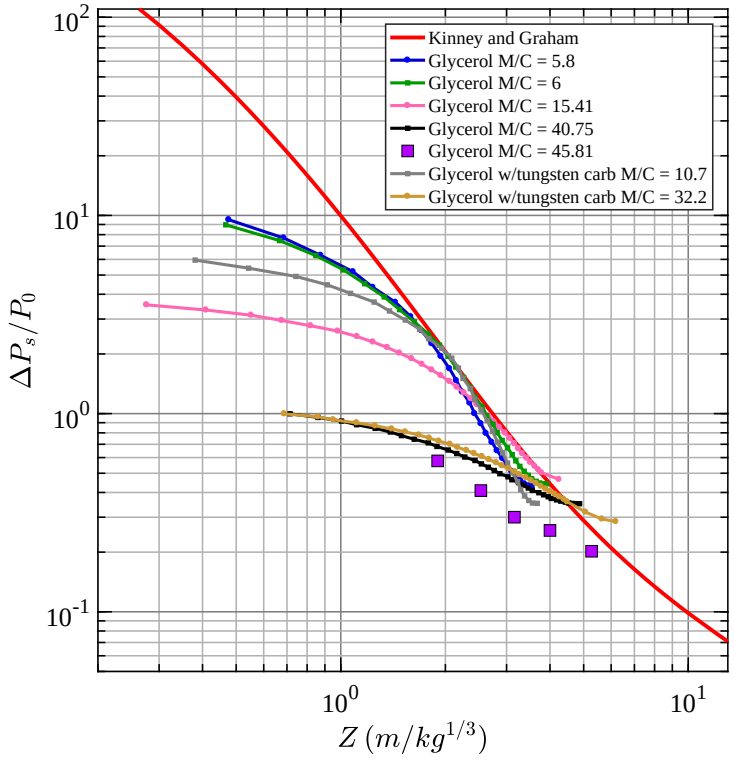

Fig. C.15 Peak overpressure as a function of Z for glycerol.

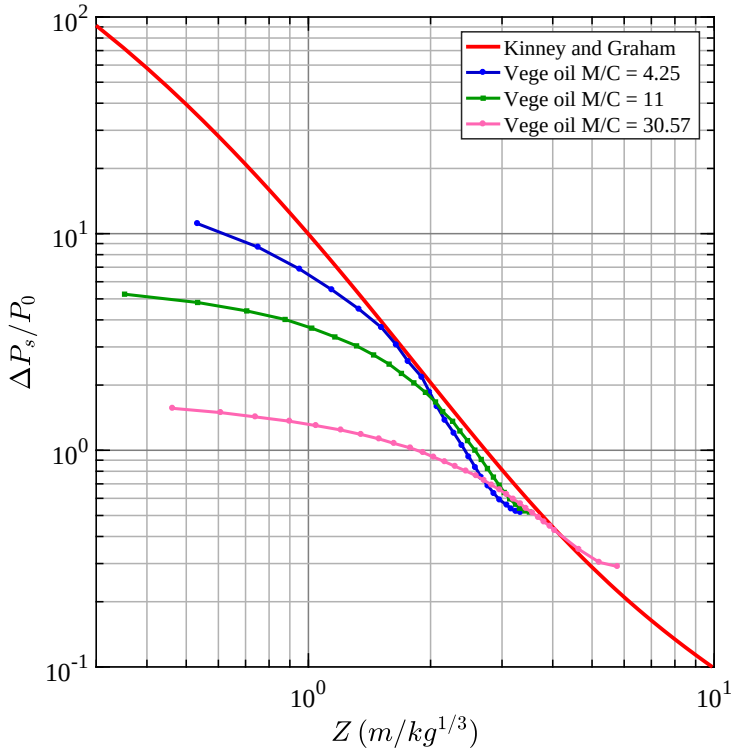

Fig. C.16 Peak overpressure as a function of Z for vegetable oil.

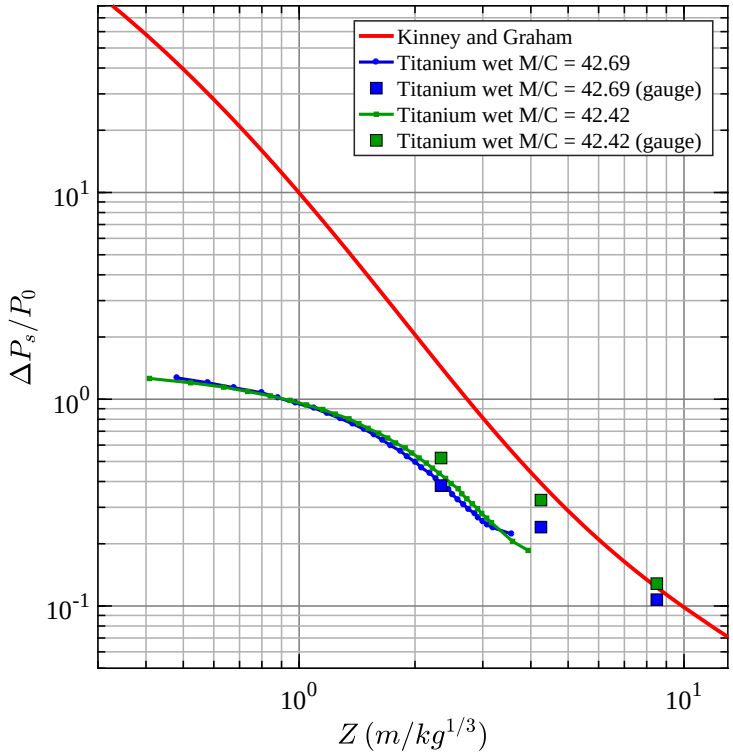

Fig. C.17 Peak overpressure as a function of Z for titanium saturated with water.

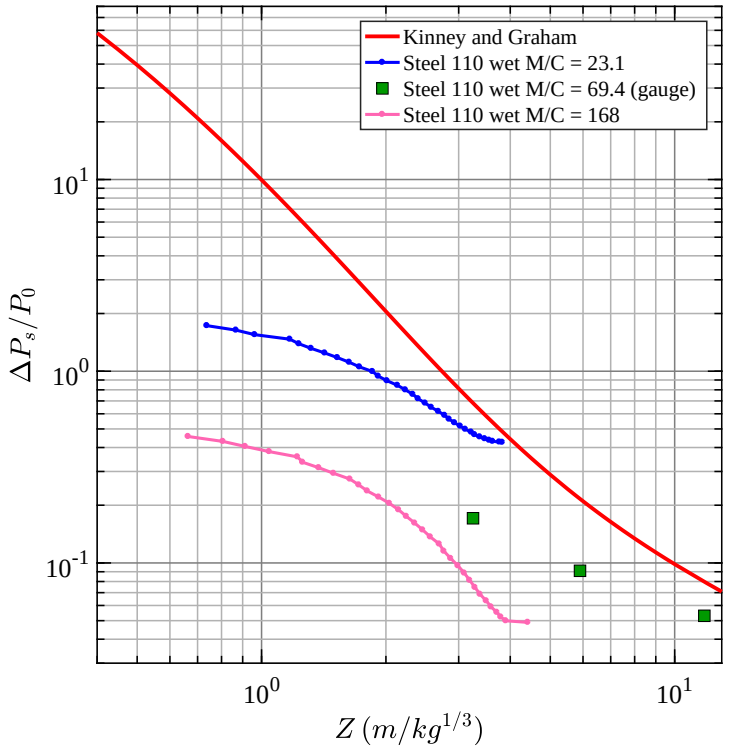

Fig. C.18 Peak overpressure as a function of Z for steel 110 saturated with water.

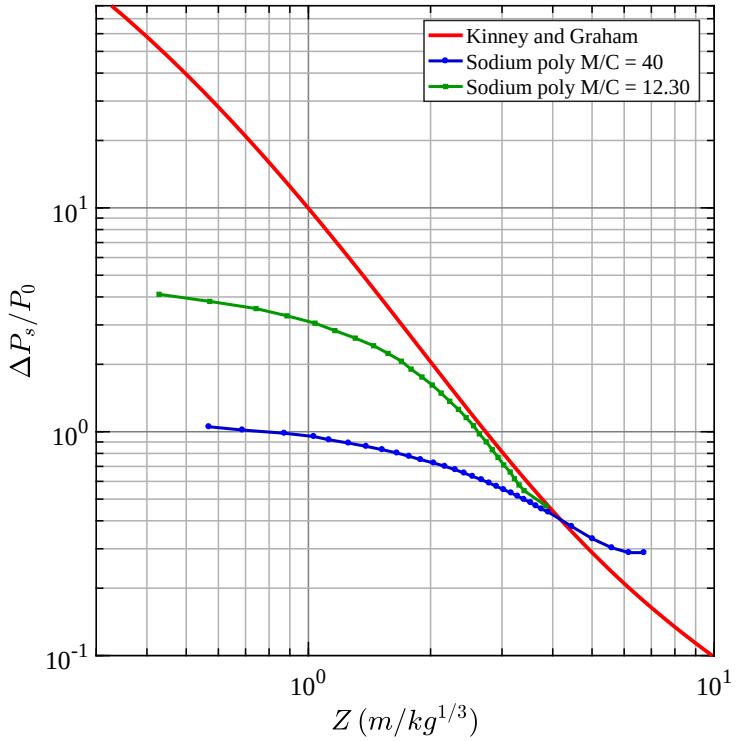

Fig. C.19 Peak overpressure as a function of Z for sodium polytungstate.

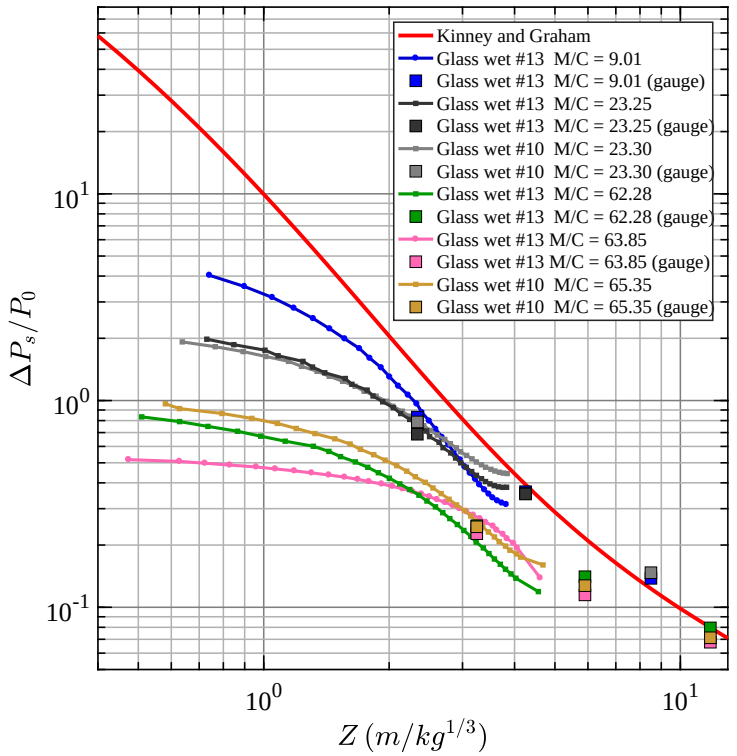

Fig. C.20 Peak overpressure as a function of Z for glass saturated with water.

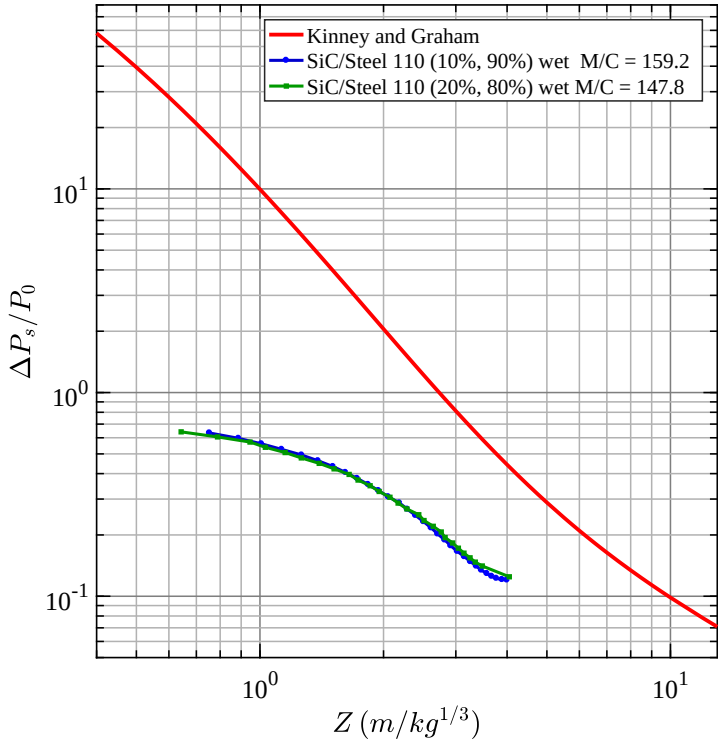

Fig. C.21 Peak overpressure as a function of Z for SiC/steel 110 saturated with water.

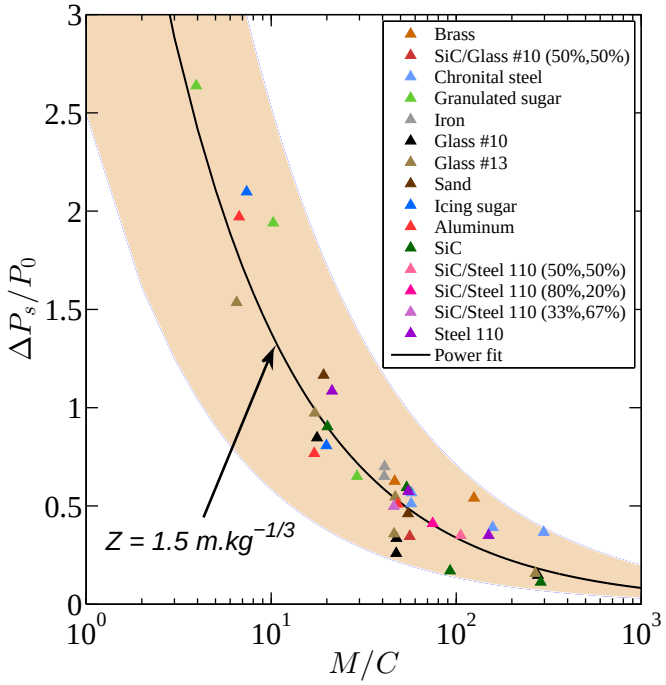

Fig. C.22 Peak blast wave overpressure as a function of M/C at $Z = 1.5$ m/kg$^{1/3}$ in the case of solid powders. Coefficients of the power law fit are $(\alpha, \beta) = (5.64, 0.611)$.

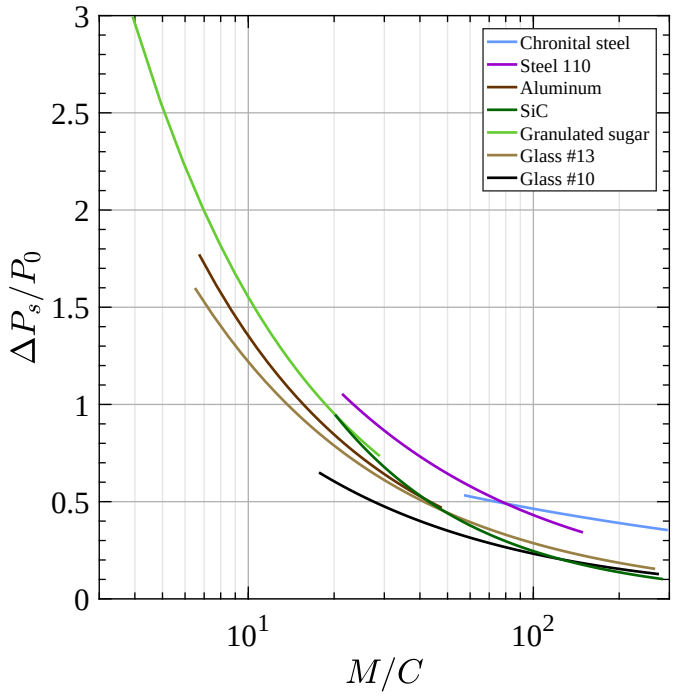

Fig. C.23 Comparison between peak blast wave overpressure as a function of M/C at $Z = 1.5$ m/kg$^{1/3}$ in the case of solid powders.

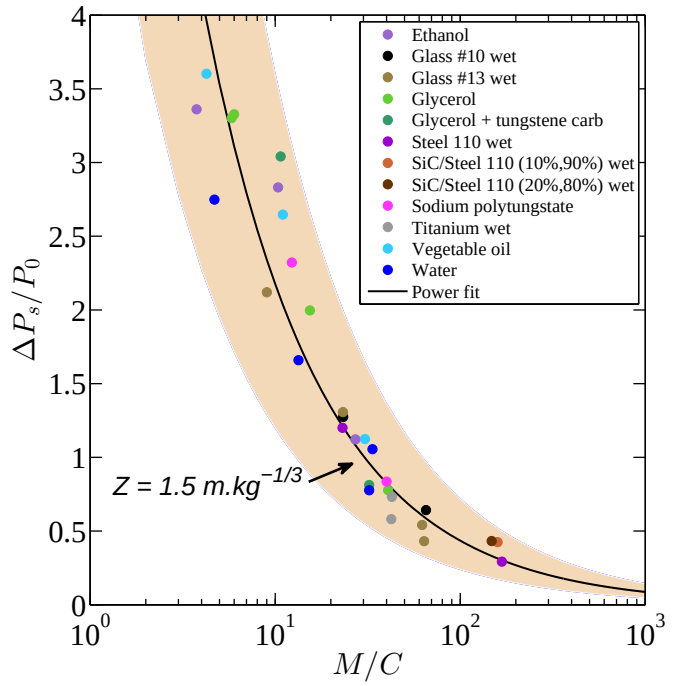

Fig. C.24 Peak blast wave overpressure as a function of M/C at $Z = 1.5$ m/kg$^{1/3}$ in the case of liquids/powders saturated with water. Coefficients of the power law fit are $(\alpha, \beta) = (10.88, 0.699)$.

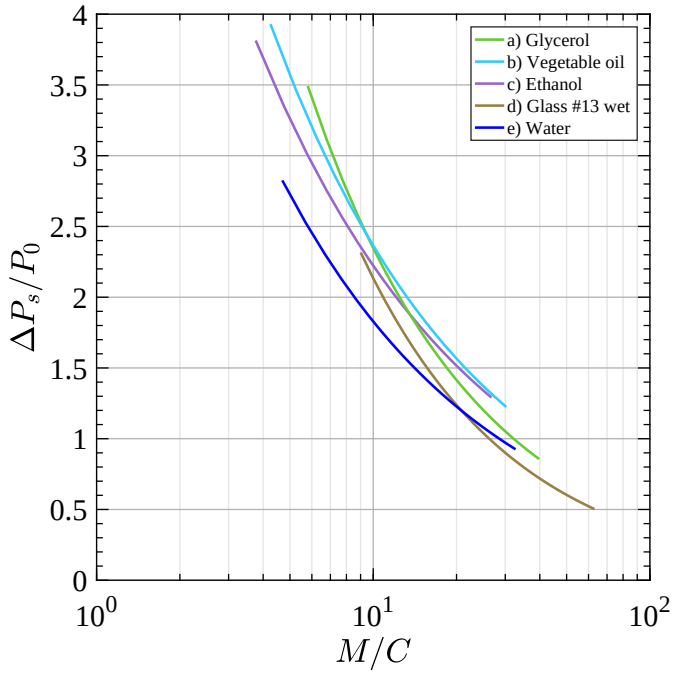

Fig. C.25 Comparison between peak blast wave overpressure as a function of M/C at $Z = 1.5$ m/kg$^{1/3}$ in the case of liquids or powders saturated with water.

Table C.1 Peak overpressures obtained with pressure gauges at 0.90 m from the explosion center (gauge resolution of 0.2 μs).

Materials	C (g)	M (g)	M/C	Z (m·kg$^{-1/3}$)	$\frac{\Delta P}{P_0}$ (pressure gauges)
Sand	79	4245	53.7	1.88	0.199
Sand	82	4250	51.8	1.86	0.231
Sand	33	4250	128.78	2.51	0.127
Aluminum	34	4090	120.29	2.49	0.159
Water	33.4	2800	83.83	2.50	0.410
Glycerol	77	3528	45.8	1.90	0.577

Table C.2 Peak overpressures obtained with pressure gauges at 1.1 m from the explosion center (gauge resolution of 5 μs).

Materials	C (g)	M (g)	M/C	Z (m·kg$^{-1/3}$)	$\frac{\Delta P}{P_0}$ (pressure gauges)
Steel 110	75	1600	21.3	2.34	0.359
Steel 110	75	4130	55.1	2.34	0.281
Steel 110	28	1756	62.7	3.25	0.136
Steel 110	28	4192	149.7	3.25	0.098
Glass dry #13	75	488	6.5	2.34	0.620
Glass dry #13	28	540	19.3	3.25	0.196
Glass dry #13	28	1312	46.9	3.25	0.187
Glass dry #13	28	1294	46.2	3.25	0.095
Glass dry #10	75	1328	17.7	2.34	0.432
Glass dry #10	28	1328	47.4	3.25	0.106
Glass dry #10	28	1332	47.6	3.25	0.117
Water	75	342	4.6	2.34	0.793
Water	28	374	13.4	3.25	0.482
Water	28	902	32.2	3.25	0.430
Glass wet #13	75	676	9.0	2.34	0.832
Glass wet #13	75	1744	23.3	2.34	0.687
Glass wet #13	28	1744	62.3	3.25	0.248
Glass wet #13	28	1788	63.9	3.25	0.227
Glass wet #10	75	1748	23.3	2.34	0.788
Glass wet #10	28	1830	65.4	3.25	0.245
Titanium wet	75	3202	42.7	2.34	0.382
Titanium wet	75	3182	42.4	2.34	0.520
Steel 110 wet	28	1950	69.9	3.25	0.171

Table C.3 Peak overpressures obtained with pressure gauges at 1.2 m from the explosion center (gauge resolution of 0.2 μs).

Materials	C (g)	M (g)	M/C	Z (m·kg$^{-1/3}$)	$\frac{\Delta P}{P_0}$ (pressure gauges)
Sand	79	4245	53.7	2.51	0.138
Sand	82	4250	51.8	2.47	0.171
Sand	33	4250	128.78	3.35	0.094
Aluminum	34	4090	120.29	3.32	0.120
Water	33.4	2800	83.83	3.34	0.289
Glycerol	77	3528	45.8	2.53	0.409

Table C.4 Peak overpressures obtained with pressure gauges at 1.5 m from the explosion center(gauge resolution of 0.2 μs).

Materials	C (g)	M (g)	M/C	Z (m·kg$^{-1/3}$)	$\frac{\Delta P}{P_0}$ (pressure gauges)
Sand	79	4245	53.7	3.13	0.107
Glycerol	77	3528	45.8	3.16	0.300

Table C.5 Peak overpressures obtained with pressure gauges at 1.9 m from the explosion center(gauge resolution of 0.2 μs).

Materials	C (g)	M (g)	M/C	Z (m·kg$^{-1/3}$)	$\frac{\Delta P}{P_0}$ (pressure gauges)
Sand	79	4245	53.7	3.97	0.100
Sand	82	4250	51.8	3.92	0.086
Sand	33	4250	128.78	5.31	0.055
Aluminum	34	4090	120.29	5.26	0.070
Water	33.4	2800	83.83	5.29	0.150
Glycerol	77	3528	45.8	4.00	0.257

Table C.6 Peak overpressures obtained with pressure gauges measurements at 2.0 m from the explosion center (gauge resolution of 5 μs).

Materials	C (g)	M (g)	M/C	Z (m·kg$^{-1/3}$)	$\frac{\Delta P}{P_0}$ (pressure gauges)
Steel 110	75	1600	21.3	4.25	0.167
Steel 110	75	4130	55.1	4.25	0.138
Steel 110	28	1756	62.7	5.90	0.074
Steel 110	28	4192	149.7	5.90	0.052
Glass dry #13	75	488	6.5	4.25	0.292
Glass dry #13	28	540	19.3	5.90	0.109
Glass dry #13	28	1312	46.9	5.90	0.096
Glass dry #13	28	1294	46.2	5.90	0.054
Glass dry #10	75	1328	17.7	4.25	0.233
Glass dry #10	28	1328	47.4	5.90	0.063
Glass dry #10	28	1332	47.6	5.90	0.063
Water	75	342	4.6	4.25	0.365
Water	28	374	13.4	5.90	0.197
Water	28	902	32.2	5.90	0.206
Glass wet #13	75	676	9.0	4.25	0.362
Glass wet #13	75	1744	23.3	4.25	0.353
Glass wet #13	28	1744	62.3	5.90	0.141
Glass wet #13	28	1788	63.9	5.90	0.115
Glass wet #10	75	1748	23.3	4.25	0.355
Glass wet #10	28	1830	65.4	5.90	0.127
Titanium wet	75	3202	42.7	4.25	0.241
Titanium wet	75	3182	42.4	4.25	0.325
Steel 110 wet	28	1950	69.9	5.90	0.091

Table C.7 Peak overpressures obtained with pressure gauges measurements at 2.5 m from the explosion center (gauge resolution of 0.2 μs).

Materials	C (g)	M (g)	M/C	Z (m·kg$^{-1/3}$)	$\frac{\Delta P}{P_0}$ (pressure gauges)
Sand	79	4245	53.7	5.22	0.074
Sand	82	4250	51.8	5.16	0.070
Sand	33	4250	128.78	6.98	0.042
Aluminum	34	4090	120.29	6.91	0.052
Water	33.4	2800	83.83	6.96	0.104
Glycerol	77	3528	45.8	5.27	0.202

Table C.8 Peak overpressures obtained with pressure gauges at 4.0 m from the explosion center (gauge resolution of 5 μs).

Materials	C (g)	M (g)	M/C	Z (m·kg$^{-1/3}$)	$\frac{\Delta P}{P_0}$ (pressure gauges)
Steel 110	75	1600	21.3	8.50	0.075
Steel 110	75	4130	55.1	8.50	0.086
Steel 110	28	1756	62.7	11.80	0.044
Steel 110	28	4192	149.7	11.80	0.031
Glass dry #13	75	488	6.5	8.50	0.129
Glass dry #13	28	540	19.3	11.80	0.044
Glass dry #13	28	1312	46.9	11.80	0.048
Glass dry #13	28	1294	46.2	11.80	0.031
Glass dry #10	75	1328	17.7	8.50	0.110
Glass dry #10	28	1328	47.4	11.80	0.036
Glass dry #10	28	1332	47.6	11.80	0.036
Water	75	342	4.6	8.50	0.131
Water	28	374	13.4	11.80	0.094
Water	28	902	32.2	11.80	0.100
Glass wet #13	75	676	9.0	8.50	0.138
Glass wet #13	75	1744	23.25	8.50	N.A.
Glass wet #13	28	1744	62.3	11.80	0.079
Glass wet #13	28	1788	63.9	11.80	0.068
Glass wet #10	75	1748	23.3	8.50	0.147
Glass wet #10	28	1830	65.4	11.80	0.071
Titanium wet	75	3202	42.7	8.50	0.107
Titanium wet	75	3182	42.4	8.50	0.128
Steel 110 wet	28	1950	69.9	11.80	0.053

Table C.9 Blast impulse calculated from pressure gauge measurements at 0.90 m from the explosion center (gauge resolution of 0.2 μs).

Materials	C (g)	M (g)	M/C	Z (m·kg$^{-1/3}$)	I^+ (bar·ms)	I_s^+ (bar·ms/kg$^{1/3}$)
Sand	79	4245	53.7	2.00	0.153	0.340
Sand	82	4250	51.8	1.98	0.146	0.321
Sand	33	4250	128.78	2.68	0.048	0.143
Aluminum	34	4090	120.29	2.65	0.045	0.132
Water	33.4	2800	83.83	2.67	0.235	0.698
Glycerol	77	3528	45.8	2.02	0.367	0.823

Table C.10 Blast impulse calculated from pressure gauge measurements at 1.1 m from the explosion center (gauge resolution of 5 μs).

Materials	C (g)	M (g)	M/C	Z (m·kg$^{-1/3}$)	I^+ (bar·ms)	I_s^+ (bar·ms/kg$^{1/3}$)
Steel 110	75	1600	21.3	2.49	0.131	0.296
Steel 110	75	4130	55.1	2.49	0.088	0.199
Steel 110	28	1756	62.7	3.46	0.048	0.151
Steel 110	28	4192	149.7	3.46	0.033	0.104
Glass dry #13	75	488	6.5	2.49	0.194	0.438
Glass dry #13	28	540	19.3	3.46	0.094	0.296
Glass dry #13	28	1312	46.9	3.46	0.058	0.182
Glass dry #13	28	1294	46.2	3.46	0.054	0.171
Glass dry #10	75	1328	17.7	2.49	0.195	0.440
Glass dry #10	28	1328	47.4	3.46	0.062	0.193
Glass dry #10	28	1332	47.6	3.46	0.065	0.203
Water	75	342	4.6	2.49	0.252	0.570
Water	28	374	13.4	3.46	0.149	0.468
Water	28	902	32.2	3.46	0.162	0.509
Glass wet #13	75	676	9.0	2.49	0.241	0.546
Glass wet #13	75	1744	23.3	2.49	0.265	0.601
Glass wet #13	28	1744	62.3	3.46	0.152	0.478
Glass wet #13	28	1788	63.9	3.46	0.146	0.459
Glass wet #10	75	1748	23.3	2.49	0.288	0.652
Glass wet #10	28	1830	65.4	3.46	0.139	0.438
Titanium wet	75	3202	42.7	2.49	0.244	0.553
Titanium wet	75	3182	42.4	2.49	0.262	0.592

Table C.11 Blast impulse calculated from pressure gauge measurements at 1.2 m from the explosion center (gauge resolution of 0.2 μs).

Materials	C (g)	M (g)	M/C	Z (m·kg$^{-1/3}$)	I^+ (bar·ms)	I_s^+ (bar·ms/kg$^{1/3}$)
Sand	79	4245	53.7	2.67	0.081	0.180
Sand	82	4250	51.8	2.64	0.127	0.278
Sand	33	4250	128.78	3.57	0.030	0.089
Aluminum	34	4090	120.29	3.54	0.032	0.095
Water	33.4	2800	83.83	3.56	0.173	0.513
Glycerol	77	3528	45.8	2.69	0.308	0.691

Table C.12 Blast impulse calculated from pressure gauge measurements at 1.5 m from the explosion center (gauge resolution of 0.2 μs).

Materials	C (g)	M (g)	M/C	Z (m·kg$^{-1/3}$)	I^+ (bar·ms)	I_s^+ (bar·ms/kg$^{1/3}$)
Sand	79	4245	53.7	3.34	0.075	0.166
Glycerol	77	3528	45.8	3.37	0.239	0.537

Table C.13 Blast impulse calculated from pressure gauge measurements at 1.9 m from the explosion center (gauge resolution of 0.2 μs).

Materials	C (g)	M (g)	M/C	Z (m·kg$^{-1/3}$)	I^+ (bar·ms)	I_s^+ (bar·ms/kg$^{1/3}$)
Sand	79	4245	53.7	4.23	0.066	0.147
Sand	82	4250	51.8	4.17	0.061	0.134
Sand	33	4250	128.78	5.65	0.018	0.055
Aluminum	34	4090	120.29	5.60	0.023	0.067
Water	33.4	2800	83.83	5.63	0.098	0.289
Glycerol	77	3528	45.8	4.26	0.188	0.421

Table C.14 Blast impulse calculated from pressure gauge measurements at 2.0 m from the explosion center (gauge resolution of 5 μs).

Materials	C (g)	M (g)	M/C	Z (m·kg$^{-1/3}$)	I^+ (bar·ms)	I_s^+ (bar·ms/kg$^{1/3}$)
Steel 110	75	1600	21.3	4.53	0.074	0.168
Steel 110	75	4130	55.1	4.53	0.053	0.119
Steel 110	28	1756	62.7	6.29	0.030	0.094
Steel 110	28	4192	149.7	6.29	0.020	0.064
Glass dry #13	75	488	6.5	4.53	0.126	0.286
Glass dry #13	28	540	19.3	6.29	0.057	0.178
Glass dry #13	28	1312	46.9	6.29	0.041	0.130
Glass dry #13	28	1294	46.2	6.29	0.033	0.102
Glass dry #10	75	1328	17.7	4.53	0.123	0.278
Glass dry #10	28	1328	47.4	6.29	0.037	0.115
Glass dry #10	28	1332	47.6	6.29	0.039	0.124
Water	75	342	4.6	4.53	0.159	0.361
Water	28	374	13.4	6.29	0.088	0.277
Water	28	902	32.2	6.29	0.097	0.306
Glass wet #13	75	676	9.0	4.53	0.140	0.318
Glass wet #13	75	1744	23.3	4.53	0.176	0.397
Glass wet #13	28	1744	62.3	6.29	0.087	0.274
Glass wet #13	28	1788	63.9	6.29	0.085	0.267
Glass wet #10	75	1748	23.3	4.53	0.177	0.401
Glass wet #10	28	1830	65.4	6.29	0.081	0.254
Titanium wet	75	3202	42.7	4.53	0.161	0.364
Titanium wet	75	3182	42.4	4.53	0.172	0.389

Table C.15 Blast impulse calculated from pressure gauge measurements at 2.5 m from the explosion center (gauge resolution of 0.2 μs).

Materials	C (g)	M (g)	M/C	Z (m·kg$^{-1/3}$)	I^+ (bar·ms)	I_s^+ (bar·ms/kg$^{1/3}$)
Sand	79	4245	53.7	5.56	0.053	0.119
Sand	82	4250	51.8	5.49	0.055	0.122
Sand	33	4250	128.78	7.44	0.016	0.048
Aluminum	34	4090	120.29	7.37	0.019	0.056
Water	33.4	2800	83.83	7.41	0.076	0.226
Glycerol	77	3528	45.8	5.61	0.160	0.358

Table C.16 Blast impulse calculated from pressure gauge measurements at 4.0 m from the explosion center (gauge resolution of 5 μs).

Materials	C (g)	M (g)	M/C	Z (m·kg$^{-1/3}$)	I^+ (bar·ms)	I_s^+ (bar·ms/kg$^{1/3}$)
Steel 110	75	1600	21.3	9.05	0.045	0.102
Steel 110	75	4130	55.1	9.05	0.026	0.059
Steel 110	28	1756	62.7	12.57	0.016	0.049
Steel 110	28	4192	149.7	12.57	0.010	0.031
Glass dry #13	75	488	6.5	9.05	0.054	0.123
Glass dry #13	28	540	19.3	12.57	0.016	0.093
Glass dry #13	28	1312	46.9	12.57	0.020	0.062
Glass dry #13	28	1294	46.2	12.57	0.018	0.056
Glass dry #10	75	1328	17.7	9.05	0.062	0.140
Glass dry #10	28	1328	47.4	12.57	0.019	0.059
Glass dry #10	28	1332	47.6	12.57	0.020	0.063
Water	75	342	4.6	9.05	0.073	0.165
Water	28	374	13.4	12.57	0.044	0.138
Water	28	902	32.2	12.57	0.049	0.154
Glass wet #13	75	676	9.0	9.05	0.074	0.168
Glass wet #13	75	1744	23.3	9.05	N.A.	N.A.
Glass wet #13	28	1744	62.3	12.57	0.045	0.142
Glass wet #13	28	1788	63.9	12.57	0.044	0.137
Glass wet #10	75	1748	23.3	9.05	0.092	0.208
Glass wet #10	28	1830	65.4	12.57	0.043	0.134
Titanium wet	75	3202	42.7	9.05	0.072	0.162
Titanium wet	75	3182	42.4	9.05	0.076	0.172

Table C.17 Trial matrix for dry powders.

Material	**C4 mass C (g)**	**Mitigant mass M (g)**	M/C
Data extracted from	**P: Pressure gauges**	**V: Videos**	
H95 aluminum (V)	75	1282	17.09
H95 aluminum (V)	28	1354	48.36
H95 aluminum (V)	75	504	6.72
H95 aluminum (P)	34	4090	120.29
Chronital steel (V)	75	4297.8	57.30
Chronital steel (V)	75	4283.7	57.12
Chronital steel (V)	28	4409.2	157.47
Chronital steel (V)	15	4456.4	297.1
Iron 114 (V)	75	3067.4	40.90
Iron 114 (V)	75.1	3079.3	41.00
Steel 110 (V+P)	75	1600	21.33
Steel 110 (V+P)	75	4130	55.07
Steel 110 (P)	28	1756	62.71
Steel 110 (V+P)	28	4192	149.71
Granulated sugar (V)	28	815	29.11
Granulated sugar (V)	75	295	3.93
Granulated sugar (V)	75	769	10.25
Icing sugar (V)	28	557	19.89
Icing sugar (V)	75	553	7.37
Brass (V)	28	3495	124.82
Brass (V)	75	3490	46.53
Silicon carbide-Steel 110 (50:50) (V)	28	2961	105.75
Silicon carbide-Steel 110 (80:20) (V)	28	2091	74.68
Silicon carbide-steel 110 (33:67) (V)	75	3453	46.04
Glass dry #13 (V+P)	75	488	6.51
Glass dry #13 (V)	75	1290	17.20
Glass dry #13 (P)	28	540	19.29
Glass dry #13 (V+P)	28	1312	46.86
Glass dry #13 (V+P)	28	1294	46.21
Glass dry #13 (V)	28	7502.1	267.93
Glass dry #10 (V+P)	75	1328	17.71
Glass dry #10 (V+P)	28	1328	47.43
Glass dry #10 (V+P)	28	1332	47.57
Glass dry #10 (V)	28	7747.2	276.68
Silicon carbide (240 grit) (V)	28	1512.52	54.02
Silicon carbide (240 grit) (V)	75	1511.65	20.16
Silicon carbide (240 grit) (V)	75	6948.21	92.64
Silicon carbide (240 grit) (V)	28	8011.52	286.13
Sand (V)	28	1537.16	54.90
Sand (V)	75	1440.14	19.20
Sand (P)	79	4245	53.73
Sand (P)	82	4250	51.83
Sand (P)	33	4250	128.79

Table C.18 Trial matrix for liquids and powders saturated with water.

Material	**C4 mass C (g)**	**Mitigant mass M (g)**	M/C
Data extracted from	**P: Pressure gauges**	**V: Videos**	
Silicon carbide-glass #10 (50:50) (V)	28	1572	56.14
Water (V)	75	352	4.69
Water (P)	75	342	4.56
Water (V+P)	28	374	13.36
Water (V)	28	940	33.57
Water (V+P)	28	902	32.21
Water (P)	33.4	2800	83.83
Glycerol (V)	75	450	6.00
Glycerol (V)	75	436	5.81
Glycerol (V)	75	1156	15.41
Glycerol (V)	28	1141	40.75
Glycerol (P)	77	3528	45.82
Glycerol with tungstene carbide (V)	75	803	10.71
Glycerol with tungstene carbide (V)	28	902	32.21
Vege oil (V)	75	319	4.25
Vege oil (V)	75	825	11.00
Vege oil (V)	28	856	30.57
Ethanol (V)	75	778	10.37
Ethanol (V)	75	282	3.76
Ethanol (V)	28	760	27.14
Sodium poly (V)	28	1120	40.00
Sodium poly (V)	75	923	12.31
Titanium wet (V+P)	75	3202	42.69
Titanium wet (V+P)	75	3182	42.43
Glass wet #13 (V+P)	75	676	9.01
Glass wet #13 (V+P)	75	1744	23.25
Glass wet #13 (V+P)	28	1744	62.29
Glass wet #13 (V+P)	28	1788	63.86
Glass wet #10 (V+P)	75	1748	23.31
Glass wet #10 (V+P)	28	1830	65.36
Steel 110 wet (V)	28.25	4748	168.07
Steel 110 wet (P)	28	1950	69.64
Steel 110 wet (V)	75	1734	23.1
Silicon carbide-steel 110 wet (20:80) (V)	28.2	4168	147.80
Silicon carbide-steel 110 wet (10:90) (V)	28	4458	159.21